Modelling and Topographical Study of the Precision Grinding Process

Nguyen Tuan Anh

School of Mechanical & Aerospace Engineering

A thesis submitted to the Nanyang Technological University
in fulfilment of the requirement for the degree of
Doctor of Philosophy

2006

Công Cha như núi Thái Sơn
Nghĩa Mẹ như nước trong nguồn chảy ra

Acknowledgements

This thesis could not have been completed without help from many people in the last three years. First of all, I would like to express sincere appreciation to my research supervisor, Prof. David Lee Butler, for his encouragement, support, and guidance; special thanks for his patience and support in my lowest moments. It was privileged to have him as a supervisor in the last three years.

The grateful appreciation is also to Prof. Lam Yee Chong for his advices, especially in the first year. Sincere thanks also go to Prof. Idapalapati Shridhar for his helpful comments, and Prof. Liew Kim Meow for providing working space and computing facilities.

Many people, some of them I have never met, have generously offered their great help. To those I would like to take this opportunity to express sincere gratitude. Those include Prof. Andrew Torrance (Trinity College) and Prof. Kato (Tohoku) for the copies of their papers, Prof. Jaroslav Mackerle (Linkoping) for accessing to his bibliographical database, Dr. Chandrakanth Shet (Florida State University) for the FEM model, the support engineers at HKS Inc. and Worley Ltd., Mr. Mack Wong (CNC Lab) and Mr. Chen Wei Kian (Simtech) for helping with experiments, my friend Manh for providing scanned copies of papers.

I am indebted to Nanyang Technological University for the research scholarship. The opportunity of doing research at NTU has been introduced to me by Prof. Stephen Lee and Prof. Nguyen Phu Hung, whom I would like acknowledge.

Deepest thanks and love to my family, the small one and the bigger one.

Contents

List of figures

List of tables

List of symbols

a	wheel depth of cut
a_d	truing depth
A_r	area of side ridge
a_r	actual depth of cut
b	width of grinding
D	subset of n-dimensional space R^n (parameter space)
d_e	equivalent wheel diameter
d_g	mean diameter of abrasive grains
d_{ij}	distance from cutting edge to the centre of a grinding wheel
d_s	wheel diameter
d_w	workpiece diameter
$E[.]$	expectation
F, F_{XX}, F_{YY}	distribution function
F^{-1}	inverse function of F
$\mathcal{F}$	σ-algebra of events
f, f_p, f_q	frequency
f_X, f_Y	marginal probability density function
f_{XX}, f_{YY}	joint probability density function
g_{mn}, g_{ij}	workpiece surface topography
h	perpendicular bisector (or median) of triangle
h_{max}	the highest point in the grinding wheel topography
h_{mn}, h_{ij}	grinding wheel topography
$J(.)$	Jacobian
k_a	contact stiffness
k_c	cutting stiffness
k_e	effective stiffness
k_m	machine stiffness
$K_X(\boldsymbol{r}_1, \boldsymbol{r}_2)$	covariance function
l	base side of a triangular side ridge
ΔL_{ij}	peripheral distance of cutting point h_{ij}

L_x, L_y	sampling length in x and y directions
M	sampling matrix size in x direction
$m_X(.)$	mean of random variable X
N	sampling matrix size in y direction
ΔO_{ij}	distance in x coordinate between the local and global coordinate origins O', O
P	probability
R	radius of grain tip
r	grain depth of cut
r_{ij}	distance in z coordinate between the local and global coordinate origins O', O
R_s	radius of the stylus
$\boldsymbol{r}, \boldsymbol{r}_i$	point in parameter space D
S_{al}	fastest decay autocorrelation length
S_{bi}	surface bearing index
S_{ci}	core fluid retention index
S_{ds}	density of summits
S_{dr}	developed surface area ratio
S_{ku}	kurtosis of height distribution
S_q	root mean square deviation
S_{sc}	arithmetic mean summit curvature
S_{sk}	skewness of height distribution
S_{td}	texture direction
S_{tr}	texture aspect ratio
S_{vi}	valley fluid retention index
S_z	ten point height
$S_{\Delta q}$	root- mean- square slope
s_d	truing lead
v_d	peripheral velocity of truer
v_s	peripheral velocity of grinding wheel
v_w	workpiece velocity
w	transverse step in surface grinding
X, X_1, X_2	random variable
x	Cartesian coordinate
$X(\boldsymbol{r})$	random field
Δx	sampling interval in x direction

Δx_s	sampling step between rows of grinding wheel topographic array $[h_{ij}]$
Δx_w	sampling step between rows of workpiece topographic array $[g_{ij}]$
Y, Y_1, Y_2	random variable
y	Cartesian coordinate
Δy	sampling interval in y direction
Z	random variable of the standard normal distribution
z	Cartesian coordinate
α	attack angle of cutting edge
α_p	critical attack angle, smaller than which a cutting edge will only plough
α_r	critical attack angle, smaller than which a cutting edge will only rub
β	decay parameter
β_1	square of skewness
β_2	kurtosis
γ	Johnson transform shape factor
δ	Johnson transform shape factor
$\eta(x,y)$	surface height from the reference plane
θ	rotation angle of grinding wheel
κ	summit curvature
λ	Johnson transform scale factor
λ_s	smallest wavelength measurable by the stylus instrument
ξ	Johnson transform location factor
$\boldsymbol{\tau}$, τ	lag vector, distance
φ	ploughing coefficient
Φ	standard normal distribution function
ψ	clearance angle of cutting tool
Ω	sample space (the set of all possible outcome)
ω	outcome of a random experiment
ω, ω_x, ω_y	harmonic frequency

Abstract

Despite its long history, grinding is still an important component of a modern manufacturing process. Its important role, together with its complex nature has made the grinding process a fascinating object of extensive research in the last 30 years. This thesis reports research focused on two issues in grinding: topographical characterisation of the grinding wheel surface and modelling of the grinding process.

Characterisation of the grinding wheel surface entails two aspects: measurement and analysis. A majority of grinding wheel surfaces studied in this thesis were measured on a three-dimensional stylus system. Direct measurement of the grinding wheel surface using a stylus system is impossible or undesirable due to the wheel bulky size, complicated wheel re-positioning or difficulty in-process monitoring; hence replication of the surface is often required. A novel technique for replicating the grinding wheel surface is described and verified for a broad range of grinding wheels. The other problem concerning the measurement of the grinding wheel surface is the selection of the stylus speed. The effects of the stylus speed on the measurement fidelity are studied, especially in the context of measuring the grinding wheel surface.

The analysis approach applied in this study is three-dimensional surface parameters. In order to apply the 3D parameters, a MATLAB toolbox is designed and coded. The algorithms for the toolbox are discussed. The toolbox is verified for various types of surfaces; its results are compared with other commercial software. As the estimation of the 3D parameters is dependent on the sampling conditions, the sampling conditions are discussed. The effects of the sampling interval on the 3D parameters are explained on the basis of radial power spectrum analysis. Criteria for selecting the

sampling conditions for grinding wheel and ground workpiece surfaces are studied and proposed. The criteria are based on the correlation length of the topography. It is shown that the criteria can be applied to other isotropic and anisotropic surfaces.

In order to prove the applicability of the 3D parameters for characterising the grinding process, a set of experiments are conducted. The correlation between the parameters, the grinding forces, and workpiece surface quality are proved through a 2^3 factorial experiment design, in which the truer velocity, truing lead, and truing depth are varied. Studying the parameters S_q, S_{ds}, and S_{sc} of the wheel and workpiece surfaces, and the grinding forces shows that there exits a dependence between the parameters.

The modelling approach used in this study is kinematic modelling, in which the workpiece surface is generated from the grinding wheel topography using the kinematic relationship between the wheel and the workpiece. Two issues that are essential to modelling are discussed. Those are the generation of the grinding wheel surface and the interaction between the workpiece and the abrasive grain.

For generating the grinding wheel surface, a novel numerical procedure is proposed. By appropriate choosing transform functions, it is shown that grinding wheel surfaces can be effectively simulated. The sufficient condition for choosing the transform function is discussed. To illustrate the approach a few examples of grinding wheel surface are used. It is proved that the sampled and simulated surfaces are statistically identical.

The interaction of the workpiece and the abrasive grain involves three modes: cutting, ploughing, and rubbing. To account for the three modes, an attack angle of the abrasive grain is proposed as the criterion. An algorithm for identifying the active grains on the surface and to estimate their attack angles is described; the problem of side ridges

formed on the workpiece surface is also taken into account. A simulation procedure for the kinematic modelling is suggested. The simulation inputs are the wheel topography, wheel velocity, workpiece velocity, wheel diameter and depth of cut. The output is the workpiece surface topography. In order to prove the concepts, two sets of experiments are implemented. The experiments show that the simulation procedure can adequately simulate the workpiece surface.

Chapter 1

Introduction

1.1 Motivation

Grinding is probably the oldest manufacturing process in the history of civilisation. The birth of grinding technology could be traced back to the Stone Age when prehistoric men learned to grind stone and other materials to form tools and other useful objects. The invention of the grinding method was almost crucial for mankind civilisation as it enabled primitive man to produce tools of superior quality than he had been able to do by chipping and flaking. By the use of grinding techniques early man then could make stone axes, knives and other cutting tools out of nearly any hard material available to him. With the beginning of the Industrial Revolution, grinding's role as a manufacturing process became more significant. Mass production of precision hardened steel parts, required for automobile industry and others would not be possible without the invention of the first grinding wheel and machine in the 19th century (Woodbury 1972).

Nowadays, grinding remains an important component of a modern manufacturing process despite the availability of new manufacturing technology. In fact, it has taken on an increased importance because it is a finishing process with a low material removal rate, making it the process best suited for producing parts of high precision and high surface quality. Moreover, it is the process suitable to machining many advanced ceramic materials, which are difficult to machine due to their high hardness and brittleness. In a 1997 survey (Tonshoff et al. 1998), answering the question about the application of cutting and abrasive processes, 25% of surveyed manufacturing companies nominated grinding as the most important technology while for turning, milling, and drilling the number was only 67% in total. The machine park distribution in the manufacturing plants showed an even greater dominance of grinding as a major production process; 42% of the installed machine tools are grinding machines. More recent data (EMO 2001) shows that grinding machines still form a large part of precision machines.

The importance of grinding as a manufacturing process is even more evident if considering the percentage of the process in terms of cost, which can range from 50% of the total manufacturing cost for metal (Machinability Data Center 1980) to 80% for ceramics (Malkin and Huang 1996). It is not surprising that the grinding process has been the subject of extensive research, especially during the past 35 years (Malkin 1989). This is because only the fundamental understanding of the process allows for its optimisation.

1.2 Issues in grinding research

Despite the vast amount of research, a complete understanding of the grinding process has yet to be achieved. It is due to the complex nature of the process, which is

affected by many factors, involving wheel, workpiece, machine, and process setting (Figure 1.1). In order to optimise the process, understanding the influence of the factors on grinding performance is essential. Unfortunately, studying the grinding process is not an easy task due to the interaction of the factors, which could include chemical, thermal, and mechanical effects.

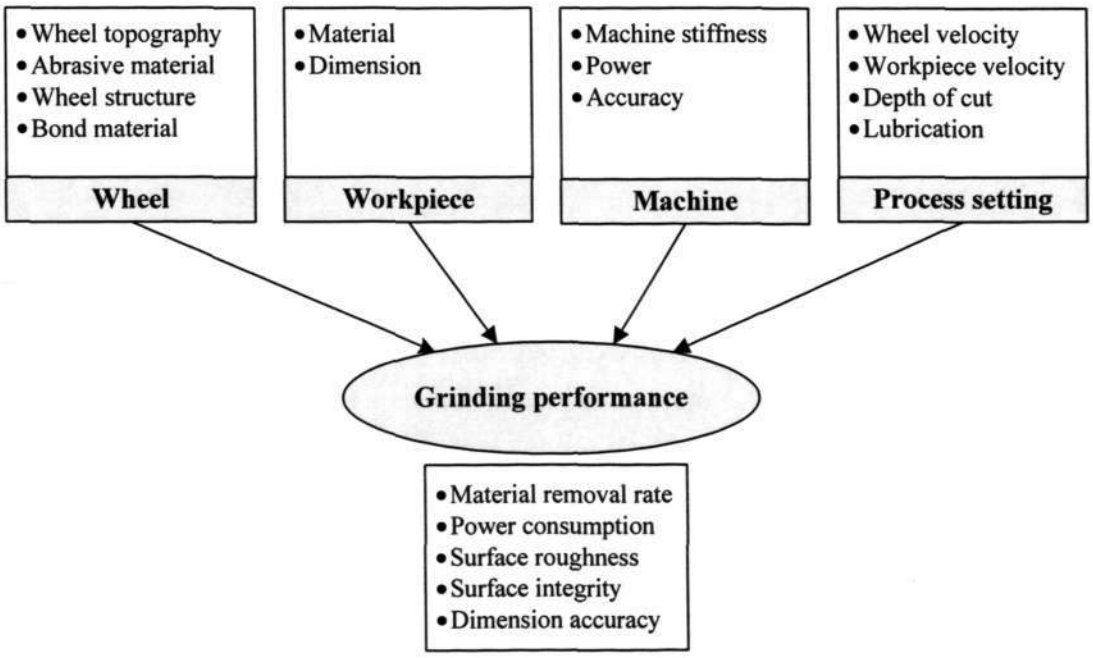

Figure 1.1 Grinding performance and contributing factors

Among the factors, the grinding wheel is a unique one, differentiating the grinding process from other machining techniques. While turning uses single-point tools, drilling uses double-point tools, and milling uses multiple-point tools, the grinding process utilises simultaneously thousands of points, located on bonded abrasive grains. To understand the grinding process it is important to *characterise the grinding wheel topography* as it is evident that the grinding performance is strongly correlated to the grinding wheel and the conditions under which it is prepared (Malkin 1989, p. 79).

A good characterisation technique should have the following features: it should be reliable and consistent; it should be easy-to-use and inexpensive; it should describe the intrinsic characteristics of the grinding wheel that correlates with the grinding performance. On the other hand, the characterisation of the grinding wheel has to overcome the following difficulties: the wheel is bulky while the cutting edges are at micro-scale; the cutting edges are stochastic in nature; and the grinding topography is non-stationary subjected to changes caused by wear mechanisms. Although measuring the grinding wheel topography has been attempted since the 1970's, a perfect technique, which can satisfies the above requirements, does not exist (Malkin 1989, p.93).

Generally, the grinding process is studied by two approaches: experimental and analytical. Each approach has its own merits and drawbacks. An experimental study normally explores the process under limited conditions to yield a practical solution. Results from experimental studies help in establishing the relationships between the process parameters and performance, which are keys to the solution of many machining problems. Nevertheless, an experimental study often requires complicated test set-ups while the number of parameters and phenomena which can be observed is limited. Thus, it is difficult to generalise experimental results to a broader framework.

On the other hand, it is difficult for an analytical model to give quantitative predictions because of the unavoidable assumptions and simplifications. However, an adequate analysis can enable one to understand the major role of various grinding parameters. It provides a theoretical framework that has a broader applicability in understanding the process than a pure empirical approach. Hence, it is not surprisingly to see numerous types of grinding models proposed in the last 30 years (more details are given in Chapter 2).

Among the grinding models, *kinematic models*, in which the kinematic relationship between the grinding wheel and the workpiece is used to generate the workpiece surface, have received a large attention from researchers. The reasons for the attention could be the capability of these types of models to relate the process setting and the grinding wheel characteristics to the grinding performance. Kinematic models not only give insights into the influence of the parameters, but may also give quantitative prediction regarding grinding performance, such as surface roughness or grinding forces.

For a realistic simulation of the grinding process, any kinematic simulation scheme has to consider two problems: the generation of the grinding wheel, and the interaction between the workpiece surface and the abrasive grains. Regarding the grinding wheel, most of the available models assume that it is built from abrasive grains of simple shapes. For the interaction mode, only cutting was considered while ploughing and rubbing were neglected. With the move toward higher precision grinding, such simplification regarding the grinding wheel and interaction mode could hinder the application of kinematic models in new frontiers of the process.

1.3 Objectives

In this project, the object of our study is *precision grinding*, in which surface finish and dimension control of the workpiece are major concerns. Precision grinding can be considered as grinding to exacting tolerances and finishes. However, the quantitative definition of "tolerances and finishes" may vary from time to time and from people to people (Taniguchi 1992). Considering that there exists ultra-precision grinding, which often refers to grinding to surface finishes from a few to less than one hundred nanometers and form accuracy less than one micrometer, precision grinding

can be defined as grinding to dimensional accuracy from a few micrometers to submicron, surface finish less than one micrometer, and form accuracy from few to one micrometers.

The aims of the research are as follows:

- Establishing a reliable technique for characterisation of the grinding wheel topography.
- Characterising the grinding wheel topography using new available 3-D surface characterisation parameters.
- Building a kinematic model of the grinding process to understand the influence of the grinding wheel topography. The model should avoid shortcomings of previous models.

1.4 Thesis layout

The rest of the thesis is divided into seven chapters. Chapter 2 reviews the state-of-the art methods for characterising the grinding wheel and models of the grinding process. The characterisation methods reviewed include contact and non-contact techniques. For modelling, four approaches, namely, abrasive wear, kinematical, statistical and finite element method will be discussed. The superiority and drawback of the approaches and methods will be analysed and compared.

In Chapter 3, three-dimensional (3-D) surface characterisation is introduced. The chapter lays the groundwork for further application of 3-D approach in surface characterisation. First, the algorithms for 3-D surface parameters are described; its implementation in MATLAB scripts is verified with other commercial available

software. Next, a novel technique for surface replication will be verified for grinding wheel characterisation. The chapter ends with the study of the effects of the stylus speed on measurement fidelity.

The application of 3-D surface characterisation parameters requires a user to specify the sampling condition. In comparison with two-dimensional parameters, some 3-D parameters are very dependent on the sampling condition. Chapter 4 focuses on the selection of the sampling conditions for grinding process study. Criteria for choosing the conditions for grinding wheel and ground workpiece surfaces will be proposed.

In recent years, cubic boron nitride (CBN) wheels have become more popular on the shop floor, especially for difficult-to-grind materials and high specific material-removal- rate grinding. Until now studying CBN wheels have been limited to the effect of wheel preparation on the grinding performance. While such a study is very useful, a study that can correlate the change of wheel conditionings to the change of wheel topography, and ultimately the change of the grinding performance, would be more beneficial to understanding the process. In Chapter 5, the correlation of the truing factors, 3-D parameters of wheel topography and the grinding performance will be revealed through a factorial experiment. The experiment shows that by careful choosing the sampling condition, selected 3-D parameters can successfully characterise the grinding process.

The next two chapters are concerned with kinematic modelling of the grinding process. Two essential problems, the generation of the grinding wheel topography and the interaction between the workpiece surface and the abrasive grain, will be considered in Chapter 6 and 7 respectively. In Chapter 6, a novel numerical procedure that can simulate realistic wheel surfaces is proposed. The numerical procedure avoids

assumptions such as simple grain shape or Gaussian probability distribution of wheel surfaces that were often met in past work.

Chapter 7 deals with the interaction of the workpiece and the abrasive grain. Three modes of interaction, namely cutting, ploughing and rubbing, are accounted for using the attack angle of the abrasive grain. Furthermore, a simulation procedure is described. The input of the simulation is the wheel velocity v_s, the workpiece velocity v_w, the depth of cut a, the grinding wheel diameter d_s and the wheel topography. The output of the simulation is the workpiece surface. Two sets of surface grinding experiments were conducted to verify the model.

Finally, the last two chapters give the conclusions and the recommendations for future work in the area.

Chapter 2

Literature review

2.1 Introduction

This chapter gives an overall view of state-of-the art characterisation methods and models for the grinding process. Although numerous methods for characterising the grinding wheel surface have been proposed in the past, a "one fits all" method does not exist. The CIRP studies (Verkerk et al. 1977, Tonshoff et al. 1998) showed that the comparability among the results from different and the same methods was low. This fact is probably due to the complex nature of the grinding wheel. The wheel size, random nature of grains and wear phenomena all hinder a complete description of the wheel.

There exist empirical and analytical types of grinding process modelling. A review of empirical models can be found in Tonshoff et al. (1992). As the focus of this thesis is kinematic models, they will be discussed extensively in this chapter. However, other types of analytical models are still reviewed for the complete perspective.

2.2 Characterisation of the grinding wheel topography

Characterisation of the grinding wheel involves two aspects: measurement and analysis, in other words, obtaining the grinding wheel topography and extracting information that is useful for understanding the process.

2.2.1 Measurement methods

Measurement methods for grinding wheel characterisation can be classified as contact and non-contact methods. Among the non-contact methods, scanning electron microscope (SEM) is widely used for characterising the grinding wheel topography. In SEM, an electron beam is bombarded across a sample surface. When an electron hits the sample, a variety of signals is generated owing to the interaction of the electron with matter. These signals give information regarding not only the sample topography but also its chemical content (Goldstein 2003). Thanks to its large depth of focus and high resolution, SEM is often employed to observe small cutting edges of the grinding wheel. Unfortunately, for non-conducting materials like grinding abrasives, SEM can cause charging up sample surfaces; which can lead to image distortion and, in some cases sample damage.

Although a contour map of the grinding wheel topography can be obtained (Verkerk 1977), topographical information given by SEM is rather qualitative than quantitative. For quantitative characterisation of the grinding wheel surface, non-contact methods such as laser triangulation and interferometry can be used. In laser triangulation, a laser beam is focused on the object to be analysed, and the light reflected by the surface is focused on a photo detector. When the object is moved, the height variations encountered along the surface result in a displacement of the spot on

the photo diode. The position of the spot on the detector is converted into an electric signal which is proportional to the height of each point on the scanned profiles (Brinksmeir 1992).

On the other hand, an optical interferometer is based on the principle of interference. The principle works by bringing together two waves or wave fronts originating from a reference and the surface to be studied. The light reflected from these surfaces recombines and a fringe interference pattern is formed. The two widely used techniques are phase shift interferometry and vertical scanning interferometry (Mayinger 2001).

The main advantage of the optical methods is probably the possibility of surface characterisation without physical contact, thus avoiding damage to the specimen or the system. Furthermore, the measurement duration is rather short in comparison with other methods. However, for the purpose of measuring the grinding wheel, the optical systems have some limitations: (i) the measured surface should have certain reflectivity; (ii) steep slopes (>15°) are difficult to detect. Recently, another non-contact method, confocal scanning microscopy has been applied for grinding wheel characterisation (Hegeman 2000). In this method, the sample is scanned vertically in steps so that every point on the surface passes through the focus. The height of the surface at each point is found by detecting the focus. Despite the ability of the method to detect high slopes (>50°), the requirement on the reflectivity still limits its application in grinding wheel characterisation.

Other methods like scratching, thermocouple, dynamometer, imprint, and stylus can be considered as contact methods. A review of these techniques can be seen in Verkerk (1977) or Malkin (1989, Chapter 5). Scratching is based on generating isolated

scratches by moving rapidly a mirror finished surface past a slowly turning wheel. In contrast, imprint methods generally consist of imprinting the wheel surface on a soot-coated glass slide or a carbon paper covering around a plastic tapered roller. On the other hand, thermocouple and dynamometer methods quantify the cutting points by detecting a heat or force impulse generated in the grinding pass respectively. Except for the stylus method, these methods give only rudimentary information about the grinding wheel; in most cases only the count of the cutting edges is available.

Among the methods of measuring the grinding wheel surface, the stylus one is the most extensively used. The stylus method employs a very small tip (radius 2 to 10 μm) traversing across the surface to be measured. A pick-up (either an optical transducer or more commonly a linear variable differential transducer) converts the vertical displacement into an electrical signal. Three-dimensional surface characterisation using stylus instruments is possible by raster scanning successive profiles on the surface. Owing to its tip size, the radial penetration of the stylus can be limited to about 70 μm (Malkin 1989, p.95). However, Scott and Baul (1979) concluded that the limited depth of stylus penetration actually allowed a higher degree of resolution of the outermost grinding wheel surface.

In comparison with the optical systems, the main disadvantage of the stylus method is the physical contact between the specimen and the stylus. For abrasive surfaces such as grinding wheels, the contact can cause substantial wear to the stylus. Moreover, measurement time for stylus systems is generally longer than for optical systems. Despite the limitations, the stylus method is still widely used for measuring engineering surfaces. Their continued popularity can be attributed to the following features: (i) robust and easy to operate; (ii) less affected than an optical system by measurement environments; (iii) inexpensive in comparison with optical systems; (iv)

versatile due to its large range to resolution ratio; (v) all surface characterisation standards are based on stylus instruments.

2.2.2 Analysis

The analysis aspect of grinding wheel characterisation is concerned with extracting information that is useful to understanding the grinding process. Grinding wheels are often characterised by the density of abrasive grains and cutting edges. Verkerk (1977) differentiated the static grains and cutting edges, which are present in the wheel surface, from the dynamic ones, which are those actually taking part in the material removal process. Methods such as scratching, thermocouple, and dynamometer are supposed to give dynamic information as obtained data could be directly correlated with the interaction of abrasive grains and the workpiece. In contrast, the stylus method and non-contact ones are considered as static.

Generally, the number of abrasive grains can be counted from a contouring map of the topography. However, such counting is rather time-consuming and arbitrary. Alternatively, Higuchi et al (1994) defined a fractal dimension as an equation of area and perimeter of grain cross sections. They found that the fractal dimension of grain profiles became higher with the approach to the grain tip. In other words, the edge shape near the grain tip increases in roughness and irregularity. Liao (1995) estimated the fractal dimension using the length of wheel profiles. He found that the fractal dimension of a coarser wheel was larger than of a finer wheel; and highly correlated to the grinding responses. On the other hand, Tamaki and Kitagawa (1995) characterised the abrasive grain flatness using two cross-sectional profiles.

Recently, there were attempts to characterise the grinding wheel surface with three-dimensional (3-D) surface parameters. Blunt and Ebdon (1996) showed that by

appropriate choosing of the sampling interval, surface characterisation parameter S_{ds} could relate to the density of abrasive grains. Butler et al. (2002, 2004) showed that the grinding performance was correlated to surface characterisation parameter S_{ds} and S_{sc}. However, the use of the 3-D parameters for grinding wheel surface characterisation should be cautious as studies showed that some parameters are strongly affected by the sampling conditions (Dong et al. 1994).

2.3 Models of the grinding process

There exist a variety of analytical models for the grinding process. Because grinding is a stochastic process in nature, models of the grinding process would certainly involve some elements of the theory of probability. On the basis of their underlying principles, the models reviewed in this chapter are divided into: abrasive wear, finite element method (FEM), statistical and kinematic model.

2.3.1 Abrasive wear models

This type of model is based on the basic premise that the grinding process is essentially an abrasive process, in which abrasive grains attack a workpiece surface and remove material. Thus, it is quite plausible to apply abrasive wear theory for studying grinding processes. In contrast with abrasive wear theory, where the object of study is often simplified to a single hard asperity interacting with a soft surface, the grinding process involves multiple abrasive grains with different sizes and shapes. Thus, an adaptation from abrasive wear theory to grinding process model is necessary.

Typical models based on abrasive wear theory can be seen in Tichy and DeVries (1989), Torrance and Brenner (1994), and Badger and Torrance (2000). To account for the stochastic nature of grinding grains, Tichy and DeVries (1989) assumed normal

distribution of grain height. The grinding forces and the material removal rate were, therefore, the integration of cutting force and wear amount by individual grain-surface interaction over the range of considered grit height. For simplification, the model considered all abrasive grains as spheres having uniform diameter, and neglected ploughing and rubbing modes in grinding.

Similarly, the model of Torrance and Brenner (1994) relied on the abrasive wear theory by Challen et al. (1979, 1984). In contrast with Tichy and DeVries (1989), Torrance and Brenner (1994) assumed a normal distribution of grain slopes (or attack angle), which was determined by analyzing grinding wheel profiles. The grinding force was calculated using material hardness, interfacial shear strength of lubrication film, grinding speed and equivalent chip thickness. A number of grains in contact with the workpiece surface were determined from the bearing area curve of the wheel profile in grinding wheels.

An improvement from the previous models was the model developed by Badger and Torrance (2000), which was based on the three dimensional abrasive wear model proposed by Williams and Xie (1992). The workpiece material was assumed rigid perfectly plastic. The coefficient of friction and wear was calculated as a function of material properties, interfacial boundary condition and grit attack angle by applying an upper- bound method. The model, however, only considered the cutting action of abrasive grains.

All above-described grinding models gave the estimation of grinding forces, which were in fair agreement with experimental measurements obtained. However, considerable deviation was observed in all the models at lower depths of cut (or equivalent chip thickness). The interfacial shear strength, needed in calculation of force,

was hard to measure in practice and was often assigned arbitrarily. Moreover, except for grinding forces, other grinding parameters are almost impossible to be derived from abrasive wear theory.

2.3.2 Finite element models

In recent years, finite element method (FEM) has found wide application in studying manufacturing processes. While FEM is proved to be a valuable tool for the optimisation of metal forming in terms of cost, quality and time (Rowe et al. 1991); or receives extensive research in metal cutting simulation, only a few FEM simulations are documented for grinding processes, and these mainly focus on thermal aspects of the process.

Such a model is Li and Chen (1989) work, which proposed a FEM model which simulated the surface grinding process and predicted the transient temperature field and stresses in the workpiece. The model was fully coupled thermo-mechanical in plane strain geometry. The action of the grinding wheel was approximately modelled by moving force tractions on the workpiece. Using this model, Li and Chen (1989) have been able to predict the distribution of residual stresses and the microstructure for a steel workpiece.

More extensive investigation of stresses and phase transformation in grinding processes was undertaken by Mahdi and Chang (1997, 1998, 1999). The thermo-mechanical action of the grinding wheel was simulated by the combination of a moving heat flux and traction force with triangular profile. The cooling mechanism was modelled as a convection process at the workpiece surface. The effect of grinding and cooling conditions on the workpiece surface integrity was studied by changing the values of the heat flux and the effective cooling factor at boundaries. Similarly, Weinert

and Schneider (2000) carried out a thermal and thermo-mechanical analysis for grinding of cutting tools. Another application of FEM was the study of grinding wheel vibration of hub materials while grinding hard metals (Warnecke and Barth 1999).

Overall, FEM application in modelling the grinding process is still at the preliminary stage. Most of the applications focus on studying temperature effects in the process. To avoid considering the stochastic nature of the process, the grinding wheel is modelled as a moving heat source. This approach ignores the fact that heat in the grinding process is generated by the interaction of abrasive grains and the workpiece, which are essentially random. Moreover, the heat flux requires the measurement of grinding power and the partition of energy.

2.3.3 Statistical models

This type of modelling tries to predict the grinding performance based on the statistical analysis of the grinding process. In order to derive an analytical function correlating the grinding performance and parameters, statistical models have to assume that the grinding wheel surface follows certain probability distribution. In this sense, statistical models are quite similar to the models based on the abrasive wear theory.

Malkin (1989, p.184) gave formulae for estimating surface roughness. The formulae were derived assuming that the abrasive grains were distributed evenly on the grinding wheel as with a milling tool. A similar approach was followed by Tawfik (1997). It was not surprisingly to see that such formulae often give unsatisfactory results because of the simple assumption for wheels.

Hasegawa (1974) presented a more complex analysis to determine root-mean-square roughness of a ground surface. The root mean square of the workpiece surface

was calculated from wheel speed, wheel diameter, workpiece speed, the apex angle of the dresser, size sample and the distribution of cutting edges on the circumferential direction of the wheel. The probability density function of peaks was approximated as a Gamma distribution. On the other hand, Hecker (2002) gave a model for surface roughness prediction of ground parts, which was based on the Rayleigh distribution of the undeformed chip thickness.

Pandit and Sathyanarayanan (1982, 1984) suggested that abrasive grains and their cutting edges could be represented by a sine wave of large and small wavelengths respectively. These wavelengths were called "characteristics grain". Using the characteristics grain, Pandit and Sathyanarayanan (1982, 1984) showed that they could estimate the elastic deflection of the abrasive grains and the ground surface roughness.

Statistical models were not limited to the prediction of the surface roughness but could be extended to other aspects of the process. For example, Sharp et al. (2000), assuming uniform distribution of grains on the grinding wheel surface and spherical grain of constant size, analysed the grain depth of cut in plunge grinding. Hou and Komanduri (2003) estimated the number of active cutting edges assuming that the abrasive grain sizes are Gaussian distributed.

Generally, statistical models provide simple formulae for predicting grinding performance. However, in order to obtain a closed- form solution, probability distributions such as uniform, Gaussian or exponential-related distributions have to be imposed on the stochastic features of the grinding process, let it be the cutting edges or undeformed chip thickness etc. Such formulae would be non-applicable if the real distribution differs significantly from the assumed one.

2.3.4 Kinematic models

Kinematic grinding models are based on the premise that surface generation in grinding is inherently a random process and a ground surface is the cumulative outcome of multiple abrasive grain- workpiece interaction events. Then, the characteristics of ground surface are basically governed by the topography of the grinding wheel, the process kinematics, and the work-material properties. Thus, the ground groove on the workpiece surface can be considered as an imprint of abrasive grain shapes with due adjustment for kinematic relationship between the grinding wheel and the workpiece.

One of the early works in kinematic modelling of grinding processes is probably that of Bhateja (1977). In this model, the fundamental relationship between the grinding wheel and the workpiece surface was hypothesized as an "enveloping profile" model. This model simply stated that under pure cutting condition of material removal, a transverse profile of the workpiece surface should be a replica of the "envelope" of a certain peripheral length of the grinding wheel's cutting surface. Such an enveloping profile was essentially a result of cumulatively superimposing digitised axial profile data taken at consecutive points of the wheel periphery in the length of the contact zone. The main assumptions for the model are that: grinding wheel surface is of uniform characteristics and statistically stationary; the wheel is perfectly round with no runout in rotation; there is no vibration in grinding; all metal removal occurs only through clean cutting with no pile-up. Using this model, Bhateja (1977) has established the pattern of relationship between various surface roughness parameters of the grinding wheel and the workpiece.

Wang and Moon (1997) suggested multi-resolution analysis that was based on wavelet transformation as a method for processing wheel surface topography. Wavelet

transformation was the mathematical tool that separated the data into different frequency components, and then studied each component with a resolution matched to its scale. Using this technique, the grinding wheel surface profile could be decomposed into profiles of multiple scales. The information of the wheel surface was contained in a few wavelet coefficients that were called "characteristic wavelet coefficients", which were later used for simulating the grinding wheel surface. Salisbury et al. (2001a, 2001b) applied the same approach, except that the grinding wheel surface was simulated with Fourier coefficients. They both ignored ploughing and rubbing modes of abrasive grains in grinding.

Inasaki (1996) proposed an algorithm for simulation of grinding processes with superabrasive wheels. The three-dimensional topography was subjected to computer processing to extract data regarding the cutting edge distribution and the angles of the cutting edges. Extracted data then became the input for computer simulation. The simulated surface texture was assumed to be generated by cutting only, whereby the cutting edges removed all material that they interact with on the cutting path. Furthermore, Inasaki (1996) estimated the cutting forces by multiplying the cross sectional area removed by cutting with the assumed specific cutting force.

The above-mentioned models are based on measured wheel profiles. The alternative is modelling of the grinding wheel surface. In this approach, the position of the grain in wheel space and its size are simulated by using a random number generator with certain assumption about their probability distributions. Such an approach is often called Monte Carlo simulation. One of such models is from Chen and Rowe (1996a-c). The wheel structure was assumed to have spherical abrasive grain of uniform diameter. All grains were located in the wheel volume randomly following uniform distribution. The helical trace and sine wave functions were superimposed on each grain in sequence

to simulate dressing effect on abrasive grains. The ground surface was generated with consideration for the pile-up and deflection effects of the abrasive grains.

A similar approach, but for diamond wheels, was suggested by Koshy et al. (1997, 1999). The dressing operation assumed that no grit loss was induced by way of either grain fracture or dislodgement. The simulation of grinding processes was implemented in two steps. First, the three dimensional structure of the diamond wheel was simulated with the abrasive grit size and the concentration as the input. Grain shape was assumed spherical; grain diameter was normally distributed and grains located in wheel space following uniform distribution. Then, the surface was generated geometrically with reference to the simulated wheel and the process kinematics. Only cutting action of abrasive grains was considered in surface generation.

A similar exploration of the Monte Carlo concept was undertaken by Ghosh (1993) who assumed conical shape of abrasive grain. Hegeman (2000), on the other hand, assumed spheroidal shape, the diameters of which varied in three dimensions following the normal distribution. Instead, Gong and Wang (2002) preferred a uniform distribution of abrasive grains diameter. Cooper and Lavine (2000) modelled the abrasive grain as a truncated cone. Zhou and Xi (2002) presented the grain protrusion heights as a random variable of Gaussian distribution.

Warnecke and Zitt (1998) presented a complex modular simulation program, in which the wheel surface topography was represented by a 3D synthetic model. The model consisted of macro-geometry that described the axial and circumferential profiles of grinding wheels in terms of lines, circle segment; and micro-geometry that described super-abrasive grains by simple shapes such as octahedrons, cuboids, and tetrahedrons. The model could estimate surface roughness of the workpiece, grinding forces as well

as other kinematic cutting parameters. However, ploughing of the materials was neglected.

On the whole, kinematic models of the grinding process have to rely on grinding wheel topography, either measured or simulated ones. Measuring the grinding wheel is a tedious task while simulating requires simplifying assumptions about the grinding wheel topography. Until now most of the kinematic models ignore the effect of rubbing and ploughing in grinding, which may be considerable at lower depth of cut and ductile work materials.

2.4 Chapter summary

Table 2.1 gives a comparison between various models studied. In summary, there are four approaches toward the modelling of grinding processes, namely, abrasive wear, statistical, finite element method, and kinematic model. The abrasive wear approach is normally based on an analytical abrasive wear theory, which considers only rigid-perfectly plastic material behaviour. Models following this approach are often limited to only predicting the grinding forces. For the statistical models, its advantage is the ability to predict the grinding performance with simple equations; however, the assumption regarding the wheel topography could limit its application on more complex problems. In the four approaches, application of finite element approach in modelling of grinding processes is still preliminary. The reason for this may be due to stochastic behaviour of grinding, which causes considerable difficulty in modelling.

Table 2.1 Models of the grinding process

Type	Author	Output	Feature
Abrasive wear	Tichy and Devries (1989)	Grinding forces	Based on a 2D abrasive wear theory
	Torrance and Brenner (1994)	Grinding forces	Based on a 2D abrasive wear theory
	Badger and Torrance (2000)	Grinding forces	Based on a 3D abrasive wear theory
FEM	Li and Chen (1989)	Residual stress, microstructure of the surface	Grinding wheel is approximated as a moving force
	Mahdi and Chang (1997-1999)	residual stress, phase transformation	Grinding wheel is approximated as a moving force and heat flux
	Warnecke and Barth (1999)	Amplitude of wheel vibration	Grinding wheel is approximated as continuous body
	Weinert and Schneider (2000)	Residual stress	Grinding wheel is approximated as a moving force and heat flux
Statistical	Hasegawa (1974)	Surface roughness R_q	Gamma distribution of cutting edges
	Pandit and Sathyanarayanan (1982, 1984)	Surface roughness R_q, elastic deflection of grains	Time-series
	Malkin (1989)	Surface roughness, R_a	Grinding wheel as a milling tool
	Tawfik (1997)	Surface roughness, R_a	Grinding wheel as a milling tool
	Sharp et al. (2000)	Grain depth of cut	Uniform distribution of cutting edges
	Hecker (2002)	Surface roughness, R_a	Rayleigh distribution of the undeformed chip thickness
	Hou and Komanduri (2003)	Number of active cutting edges	Gaussian distribution of grain sizes
Kinematic	Bhateja (1977)	Workpiece surface profiles	Based on measured profiles of the grinding wheel
	Ghosh (1993)	Workpiece surface profiles	Abrasive grains of conical shape
	Inasaki (1996)	Workpiece surface profiles	Based on 3D topography of the grinding wheel
	Chen and Rowe (1996)	Workpiece surface topography, grinding forces	Abrasive grain of spherical shape
	Wang and Moon (1997)	Workpiece surface topography	Wavelet decomposition
	Koshy et al (1997, 1999)	Workpiece surface topography	Abrasive grain of spherical shape
	Warnecke and Zitt (1998)	Workpiece surface topography, chip geometry, grinding force	Abrasive grains of octahedron, cuboid and tetrahedron shapes
	Cooper and Lavine (2000)	Depth of cut, removal rate etc.	Abrasive grains of truncated cone shape
	Hegeman (2000)	Workpiece surface topography	Abrasive grains of spheroidal shape
	Salisbury et al. (2002)	Workpiece surface topography	Fourier transform
	Gong and Wang (2002)	Workpiece surface topography	Abrasive grain of spherical shape
	Zhou and Xi (2002)	Workpiece surface topography	Gaussian distribution of protrusion heights

Kinematic approach allows simulation of workpiece surface profiles, and consequently its roughness parameters. Grinding forces can be predicted if the specific grinding forces are known. However, most of the available models assume either cutting-only mechanism of grinding and/or a simple topography of the grinding wheel. This assumption may render the predicted results inaccurate in high precision grinding, where ploughing and rubbing mechanisms of grinding are important. These shortcomings could be rectified by treating the grinding wheel topography as a random field and using the grain curvature to differentiate between the grinding modes. Details of this approach will be explained in Chapter 6 and Chapter 7.

Characterisation of the grinding wheel surface requires two problems to be solved: measuring and analysing. The measurement methods can be classified as non-contact and contact. Despite some advantages such as non-destructive measurement and short data logging time, the application of the non-contact methods is limited due to the poor reflectivity of grinding wheel surfaces. Among the methods, the stylus is considered the most reliable and widely used in characterising grinding wheel topography.

Techniques for analysing grinding wheel topography include inspecting a topographical map and fractal dimension. Recent developments in surface metrology have seen the application of 3-D parameters in characterising the grinding wheel surface. The application of 3-D parameters in the grinding process needs more extensive research because it is well known that these parameters can be influenced by the sampling conditions.

Chapter 3

Algorithms, replication, and selection of stylus speeds for surface characterisation

3.1 Introduction

The relationship between surface topography and its functional performance has been partially investigated using two-dimensional surface analysis, but even this limited analysis is not yet fully understood. A three-dimensional (3-D) approach to surface characterisation could provide increased understanding on this relationship. The benefit of the 3-D approach, achieved by scanning the surface as a number of parallel profiles logged over an area, is that it provides extensive data in a structured format. The information obtained can be used to overcome directional sampling variation problems, the acquired data can be statistically analysed and parameters computed are directly related to the 3-D topography of the surface.

Despite its recent development, 3-D surface parameters have been successfully applied to characterising various engineering surfaces (Stout et al. 1993), especially ground surfaces and grinding wheel surfaces (Butler et al. 2002). At present, 3-D surface measurement is not yet covered by international standards, but it is the object of on-going research; standards concerning this area are expected to appear in the near future (Chiffre et al. 2000). The lack of a common standard is probably the main reason for a considerable variation of the results from different commercial metrology software (Sacerdotti et al 2001). Hence, it is important to clarify the algorithms used in the estimation of the 3-D parameters before they can be meaningfully applied in surface characterisation.

One unique feature of the grinding wheel is the contrast between its overall large size and the small scale of its cutting edges. As a wheel is too bulky for setting on most types of measurement instruments, replication of the grinding wheel surface is necessary. Furthermore, replication of the wheel surface will facilitate in-process monitoring when it is undesirable to mount and un-mount the wheel repeatedly. For replicating grinding wheel surfaces, the impression material should possess the following properties. It should have low viscosity to penetrate the deep valleys of the wheel topography, and be strong and flexible for easy removal from re-entrant geometry without damage and shrinkage. For stylus instruments, the replica should be not easily deformed by the stylus load; and for optical systems, its surface should possess certain reflectivity. Hecker (2002) applied lead as the imprint for wheel replication; however, the high viscosity of lead will probably prevent it from replicating grinding wheels of small grain sizes. Recently a relatively new material Microset 101 has been tested for cubic boron nitride wheel replication with good results (Cai et al. 2002).

Although the source of errors for stylus is rather numerous, the effect of stylus speed on measurement fidelity is rather important as it is arbitrarily chosen by users. A reduced speed however will make measurement time longer than acceptable. An increased speed can cause the stylus to lose contact with the measured surface, which can result in an effect of low-pass filtering (Lonardo et al. 1996). Moreover, on rough surfaces such as grinding wheels an increased stylus speed can create excessive stylus vibration, which will certainly affect the measurement fidelity and possibly cause damage to the stylus. In fact, so as to minimise the vibration, stylus speed is often limited to less than 0.5 mm/s on many measurement systems.

In the next section, a set of 3-D surface parameters, used in this thesis will be described. Then the algorithms for their estimation will be discussed. These algorithms were implemented in a MATLAB toolbox, which evaluates a broad set of 3-D surface parameters. For verification, a few examples of surface characterisation are discussed and compared with available commercial software. The third section describes a novel replication technique for the grinding wheel surface. The technique was validated on various types of grinding wheel surfaces. The last section gives the chapter conclusions following the investigation of the stylus velocity on the characterisation of the grinding wheel surface.

3.2 Three-dimensional surface analysis

3.2.1 Three-dimensional surface parameters

Stout et al. (1993) proposed a set of fourteen 3-D parameters estimated in this toolbox. Strictly speaking, most of the parameters of the set are derived from the corresponding 2D parameters, while only a few are uniquely devised for 3-D surface

characterisation. These parameters are denoted by "S" to indicate that they are calculated over a surface rather than a profile. This so-called Birmingham set comprises the majority of the parameters used in this thesis. In addition to the set, three amplitude parameters S_t, S_p, and S_v are estimated. The parameters can be roughly divided into four groups: amplitude, spatial, hybrid and functional. Their symbols and meanings are given in Table 3.1. More description of the parameters is given in Appendix A.

Table 3.1 Three-dimensional surface characterisation parameters

Group	Symbol	Meaning
Amplitude	S_q	Root-mean-square
	S_z	Ten point height (average peak-to-valley)
	S_t	Total height
	S_p	Highest peak
	S_v	Deepest valley
	S_{sk}	Skewness
	S_{ku}	Kurtosis
Spatial	S_{ds}	Density of summits
	S_{al}	Fastest decay autocorrelation length
	S_{tr}	Texture aspect ratio
	S_{td}	Texture direction
Hybrid	$S_{\Delta q}$	Root-mean-square slope
	S_{sc}	Arithmetic mean summit curvature
	S_{dr}	Developed interfacial area ratio
Functional	S_{bi}	Surface bearing index
	S_{ci}	Core fluid retention index
	S_{vi}	Valley fluid retention index

3.2.2 Algorithms

Stout et al. (1993) discussed extensively about the 3-D parameters. However, due to the lack of standards, some aspects of parameters estimation are rather ambiguous. The following sections discuss the algorithms for parameters estimation.

3.2.2.1 Definition of summit

A problem arises when calculating parameters S_z, S_t, S_p, S_v, S_{ds} and S_{sc}. Calculation of these parameters requires the definition of summits and valleys of areal topographic data. Compared with the profile data, there exist various definitions of summits and valleys for topographic data (Greenwood 1984, Scott 2001). The choice of the definitions thus can result in different values of summits and valleys. In this toolbox, the summits and valleys of the surfaces are identified using the eight nearest neighbouring definition. The point is considered as a summit or valley if it is the highest or deepest point among its eight neighbouring points (Figure 3.1).

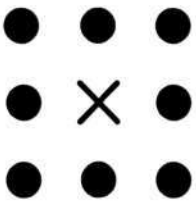

Figure 3.1 A summit defined as eight nearest neighbouring points

3.2.2.2 Areal autocorrelation function

The calculation of 3-D parameters S_{al} and S_{tr} requires the estimation of areal autocorrelation function (AACF). The AACF is defined as

$$R(\tau_x, \tau_y) = E[\eta(x, y)\eta(x + \tau_x, y + \tau_y)] \tag{3.1}$$

where $\eta(x, y)$ is the surface height from the reference plane; τ_x, τ_y is the lag distance in x and y directions.

Generally, there are two methods for the numerical computation of AACF. The first method is the standard approach by direct computation of average products among

the sample data. The second method is the roundabout approach based on the Wiener-Khinchine theorem (Bendat and Piersol 2000). In this toolbox, the second method is implemented. The algorithm is summarised as follows:

- Augment the *MxN* values of $\eta(x,y)$ with zeros to obtain a new *2Mx2N* array $\eta(x,y)$.
- Compute the *2Mx2N* -point Fast Fourier Transform (FFT) of $\eta(x,y)$.
- Inverse-FFT the square of the absolute of the above FFT.
- Normalize the result so that $R(0,0)=1$.

3.2.2.3 Power spectral density

The evaluation of 3-D parameter S_{td} depends on the estimation of areal power spectral density (APSD). Similar to AACF, there exist two methods for the computation of APSD (Marple 1987). The first method is based on Fourier transform relation to the autocorrelation function while the second is founded on Fourier transform of the topographic data. In this toolbox, the second method is applied as follows

$$P(f_p, f_q) = \frac{1}{MN}\left|F(f_p, f_q)\right| = \frac{1}{MN}\left|\sum_{n=0}^{N-1}\sum_{m=0}^{M-1}\eta(x_{m+1}, y_{n+1})e^{-i2\pi\left(\frac{p}{M}m+\frac{q}{N}n\right)}\right| \tag{3.2}$$

with $f_p = \frac{p}{\Delta x M}, f_q = \frac{q}{\Delta y N}$,and $p = 0, 1, \ldots, M-1, q = 0, 1, \ldots, N-1$

where M and N are the numbers of topographic points in x and y direction; Δx and Δy are the sampling intervals. The periodogram estimated by Equation (3.2), however is a

noisy estimator of power spectral density. An improvement could be achieved by using data windowing (such as Hanning), which nevertheless is ignored in this toolbox.

3.2.2.4 Slowest decay of AACF

The calculation of 3-D parameter S_{tr} requires the distance that the AACF has slowest decay. In this toolbox, this value is estimated by the following equation

$$max\left\{\sqrt{(\tau_x+\Delta x)^2+(\tau_y+\Delta y)^2}\right\} \; and \; R(\tau_x,\tau_y)>0.2 \tag{3.3}$$

where τ_x and τ_y are the lag distances in x and y directions. Note that the estimation of slowest decay AACF depends on the threshold value $R(\tau)>0.2$. Whitehouse and Archard (1970) defined a threshold value as $R(\tau)>0.1$. However, Dong et al. (1994) suggested a threshold of 0.2 as the existence of the long wavelength components on the surface can made it unstable.

3.2.2.5 Bearing surface area

The calculation of 3-D parameter S_{bi}, S_{vi}, and S_{ci} involves the calculation of bearing surface area at a given height. For the digital surface topography, the bearing area can be approximated by a direct cell accumulating approach (Stout et al. 1993). According to this approach, each cell may be classified as non-bearing, or partially bearing or full bearing. This approach however, entails a computationally expensive search algorithm. In this toolbox, a simplified version of bearing surface area at the height h is used as follows

$$\begin{aligned} S_{ip}(h) &= \frac{|A|(M-1)(N-1)\Delta x\Delta y}{MN} \\ A &= \{\eta(x,y):\eta(x,y)>h\} \end{aligned} \tag{3.4}$$

where $|A|$ is the cardinality of the set A.

3.2.3 Verification of the MATLAB toolbox

The above algorithms were implemented in a MATLAB toolbox (Appendix A). By using the MATLAB programming language, the toolbox can utilise MATLAB's strong graphical capability and is capable of batch processing. For verification of the toolbox, various engineering surfaces were measured and characterised by the toolbox and other commercial packages. The surfaces were measured on Talyscan 150 stylus system (Appendix B). The topographic data was first imported into MATLAB. Then form was removed from the topography using appropriate polynomial fitting before the 3-D parameters were estimated. Similar steps were carried out with the commercial software. The commercial software packages were Talymap 3.0 (available from Taylor Hobson Ltd.) and Surfstand 2.0 (available from the University of Huddersfield). The results are given in Table 3.2.

A comparison of the results shows that the parameters computed by the toolbox have a good agreement with the ones estimated by the other packages. The discrepancy of the parameters S_q, S_{sk} and S_{ku} are probably due to the rounding-off. The large variation observed for the parameter S_{ds} between the toolbox and the Surfstand results is interesting to be noted, as both packages uses the same definition of summits. The variation could be due to the implementation of the search algorithm for identifying the summits in the sampling area. The same explanation can be given to the variation of S_z. However, other summit-dependent parameters S_{sc}, S_t, S_p, and S_v, which are based on the definition of summits, show perfect match among the packages. It suggests that these parameters are rather insensitive to the choice of the algorithm. The variation in functional parameters S_{bi}, S_{ci}, and S_{vi} may be due to the simplified version of bearing area estimation or the approximation of the bearing curve.

Table 3.2 Comparison of 3-D surface parameters given by different software

Parameter	Ground workpiece			Grinding wheel			Turned workpiece		
	MATLAB	Surfstand 2.0	Talymap 3.0	MATLAB	Surfstand 2.0	Talymap 3.0	MATLAB	Surfstand 2.0	Talymap 3.0
S_q, μm	0.518	0.518	0.518	38.197	38.197	38.2	1.231	1.231	1.23
S_z, μm	3.928	3.928	3.91	216.842	223.800	202	12.383	12.383	11.9
S_{sk}	-0.010	-0.010	-0.01	-0.779	-0.778	-0.778	0.369	0.369	0.369
S_{ku}	2.814	2.814	2.81	4.009	4.008	4.01	4.944	4.944	4.94
S_{ds}, mm^{-2}	1833	1305		34.500	31.250		215.250	201.500	
S_{tr}	0.064	0.065		0.707	0.707		0.039	0.118	
S_{al}, mm	0.040	0.040		0.179	0.179		0.040	0.040	
S_{td}, °	0.000	0.000		0.000	0.000		0.000	0.000	
$S_{\Delta q}$, %	0.040	0.040		0.698	0.697		0.070	0.070	
S_{sc}, μm^{-1}	0.007	0.008		0.019	0.019		0.006	0.006	
S_{dr}	0.081	0.080		22.499	20.397		0.246	0.245	
S_{bi}	0.602	0.620		0.700	0.760		0.599	0.657	
S_{ci}	1.738	1.524		1.418	1.180		1.832	1.380	
S_{vi}	0.153	0.113		0.183	0.143		0.161	0.124	
S_t, μm	4.446		4.45	246.553		247	14.522		14.5
S_p, μm	2.791		2.79	97.038		97	9.489		9.49
S_v, μm	1.655		1.65	149.515		150	5.033		5.03

3.3 Replication technique

As replicating will certainly cause information loss, fidelity is the first consideration for any replication technique; other requirements such as cost and handleability are also important. A novel technique is suggested for grinding wheel replication. The technique employs a two-part synthetic rubber and resin compounds. By using a two-stage replicating procedure, the technique can provide a replica that can satisfy the above requirements. The technique was first reported by Butler et al. (2002).

3.3.1 Replicating procedure

The replication process consists of two stages. The grinding wheel surface is first replicated with a two-part synthetic rubber compound Examix™ (hydrophilic vinyl polysiloxane). The compound is supplied in cartridges, which are dispensed using hand-operated dispensers. The impression material possesses low viscosity that allows it to fill in deep pores in the wheel surface. Upon curing, it is hard and flexible enough to be removed from the surface without damage. Generally, its shrinkage is less than 0.2% (see product data in Appendix C). However, the rubber replica is rather soft to be measured directly on the stylus system. Thus a positive replica is required. The positive replica is acquired by using Technovit™ 3040, which is a fast curing methyl methacrylate-based resin. The resin is supplied in two components: powder and liquid. Upon mixing the two components (2 parts per volume power: 1 part per volume liquid) the substance is poured onto the negative replica to form a hard positive replica that can be measured on the stylus system. The duration time for replicating one sample is approximately 15 min. The replication procedure is shown in Figure 3.2.

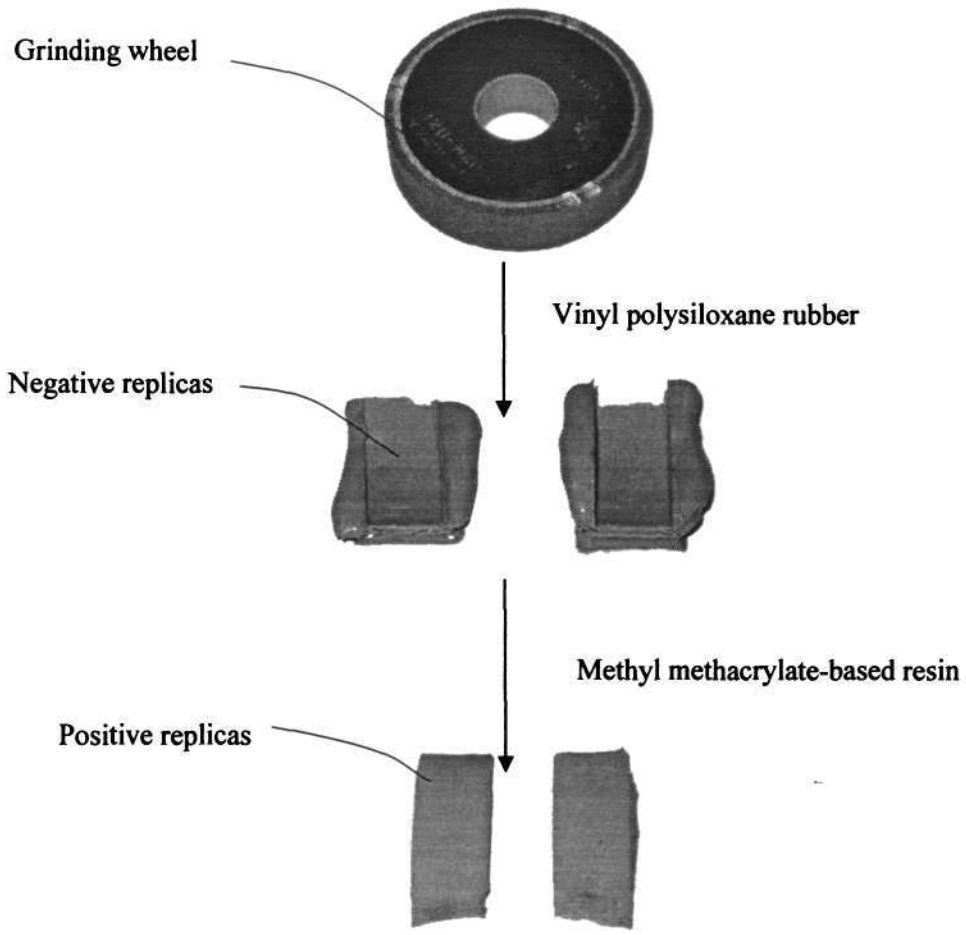

Figure 3.2 Two-stage replication procedure

3.3.2 Technique verification

In order to verify the technique, three types of grinding wheels were replicated. The specifications of the grinding wheels are given in Table 3.3. The wheels were selected to represent the broad range of wheels used in production. The average size of the grain was estimated following an equation given by Malkin (1989, p.20). Before replicating, the wheels were marked so that the same areas of the grinding wheel surfaces and their replicas were evaluated for the verification.

Table 3.3 Specifications of grinding wheels

Specification	Abrasive type	Average grain size, mm
A80KV	Aluminium oxide	0.226
B120H200V	Cubic boron nitride	0.139
C120J8V	Silicon nitride	0.144

Each wheel was replicated at four locations using the above procedure. The wheel surfaces and their replicas were measured on the 3-D stylus system Talyscan 150 to obtain the topography. The measurement conditions are given in Table 3.4. The sample area was chosen so that every sample encompassed more than 10 grains.

Table 3.4 Measurement conditions for replication technique verification

Grinding wheel	Sampling area, mm	Sampling interval, mm	Stylus speed, mm/s
A80KV	3x3	0.020	0.3
B120H200V	2x2	0.010	
C120J8V	2x2	0.020	

The topography of the selected grinding wheel samples and their replicas are shown in Figure 3.3 to 3.5. Overall, visual comparison shows that the samples and their replicas match closely with most of the features replicated. In comparison to the original samples, the replicas tend to lose small features in the deep valleys (Figure 3.3b, area

marked by a rectangle). This loss may be due to the inability of the imprint material to penetrate deep valleys. Another explanation is that the small features could be separated from the soft replica owing to re-entrant geometry in wheel surfaces. In some cases, the weak penetration of the imprint has caused small pores of the grinding wheel surfaces disappearing from the replicas (Figure 3.4b, area marked by a circle). The same reason can explain for the shallowness of some valleys on the replicas in comparison with the original samples (Figure 3.4b, area marked by a rectangle). In other cases, some valleys on the replicas can appear to be larger than on the original ones (Figure 3.5b, area marked by a rectangle). Hence, the replication process tends to cause information loss at the bottom of the grinding wheel surfaces. The top of the surfaces, in contrast, give good replication.

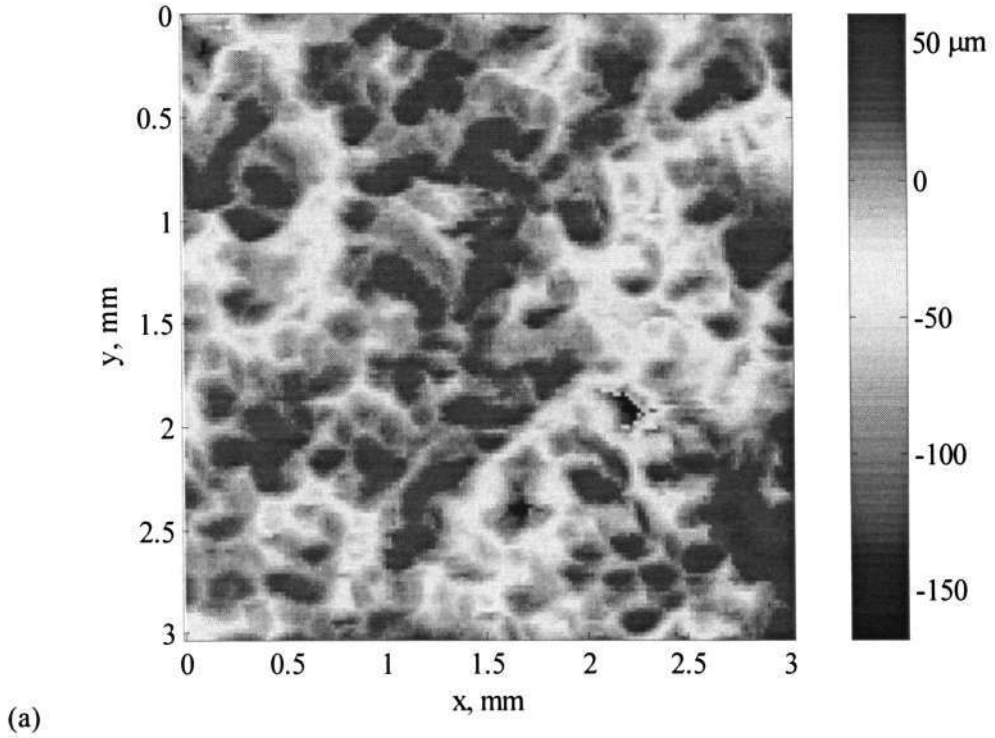

(a)

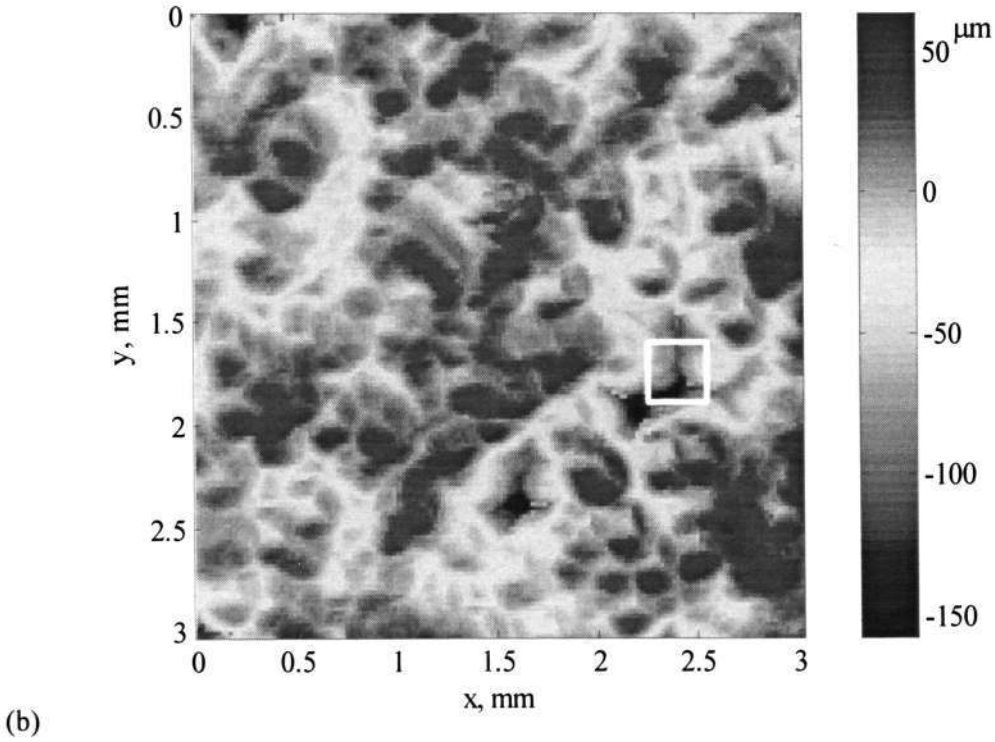

(b)

Figure 3.3 Topography of A80KV grinding wheel (a) sample and (b) its replica. The rectangle marks the feature missing in the replica

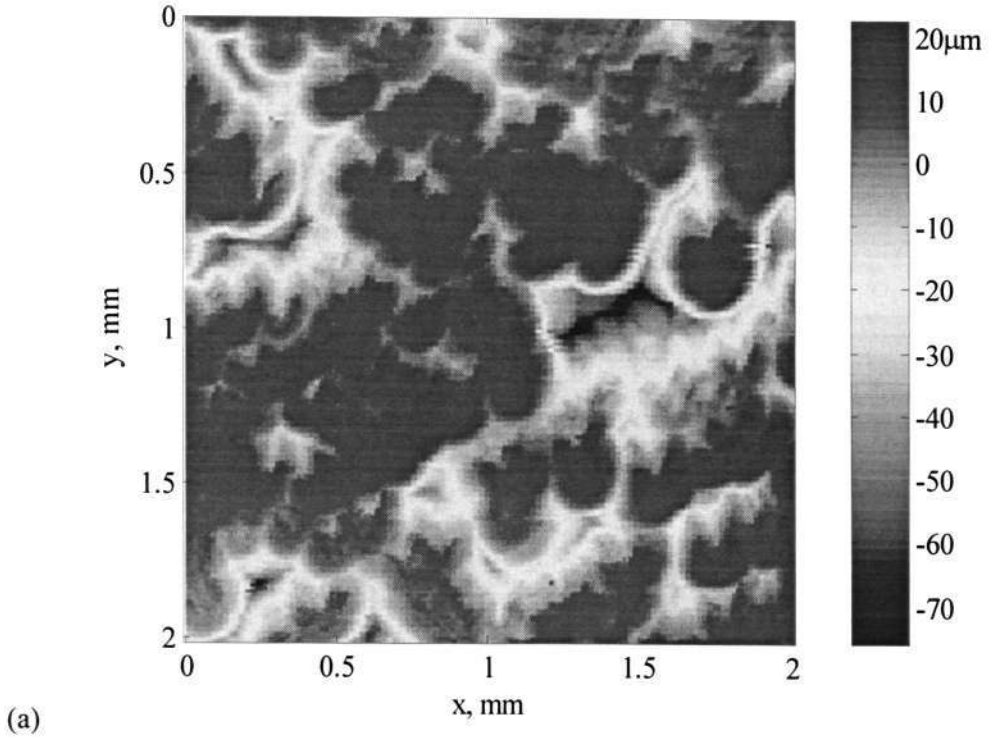

(a)

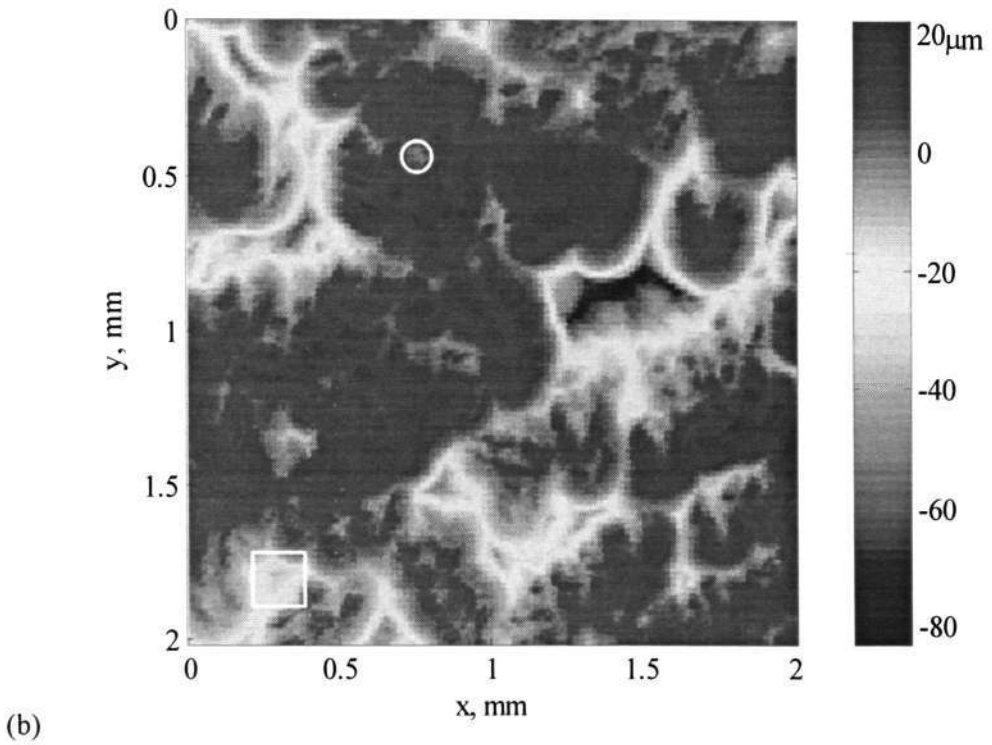

(b)

Figure 3.4 Topography of B120H200V grinding wheel (a) sample and (b) its replica. The circle marks a missing valley and the rectangle marks the valley being shallower on the replica

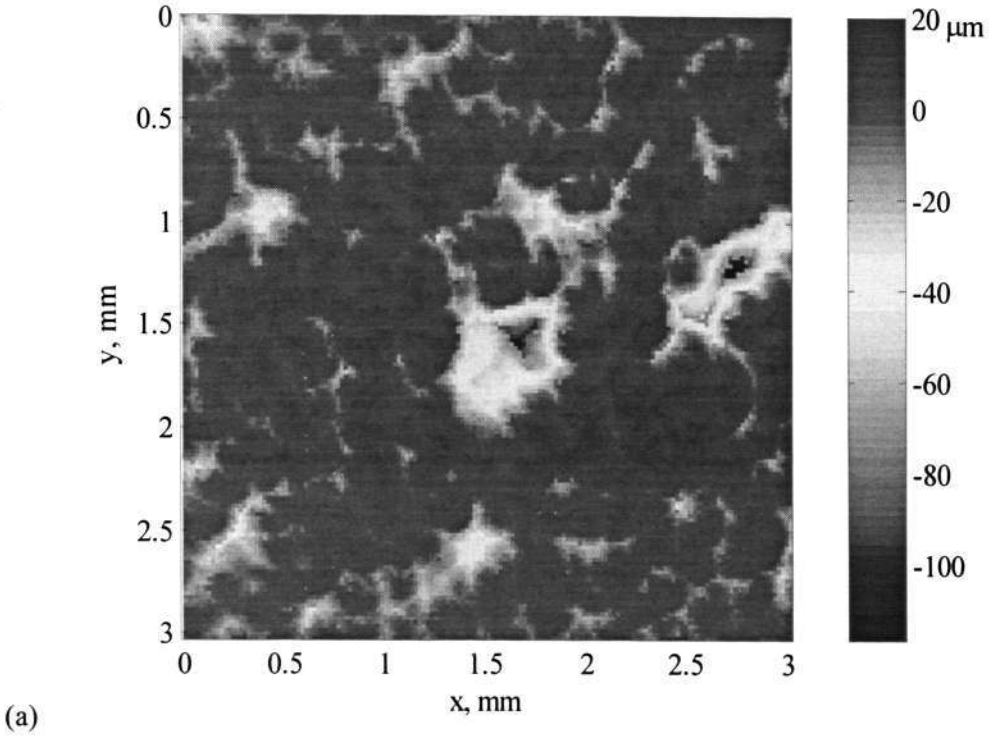

(a)

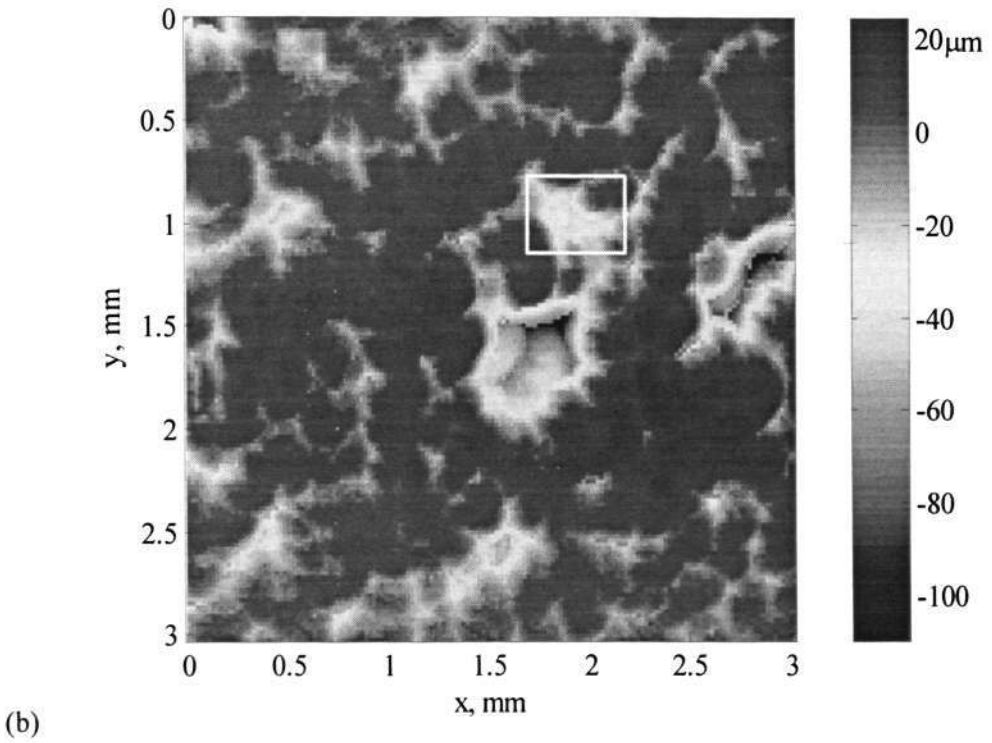

(b)

Figure 3.5 Topography of C120J8V grinding wheel (a) sample and (b) its replica. The rectangle marks the valley being larger on the replica

For quantitative verification, a set of three-dimensional characterisation parameters were estimated for the samples and their replicas. The average deviations of the parameters for each type of wheels are given in Table 3.5. The full listing of the parameters of all the samples and replicas are given in Appendix D.

Table 3.5 Average deviations of three-dimensional parameters of the replicas from the grinding wheel samples (%)

Parameter	Grinding wheel		
	A80KV	B120H200V	C120J8V
S_q, μm	6.17	7.97	13.04
S_z, μm	7.12	8.28	8.72
S_{sk}	4.28	4.74	-7.72
S_{ku}	4.29	9.59	-10.19
S_{ds}, mm^{-2}	-1.91	-20.04	-17.99
S_{al}, mm	5.55	6.69	11.72
S_{tr}	1.82	-7.24	4.59
S_{td}, °	0.00	0.00	0.00
$S_{\Delta q}$	-1.22	0.85	-2.25
S_{sc}, μm^{-1}	-13.92	-17.00	-23.64
S_{dr}, %	-1.46	2.41	-4.67
S_{bi}	1.66	0.01	10.25
S_{ci}	-1.42	1.36	-10.51
S_{vi}	2.86	-1.21	-6.56
S_t, μm	6.41	11.50	-2.95
S_p, μm	6.17	8.31	1.84
S_v, μm	7.12	13.32	-3.64

In general, most of the parameters have less than 10% deviation from the original value. The replicas seem to have a larger range of surface heights, as evidenced by the amplitude parameters. Most of the amplitude parameters of the replicas, such as root-mean-square deviation S_q, ten-point height S_z and total height S_t give an increased value. The distribution of surface heights for the replicas is rather closely matched to the samples, judged by their values of skewness and kurtosis. The largest deviations are

observed for density of summits S_{ds} and arithmetic mean summit curvature S_{sc}. The reduced values of S_{ds} and S_{sc} mean that the surfaces of the replicas are generally smoother than the grinding samples, probably owing to the penetration of the replicating material. The good match between other spatial parameters: fastest decay autocorrelation length S_{al}, texture aspect ratio S_{tr} and texture direction S_{td} suggest that the spatial relationship of the topography is preserved in the replicas.

3.4 Effect of stylus speed on measurement fidelity

In order to determine an optimal stylus speed for grinding wheel characterisation, a series of measurements were conducted on various types of grinding wheels. The specification of the grinding wheels is given previously in Table 3.3. From each type of grinding wheels, four samples were selected. Each sample was measured at stylus speeds of 0.3, 0.5, 0.75 and 1 mm/s. The sampling interval and area is given previously in Table 3.4. A total of 48 measurements were completed.

For each measurement, a set of 3-D characterisation parameters were evaluated. The listing of all the parameters is given in Appendix E. Figure 3.6-8 show the selected values of parameters S_q, S_z, S_{ds} and S_{sc} at various speeds. Although the deviation of some parameters such as S_{ds} and *Ssc* due to stylus speed is noticeable, the trends of change are not clear from the graph. For the grinding wheels A80KV (Figure 3.6c,d) and B120H200V (Figure 3.7c,d), it seems there are peak values of S_{ds} and S_{sc} as the stylus speed is increased while for the grinding wheel C120J8V (Figure 3.8c,d) the parameters tend to decrease. On the other hand, parameters S_q and S_z seem to be not affected by the stylus speed except for S_z values of C120J8V. This complex behaviour can be explained by the fact that at higher speed the stylus will lose contact with the surface, thus producing low- pass filtering effect and a reduction in the higher

frequencies. However, higher speed also causes vibration of the stylus, hence introducing some high frequency components into the electronic signal.

Figure 3.9 displays the deviations of the values of the parameters due to increased stylus speeds; the deviations were estimated by selecting the values of the parameters at the stylus speed of 0.3 mm/s as a benchmark. Among the variations, the fluctuations of the spatial parameters S_{ds} and S_{sc} are the most remarkable. For other parameters, the deviations are generally less than 5%. In fact, the ANOVA tests on the parameters show that only the stylus speed influence on these parameters is statistically significant. This deviation, as mentioned above, is due to the loss or introduction of high-frequency components in the acquired signals. This explanation is confirmed by re-estimating the 3-D characterisation parameters at increased sampling intervals (Figure 3.10). At an increased sampling intervals (which in fact is a low-pass filtering), the changes in the parameters are considerably reduced.

The investigation suggests that care should be taken in interpreting frequency-sensitive parameters such as S_{ds} and S_{sc} as these parameters would be strongly affected by the stylus speed, especially at small sampling intervals. However, regarding amplitude-related parameters, the deviation, induced by the stylus speed is generally negligible for the studied range of speeds.

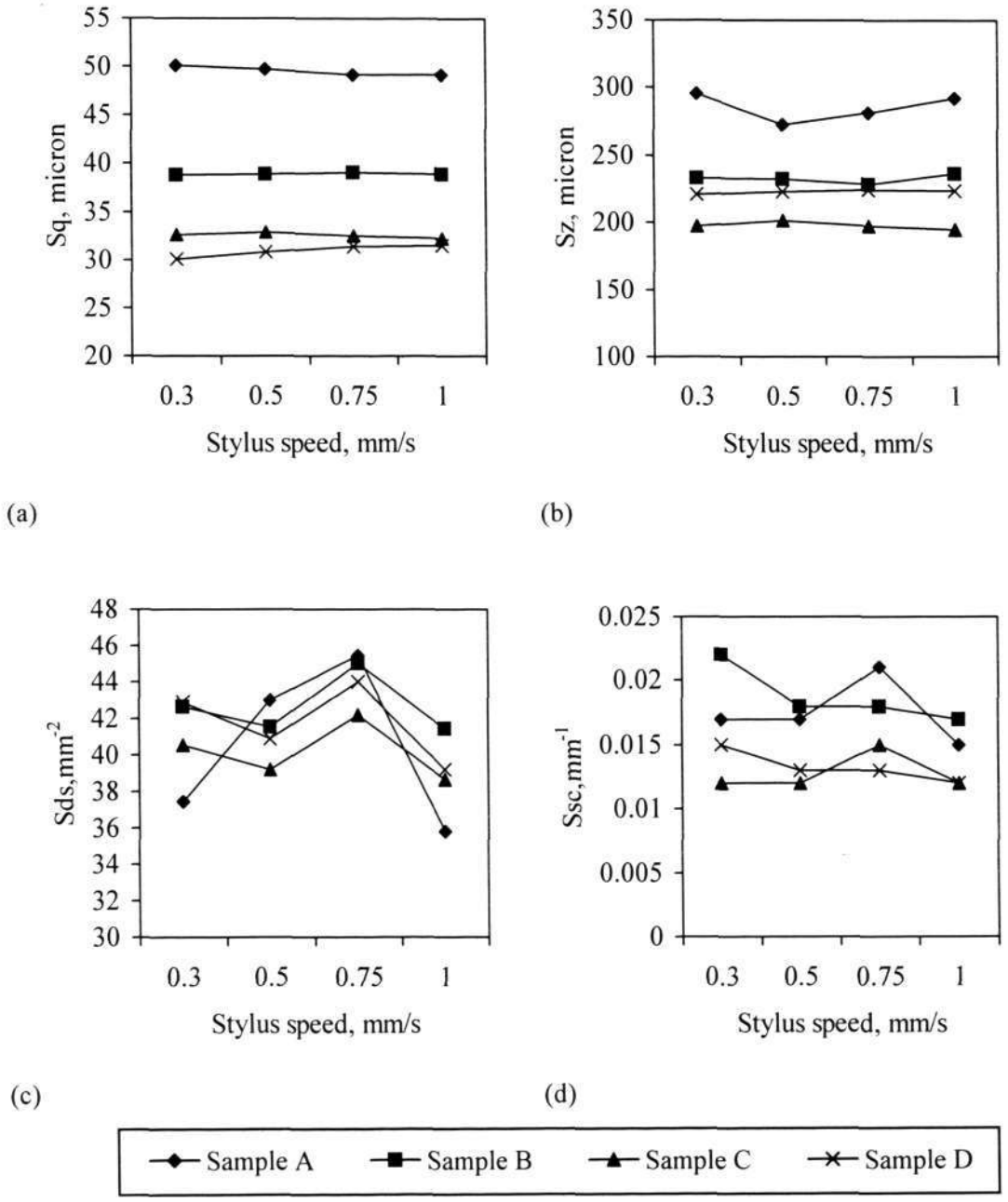

Figure 3.6 3-D characterisation parameters of A80KV grinding wheel samples at various stylus speeds

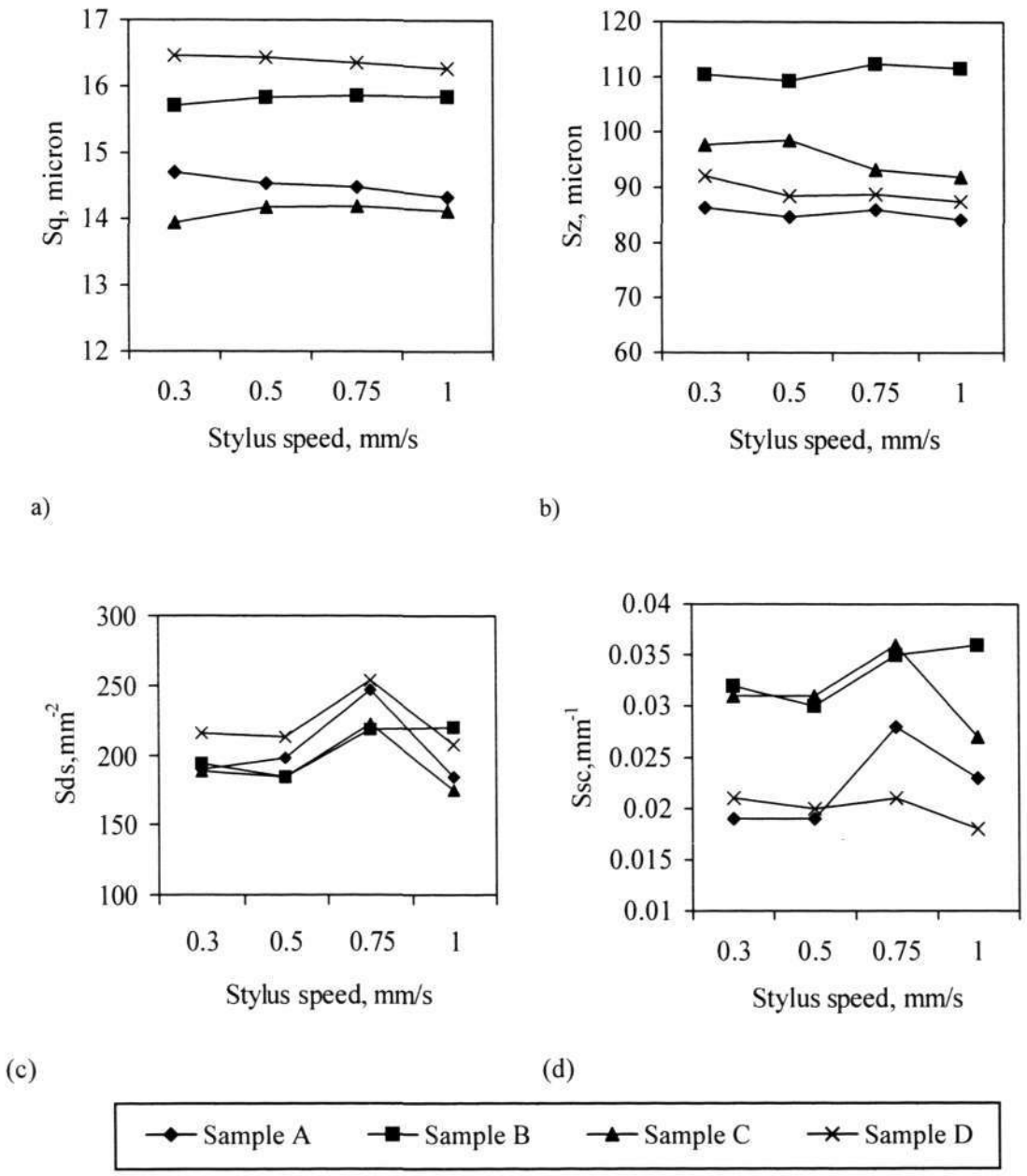

Figure 3.7 3-D characterisation parameters of B120H200V grinding wheel samples at various stylus speeds

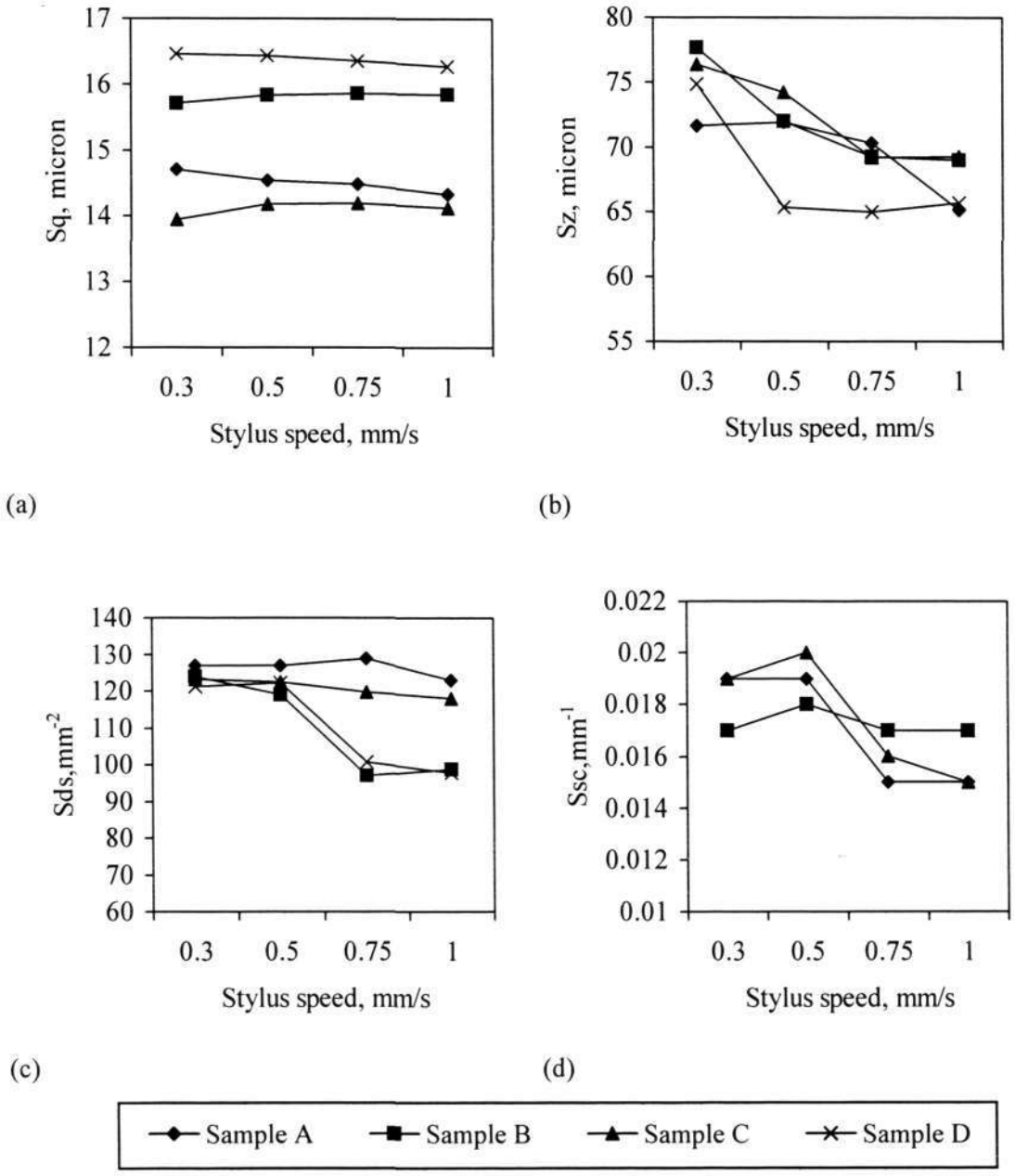

Figure 3.8 3-D characterisation parameters of C120J8V grinding wheel samples at various stylus speeds

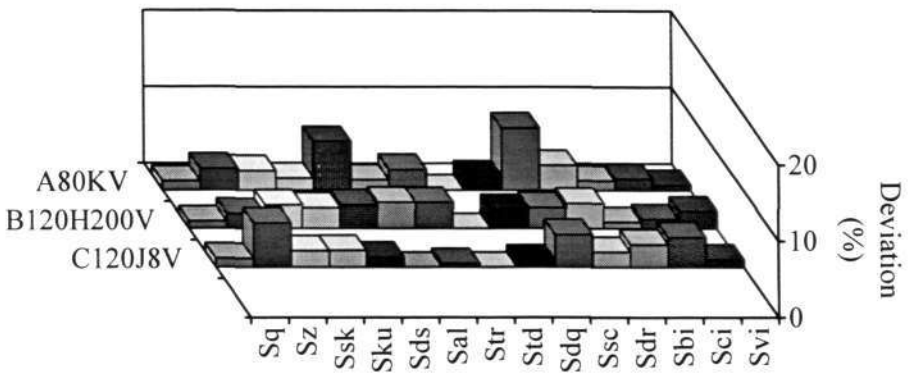

(a)

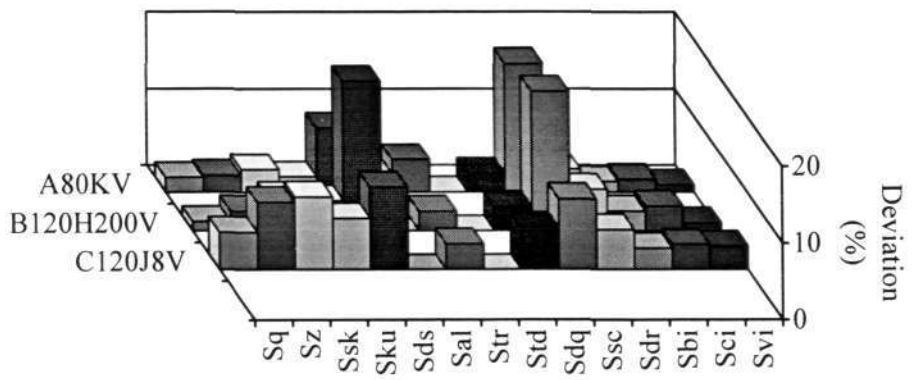

(b)

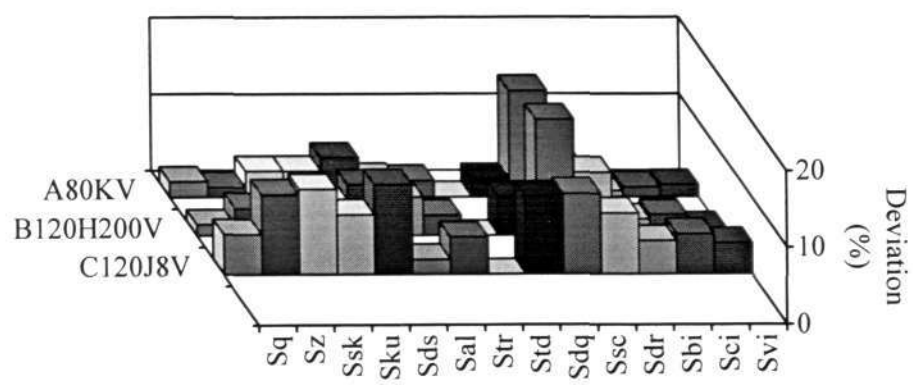

(c)

Figure 3.9 Deviation of 3-D characterisation parameters from increasing the stylus speed (values at 0.3 mm/s as benchmarks): (a) 0.5 mm/s, (b) 0.75 mm/s, (c) 1 mm/s

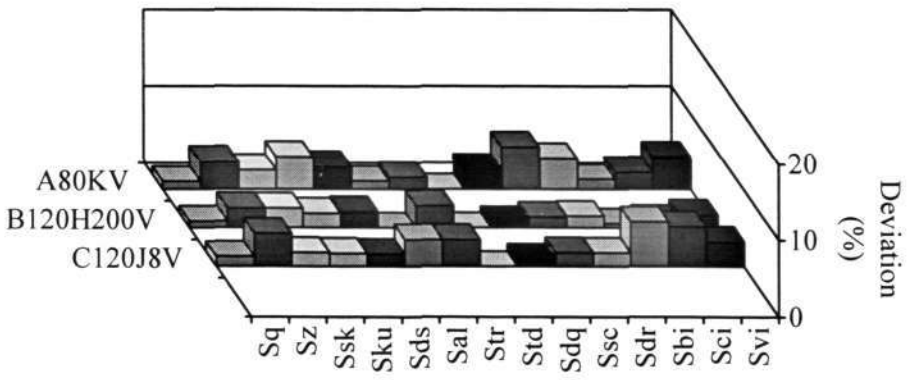

(a)

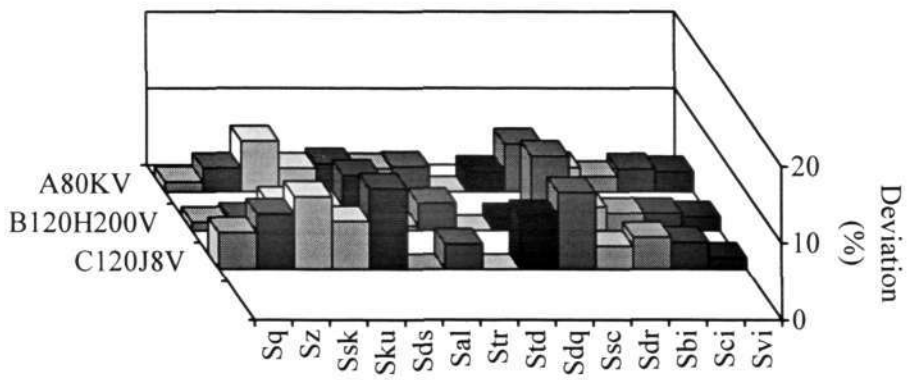

(b)

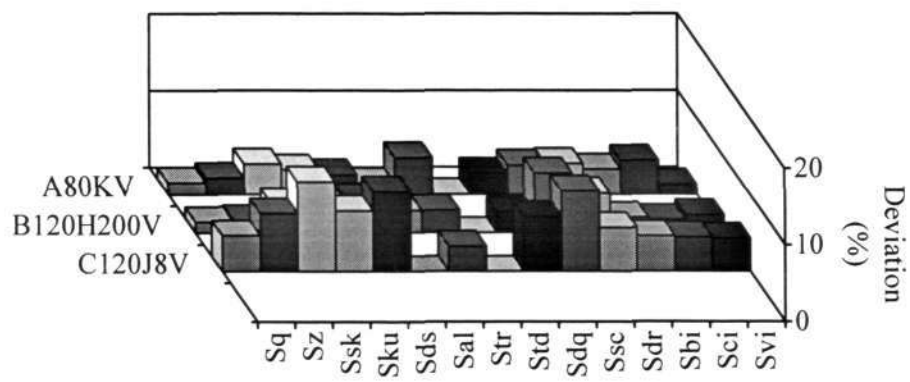

(c)

Figure 3.10 Deviation of 3-D characterisation parameters from increasing the stylus speed (values at 0.3 mm/s as benchmarks): (a) 0.5 mm/s, (b) 0.75 mm/s, (c) 1 mm/s. The parameters are estimated with increased sampling intervals

3.5 Chapter summary

A MATLAB toolbox has been coded for calculating 3-D surface parameters. The toolbox can evaluate a broader set of 3-D parameters in comparison with other commercial packages. Its other advantages are batch-processing capability and the utilisation of the strong MATLAB graphical functions. The verification of the toolbox confirms that it is important to clarify the algorithm for surface parameters estimation.

A novel technique for the replication of the grinding wheel surface was described and verified for a variety of wheel surfaces. The experimental results show that the technique is capable of producing replicas with good fidelity. Most of data loss occurs at the valleys of the surface; hence, its effect is insignificant on the analysis of the grinding wheel surfaces.

Up to 1 mm/s, the stylus speed of stylus instrument shows little influence on most of the 3D- characterisation parameters. The effect of the stylus speed exerted on the parameters is mainly filtering or introducing of high frequency components. The influence of stylus speed on high-frequency sensitive parameters can be ignored when measuring with large sampling intervals.

Chapter 4

Sampling conditions for the characterisation of the grinding wheel surface

4.1 Introduction

Three-dimensional surface characterisation is based on digital areal topographic data, and therefore the sampling condition is represented by the sampling interval, the size of sampling matrix, and the sampling area. The selection of the optimum measuring condition is vital in order to enable an accurate and realistic representation of the actual surface topography to be recorded. It is well known that the selection of the sample interval can strongly affect 3-D characterisation parameters (Stout et al. 1993). The relationship between the sampling interval, the sampling area, and the size of the sampling matrix are expressed as follows

$$L_x = (M-1)\Delta x \quad , \qquad L_y = (N-1)\Delta y \tag{4.1}$$

where L_x and L_y are the sampling length in x and y directions; M and N are the sampling matrix sizes; Δx and Δy are the sampling intervals in x and y directions. From a functional point of view, the size of the sampling area and the sampling interval are the most important because they directly determine the long-wavelength and short-wavelength limits of the measurements. From a statistical point of view, the sampling matrix size is crucial as it is directly related to the statistical reliability of data.

Generally, the choice of the sampling interval is limited by instrument capability, functional requirements, computing power and the requirements of the Nyquist sampling theorem. Given a stylus of radius R_s, the smallest wavelength measurable by the stylus instrument is (Stout et al. 1993):

$$\lambda_s = 2*R_s \tag{4.2}$$

Thus, R_s is the minimum sampling interval imposed by the instrument capability. When the sampling interval is less than the stylus dimension, the obtained data points appear to highly similar, therefore mainly redundant. Furthermore, the Nyquist criterion requires that the sample interval is less than half the shortest wavelength presented in the signal if all information is to be reconstructed (Papoulis 1962). Failure to obey this causes "aliasing", i.e. a higher frequency component is folded into a lower frequency component. Hence, the problem is rather dilemmatic. A larger sampling interval may distort the acquired information and give a poor visual representation while a finer interval would result in many redundant data and increasing computing and measurement time.

Similarly, the determination of the sampling area is dictated by many factors involving instrument and functional requirements. The wavelength of the longest

component which can be identified in the sample is

$$\frac{1}{M\Delta x} \quad and \quad \frac{1}{N\Delta y} \tag{4.3}$$

where M and N are the sampling matrix sizes; Δx and Δy are the sampling intervals in x and y directions.

As the length or area of the sample is increased, longer wavelength features can be observed, and as a result the statistical properties change. This fact is well-known as "non-stationary' of surfaces (Sayles 1982). On the other hand, a large sampling area can result in long data logging time and computing problems.

The dilemma of choosing the sampling conditions is actually not new. Many researchers have already carried out 3-D topographic analysis in great depth with their preferred sampling conditions. Sayles (1982) proposed a concept of "functional filtering" in which the short-wavelength and long-wavelength limits are defined by the phenomenon under investigation. Yim and Kim (1991) derived the equation for optimal interval assuming that surface parameters follow the Gaussian distribution. Stout et al. (1993) gives a list of recommended rules for the sampling matrix size and the sampling intervals. Lin (1993) suggested that the selection of the sampling interval can be based on the radial spectrum analysis. Butler (1999) determined the sampling conditions for engine liner characterisation by setting the limits on the sampling area and sampling matrix.

In this chapter, the influence of the sampling conditions, especially the sampling interval on grinding wheel characterisation is investigated. From the investigation, a set of rules for determining optimal sampling conditions will be proposed. The next section will discuss the influence of the sampling interval on 3-D parameters. Sections

4.3 and 4.4 deal with the criteria for selecting the sampling conditions for wheel surface characterisation. In Section 4.5, the criteria are extended for the case of anisotropic surface while the chapter conclusions are given in the last section.

4.2 Influence of the sampling interval on the 3-D parameters

A series of experiments were conducted to investigate the relationship between 3D- characterisation parameters, the sampling interval, and the radial power spectrum of a surface for various grinding wheels. The specifications of the grinding wheels and the sampling area sizes are given in Table 4.1. Each grinding wheel was measured at 2 separate locations with the sampling interval of 5 μm.

Table 4.1 Specification of grinding wheels for power spectrum investigation

Specification	Abrasive type	Sampling area, mm	Sampling interval, mm
A46H7V	Aluminium oxide	4x4	0.005
A80J8V		3x3	
B120H200V	Cubic boron nitride	2x2	
B140N200V		2x2	
C80M7V	Silicon nitride	3x3	
C120J8V		2x2	

For each measured sample, a set of 3-D surface characterisation parameters were evaluated at different sampling intervals. The data is given in Appendix F. The relationship between the 3-D parameters and the sampling interval is shown in Figure 4.1. In Figure 4.1, the values of the parameters are normalised so that the value of the parameters at the smallest sampling interval is one. Similarly, the sampling intervals are normalised by dividing the sampling intervals by the values of S_{al} at the smallest interval.

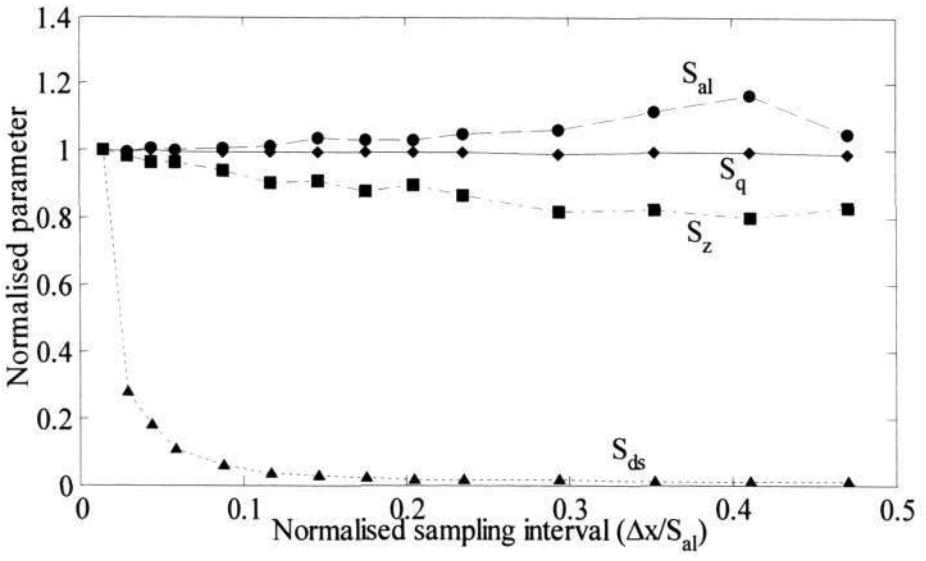

(a)

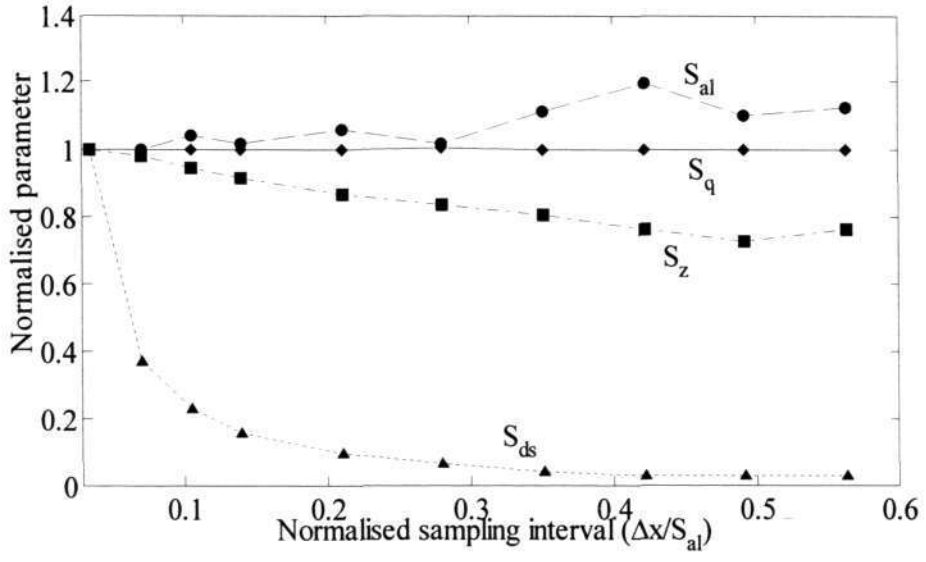

(b)

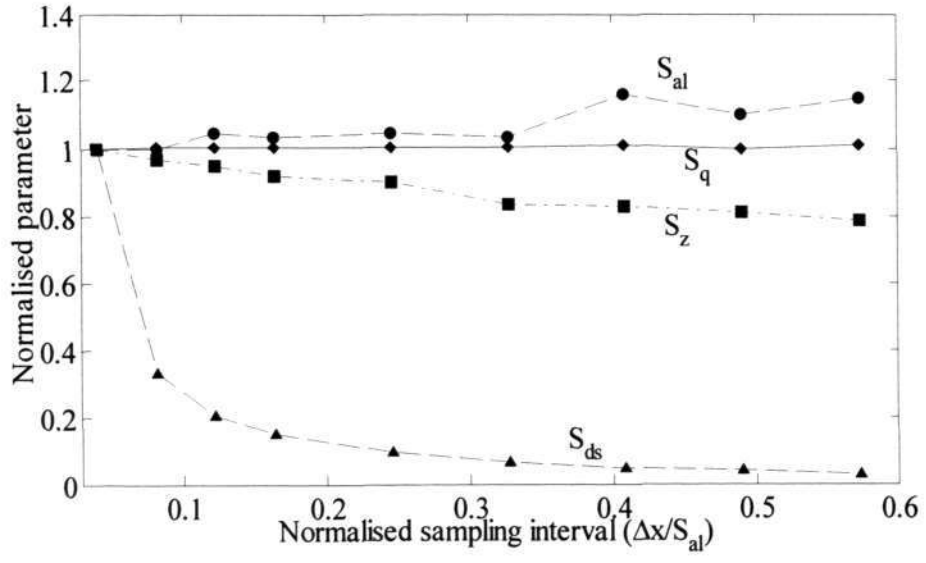

(c)

Figure 4.1 3-D characterization parameters at various sampling intervals: (a) A46H7V, (b) B140N200V, (c) C80M7V

The results reveal that the 3D-parameters can be classified into 4 groups on the basis of their behaviour when the sampling interval is changed. There is one group of parameters (S_q, S_{sk}, S_{ku}, S_{bi}, S_{ci}, S_{td} and S_{vi}) that are hardly affected by sampling intervals. On the other hand, parameters S_{ds}, S_{sc}, S_{dq} and S_{dr} decrease significantly as the sampling interval increases. In contrast, parameters S_z and S_{tr} display a small influence of the sampling interval, in which the values of the parameters reduces slightly. The remaining parameter S_{al} shows a unique behaviour. Its value is not affected by the sampling interval until some critical value of the sampling interval is reached; at which the parameter starts fluctuating strongly.

This behaviour is shown across the grinding wheels regardless of grain size and abrasive types (Figure 4.1). The behaviour can be explained by looking at the radial power spectra of the topography. The radial power spectral density $G(\omega)$ is defined as follows

$$G(\omega) = \int_0^{2\pi} S(\omega,\theta)d\theta \tag{4.4}$$

with $S(\omega,\theta)$ is the power spectral density in the polar coordinates:

$$\omega = \sqrt{\omega_x^2 + \omega_y^2} \tag{4.5a}$$

$$\theta = \arctan\left(\frac{\omega_y}{\omega_x}\right) \tag{4.5b}$$

where ω_x and ω_y are the harmonic frequencies.

The above integral can be approximated by the periodogram as:

$$G(\omega) = \sum_{\omega_i<\omega<\omega_j} \left|X(\omega_x,\omega_y)\right|^2 \tag{4.6}$$

where $X(\omega_x, \omega_y)$ is the Fourier transform of the surface, and $\omega_i < \omega_j$ are the discrete values on the frequency axis. From the radial power spectral density, its cumulative spectral function can be defined as:

$$G_c(\omega) = \int_0^{\omega} G(\omega) d\omega \tag{4.7}$$

Figure 4.2 to 4.4 show the power spectra for three samples of grinding wheel topographies. The spectrum shows that it is dominated by a few low frequency components with the power of the frequency components decreasing exponentially with an increase in the frequency. When increasing the sampling interval, we in fact have lowered the cut-off value of the low-pass filtering. However, as the power spectrum is dominated by a few low-frequency components, the total power of the spectrum is hardly affected. This fact explains the behaviour of the parameter S_q and other amplitude-related parameters. The parameters S_q is the equivalent of the total power of the spectrum as shown by the Parseval's theorem (Papoulis 1962). The same fact can be used to explain the behaviour of S_{tr}, which is defined as the angular position of the largest value of the angular power spectrum.

The functional parameters S_{bi}, S_{vi} and S_{ci} are based on the bearing area curve, which is in fact the probability distribution of surface heights, thus related to amplitude parameters (Sayles 1982). The insensitivity of the probability distribution to the sampling interval can be explained from the following equation.

$$\sigma^2 = (Sq)^2 = \int_{-\infty}^{+\infty} x^2 f_X(x) dx \tag{4.8}$$

where σ is the standard deviation and f_X is the density function. As S_q is negligibly affected by the sampling interval, the above relation means f_X is fairly constant.

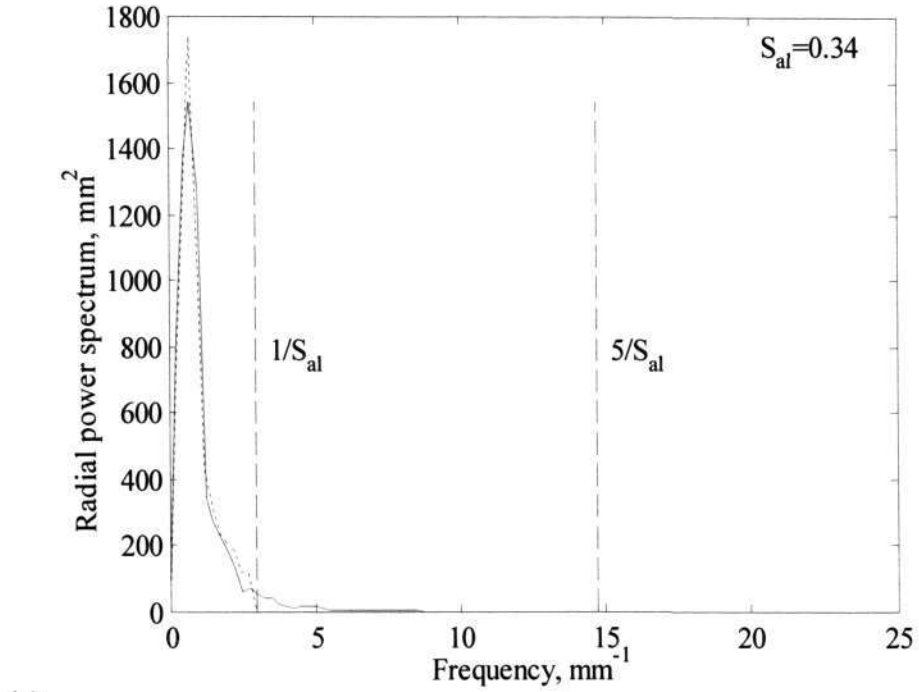

(a)

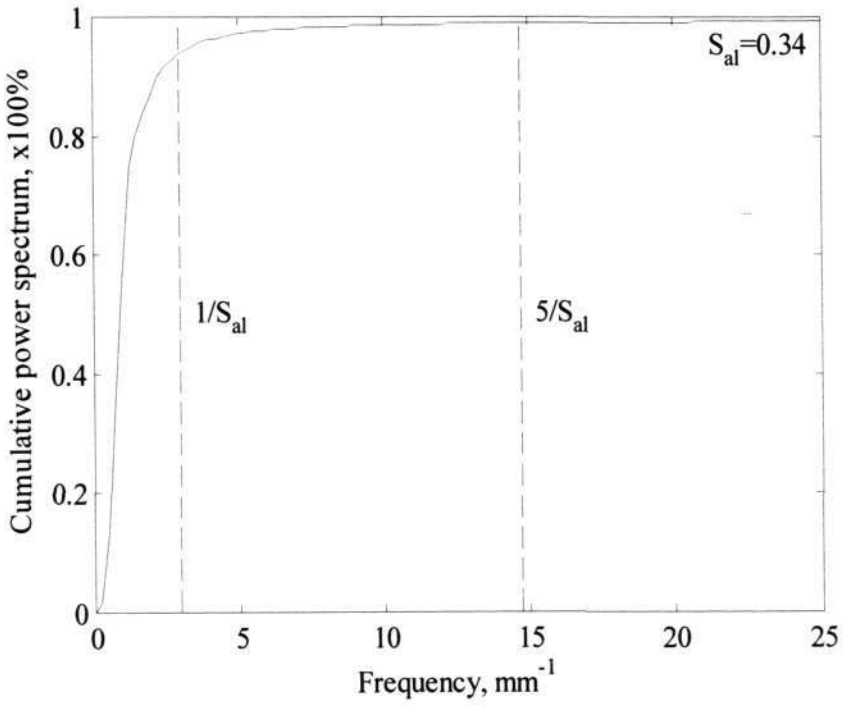

(b)

Figure 4.2 Power spectrum of grinding wheel A46H7V: (a) radial power spectrum, (b) cumulative power spectrum. Line "—" is the power spectrum sampled at 5 µm. Line "--"the power spectrum sampled at 170 µm

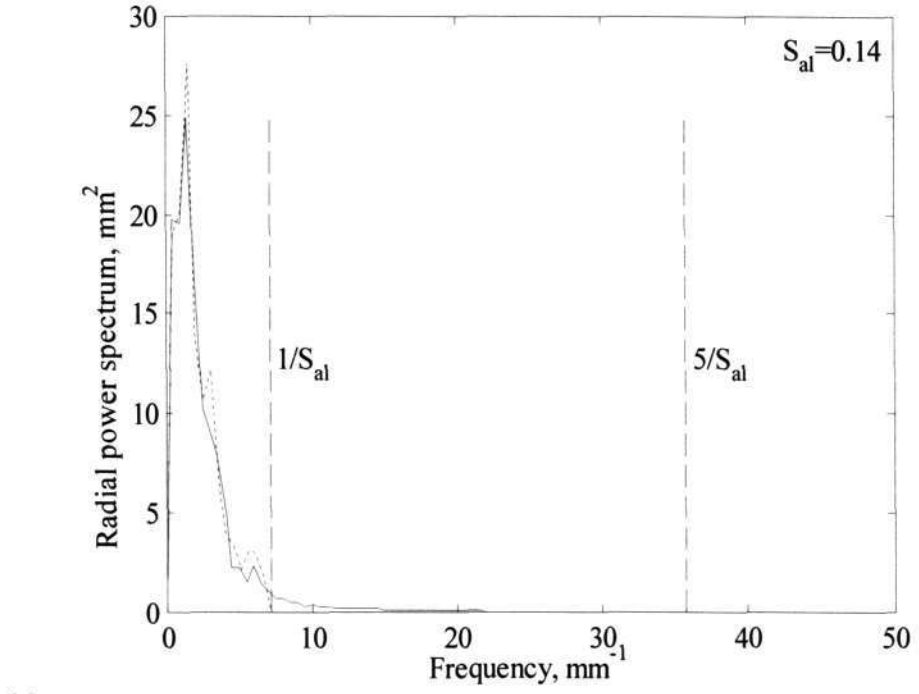

(a)

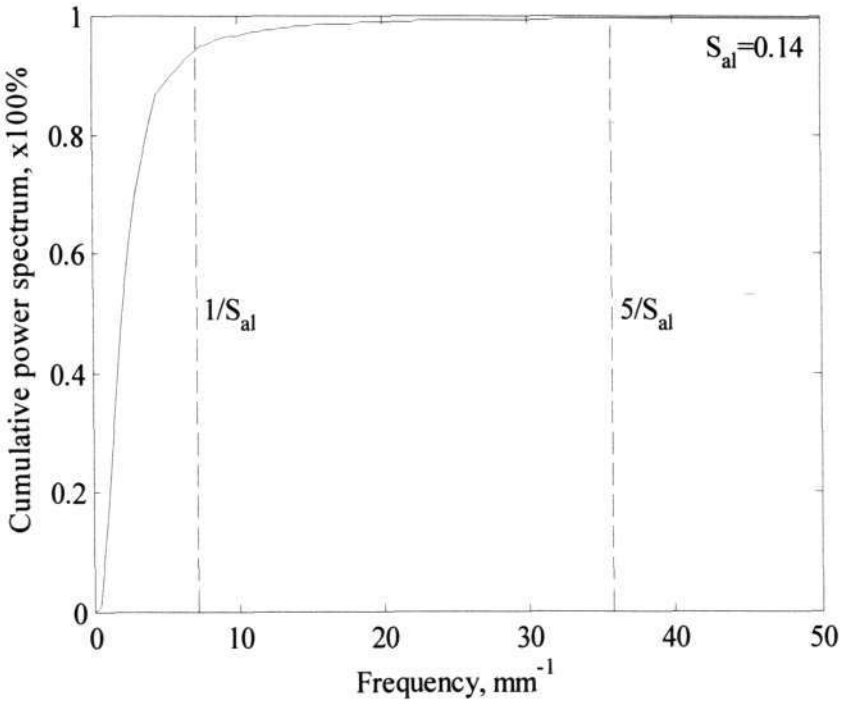

(b)

Figure 4.3 Power spectrum of grinding wheel B140N200V:(a) radial power spectrum, (b) cumulative power spectrum. Line "—" is the power spectrum sampled at 5 µm. Line "--"the power spectrum sampled at 170 µm

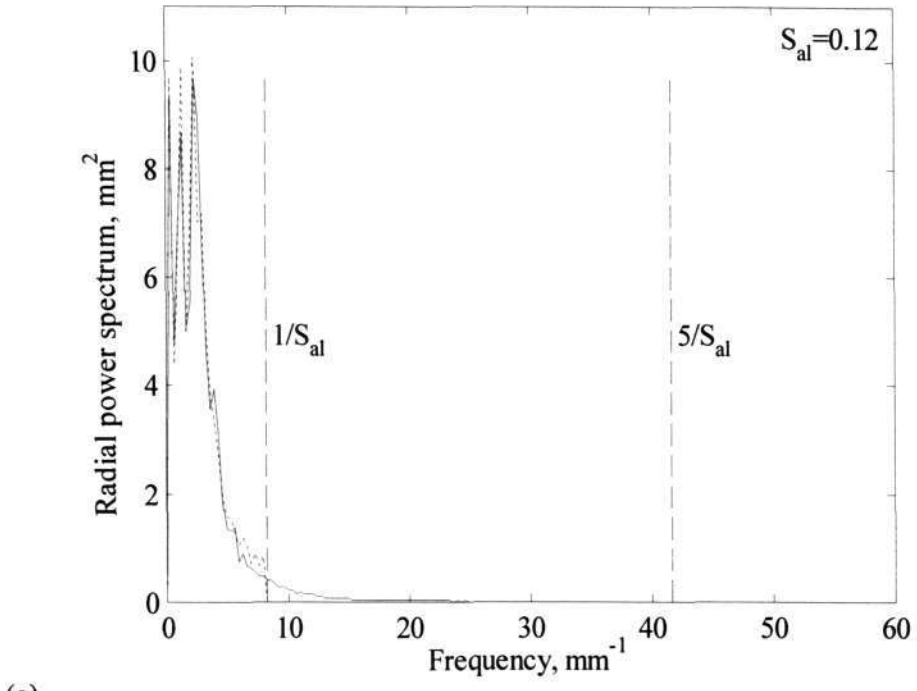

(a)

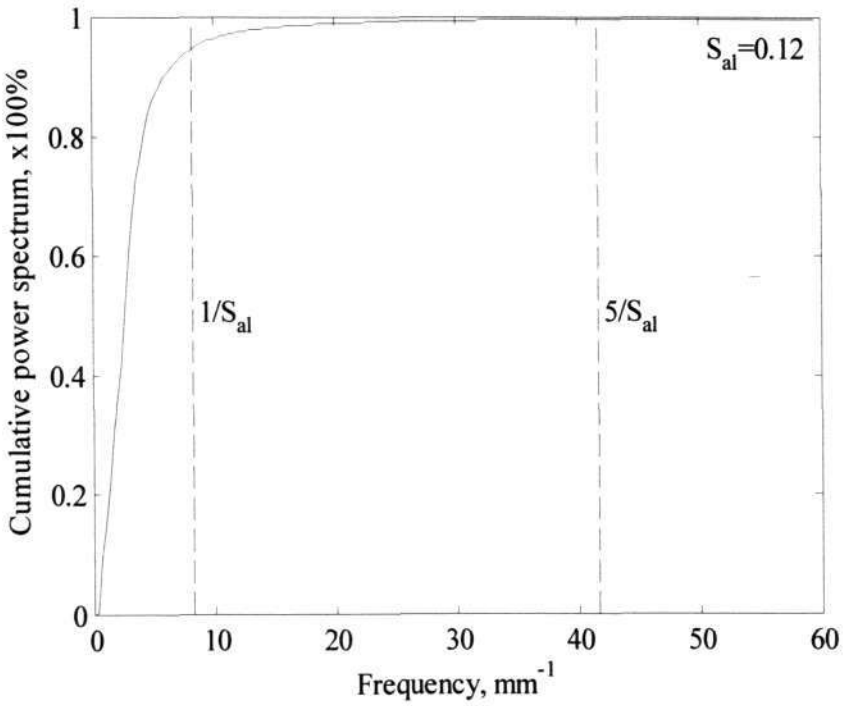

(b)

Figure 4.4 Power spectrum of grinding wheel C80M7V: (a) radial power spectrum, (b) cumulative power spectrum. Line "—" is the power spectrum sampled at 5 µm. Line "--"the power spectrum sampled at 60 µm

On the contrary, the strong relationship between parameters such as S_{ds} and S_{sc} and the sampling interval can be explained by low-pass filtering. These parameters depend on the local definition of the summits and are sensitive to the presence of high frequency in the spectrum. This is also the reason why S_z is slightly reduced as the sampling interval is increased as S_z characterises the highest peaks and lowest valleys of the topography, thus is rather sensitive to the presence of high-frequency components.

Table 4.2 Correlation between abrasive grain size and S_{al}

Specification	Average grain size	S_{al}, mm
A46H7V	0.415	0.34
A80J8V	0.226	0.30
B120H200V	0.139	0.13
B140N200VT2	0.114	0.14
C80M7V	0.226	0.12
C120J8V	0.144	0.13

The behaviour of S_{al} is rather unique as it seems unaffected until the normalised sampling interval does not exceed 0.3. This can be explained by the Wiener- Khinchine theorem (Bendat and Piersol 2000) which states that the autocorrelation and the power spectrum are a pair of the Fourier transform. Thus, S_{al} is affected by a few dominant frequency components in the spectrum. Until the sampling interval increases to some critical value these components are not affected, hence S_{al} remains unchanged. It can be confirmed by the fact that the critical value is approx 0.3-0.5 as the requirement of the Nyquist sampling theorem (Papoulis 1962). In addition, Figure 4.2 to 4.4 expose an interesting relationship between the inverse of S_{al} and the accumulative power spectrum. The value of the inverse corresponds to the frequency at which the sampled power spectrum will contain all major power of the original power spectrum. Moreover, the proportion between the average grain sizes and S_{al} can be noticed (Table 4.2). It is

certainly due to the facts that the grain size is a major component of grinding wheel structure.

4.3 Criteria for determining the sampling condition

Lin (1993) proposed that the analysis of cumulative radial spectra could be used for choosing the sampling condition. The sampling interval is estimated using the high frequency cut-off, at which a preset percentage of a cumulative spectrum can be reached. While this method can give good sampling intervals, the use of power spectral analysis is rather cumbersome for industrial application. The above investigation suggests that the autocorrelation length could be used as the criterion for determining sampling conditions. It is the fact that there is a correlation between the autocorrelation length and high frequency cut-off. Figure 4.2 to 4.4 show that a sampling interval of $0.5S_{al}$ would give a high frequency cut-off at more than 90% of the cumulative spectrum. The stability of S_{al} further justifies it being used as the criterion for sampling interval determination. It is further noted that the correlation between the autocorrelation length and the high frequency cut-off has been observed by Whitehouse and Archard (1970) for random processes of an exponential autocorrelation function. Thus, the upper limit for selecting sampling intervals is suggested as

$$\Delta x \leq 0.5S_{al} \tag{4.9}$$

It is obvious that decreasing the sampling interval will increase the high frequency cut-off. However, the spectra of the grinding wheels (Figure 4.2-4) disclose that the frequencies higher than $1/S_{al}$ possess insignificant magnitudes. As a rule of thumb the lower limit for selecting sampling intervals can be set as

$$\Delta x \geq 0.1S_{al} \tag{4.10}$$

It is equivalent to the high frequency cut-off of $5/S_{al}$. For the investigated grinding wheels, this limit corresponds to more than 99% of the power spectrum. A further justification is that sampled points at less than $0.1S_{al}$ (0.1 of the correlation length) would be highly correlated; thus redundant.

The above criteria can be further justified by examining the radial power spectra of a random field $X(\mathbf{r})$ with the autocorrelation function as follows

$$R(\tau) = exp(-\tau / \beta) \tag{4.11}$$

where $\tau = \sqrt{\tau_x^2 + \tau_y^2}$ is the radial lag; τ_x and τ_y are the lag distance in the 2-D lag space, β is the decay parameter (it is also called a correlation distance in some literature).

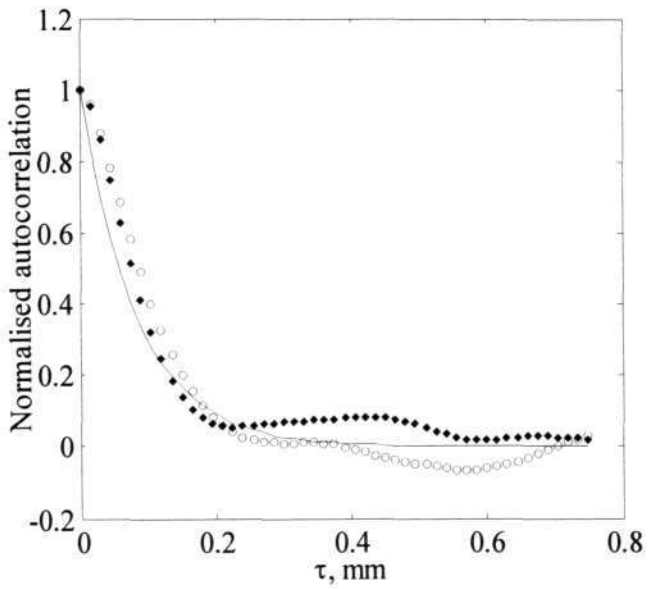

Figure 4.5 Autocorrelation of a grinding wheel surface. Lines "○" and "♦" are the autocorrelation at two perpendicular directions. Line "—" is an exponential best fit line

The above random field is isotropic as its covariance depends only on the distance between observation points. It is reasonably to assume grinding wheel surfaces are isotropic as the values of parameter S_{tr} are generally much larger than 0.5. Figure 4.5

displays autocorrelation functions of a grinding wheel surface at two perpendicular directions. The similarity of the two autocorrelation lines indicates an isotropy of the surface. The matching between the autocorrelation lines and the exponential curve justifies the applicability of the exponential decay autocorrelation model to the grinding wheel topography. Note that the exponential autocorrelation function was also found to fit a large number of surface profiles (Whitehouse and Archard 1970).

The radial spectral density of the above autocorrelation function is (Prigarin 2001):

$$G(\omega)=\frac{\omega\beta^2}{\sqrt{\left(\omega^2\beta^2+1\right)^3}} \tag{4.12}$$

and the cumulative radial spectral function is

$$G_c(\omega)=1-\frac{1}{\sqrt{\omega^2\beta^2+1}} \tag{4.13}$$

where ω is the harmonic frequency and β is the decay parameter.

According to Dong et al (1994), it is recommended to use $R(\tau)=0.2$ as the threshold for the correlation length, then the parameter S_{al} is defined as follows

$$S_{al}=min\left(\sqrt{\tau_x^2+\tau_y^2}\right),\quad R(\tau_x,\tau_y)\le 0.2 \tag{4.14}$$

with τ_x and τ_y are the lag distances in the 2-D lag space.

Then, the value of S_{al} for the autocorrelation function (4.11) is

$$S_{al}=1.6\beta \tag{4.15}$$

At the sampling interval of $0.1S_{al}$, according to the Nyquist theorem, the largest frequency that can be sampled is $5/S_{al}$. The corresponding value of the cumulative power spectrum is

$$G_c(10\pi/S_{al}) = 0.949 \tag{4.16}$$

For the sampling interval of $0.5S_{al}$, the largest frequency that can be sampled is $1/S_{al}$, which corresponds to

$$G_c(2\pi/S_{al}) = 0.753 \tag{4.17}$$

If the sampling area is selected as $10S_{al}$ then the smallest frequency that can be sampled is $1/10S_{al}$, which gives

$$G_c(2\pi/10S_{al}) = 0.069 \tag{4.18}$$

Increasing the sampling area to $20S_{al}$ would have G_c reducing to

$$G_c(2\pi/10S_{al}) = 0.019 \tag{4.19}$$

The analysis shows that the loss of power spectrum due to omitting higher frequency components would be 5% if the surface is sampled the interval of $0.1Sal$. The information loss will rise up to 25% if the sampling interval is $0.5S_{al}$. On the other hand, if the sampling area is $10S_{al}$ or $20S_{al}$, the loss of power spectrum due to omitting lower frequency components is 7% or 2% respectively. Thus, Equation (4.9) and (4.10) ensure that more than 70% of the surface power spectrum is covered, justifying the criteria for selecting the sampling interval.

Furthermore, the analysis suggests that the following criteria could be proposed for selecting the sampling area

$$10S_{al} \leq L_x, L_y \leq 20S_{al} \tag{4.20}$$

A sampling area larger than $20S_{al}$ would negligibly reduce the information lost, but significantly increase measurement time.

4.4 Criteria for counting abrasive grains

From a functional point of view, the number of abrasive grains is one of the most important characteristics of the wheel surface. It has been suggested that parameter S_{ds} could be considered as the static number of cutting edges or cutting grains (Blunt and Ebdon 1996). The use of this parameter however, should be with caution due to its dependence on the sampling interval.

The correlation between S_{al}, abrasive grain diameter and the dominant frequency of the power spectrum suggests that the sampling interval for counting abrasive grain could be chosen on the basis of S_{al}. The reason for using S_{al} is that abrasive grains are the major component of the grinding wheel. Hence, its distribution, size and shape will determine the topography of the wheel. Consequently, it will reflect on the frequency components of the surface, and eventually on S_{al}.

An experiment was conducted to determine the optimal interval for counting abrasive grain. Three samples of grinding wheels (A80J8V, B120H200V and C120J8V) were measured on the stylus system Talyscan 150. The same three samples were also observed in the scanning electron microscope (SEM) system JEOL5600. The samples were marked so that the same area could be measured and observed on the stylus and SEM systems. For all three samples, the parameter S_{ds} was estimated at various sampling intervals. An abrasive grain was identified from the stylus image using the

"eight nearest neighbour" definition. For the SEM images, abrasive grains were counted by visual inspection.

Figure 4.6 to 4.8 show the topographies of the grinding samples obtained by the stylus and SEM systems. The dot marks the position of an abrasive grain on the images. The positions of the abrasive grains on the stylus images were identified using the MATLAB toolbox with the sampling interval varied from 0.27 to $0.37S_{al}$. The positions of the abrasive grains on the SEM images were identified by visually inspecting the samples at the different tilt angles and resolutions. From the images, it is quite clear that the distributions of the grains found on the stylus images are quite similar to the distribution on the SEM ones. Compared to the SEM images, grains in the valleys of the wheel surfaces almost can not be identified (Figure 4.6 to 4.8). It is certainly due to the limited penetration of the stylus tip in to the valley. In some cases (Figure 4.6 to 4.7), the bond can be misidentified as the abrasive grain. In other cases, flat grains covered by bonds can be skipped from counting (Figure 4.6).

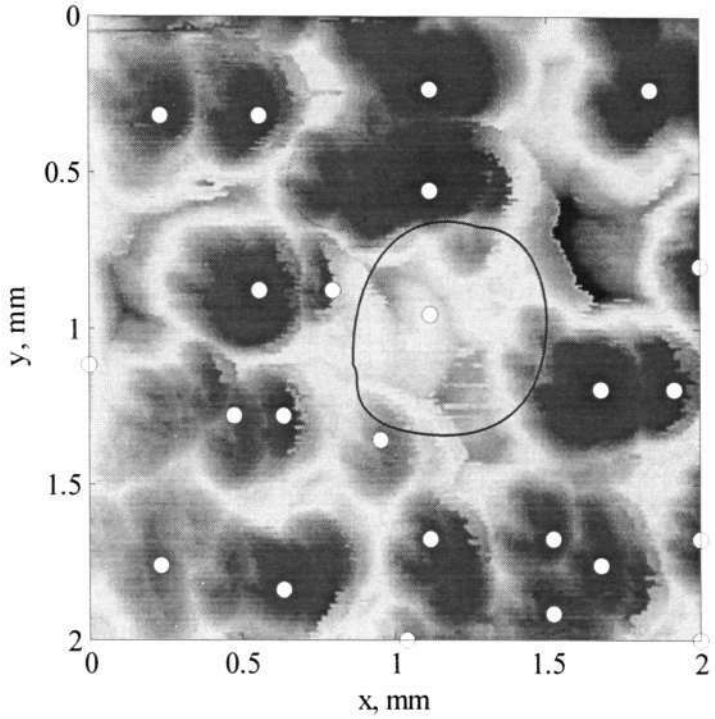

(a)

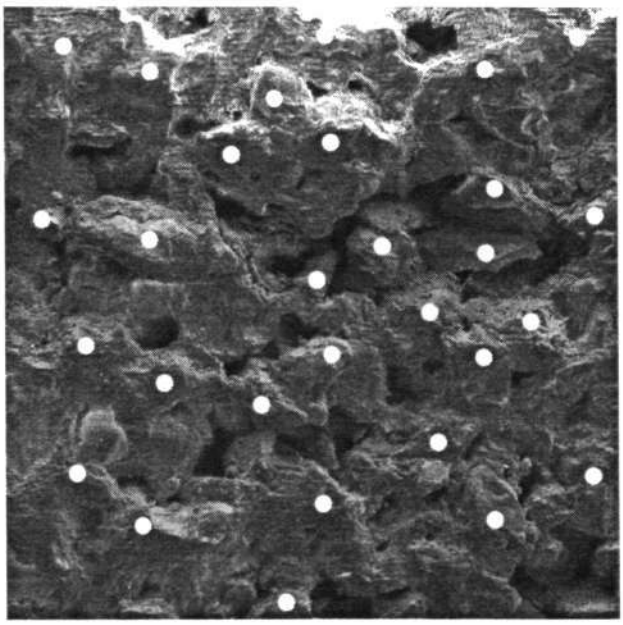

(b)

Figure 4.6 Topography of A80J8V grinding wheel sample, obtained with (a) stylus system, (b) SEM. The dot marks the abrasive grain by using the "eight nearest neighbour" summit definition (stylus) and visual inspection (SEM). The sampling interval is 80 µm ($0.33S_{al}$). Line "—" marks a deep valley that the stylus tip could not access. Line "···" marks an omitted grain. Line "– ·" marks a bond misidentified as a grain

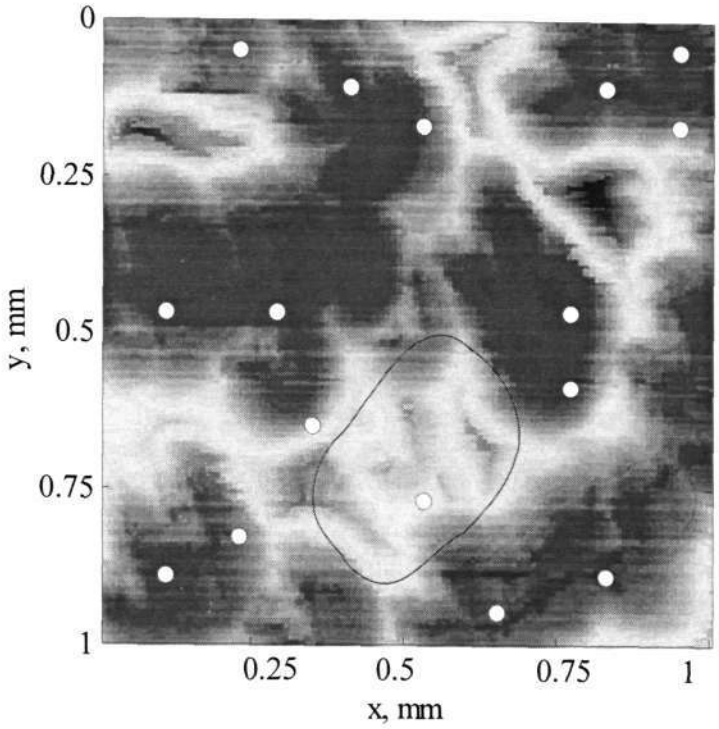

(a)

(b)

Figure 4.7 Topography of B120H200V grinding wheel sample, obtained with (a) stylus system, (b) SEM. The dot marks an abrasive grain by using the "eight nearest neighbour" summit definition (stylus) and visual inspection (SEM). The sampling interval is 60 µm ($0.37S_{al}$). Line "—" marks a deep valley that the stylus tip could not access. Line "···" marks an omitted grain

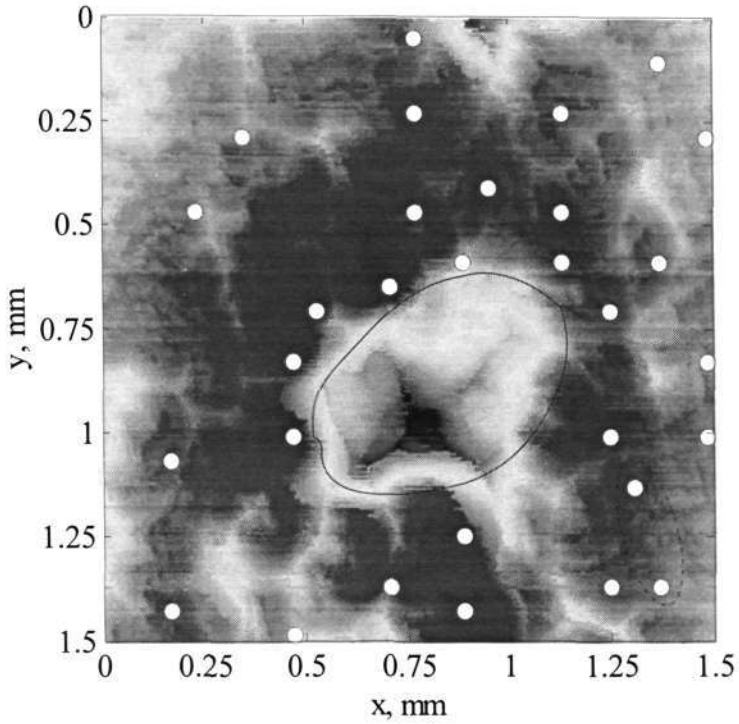

(a)

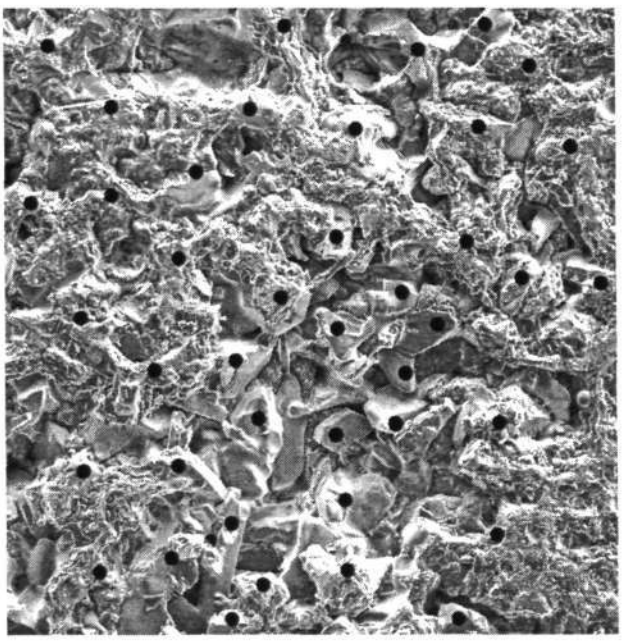

(b)

Figure 4.8 Topography of C120J8V grinding wheel sample, obtained with (a) stylus system, (b) SEM. The dot marks an abrasive grain by using the "eight nearest neighbour" summit definition (stylus) and visual inspection (SEM). The sampling interval is 60 µm ($0.28S_{al}$). Line "—" marks a deep valley that the stylus tip could not access. Line "– ·" marks a bond misidentified as a grain

Figure 4.9 shows the relationship between the parameter S_{ds} and the sampling interval. The sampling interval is normalised with parameter S_{al}. The symbols ●,■, and ▲ highlight the position of the counts of abrasive grains in relation with the sampling interval. The number of abrasive grains counted on the SEM images for the three samples corresponds to the number of summits identified on the stylus images at the sampling interval $(0.27\text{-}0.35)S_{al}$, or

$$\frac{S_{al}}{4} \le \Delta \le \frac{S_{al}}{3} \tag{4.21}$$

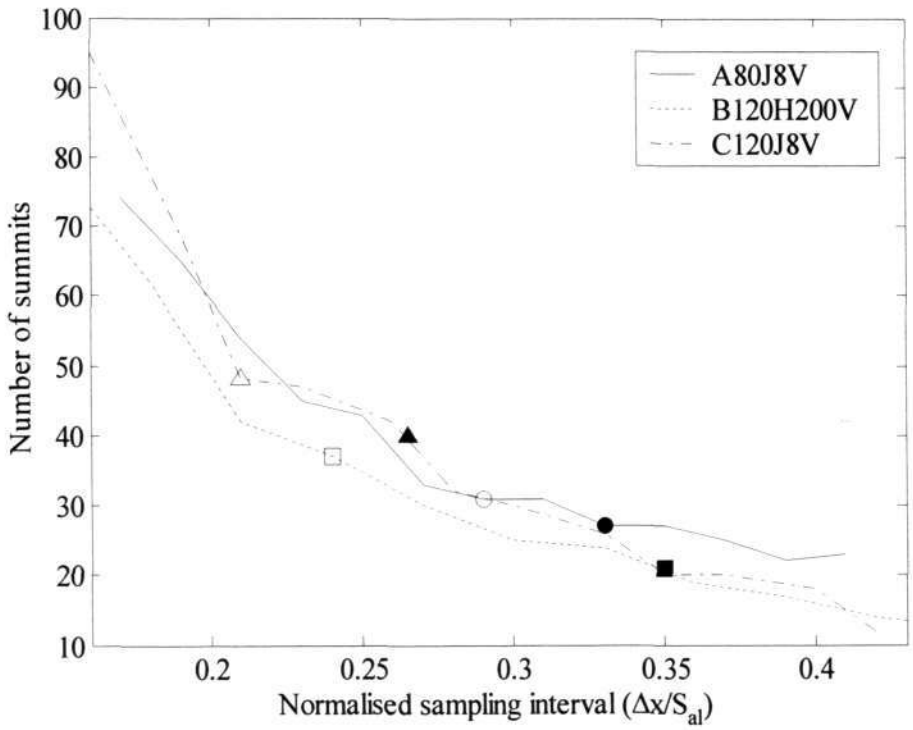

Figure 4.9 Number of summits (S_{ds}) at various intervals. Symbols ●, ■, and ▲ mark the number of grains counted on SEM images. Symbols ○,□, and Δ mark value S_{ds} at the sampling intervals according to Blunt and Ebdon (1996)

Blunt and Ebdon (1996) proposed that the optimum sampling interval Δ to use S_{ds} as measure of abrasive grains is

$$\frac{d_g}{4} \leq \Delta \leq \frac{d_g}{3} \tag{4.22}$$

where d_g is the mean diameter of grains.

Figure 4.9 shows the values of S_{ds} at the sampling intervals as recommended by Blunt and Ebdon (1996). The values are generally larger than the number of grains found on the SEM images while the sampling intervals are approximately in the range $(0.2\text{-}0.3)S_{al}$. The resemblance between Equation (4.21) and (4.22) is clear and not coincident. Their similarity is obviously due to the correlation of S_{al} and an abrasive grain dimension. Compared to a diameter of grains, S_{al} is a better criterion for selecting the sampling interval as it accounts for the uneven distribution and the variability of grains.

4.5 Criteria for determination of sampling conditions for anisotropic surfaces

For anisotropic surfaces such as ground surfaces, the correlation lengths in the lay direction and the direction perpendicular to the lay direction differ significantly (Figure 4.10). In the lay direction, the autocorrelation often decreases at a slower rate than in the other direction. The relationship between the correlation lengths at the two directions is expressed by parameter S_{tr}. Nevertheless, Figure 4.10 reveals that the exponential curve still reasonably fits the autocorrelation functions.

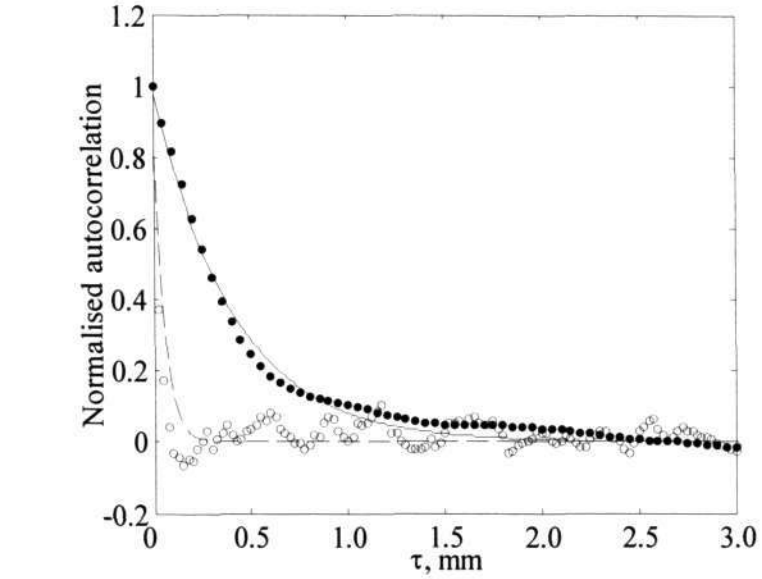

(a)

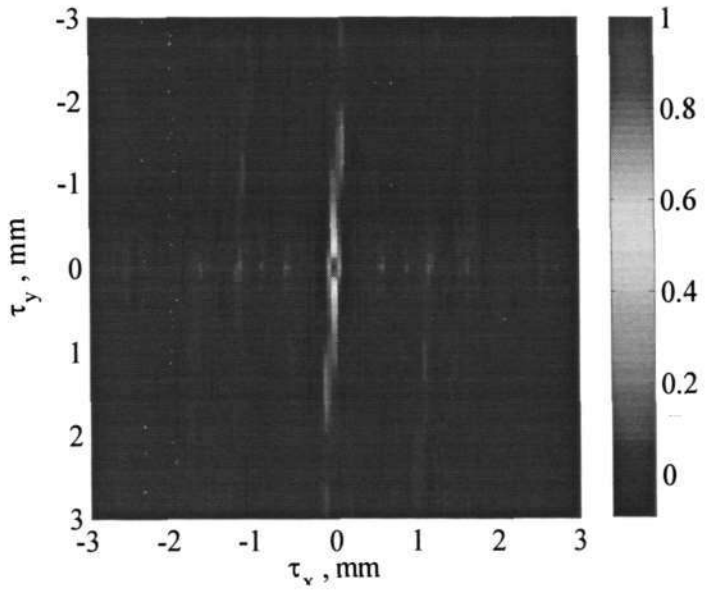

(b)

Figure 4.10 Autocorrelation of a ground surface: (a) cross section view, (b) areal view. Lines "•" and "○" are the autocorrelation at lay and perpendicular-to-lay directions. Lines "–"and "– –" are exponential best fit lines

For such an anisotropic surface, its autocorrelation function can be approximated as an ellipsoidal

$$R(\tau_x, \tau_y) = exp\left\{-\left[\left(\frac{\tau_x}{\beta_x}\right)^2 + \left(\frac{\tau_y}{\beta_y}\right)^2\right]^{1/2}\right\} \tag{4.23}$$

where τ_x, τ_y, β_x, and β_y are the lags and the decay parameters in perpendicular-to-lay and lay directions respectively.

Therefore, the analysis in Section 4.3 could be applicable to ground workpiece surfaces. Figure 4.11to 4.14 show that ground surfaces display the same behaviour as the grinding wheel surfaces. Amplitude parameters such as S_q and S_z are fairly constant while frequency-sensitive parameter S_{ds} displays a sharp drop with increased sampling interval (Figure 4.11).

Regarding the power spectra (Figure 4.12 to 4.14), they are still dominated with a few low frequency components; components with frequency higher than $1/S_{al}$ generally account for less than 15% of the power. This similarity suggests the criteria for selecting the sampling condition can be extended as follows:

For the direction perpendicular to lay, the sampling interval can be estimated as for the isotropic surfaces:

$$0.1S_{al} \leq \Delta x \leq 0.5S_{al} \tag{4.24}$$

For the lay direction, the sampling interval can be estimated as:

$$0.1S_{al} \leq S_{tr}\,\Delta y \leq 0.5S_{al} \tag{4.25}$$

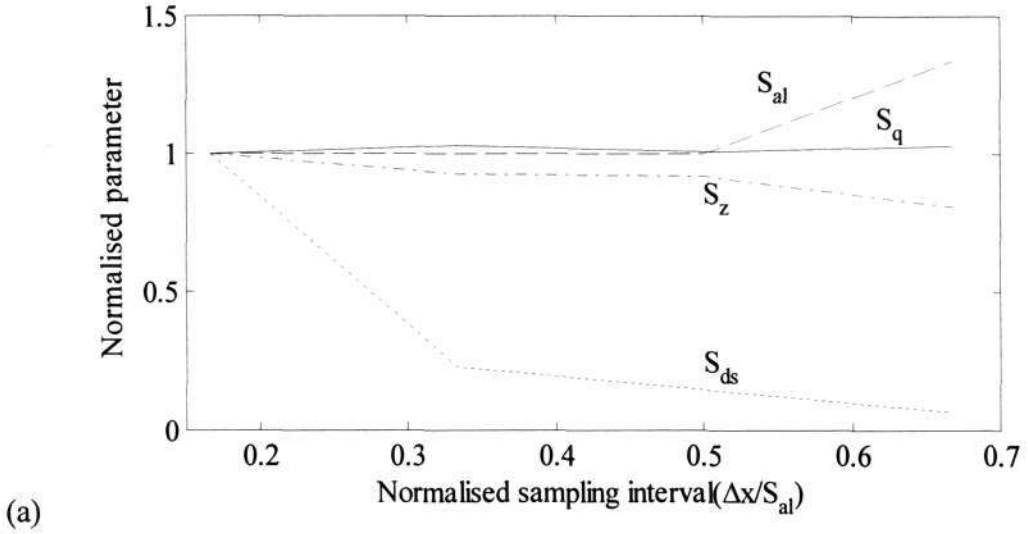

(a)

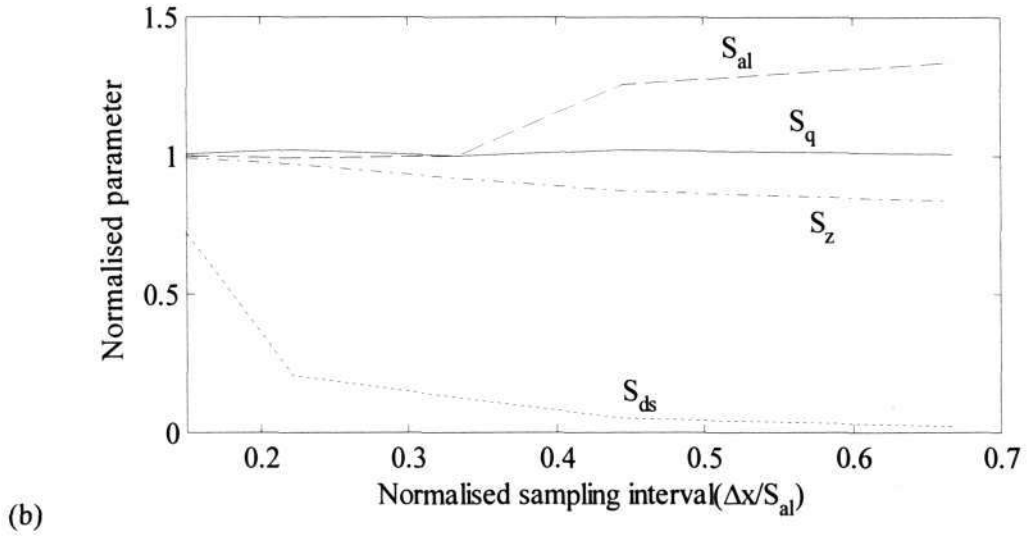

(b)

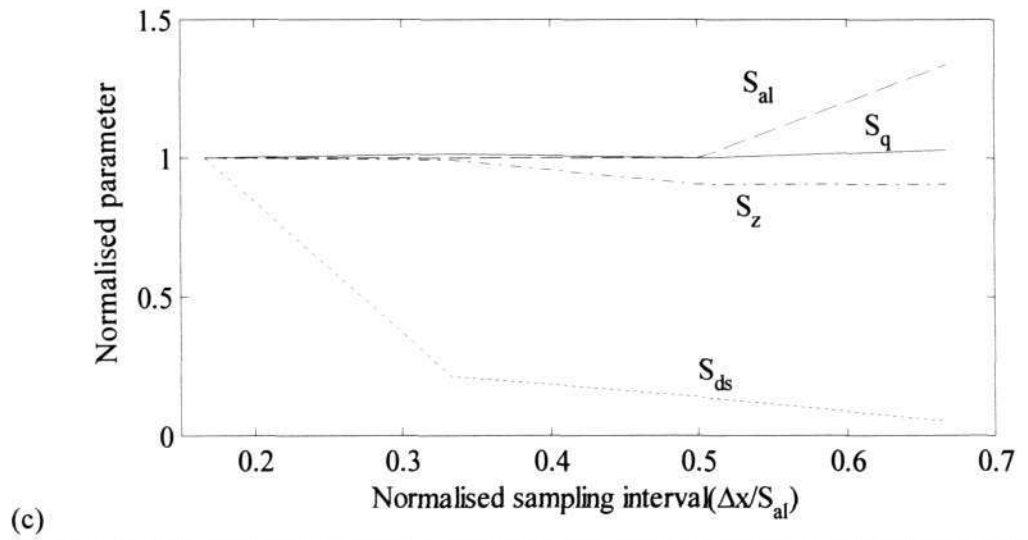

(c)

Figure 4.11 3-D characterisation parameters at various sampling intervals: (a) O1, (b) D2, (c) mild steel

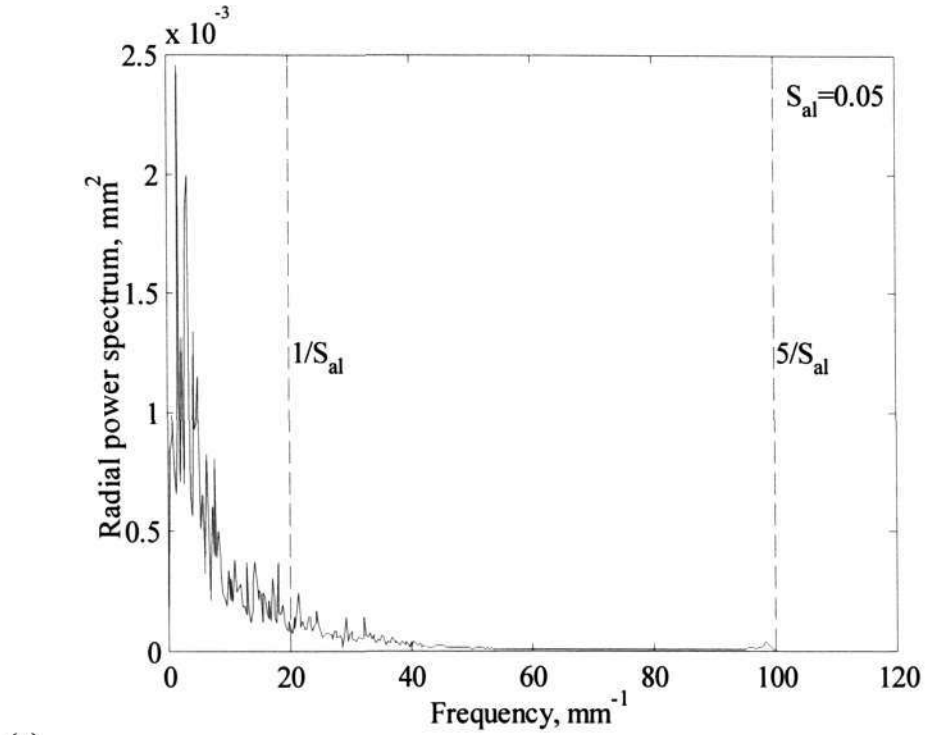

(a)

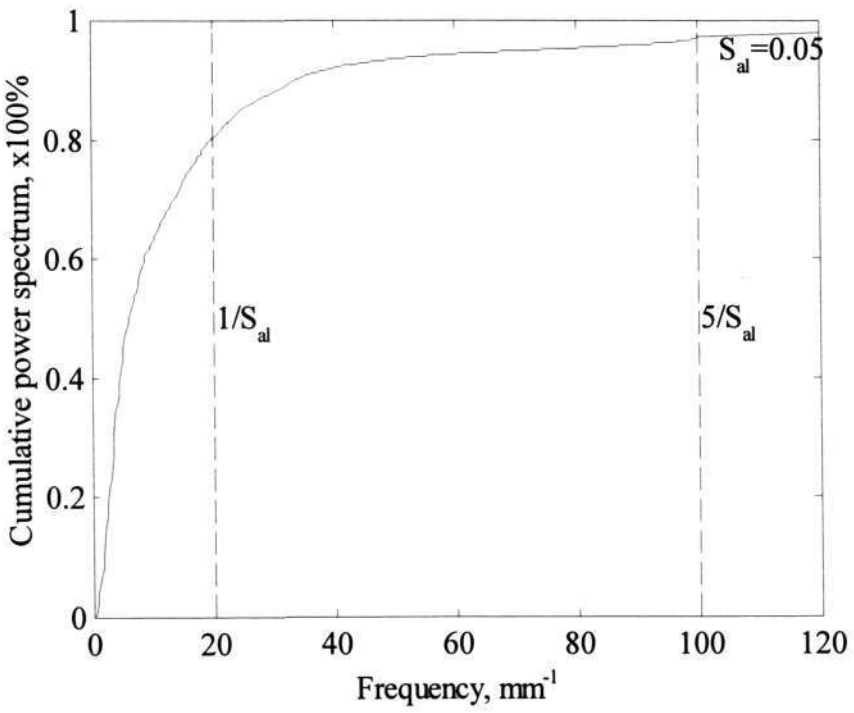

(b)

Figure 4.12 Power spectrum of ground workpiece O1: (a) radial power spectrum, (b) cumulative power spectrum

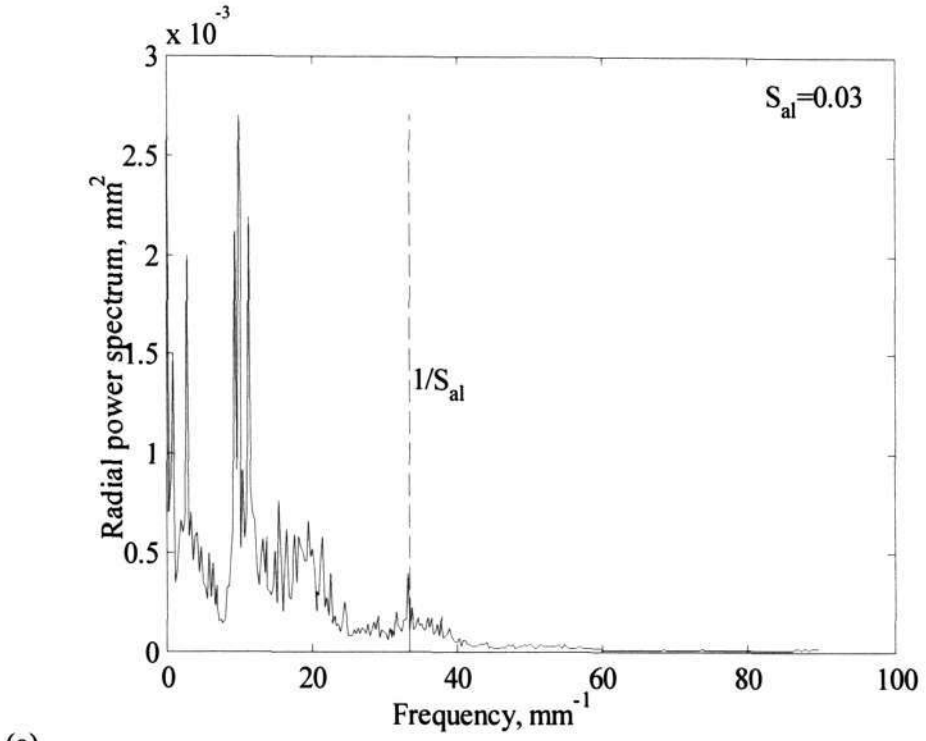

(a)

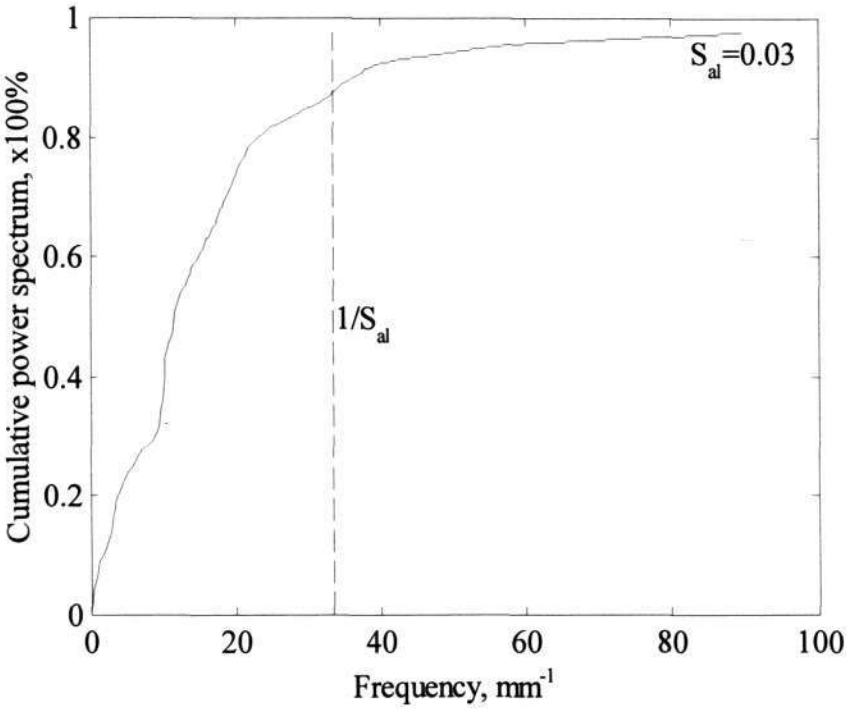

(b)

Figure 4.13 Power spectrum of ground workpiece D2: (a) radial power spectrum, (b) cumulative power spectrum

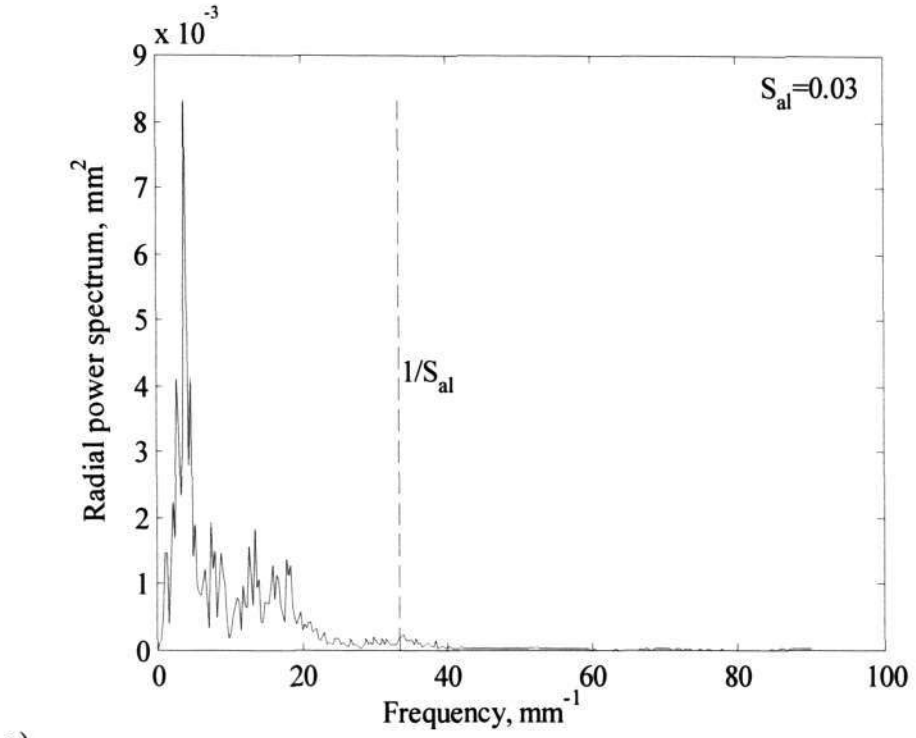

a)

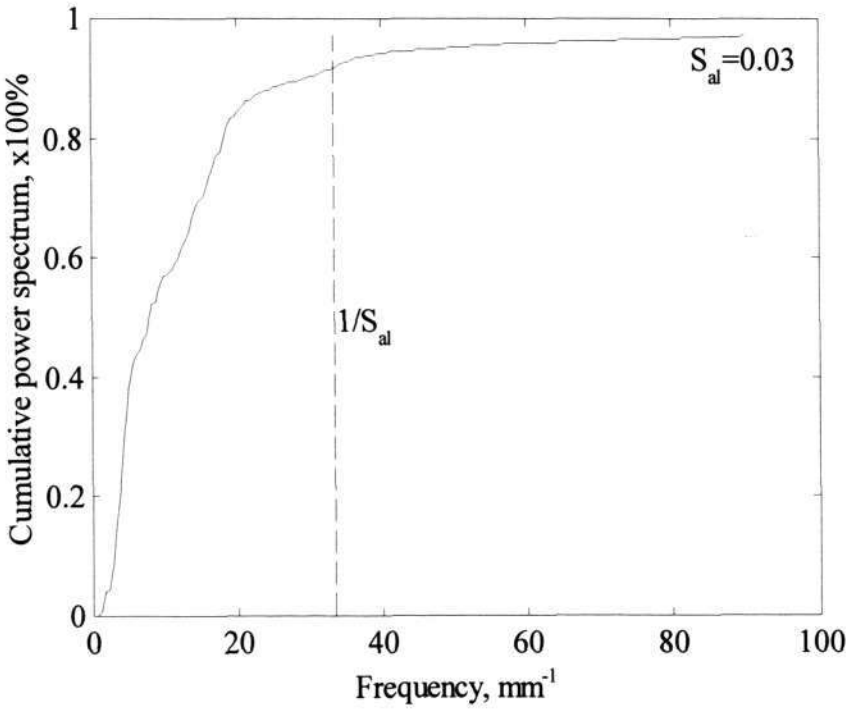

b)

Figure 4.14 Power spectrum of ground workpiece mild steel: (a) radial power spectrum, (b) cumulative power spectrum

For anisotropic surfaces such as turned surfaces, surfaces are periodic in one orthogonal direction. In such cases, the surface is composed of one or two wave components. Figure 4.15 shows the power spectrum and the autocorrelation function of a turned surface. Evidently from Figure 4.15a, the power spectrum consisted of a few components in the perpendicular-to-lay direction. Consequently, the autocorrelation is periodic in the same direction (Figure 4.15a,b). The periodicity of the autocorrelation function is the same as the frequency of the main wave component of the surface. On the other hand, the autocorrelation function in the lay direction still shows the characteristic of exponential decay. Furthermore, the above mentioned observation regarding the relationship between the 3D parameter, S_{al}, and the radial power spectra is also valid for the turned surface (Figure 4.16).

For such as surfaces, the autocorrelation can be approximated as follows

$$R(\tau_x, \tau_y) = \cos(\omega_0 \tau_x) \exp(-|\tau_y| / \beta) \tag{4.26}$$

where ω_0 is the harmonic frequency of the main component of the surface; τ_x and τ_y are the lag distances in in perpendicular-to-lay and lay directions respectively; β is the decay parameter. Hence, the value of S_{al} is one fourth of the wavelength of the main component

$$S_{al} = \pi / 2\omega_0 \tag{4.27}$$

As the result, the criterion for the sampling interval in the perpendicular-to-lay direction can be modified as follows

$$0.5 S_{al} \leq \Delta x \leq S_{al} \tag{4.28}$$

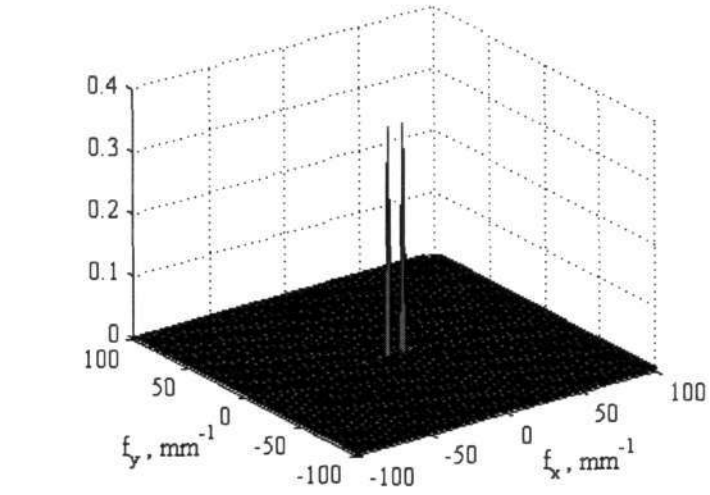

(a)

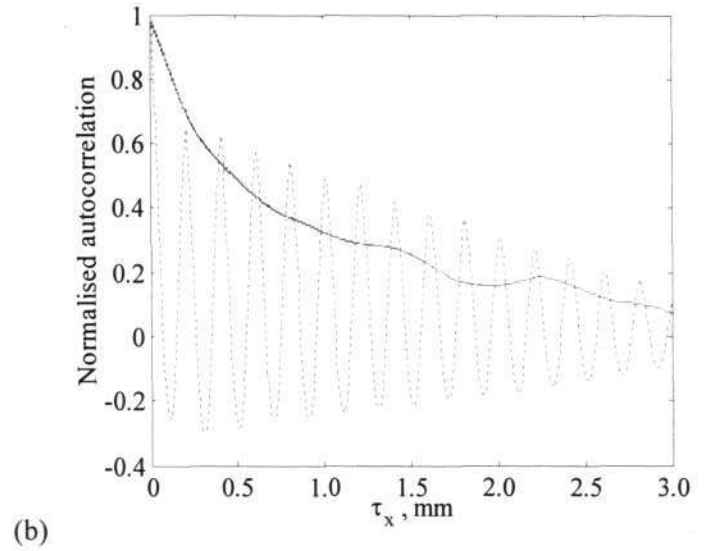

(b)

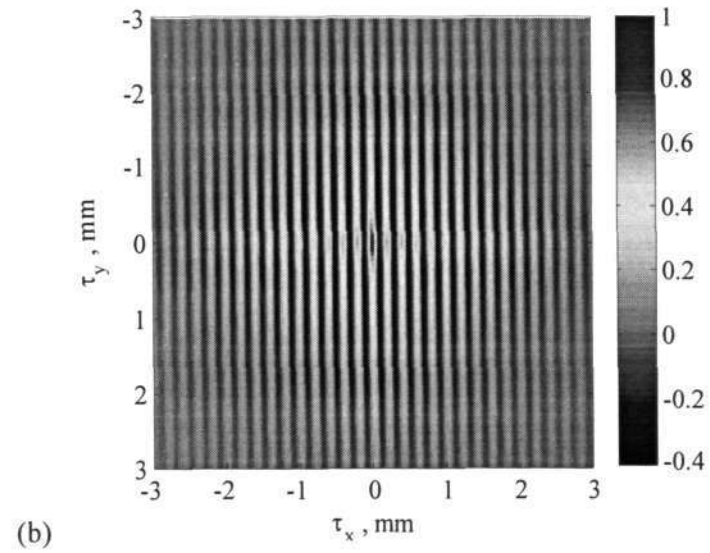

(b)

Figure 4.15 Power spectrum and autocorrelation of a turned surface: (a) power spectrum, (b) cross section view of $R(\tau)$, (b) areal view of $R(\tau)$. Lines "–" and "– –" are the autocorrelation at lay and perpendicular-to-lay directions

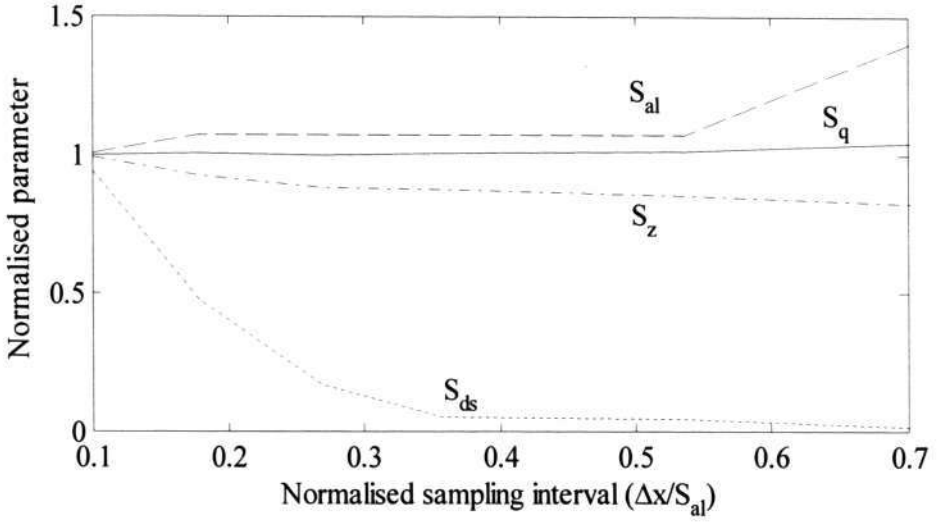

(a)

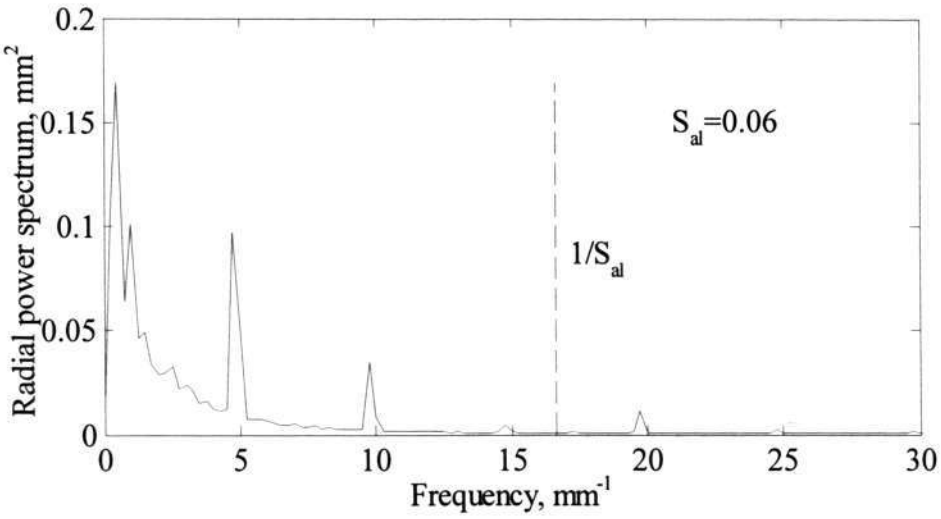

(b)

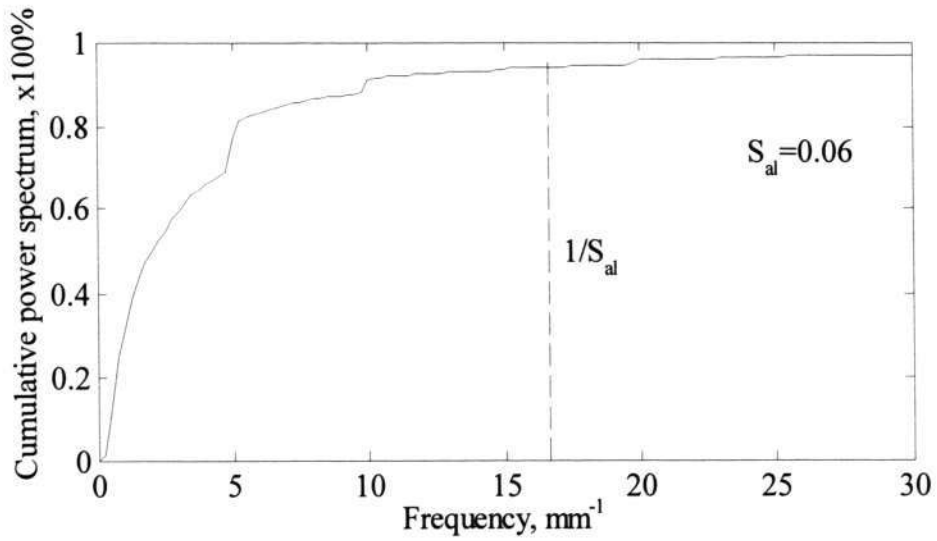

(c)

Figure 4.16 Turned workpiece: (a) 3D-parameters at various sampling interval, (b) radial power spectrum, (c) cumulative power spectrum

4.6 Chapter summary

Criteria for determining the sampling condition are proposed. For the grinding wheel surface, two set of rules are suggested on the basis of the correlation length S_{al}. The analysis shows that the correlation-length based criteria could ensure the minimum loss of information while avoiding redundant data points. For identifying abrasive grains, using the correlation length will be more advantageous than the grain diameter as it accounts for the distribution of grains and the variability of grain size.

The correlation length –based criteria can be extended to surfaces like ground or turned by taking into account the isotropic parameter S_{tr}. Although the study was concerned mainly with grinding wheels and ground workpieces, its conclusions can be applicable to other isotropic and anisotropic surfaces.

Chapter 5

Correlation of grinding wheel topography and its grinding performance

5.1 Introduction

It is a well-known fact that the wheel topography and the conditions under which it is prepared have a profound influence upon the grinding performance – as evidenced by the grinding forces, power consumption, cutting zone temperatures, and also the surface finish of the workpiece. The relationship between the wheel topography and the grinding performance has been partially investigated using two-dimensional surface analyses. Malkin (1989, p.85) concluded that the grinding wheel topography is formed mainly by bond and grain fracture. Coarse dressing by a large dressing lead and depth generally results in reduced grinding forces and rougher workpiece finish. Liao (1995) found the correlation between the fractal dimension of the wheel profiles and the surface finish of the workpiece and the grinding force, in which the grinding wheels with large fractal dimension produce smaller grinding forces and smoother finish.

Tonshoff et al. (1998) showed the correlation between the dressing conditions and the grinding performance.

Recently, preliminary studies of the three-dimensional parameters revealed that they can be used to characterise the grinding wheel topography. Blunt and Ebdon (1996) showed that by appropriate selecting the sampling conditions, three-dimensional parameter S_{ds} can be used to describe abrasive grains. Butler et al. (2002, 2004) demonstrated the correlation of the three-dimensional parameters S_{ds} and S_{sc} of the grinding wheel with the grinding performance. The application of the three-dimensional parameters, however, needs more extensive research as it has been shown in the previous chapter that some parameters are strongly affected by the sampling conditions; thus can distort the interpretation of the results.

Nickel-based alloy is a difficult-to-grind material. On the one hand, the advanced thermo-mechanical properties of the alloy are responsible for its wide use in turbine and aircraft engines while on the other they make it much less suitable for machining and grinding. Due to its work-hardenability, low thermal conductivity and diffusivity, and burn-sensitivity the selection of optimal grinding conditions is not an easy task (Jackson et al. 2001).

Traditionally, nickel-based alloy components are finished by conventional grinding methods or by the continuous dress creep feed method using an aluminium oxide wheel. In the last few years, the requirement for better grinding performance has seen the shift from conventional wheels to CBN ones in industry, especially in high-speed grinding (Chen et al. 2002, Jackson et al. 2001, Stephenson et al. 2001). Although tremendous progress has been made in the processing of the material, linited information was published about the correlation between the grinding wheel

conditioning and its performance in grinding these materials (Kumar et al.1991). Similar to the conventional wheels, the choice of wheel preparation can have a decisive impact on the workpiece quality. Ishikawa and Kumar (1991) showed that the truing and dressing parameters can alter the wheel surface conditions. Westkamper and Tonshoff (1993) cautioned that wrong selection of wheel conditioning parameters could reverse the economical advantage of CBN wheels over the conventional ones. Prusak et al (1997) determined optimum parameters to achieve steady-state grinding through a series of experiments. Stephenson et al. (2001) found that it is difficult to optimise the process due to lack of understanding wear characteristics of CBN.

In this chapter, the correlation between the CBN grinding wheel and its grinding performance is studied through the application of the three-dimensional surface parameters. By utilising the criteria proposed in the previous chapter, the correlation between wheel surface topography and it functional performance is clarified. The next section describes the experiment set-up, followed by the result discussion. The last section will give the conclusions for the investigation.

5.2 Experiment procedure

The relationship between the grinding wheel topography and its performance was studied using a 2^3 experimental design, in which the truing parameters were varied. The wheel performance was tested by grinding a workpiece of Inconel 718. Three replications of the experiment were conducted.

5.2.1 Workpiece material

The workpiece material is nickel-based alloy Inconel 718, primarily used in gas turbines, steam turbine components and aircraft engine component construction due to

its heat-resistant properties. The superalloy microstructure has some characteristics that are responsible for its poor machinability. It has an austentic matrix, and like stainless steels, work-hardens rapidly during machining. Moreover, the presence of hard abrasive carbides in their microstructure also deters machinability. The properties of Inconel 718 are given in Table 5.1 and Table 5.2.

Table 5.1 Chemical composition of Inconel 718 (supplier's specification)

Element	Composition (weight %)
Nickel	50.00-55.00
Chromium	17.00-21.00
Iron	Balance
Niobium	4.75-5.50
Molybdenum	2.80-3.30
Titanium	0.65-1.15
Aluminium	0.35-0.8
Cobalt	max. 1.00
Carbon	max. 0.08
Manganese	max. 0.35
Titanium	max. 1.15
Silicon	max. 0.35
Phosphorus	max. 0.015
Sulphur	max. 0.015

Table 5.2 Physical and mechanical properties of Inconel 718 (supplier's specification)

Density, kg/m^3	8220
Modulus of elasticity, GPa	210
Tensile strength, MPa	1240
Yield at 0.2% offset, MPa	1036
Hardness, HRC	37
Specific heat, J/kg.K	435
Thermal expansion, μm/m.K	13
Thermal conductivity, W/m.K	11.4

5.2.2 Grinding conditions

A surface grinding machine Okamoto 63DXNC (Appendix B) equipped with a high-speed and high-power spindle was used for the investigation. The spindle system was balanced by an on-machine add-on microbalancer. The amplitude of the wheel head vibration was adjusted to be less than 0.1 μm peak-to-peak at a maximum rotational speed of 5000 rpm. A 3-channel dynamometer Kistler 9265B was used to measure the grinding forces. Signals from the dynamometer were amplified by multi-channel amplifier Kistler 5019 before captured using Labview 12-bit DAQ system. The grinding conditions are given in Table 5.3.

Table 5.3 Grinding conditions

Grinding wheel velocity v_s, m/s	50
Workpiece velocity v_w, m/s	0.015
Depth of cut a, μm	20
Transverse step w, mm	3
Coolant	water-soluble coolant
Grinding wheel	B140N200V
Wheel diameter, mm	200

5.2.3 Truing and dressing conditions

The truing operation was conducted in unidirectional mode (v_s/v_d = positive). A diagram of truing operations is given in Figure 5.1. The truer velocity v_d, truing lead s_d and truing depth a_d were varied according to a 2^3 factorial design (Montgomery 1997).

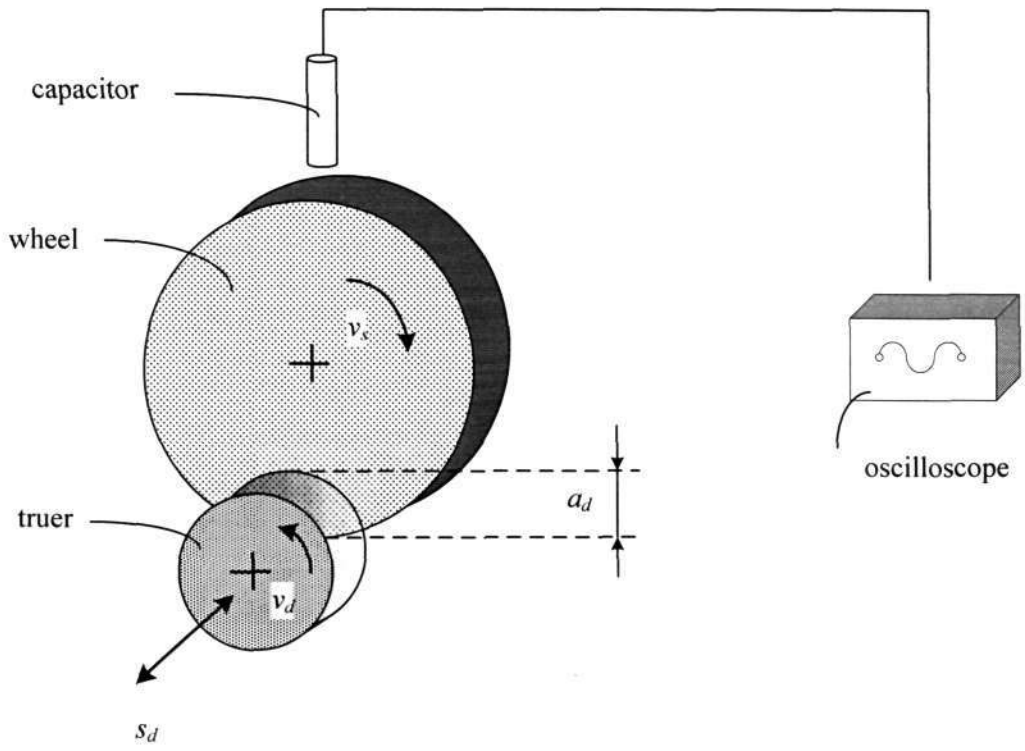

Figure 5.1 Truing operation

The wheel and truer velocities were chosen so that the speed ratios are 0.4 and 0.7 respectively. Although it is recommended that the wheel should be trued at its working speed, the grinding wheel speed in truing is limited at 1400 rpm due to the limited speed of the truer. For truing, the rotary truer with SiC wheel C80M7V was used. The speed of the truer was controlled by Eurotherm 601 variable speed drive. The wheel was trued until the run-out was less than 10 micron. The run-out of the wheel was checked using the capacitive sensing system Lion Precision DX405HA. The signal from the capacitive sensing system was recorded by the digital oscilloscope LeCroy 9300 series. After truing the wheel was dressed by plunge grinding into an abrasive stick A320 with a depth of 10-15 mm and at a plunge rate of approximate 150 mm/min. Table 5.4 summarises the truing conditions.

Table 5.4 A 2^3 factorial design for truing the grinding wheels

Run	Truer velocity, m/s	Lead, mm/rev	Truing depth, μm
1	10.5	0.3	30
2	10.5	0.3	10
3	10.5	0.1	30
4	10.5	0.1	10
5	6	0.3	30
6	6	0.3	10
7	6	0.1	30
8	6	0.1	10

5.3 Results and discussion

The topography of the workpiece and the grinding wheels were obtained using the stylus system Talyscan 150. Because it is very difficult to measure the grinding wheel directly, the grinding wheel topography was obtained by using the two-stage replication technique (Chapter 3). The sampling interval for the workpiece topography was 5 μm; and for the grinding wheel topography was 15 μm. The sampling area for the grinding wheel and the workpiece was 3x3 mm and 2x2 mm respectively. The grinding forces data captured by Labview were stored in ASCII format, and later processed using a MATLAB script. The values of the grinding forces were averaged from several grinding passes.

5.3.1 Workpiece roughness

The surface roughness S_q of the workpieces and their ANOVA result are shown in Table 5.5 and Table 5.6. The full listing of the workpiece surface characterisation parameters is given in Appendix H. The ANOVA analysis for the workpiece roughness reveals that its roughness is strongly influenced by the truer velocity, lead and truing

depth in truing. Increasing the truer velocity, truing lead or truing depth will cause the workpiece surface to degrade. Among the parameters, the truing lead and truing depth display the strongest influence while the effect of the truer velocity is significant at the confidence level of 90%. Moreover, there were significant interaction effects between the truing speed and truing depth.

Table 5.5 Workpiece surface roughness S_q

Run	S_q		
	Replica 1	Replica 2	Replica 3
1	0.43	0.52	0.52
2	0.32	0.33	0.31
3	0.38	0.37	0.34
4	0.29	0.30	0.27
5	0.47	0.46	0.47
6	0.33	0.36	0.39
7	0.33	0.38	0.38
8	0.20	0.18	0.20

Table 5.6 Analysis of Variance for S_q of the workpiece

Source of variation	v_d	s_d	a_d	v_dx s_d	v_dx a_d	s_dx a_d	v_dx s_dx a_d	Error	Total
Estimate of effect	0.02	0.11	0.13	-0.01	-0.03	0.01	0.04		
Sum of squares	0.002	0.069	0.105	0.001	0.004	0.000	0.008	0.011	0.20
Degree of freedom	1	1	1	1	1	1	1	16	23
Mean square	0.002	0.069	0.105	0.004	0.001	0.000	0.008	0.001	
F	2.65	103.83	157.74	0.75	6.63	0.38	12.41		
p-value	0.12	0.00	0.00	0.40	0.02	0.55	0.00		

5.3.2 Grinding forces

The grinding forces and the corresponding ANOVA results are shown respectively in Table 5.7, Table 5.8, and Table 5.9 respectively. The ANOVA analysis for the tangential forces highlights the considerable effects on the force by the truer velocity and truing depth. The tangential force rises when the truer velocity or the truing depth falls. On the other hand, changing the value of truing lead seems not to affect the tangential force. Meanwhile, the ANOVA analysis for the normal force indicates that all the parameters of the truing mode can influence the force at the significant level less than 10%. Among the factors, the truer velocity and truing depth display the largest effect. Similarly to the tangential force, reducing the truer velocity, truing lead and truing depth makes the normal force rise. Furthermore, the interaction effects between the truing factors on the normal force are significant at the level of 0.1 while such interaction is negligible for the tangential force.

Table 5.7 Grinding forces

Run	Tangential force, N			Normal force, N		
	Replica 1	Replica 2	Replica 3	Replica 1	Replica 2	Replica 3
1	4.59	4.28	4.40	11.55	12.50	11.34
2	4.84	4.39	4.38	13.46	12.86	11.33
3	4.10	4.45	4.93	11.58	12.64	12.84
4	4.90	4.59	4.38	12.53	11.39	10.81
5	4.63	5.07	4.89	13.78	13.12	12.31
6	5.51	5.18	5.88	14.98	14.10	14.61
7	4.43	4.93	5.07	14.09	14.98	14.98
8	5.90	5.02	4.87	15.53	15.07	15.11

Table 5.8 Analysis of Variance for tangential forces

Source of variation	v_d	s_d	a_d	v_dx s_d	v_dx a_d	s_dx a_d	v_dx s_dx a_d	Error	Total
Estimate of effect	-0.60	0.04	-0.34	-0.12	0.22	-0.05	0.06		
Sum of squares	2.13	0.01	0.69	0.08	0.28	0.01	0.02	1.88	5.10
Degree of freedom	1	1	1	1	1	1	1	16	23
Mean square	2.13	0.01	0.69	0.08	0.28	0.01	0.02	0.12	
F	18.15	0.07	5.89	0.71	2.43	0.11	0.17		
p-value	0.00	0.79	0.03	0.41	0.14	0.74	0.69		

Table 5.9 Analysis of Variance for normal forces

Source of variation	v_d	s_d	a_d	v_dx s_d	v_dx a_d	s_dx a_d	v_dx s_dx a_d	Error	Total
Estimate of effect	-2.32	-0.47	-0.51	0.68	0.52	-0.62	-0.15		
Sum of squares	32.34	1.32	1.54	2.75	1.61	2.29	0.13	7.77	49.74
Degree of freedom	1	1	1	1	1	1	1	16	23
Mean square	32.34	1.32	1.54	2.75	1.61	2.29	0.13	0.49	
F	66.61	2.71	3.17	5.67	3.31	4.71	0.27		
p-value	0.00	0.12	0.09	0.03	0.09	0.05	0.61		

5.3.3 Grinding wheel topography

The 3-D parameters of the grinding wheel topographies and their corresponding ANOVA results are presented respectively in Table 5.10 to 5.15. For the evaluation of the grinding wheel topography, the grinding wheel topography was replicated at two separate locations. The values of the surface characterisation parameters were averaged from the two samples for each experimental run. The full listing of the characterisation parameters is given in Appendix G.

The coarseness of the grinding wheel can be evaluated through the root-mean-square parameter S_q (Table 5.10). It is evident from the ANOVA analysis that the truing parameters have similar effects on the grinding wheel topography (Table 5.11) as on the workpiece surfaces (Table 5.6). All truing factors exert considerable influence on the wheel roughness. Raising the truing velocity, the lead and the depth of cut will make the wheel rougher or, in other words coarser. Furthermore all the interaction effects between the factors are significant at the level of 0.05.

Table 5.10 Average surface roughness S_q of the grinding wheels (μm)

Run	Replica 1	Replica 2	Replica 3
1	13.61	15.44	13.82
2	13.20	13.07	14.08
3	11.44	11.50	10.48
4	14.07	12.55	13.71
5	13.86	15.27	12.76
6	9.93	10.83	9.09
7	13.20	14.25	14.59
8	10.63	10.69	9.31

Table 5.11 Analysis of Variance for S_q of the grinding wheels

Source of variation	v_d	s_d	a_d	v_dx s_d	v_dx a_d	s_dx a_d	v_dx s_dx a_d	Error	Total
Estimate of effect	1.05	0.71	1.59	0.87	-2.32	0.84	0.73		
Sum of squares	6.59	3.03	15.17	4.50	32.23	4.22	3.23	11.52	80.49
Degree of freedom	1	1	1	1	1	1	1	16	23
Mean square	6.59	3.03	15.17	4.50	32.23	4.22	3.23	0.72	
F	9.16	4.21	21.07	6.25	44.78	5.87	4.49		
p-value	0.01	0.06	0.00	0.02	0.00	0.03	0.05		

For the characterisation of the abrasive grains, the parameters density of summits S_{ds} (Table 5.12) and arithmetic curvature of summits S_{sc} (Table 5.14) are used as the indicator of the abrasive grain density and sharpness. In order to estimate the parameters S_{ds} and S_{sc}, the sampling interval for the grinding wheel topography was selected as 45 μm according to Equation (4.21). The sampling interval was estimated with the averaged value of the fastest-decay correlation lengths of the sampled wheel topography $S_{al} = 170\ \mu m$.

Table 5.12 Average density of summits S_{ds} of the grinding wheels (mm^{-2})

Run	Replica 1	Replica 2	Replica 3
1	22.22	14.85	23.07
2	23.52	21.71	20.24
3	27.89	26.13	26.64
4	20.01	21.99	20.97
5	23.69	20.97	25.28
6	27.21	27.83	31.52
7	26.07	18.71	17.12
8	26.76	29.59	34.58

Table 5.13 Analysis of Variance for S_{ds} of the grinding wheels

Source of variation	v_d	s_d	a_d	v_dx s_d	v_dx a_d	s_dx a_d	v_dx s_dx a_d	Error	Total
Estimate of effect	-3.34	-1.20	-2.77	-1.81	4.83	-0.88	-2.95		
Sum of squares	66.92	8.57	46.13	19.64	140.10	4.68	52.31	147.26	485.60
Degree of freedom	1	1	1	1	1	1	1	16	23
Mean square	66.92	8.57	46.13	19.64	140.10	4.68	52.31	9.20	
F	7.27	0.93	5.01	2.13	15.22	0.51	5.68		
p-value	0.02	0.35	0.04	0.16	0.00	0.49	0.03		

For the density of summits S_{ds} of the grinding wheels, the augmentation of the truer velocity and truing depth will cause the drop of S_{ds} while the truing lead does not

have a significant effect on the parameter. The interaction effects of the truing factors are also significant on the S_{ds} at the confidence level of 90% (Table 5.13). In contrast, the parameter S_{sc} is affected only by the truer velocity; increasing the truing velocity will make S_{sc} decrease. The other factors show no influence at large levels of significance (Table 5.15).

Table 5.14 Average arithmetic summit curvature S_{sc} of the grinding wheels (μm^{-1})

Run	Replica 1	Replica 2	Replica 3
1	0.005	0.004	0.005
2	0.004	0.004	0.005
3	0.004	0.004	0.004
4	0.004	0.005	0.004
5	0.005	0.004	0.005
6	0.005	0.005	0.004
7	0.005	0.004	0.004
8	0.004	0.005	0.005

Table 5.15 Analysis of Variance for S_{sc} of the grinding wheels

Source of variation	v_d	s_d	a_d	v_dx s_d	v_dx a_d	s_dx a_d	v_dx s_dx a_d	Error	Total
Estimate of effect	-3.3E-4	0	-8.3E-5	8.3E-5	0	1.7E-4	-8.3E-5		
Sum of squares	6.7E-7	0	4.2E-8	4.2E-8	0	1.7E-7	4.2E-8	3.0E-6	4.0E-6
Degree of freedom	1	1	1	1	1	1	1	16	23
Mean square	6.7E-7	0	4.2E-8	4.2E-8	0	1.7E-7	4.2E-8	1.9E-7	
F	3.56	0.00	0.22	0.22	0.00	0.89	0.22		
p-value	0.08	1.00	0.64	0.64	1.00	0.36	0.64		

5.3.4 Correlation between the grinding wheel and workpiece surface parameters

Table 5.16 displays the effects of the truing factors on the grinding wheel topography and the grinding performance. It is clear from the table that there is a

similarity between the effect of truing factors on the grinding performance and the 3-D characterisation parameters of the wheel topographies. The surface roughness of the workpiece, the normal force, as well as the parameter S_q of the grinding surface are affected by all three truing factors. On the other hand, the tangential force and the parameter S_{ds} are only influenced by the truer velocity and depth of cut. This similarity of the effects on the grinding wheel topography and the grinding performance suggests there is correlation between the parameters.

Table 5.16 Effects of the truing parameters on the grinding wheel topography and grinding performance

Parameters	Truer velocity	Lead	Depth of cut
S_q (workpiece)	×	×	×
Tangential force	×		×
Normal force	×	×	×
S_q (wheel)	×	×	×
S_{ds}	×		×
S_{sc}	×		

The impact of the truing factors on the workpiece surface roughness can be explained using the grinding wheel topographical parameters. Increasing the truer velocity, lead and depth of cut would coarsen the grinding wheel, evident by the increased S_q value of the grinding wheel topography, which in turn induces a rougher workpiece surface (Figure 5.2a). The degradation of the workpiece surface finish is also due to the decrease of the number of active abrasive grains, according to the parameters S_{ds} (Figure 5.2b). The correlation of the workpiece S_q with the grinding wheel S_q and S_{ds} is however not independent as there is a linear relationship between the values S_q and S_{ds} of the grinding wheel as suggested by Figure 5.2c.

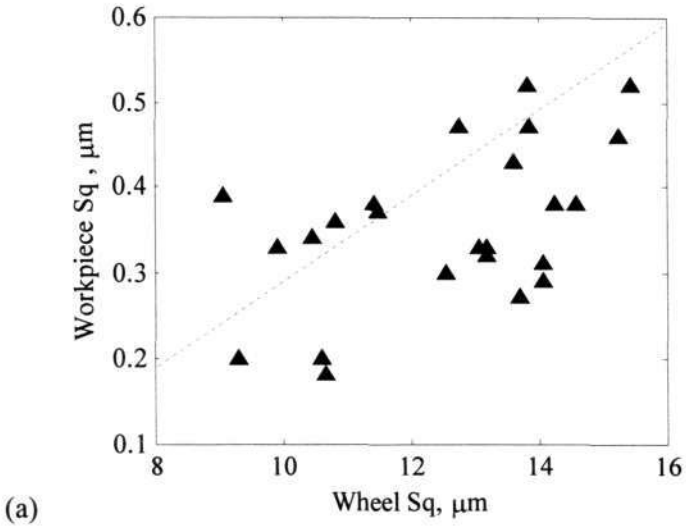

(a)

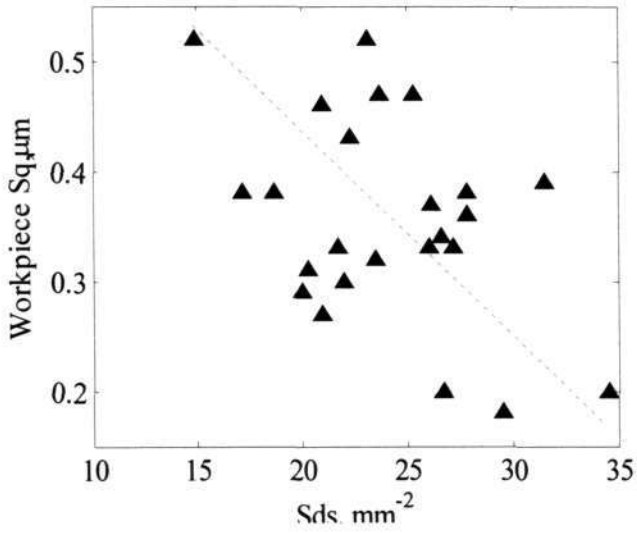

(b)

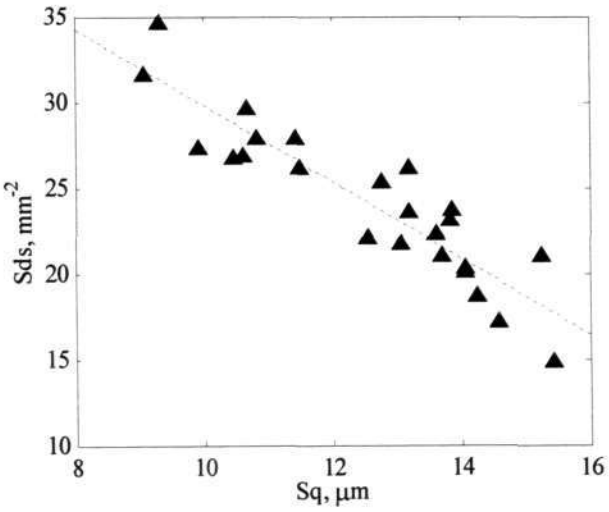

(c)

Figure 5.2 Correlation between the parameters: (a) S_q of the workpiece and S_q of the grinding wheel, (b) S_q of the workpiece and S_{ds} of the grinding wheel, (c) correlation between the parameters S_q and S_{ds} of the grinding wheel

Similarly, the influence of the truing parameters on the grinding forces can be explained by the behaviour of the parameters S_{ds} and S_{sc}. The reduction of S_{ds} at larger truer velocities, leads and truing depths suggests a smaller number of active abrasive grains on the grinding wheel, thus, lowers the grinding forces. However, the larger values of the truing speed would reduce S_{sc}, meaning lower sharpness of the abrasive grains. The combination of the reduced number of abrasive grains and the sharpness due to the higher truing speed thus makes truing speed the most influential factor on the grinding force. Figure 5.3 shows the correlation between the normal force and the

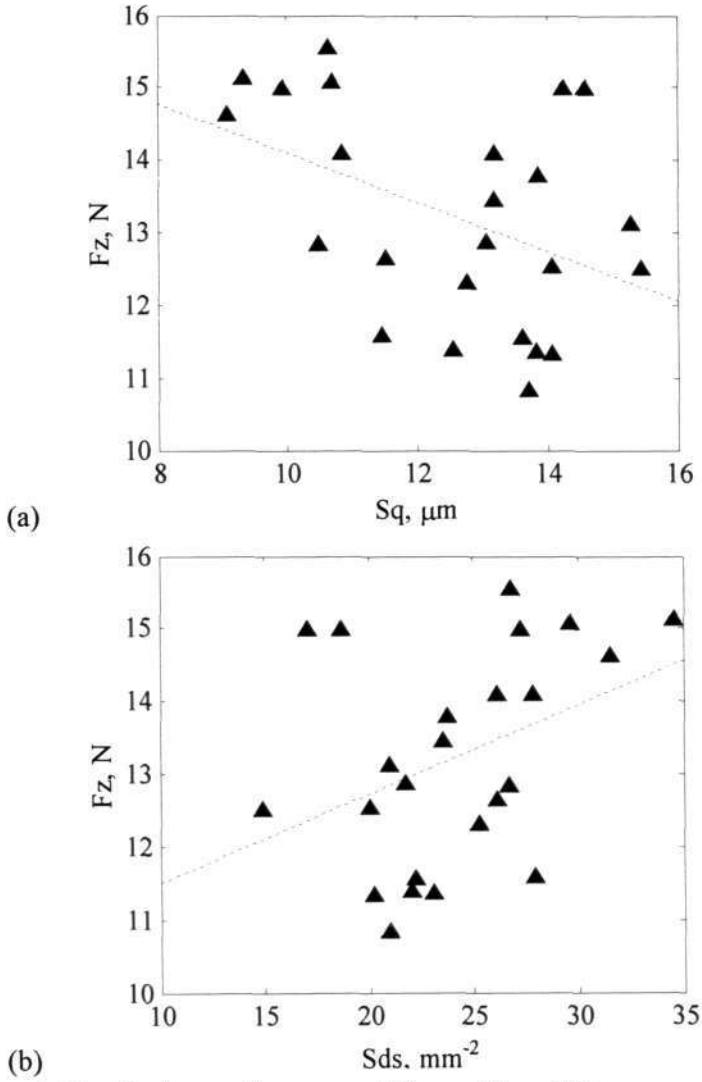

Figure 5.3 Correlation between the normal force F_z and the parameters: (a) S_q, (b) S_{ds} of the grinding wheel

parameter S_q and S_{ds} of the grinding wheel. Although the linear equation can be fitted to the data, the deviation of some data points hints that the grinding forces could be affected not only by the abrasive grain density but also by other factors.

It should be noted that the choice of the sampling interval could affect the ANOVA results as the parameters S_{ds} and S_{sc} are strongly dependent on the value of the sampling interval. Table 5.17 displays the p-values of the parameters S_q, S_{ds} and S_{sc} at the sampling interval 30, 45 and 60 μm, which satisfy the following equation

$$30 < \frac{S_{al}}{4} < 45 < \frac{S_{al}}{3} < 60 \tag{5.1}$$

Table 5.17 p-value for the grinding wheel parameters at various sampling intervals

Parameters	Sampling interval, μm	Truer velocity	Lead	Truing depth
S_q	30	0.01	0.06	0
	45	0.01	0.06	0
	60	0.01	0.06	0
S_{ds}	30	0.02	0.79	0.04
	45	0.02	0.35	0.04
	60	0.04	0.01	0.01
S_{sc}	30	0.08	0.08	0.27
	45	0.08	1.00	0.64
	60	1.00	0.51	1.00

Table 5.17 reveals that p-values for the parameter S_q are very consistent over the studied range of sampling intervals. On the other hand, the p-value for the parameters S_{ds} and S_{sc} are very sensitive to the used sampling interval. At the smaller value of the sampling interval, the truing factors would have more significant effect on S_{sc}; while at the larger sampling interval, S_{ds} is considerably influenced by all factors. Thus, care should be taken in choosing the sampling interval value for estimating S_{ds} and S_{sc}. A smaller value of the sampling interval would correlate S_{ds} and S_{sc} to random components

on the grinding topography while a larger value would omit the essential components of the abrasive grain. However, the linear relationship between S_q and S_{ds} is still maintained despite the variation of S_{ds} as shown in Figure 5.4, which suggests that S_q is a more robust parameters for characterising grinding wheel topography.

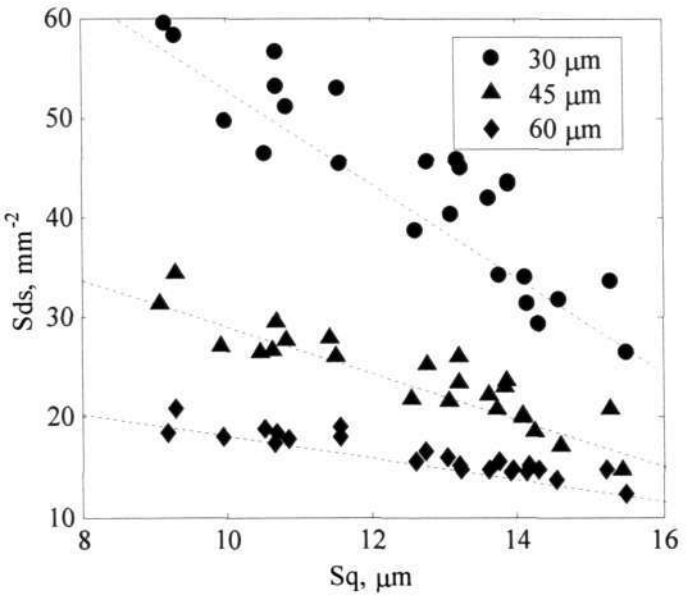

Figure 5.4 Correlation between the parameters S_q and S_{ds} of the grinding wheel at sampling interval 30, 45 and 60 μm

5.4 Chapter summary

The investigation demonstrates the effects of truing parameters on the grinding wheel topography and grinding performance. Increasing the truer velocity, truing lead and truing depth in truing operations will coarsen the grinding wheel topography; resulting in smaller grinding forces and poorer workpiece surface.

The effects of the truing parameters on the grinding wheel topography can be described through selected surface parameters. It has been shown that the characteristics of the grinding wheel topography can be quantified in terms of the three-dimensional surface characterisation parameters.

Using the three-dimensional surface characterisation, the correlation between the grinding performance and the grinding wheel topography can be described in quantitative terms. However, care should be taken in choosing the sampling interval so that the parameters will reflect the components under consideration. Among the parameters, the root-mean-square S_q is rather robust for the characterisation purpose.

Chapter 6

Generation of the grinding wheel surface

6.1 Introduction

In kinematic models of the grinding process, the kinematic relationship between the grinding wheel and the workpiece is used to generate the workpiece surface. As grinding is essentially a material removal process, there are two crucial factors that strongly influence the process performance: the cutting tool and the chip formation process involved. Consequently, any kinematic simulation scheme should consider two issues: the generation of the grinding wheel surface and the interaction of the workpiece surface and the abrasive grain if a realistic simulation is to be achieved.

With regard to the generation of the grinding wheel surface for kinematic simulation, the simplest approach is measuring and using the grinding wheel topography directly in the simulation (Bhateja 1977, Inasaki 1996). Unfortunately, measuring the whole grinding wheel is a time-consuming activity while a realistic

simulation of the grinding process requires a vast amount of wheel surface. Thus, a numerical simulation is often sought for obtaining the grinding topography.

One popular alternative adopted by many researchers is meshing the grinding wheel surface with simple shape abrasive grains. Cooper and Lavine (2000) modelled the abrasive grain as a truncated cone while Warnecke and Zitt (1998) meshed the grinding wheel surface with polyhedrons. Other researchers (Chen and Rowe 1996a, Koshy et al. 1997, Gong et al. 2002) preferred considering abrasive grains as spheres instead. Overall, the main advantage of this approach is that the information required for the simulation (such as nominal diameter of the abrasive grains, distance between grains) could be easily deduced from the grinding wheel specification. However, it neglects the fact that the shapes of the abrasive grains are often very complex.

Alternatively, Pandit and Wu (1973) modelled the grinding wheels using times series. Two-dimensional wheel profiles were treated as time series, and autoregressive (AR) or autoregressive moving average (ARMA) models were fitted to the data. However, the fitting of model order often involves some kind of trial and error. On the other hand, Wang and Moon (1997) found that the grinding wheel surface could be simulated with a small number of wavelets. Salisbury et al. (2001a), in contrast, modelled the wheel surface with Fourier coefficients while Zhou and Xi (2002) considered the grain protrusion height as a Gaussian random variable.

On the whole, the above approaches either require intensive measurement of the wheel surface, or assume abrasive grains to have simple shapes, or neglects the non-Gaussian distribution of the wheel topography. In this chapter, a numerical procedure that requires a few samples of wheel surfaces and accounts for the complex shapes and probability distribution of wheel topography, is proposed for simulating the grinding

wheel surface. The remainder of the chapter is organized into 4 sections. First, a short description of the mathematical background for the method is given, followed by a section describing the procedure. The last two sections give the numerical examples and the conclusions.

6.2 Brief review of random fields

From the mathematical point of view, the topography of the grinding wheel can be considered as a two-dimensional spatial random field, each point of which is a random variable representing the protrusion height of the surface. Formally, a random field $X(\mathbf{r})$ is a family of random variables $\{X(\mathbf{r}),\ \mathbf{r}\in D,\ \omega\in\Omega\}$ depending upon $\mathbf{r}\in D$ and defined on the probability space $(\Omega,\mathcal{F},P)$ (Vanmarcke 1983). Analogous to the case of stochastic processes, a random field is completely specified if for each finite set of $\mathbf{r}$-values, say $\{\mathbf{r}_1, \mathbf{r}_2, \ldots, \mathbf{r}_k\}$, a joint distribution function is given as follows:

$$F(x_1,\ldots,x_k)=P\{X(\mathbf{r}_1)<x_1,\ldots,X(\mathbf{r}_k)<x_k\} \tag{6.1}$$

However, unless the field is Gaussian, specification of all the joint distribution functions is a very complex task. In practical applications, one often only considers a second order description of the field that specifies the marginal distribution

$$F_X = P\{X(\mathbf{r})<x\} \tag{6.2}$$

the mean

$$m_X(\mathbf{r}) = E[X(\mathbf{r})] \tag{6.3}$$

and the covariance function

$$K_X(\boldsymbol{r}_1,\boldsymbol{r}_2) = E[(X(\boldsymbol{r}_1) - m_X(\boldsymbol{r}_1))(X(\boldsymbol{r}_2) - m_X(\boldsymbol{r}_2))] \tag{6.4}$$

Particularly important is the class of random fields that satisfy certain conditions of statistical homogeneity. A random field is called strictly homogeneous if all the joint probability distribution functions remain the same when the set of location $\boldsymbol{r}_1,\ldots,\boldsymbol{r}_k$ is translated in the parameter space D. This implies that all the probabilities depend only on the relative, not on the absolute, locations of the points. In practice, random fields that are assumed to possess these properties to any degree often do so in a limited or weak sense. A random field will be called weakly homogeneous if

$$m_X(\boldsymbol{r}) = m_X = constant \tag{6.5}$$

and

$$K_X(\boldsymbol{r}_1,\boldsymbol{r}_2) = K_X(\boldsymbol{r}_1 - \boldsymbol{r}_2) = K_X(\boldsymbol{\tau}) \tag{6.6}$$

where $\boldsymbol{\tau} = \boldsymbol{r}_1 - \boldsymbol{r}_2$ is the lag vector.

Random fields can be roughly divided into two types: Gaussian and non-Gaussian. While the methods for generating Gaussian fields are rather established, the simulation of non-Gaussian ones have only received attention in recent years (Cressie 1993). As it will be shown that the majority of the grinding wheel surfaces have some non-Gaussian characteristics, the method for non-Gaussian is discussed here.

The methods for non-Gaussian field simulation can be classified as two general classes. The first class of methods seeks to generate realizations of non-Gaussian fields by transforming a designed Gaussian field. A few techniques have been derived along this line such as Hermite polynomial expansion, inverse distribution function or iterative adjustment (Yamazaki and Shinozuka 1988, Deodatis and Micaletti 2001). In

contrast, the second class of methods seeks to simulate directly sample functions of the non-Gaussian field such as by replacing the driver Gaussian white noise with non-Gaussian noise in the spatial series (Grigoriu 1995). In practice, neither method has a superior advantage as it may involve expensive computation due to the iteration procedure, or some arbitrary judgement of the "optimal" order of the model.

6.3 Generation of non-Gaussian grinding wheel topography

In this section, an effective procedure for generating the non-Gaussian grinding wheel topography is proposed. The grinding topography is assumed to be a weakly homogenous non-Gaussian random field. The procedure involves the transformation of a non-Gaussian random field into a Gaussian one. The sufficient condition for such transformation is discussed, and two transformations satisfying the condition are presented.

6.3.1 Numerical procedure

While the above-mentioned techniques can be applied for a range of non-Gaussian fields, their main restriction is the computational cost or the arbitrary judgement of the model order involved. For the simulation of the grinding process, a vast amount of grinding wheel topography is needed for realistic simulation. To avoid the computational cost, a direct transformation method is suggested.

In this method (Figure 6.1), the sampled wheel topography is transformed directly to a Gaussian field. This Gaussian field is used to generate realizations, which are inversely-transformed to realizations of the desired wheel topography. The sufficient condition that provides the realizations will have the same probabilistic characteristics as the given field is examined as follows.

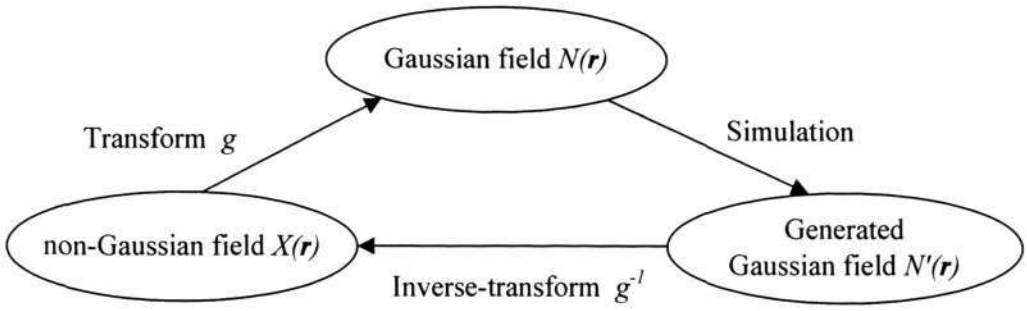

Figure 6.1 Procedure for simulating non-Gaussian grinding wheel topography

Without the loss of generality, a random field can be assumed to have a zero mean value. Equation (6.3) and (6.4) can be rewritten in integral forms as follows (provided that the integrals exist)

$$\begin{aligned} m_X(\mathbf{r}) &= E[X(\mathbf{r})] \\ &= \int_{-\infty}^{+\infty} x f_X \, dx = 0 \end{aligned} \tag{6.7}$$

and

$$\begin{aligned} K_X(\mathbf{r}_1, \mathbf{r}_2) &= E[(X(\mathbf{r}_1) - m_X(\mathbf{r}_1))(X(\mathbf{r}_2) - m_X(\mathbf{r}_2))] \\ &= E[X(\mathbf{r}_1)X(\mathbf{r}_2)] \\ &= \int_{-\infty-\infty}^{+\infty+\infty} x_1 x_2 f_{XX} \, dx_1 dx_2 \end{aligned} \tag{6.8}$$

where f_X and f_{XX} are the marginal density function of $X(\mathbf{r})$ and joint density function of $X(\mathbf{r}_1)$ and $X(\mathbf{r}_2)$ respectively. Then a weakly homogenous random field can be defined by two density functions f_X and f_{XX}.

Let X_1 and X_2 be two random variables, $f_{XX}(x_1, x_2)$ the joint density function of the variables X_1 and X_2. Random variables Y_1 and Y_2 can be defined from the transformations:

$$Y_1 = g(X_1) \tag{6.9a}$$
$$Y_2 = h(X_2) \tag{6.9b}$$

Given Y_1 and Y_2, suppose that there is one unique pair of X_1 and X_2 that satisfy the above equations, the joint density of the variables Y_1 and Y_2 can be written as (Papoulis 1990):

$$f_{YY}(y_1, y_2) = \frac{f_{XX}(x_1, x_2)}{|J(x_1, x_2)|} \tag{6.10}$$

where $J(x_1, x_2)$ is the Jacobian of the transformation, defined as

$$J(x_1, x_2) = \frac{\partial(y_1, y_2)}{\partial(x_1, x_2)} = \begin{vmatrix} \frac{\partial g(x_1)}{\partial x_1} & \frac{\partial g(x_1)}{\partial x_2} \\ \frac{\partial h(x_2)}{\partial x_1} & \frac{\partial h(x_2)}{\partial x_2} \end{vmatrix} = \frac{\partial g(x_1)}{\partial x_1} \frac{\partial h(x_2)}{\partial x_2} \tag{6.11}$$

Similarly, for the inverse transformation

$$X_1 = g^{-1}(Y_1) \tag{6.12a}$$
$$X_2 = h^{-1}(Y_2) \tag{6.12b}$$

The joint density of the variables X_1 and X_2 can be written as

$$f_{XX} = \frac{f_{YY}(g(x_1), h(x_2))}{J(y_1, y_2)} \tag{6.13}$$

where $J(y_1, y_2)$ is the Jacobian of the inverse transformation g^{-1} and h^{-1}

Combining Equation (6.10) and (6.13) , we have:

$$f_{XX} = \frac{f_{XX}(g^{-1}(g(x_1)), h^{-1}(h(x_2)))}{J(x_1, x_2) J(y_1, y_2)} = \frac{f_{XX}}{J(x_1, x_2) J(y_1, y_2)} \tag{6.14}$$

The sufficient condition for $J(x_1,x_2)J(y_1,y_2)=1$ is that the transformations g and h are one-to-one, and their Jacobians are non-zero (Taylor and Mann 1972). The same condition is applied to the density function f_X. Thus, if there exists the transformation f that is one-to-one and has no singularity of Jacobian in the concerned range, the above method will provide non-Gaussian random realizations having the desired probabilistic characteristics.

6.3.2 Transform functions

Two types of transform functions that satisfy the sufficient condition will be examined. One is the inverse distribution functions:

$$X = F_X^{-1}(\Phi(z)) \tag{6.15a}$$

$$Z = \Phi^{-1}(F_X(x)) \tag{6.15b}$$

where F_X^{-1} is the inverse distribution of the specified marginal distribution function F_X and Φ is the standard normal distribution function. If F_X is the continuous distribution function, it can be shown that given a random variable Z of the standard Gaussian distribution, the random variable X will have the marginal distribution F_X (Grigoriu, 1995). The transformation satisfies the sufficient condition as F_X and Φ and their inverse are increasing functions with non-zero Jacobian.

Another type of transformation is the Johnson transform. Johnson (1949) developed a system of curves that may be used to transform a wide variety of distributions into a standard normal distribution. It can cover a large range of distributions that are often encountered in engineering surfaces. The transform can be generally described by

$$Z = \gamma + \delta f\left(\frac{X-\xi}{\lambda}\right) \tag{6.16}$$

where Z is a standard normal variable, and X is a variable with a non-Gaussian distribution. It follows that the parameters γ and δ determine the shape of the distribution X while ξ is a location factor and λ a scale factor. Depending on the value of skewness and kurtosis, one of the following systems can be used:

The lognormal system (S_L):

$$Z = \gamma + \delta ln\left(\frac{X-\xi}{\lambda}\right) \tag{6.17a}$$

The bounded system (S_B):

$$Z = \gamma + \delta ln\left(\frac{X-\xi}{\xi+\lambda-X}\right) \tag{6.17b}$$

The unbounded system (S_U):

$$Z = \gamma + \delta \sinh^{-1}\left(\frac{X-\xi}{\lambda}\right) \tag{6.17c}$$

The parameters γ, δ, ξ and λ of the Johnson system can be obtained from the statistical tables (Pearson 1972), or computed using a numerical routine by Hill et al. (1976). By inspection it is easy to see that the Johnson transform satisfies the one-to-one and non-zero Jacobian condition.

6.4 Numerical examples

For verification of the method, a series of simulations were conducted. Six grinding wheels, which differed by abrasive grain types and dressed conditions, were used: cubic boron nitride B120H200V (worn), B140N200V (trued), silicon carbide C120J8V (undressed), C80M7V (worn), and aluminium oxide A80J8V (dressed), A46H7V (dressed).

Four replications of the wheel surface were taken at various locations for each wheel. The replications were measured on Talyscan 150 stylus system. The measurement conditions for the grinding wheel surfaces are given in Table 6.1. Selected measured topographies of the grinding wheels are shown in Figure 6.2. The topography of the grinding wheel is assumed as a homogenous random field. Furthermore, it is assumed to be ergodic, meaning all information about its joint probability distributions can be obtained from a single realisation of the field.

Table 6.1 Measurement conditions for grinding wheel surface generation

Grinding wheel	Sampling area, mm	Sampling interval, mm	Stylus speed, mm/s
A46H7V	4x4	0.080	0.3
A80J8V	3x3	0.060	
B120H200V	2x2	0.040	
B140N200V	2x2	0.030	
C80M7V	3x3	0.060	
C120J8V	2x2	0.040	

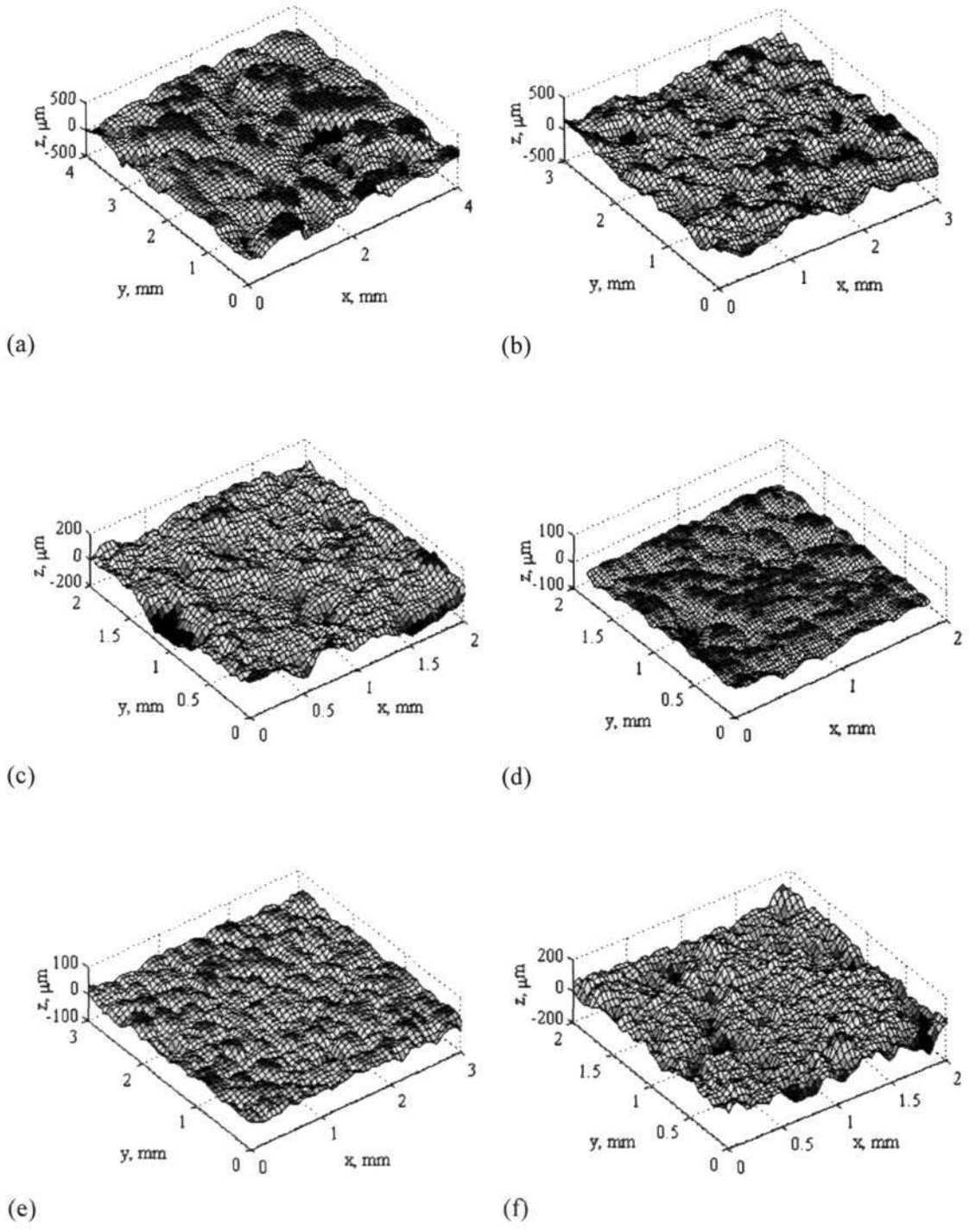

Figure 6.2 Measured topography of the grinding wheels: (a) A46H7V, (b) A80J8V, (c) B120H200V, (d) B140N200V, (e) C80M7V, (f) C120J8V

For each type of the grinding wheels, the normality plot is produced in Figure 6.3. At first glance, the distribution of the topographical heights can be approximated as Gaussian ones as only a small part of the distribution is deviated from normality. However, if one considers that only the top parts of the abrasive grains are involved in the grinding process, the deviation from the normality could not be neglected. Furthermore, Kolmogorov-Smirnov tests, conducted on the distributions, confirmed that height distributions of all wheel topographies were essentially non-Gaussian.

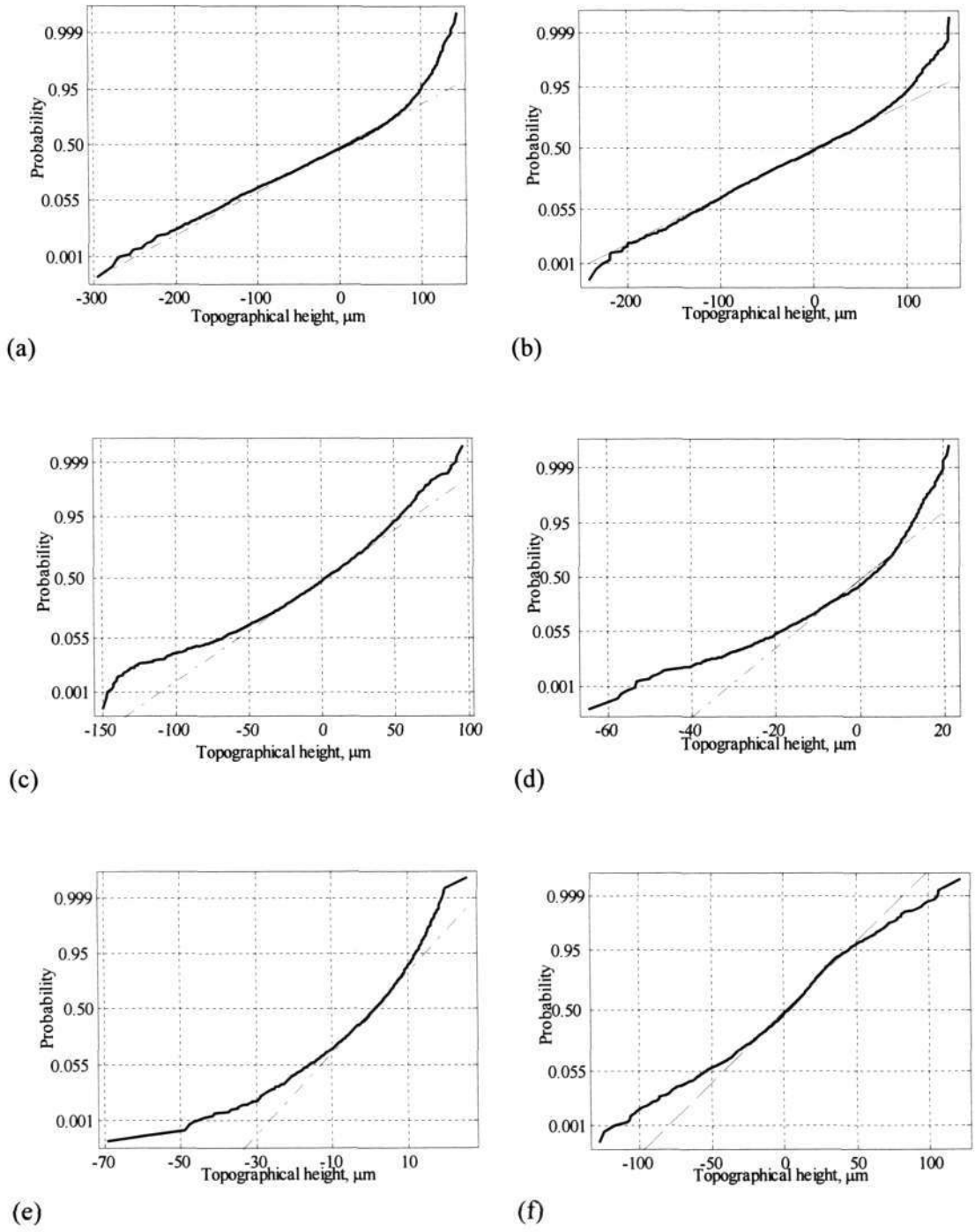

Figure 6.3 Normality plot of the grinding wheel topography: (a) A46H7V, (b) A80J8V, (c) B120H200V, (d) B140N200V, (e) C80M7V, (f) C120J8V

The proposed procedure was applied to obtain realizations of non-Gaussian fields. Both the Johnson transform and the inverse distribution function were applied to each grinding wheel topography. For each sampled topography, the coefficients for the Johnson transform were estimated by the method of moments while the inverse distribution function was derived from the point-wise cumulative distribution function of the sample. The selection of the Johnson transform system was based on the value of kurtosis and skewness of the surface (Johnson 1949). Figure 6.4 displays the position of the grinding wheel surfaces in the skewness-kurtosis plane. The figure reveals that a majority of the grinding wheel surfaces could be fitted with S_B transform function [Equation (6.17b)].

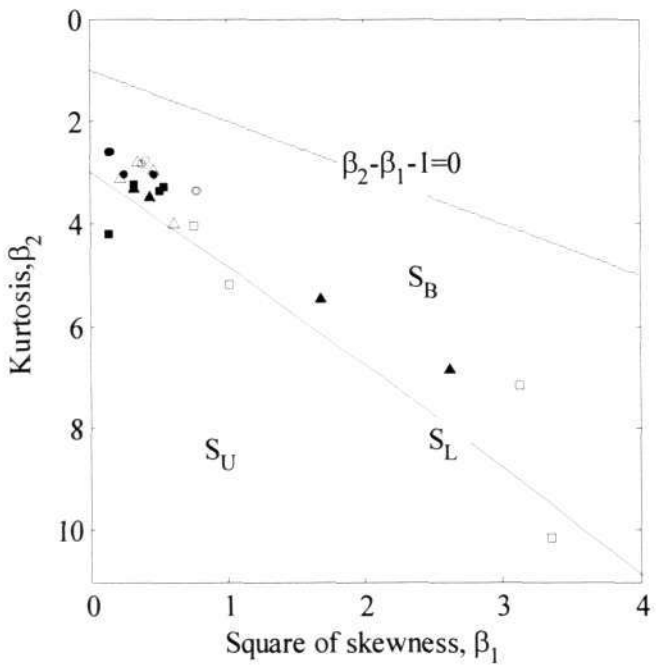

Figure 6.4 Johnson transform systems used for the grinding wheel surfaces. Symbol ○: A46H7V, symbol ●: A80J8V, symbol Δ: B120H200V, symbol ▲: B140N200V, symbol □: C80M7V, symbol ■: C120J8V

After estimating the transform functions, the non-Gaussian grinding wheel surfaces were transformed to Gaussian surfaces. For the transformed Gaussian surfaces, the power spectral density functions were estimated using Equation (3.2). With the

estimated power spectral density functions, the realizations of the Gaussian fields were generated by the spectral representation method (Shinozuka and Deodatis 1996).

Six selected topographies generated by using the Johnson transform are shown in Figure 6.5 while the topographies simulated with the inverse distribution function are given in Figure 6.6. It is clear that the measured and generated topography visually resembles each other. To test that the measured and generated topographies had the same height distribution, a Kolmogorov-Smirnov test was conducted on each pair. Six selected p-values are shown in Table 6.2. The null hypothesis (the pair had the same distribution) is well accepted at the confidence level of 95%. For further verification, Table 6.2 also displays the full set of three-dimensional surface characterisation parameters. The comparison shows that the parameters of the generated topographies are comparable with the measured ones. The full listing of the parameters of all samples is given in Appendix I.

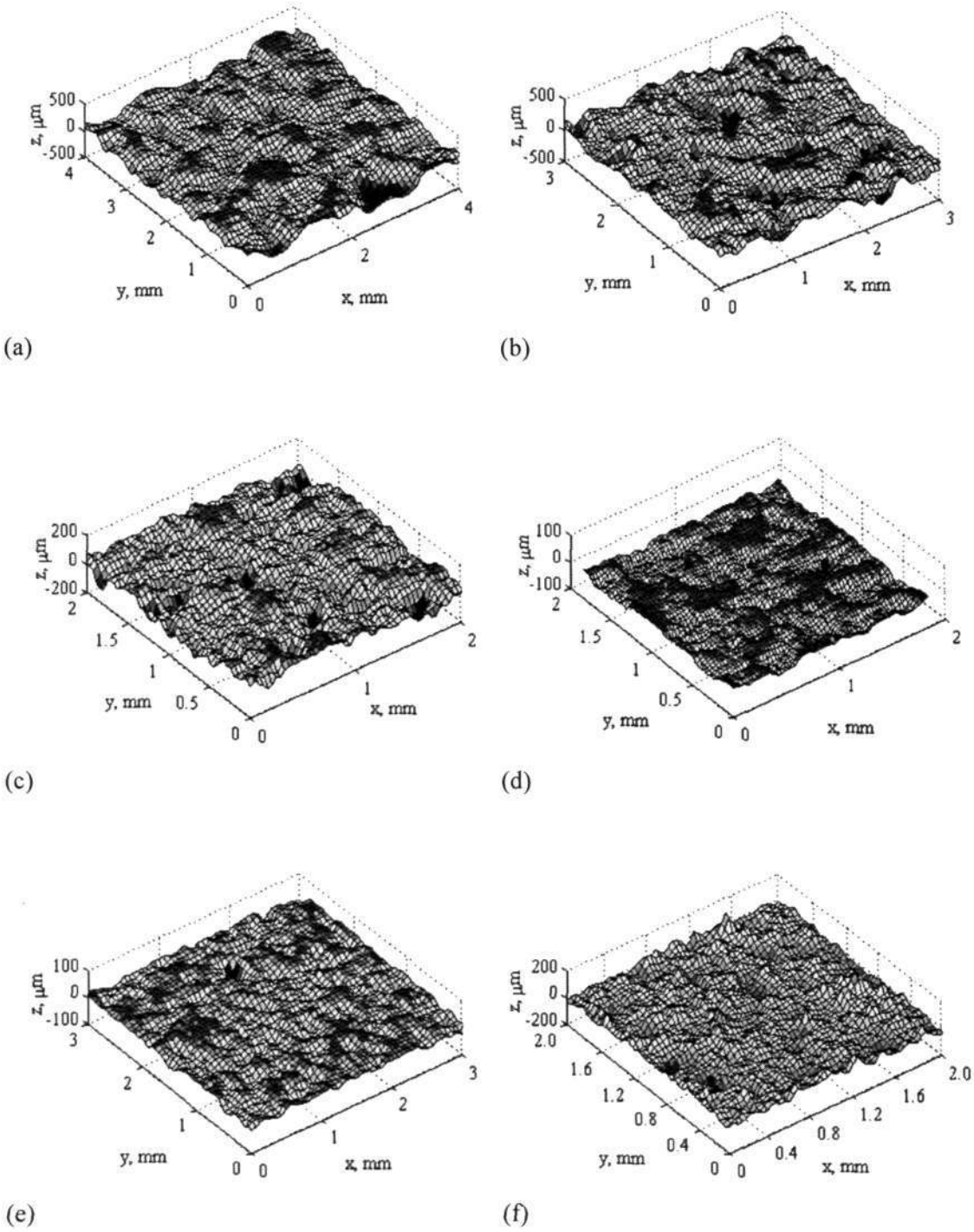

Figure 6.5. Generated topography of the grinding wheels by Johnson transform: (a) A46H7V, (b) A80J8V, (c) B120H200V, (d) B140N200V, (e) C80M7V, (f) C120J8V

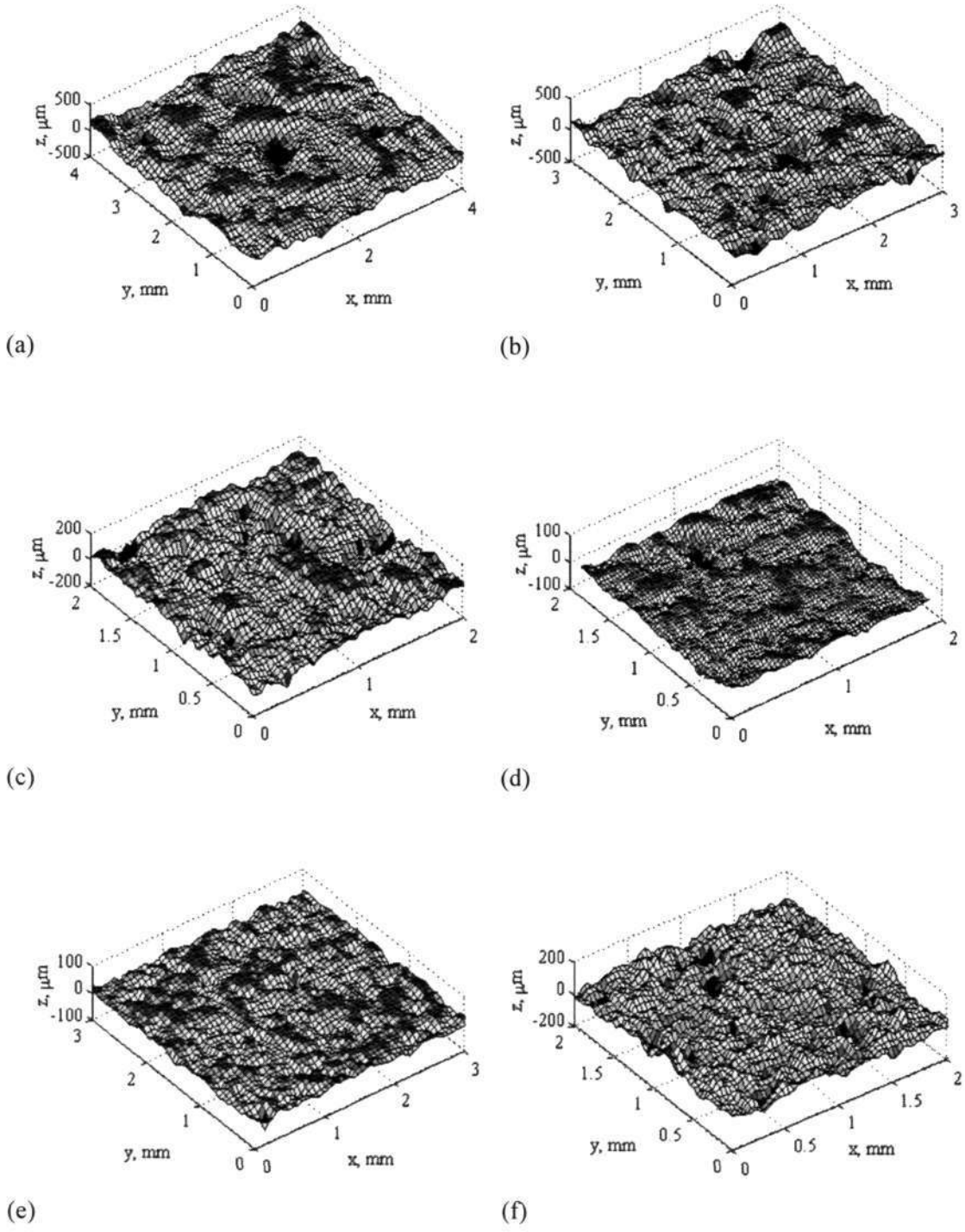

Figure 6.6 Generated topography of the grinding wheels by the inverse distribution function: (a) A46H7V, (b) A80J8V, (c) B120H200V, (d) B140N200V, (e) C80M7V, (f) C120J8V

Table 6.2 3-D topographic parameters of measured and generated topography and p-values of the Kolmogorov-Smirnov tests

Parameter	A80J8V			B120H200V			C120J8V		
	Measured	Johnson	Inverse	Measured	Johnson	Inverse	Measured	Johnson	Inverse
S_q, μm	70.60	70.38	70.69	38.20	38.14	38.43	30.00	29.53	29.60
S_z, μm	356.4	351.6	363.1	223.8	222.6	226.3	207.9	201.4	208.9
S_{sk}	-0.37	-0.41	-0.43	-0.78	-0.76	-0.92	-0.37	-0.41	-0.21
S_{ku}	2.60	2.65	2.73	4.01	3.63	4.04	4.18	3.59	3.99
S_{ds}, mm^{-2}	11.22	12.33	13.22	31.25	35.25	36.25	42.75	37.25	38.00
S_{tr}	0.81	0.81	0.71	0.65	0.65	0.58	0.63	0.65	0.57
S_{al}, mm	0.22	0.22	0.19	0.17	0.17	0.17	0.13	0.13	0.11
S_{td}, °	0.0	0.0	0.0	0.0	0.0	0.0	0.0	0.0	0.0
$S_{\Delta q}$	0.94	1.01	1.03	0.70	0.82	0.85	0.74	0.77	0.80
S_{sc}, μm^{-1}	0.02	0.02	0.02	0.02	0.02	0.02	0.02	0.03	0.03
S_{dr}, %	34.47	38.29	39.23	20.45	26.47	27.70	22.60	24.07	25.51
S_{bi}	0.71	0.70	0.71	0.75	0.74	0.77	0.70	0.69	0.66
S_{ci}	1.30	1.29	1.28	1.20	1.20	1.17	1.29	1.32	1.38
S_{vi}	0.14	0.14	0.14	0.15	0.17	0.18	0.17	0.16	0.16
S_t, μm	387.41	374.07	390.007	246.55	246.89	240.56	30.00	29.53	29.60
S_p, μm	146.03	150.28	142.778	97.03	87.41	96.10	207.9	201.4	208.9
S_v, μm	241.38	223.79	247.229	149.52	159.49	144.45	-0.37	-0.41	-0.21
p-value		0.56	0.88		0.18	0.35		0.17	0.39

In order to evaluate the conservation of the spatial distribution in the generated surfaces, the autocorrelation functions (ACF) for each pair of measured and generated topography were estimated. Pairs of ACF for selected topographies are shown from Figure 6.7 to Figure 6.9. It can be seen that the shapes of ACF resemble each other. In fact, the variation in one pair of ACF is less than 0.15 (Figure 6.7c to 6.8c). This variation is below the threshold for the correlation length (Dong et al. 1994), which suggests the difference between two autocorrelation functions is insignificant. The matching of autocorrelation functions can be further verified by the fact that the autocorrelation-based texture aspect ratio S_{tr}, texture direction S_{td} and fastest decay autocorrelation length S_{al} parameters perfectly coincide (Table 6.2).

As the parameter S_{tr} of the grinding wheel surfaces is generally larger than 0.5 (Table 6.2), the surfaces can be considered as isotropic. Then the spatial distribution of the measured and generated surfaces can be compared through the radial power spectrum. Figure 6.10 displays the radial power spectra for selected grinding wheel surfaces. The spectra are estimated using Equation (4.6). The complete match between the spectra is evident from Figure 6.10.

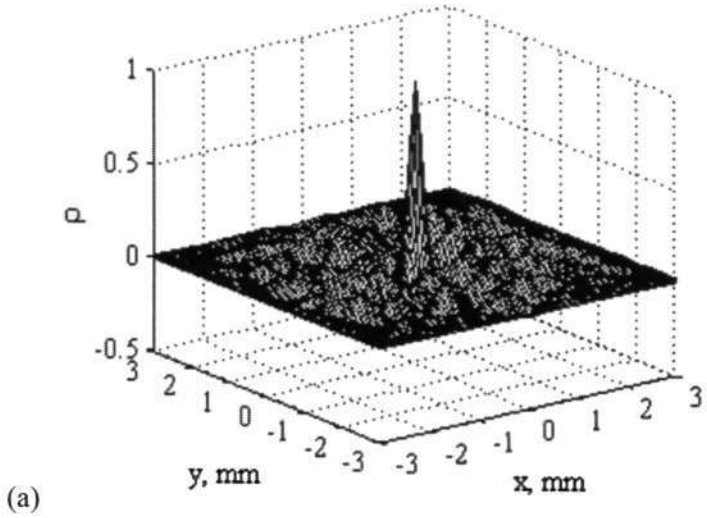

(a)

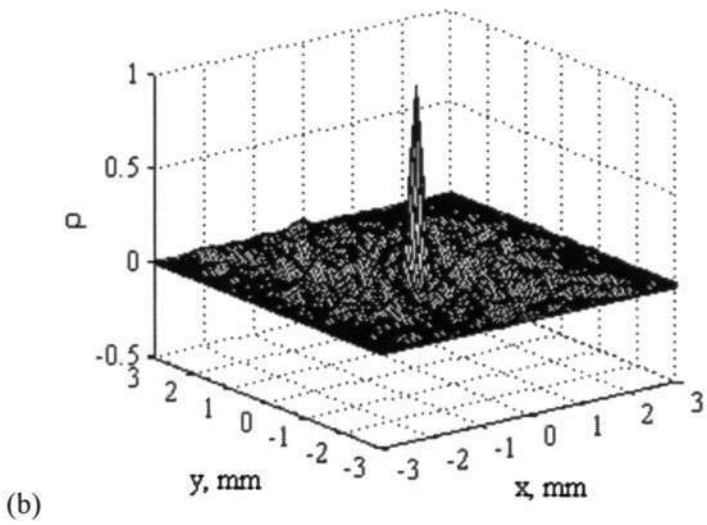

(b)

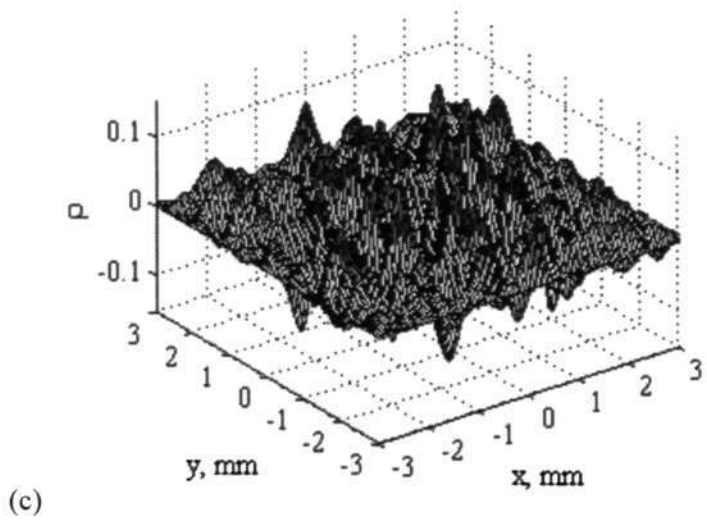

(c)

Figure 6.7 Autocorrelation functions of A80J8V grinding wheel topography: (a) measured, (b) generated, (c) the difference between the measured and generated ones

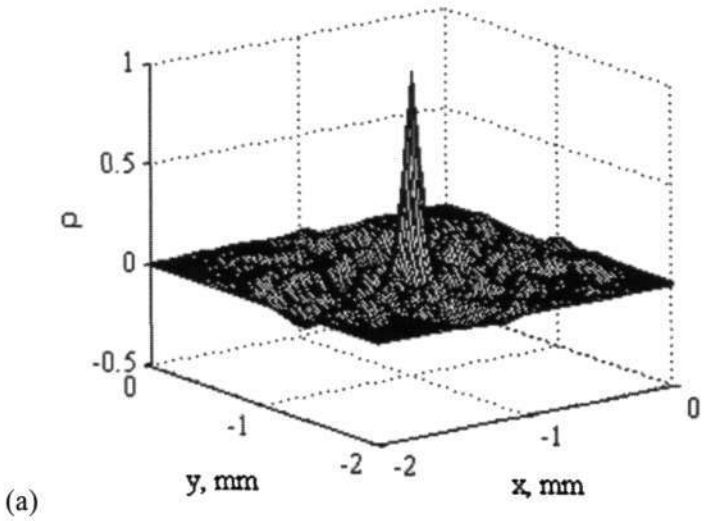

(a)

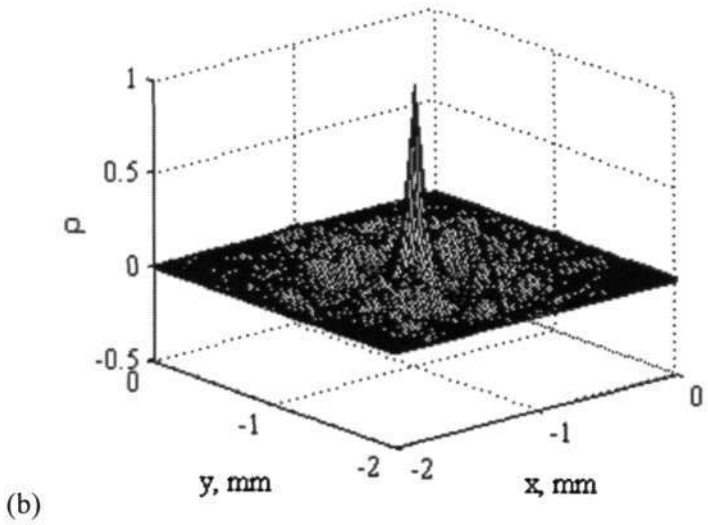

(b)

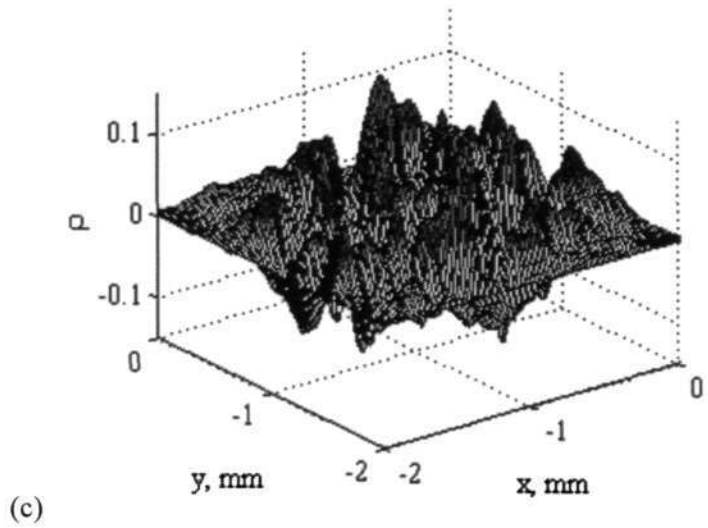

(c)

Figure 6.8 Autocorrelation functions of B120H200V grinding wheel topography: (a) measured, (b) generated, (c) the difference between the measured and generated ones

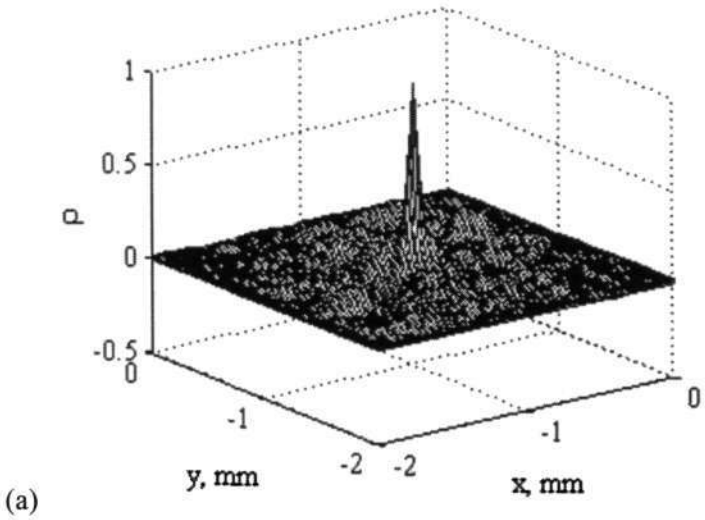

(a)

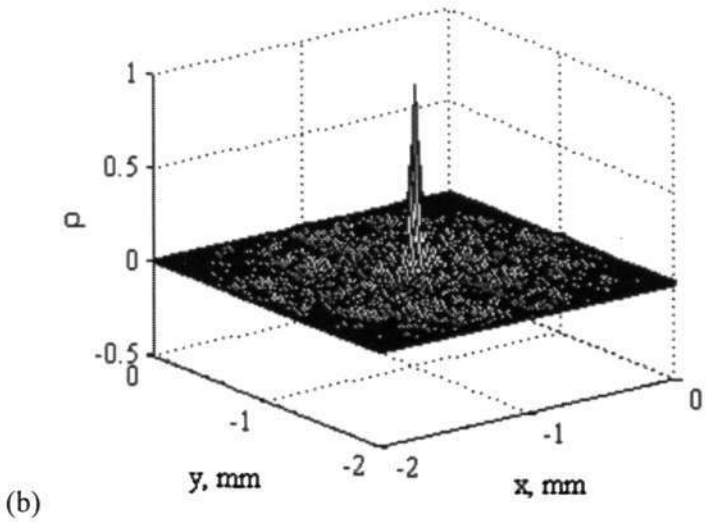

(b)

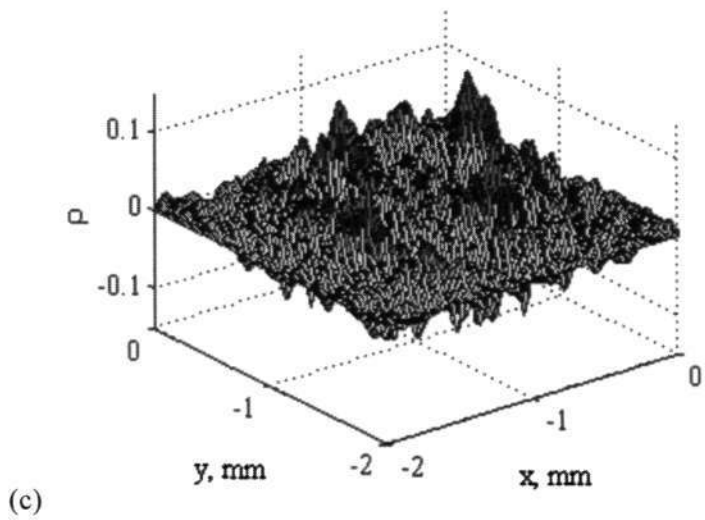

(c)

Figure 6.9 Autocorrelation functions of C120J8V grinding wheel topography: (a) measured, (b) generated, (c) the difference between the measured and generated ones

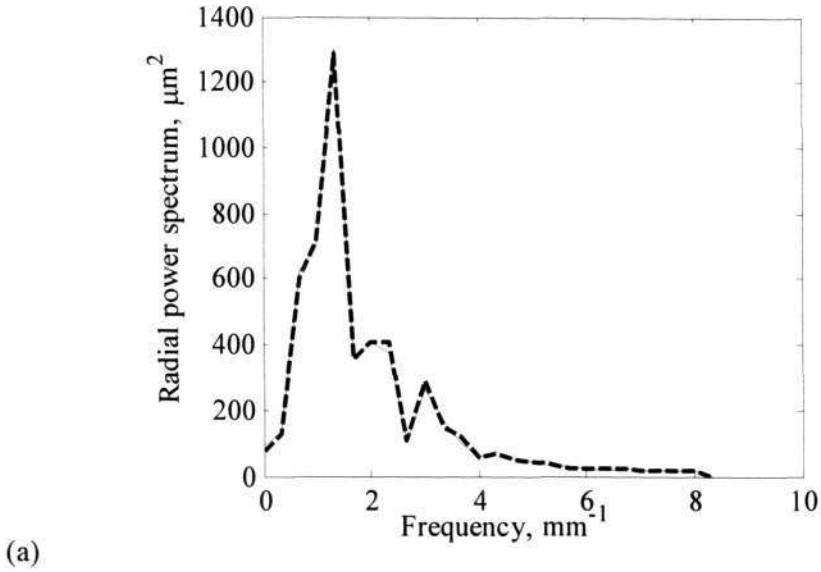

(a)

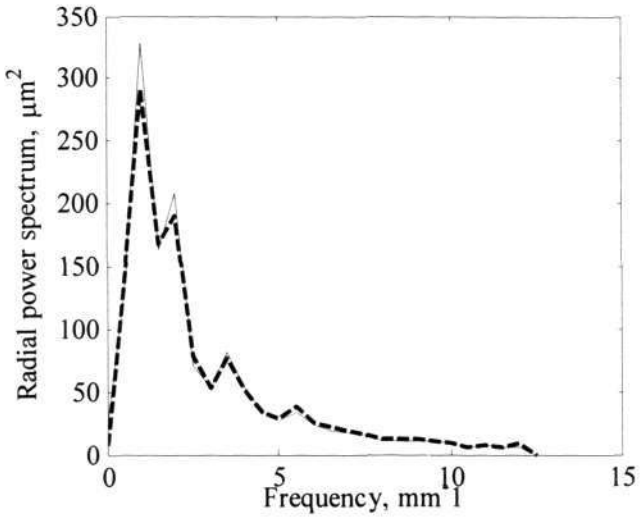

(b)

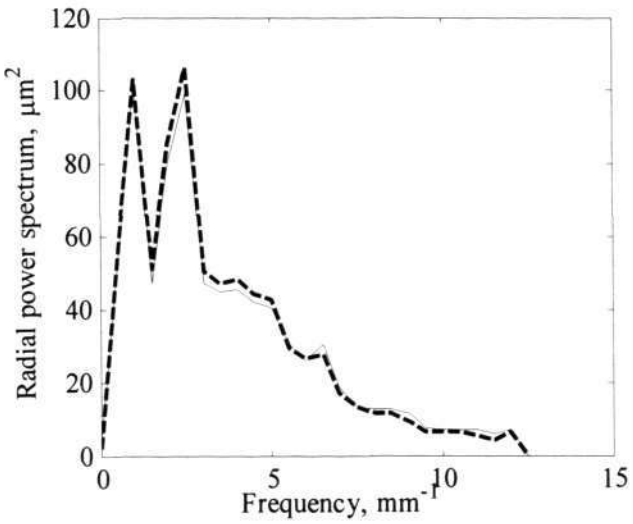

(c)

Figure 6.10 Radial power spectrum: (a) A80J8V, (b) B120H200V, (c) C120J8V. Line — is the spectrum of the measured surface. Line - - is the spectrum of the generated surface

6.5 Chapter summary

A majority of grinding wheel surfaces have non-Gaussian distributions. For effectively simulating such a surface, a numerical procedure is developed. The procedure relies on only a few samples of wheel topography with no assumption regarding its probability distribution. The measured topography is first transformed to standard normal random field. Then, a Gaussian field is generated by the spectral representation method before it was transformed back by the inverse transformation.

The sufficient condition for the transformation is that it is monotonic with non-zero Jacobian, which are satisfied by both the Johnson transform and inverse distribution functions. The generated topography is proven to have the same probability distribution and autocorrelation functions as the original one. The main advantage of the procedure is that it avoids the computational cost and arbitrary judgement of traditional non-Gaussian simulations. The study shows that a majority of the grinding wheel surface can be fitted with S_B Johnson distribution system.

Chapter 7

Interaction of the abrasive grain with the workpiece

7.1 Introduction

Although the grinding process has been a topic of extensive research for the last 30 years, a complete understanding of the process has yet to be achieved. It is partly due to the fact that grinding is a stochastic process, in which a large number of abrasive grains of random-defined geometry act as a cutting tool. The workpiece surface texture is formed as the result of the summation of individual grain action. It is often believed that grinding involves cutting, ploughing and rubbing of the abrasive grains at the workpiece surface (Hahn and Lindsay 1982). In fact, the nature of this interaction is very complex depending on various factors involving the grinding wheel, the workpiece, the machine and the process conditions.

A realistic simulation requires that the wheel-workpiece interaction is correctly modelled. However, most of the suggested simulation schemes only considered the cutting action of the grains, neglecting ploughing and rubbing (Inasaki 1996, Wang and Moon 1997, Warnecke and Zitt 1998, Salisbury et al. 2001b, Zhou and Xi 2002). Chen and Rowe (1996b) made a significant advance for the technique by considering the side

flow of the material in their work, but ploughing and rubbing of the grains were still neglected. Cooper and Lavine (2000) accounted for the ploughing and rubbing using an empirical function of the abrasive grain depth of cut.

In this chapter, a method of simulating the grinding process is described. The generation of the workpiece surface begins with the generation of the grinding wheel surface. Then the 3D topographical data is mapped to the 3D surface texture of the workpiece using their kinematic relationship. An algorithm is proposed to identify the active abrasive grains and their attack angles, based on which the interaction modes of the abrasive grains and the workpiece are determined. The model input includes the wheel velocity v_s, the workpiece velocity v_w, the depth of cut a, the grinding wheel diameter d_s and the 2D-array of grinding wheel surface heights. The output of the model is another 2-D array of surface heights, this time representing the topography of the workpiece surface.

The next section describes the basic kinematic functions, required for mapping the workpiece surface. A model of grain-workpiece interaction is discussed in Section 7.3. Sections 7.4 and 7.5 describe the simulation procedure and give some numerical examples, followed by the chapter conclusions.

7.2 Grinding process kinematics

A kinematic relationship between the grinding wheel cutting edges and the workpiece surface is briefly described in this section. Based on the relationship, the equations for mapping the grinding wheel topography to workpiece surface texture are presented.

7.2.1 Cutting point trajectory equation

A detailed grinding kinematic analysis can be found in Malkin (1989). If a *O'xyz* coordinate system is set with its origin *O'* fixed on the workpiece and coinciding with the grain at the lowest point (Figure 7.1) the cutting path *FO'F'* of the cutting point is a trochoid formed by the superposition of the circular motion around the wheel centre at

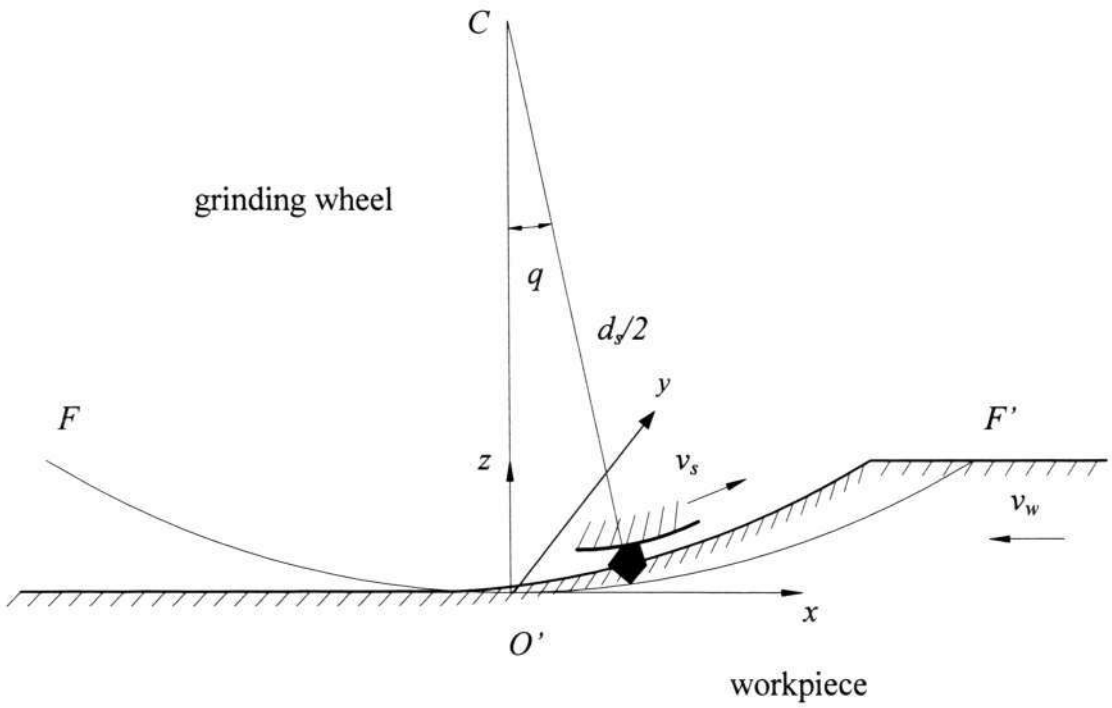

Figure 7.1 Cutting point trajectory

velocity v_s and tangential motion along the workpiece at velocity v_w. The equations for the trochoid path are described as follows:

$$x = \frac{d_s}{2} sin\theta \pm \frac{d_s v_w}{2v_s}\theta \tag{7.1a}$$

$$z = \frac{d_s}{2}(1 - cos\theta) \tag{7.1b}$$

where x and z are the coordinates of grain G; v_w is the velocity of the workpiece; v_s is the peripheral velocity of the wheel; d_s is the nominal diameter of the grinding wheel; θ is the rotation angle of the wheel. The plus sign in the equation refers to up-grinding,

and the minus sign to the down-grinding with the workpiece velocity in the opposite direction. Since θ is a very small angle in shallow grinding, the trochoid cutting path can be approximated by a parabola:

$$z = \frac{x^2}{\left[d_s \left(1 \pm \frac{v_w}{v_s} \right)^2 \right]} \tag{7.2}$$

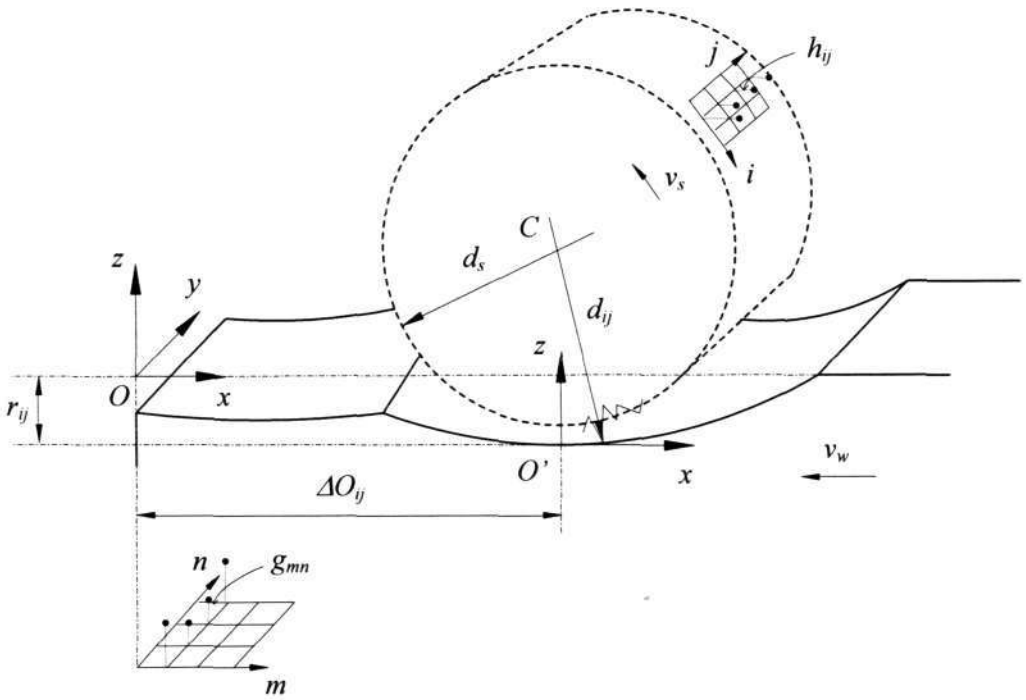

Figure 7.2 Mapping of the cutting point trajectories to the workpiece surface

Similarly, the trajectory of each cutting edge on the grinding wheel surface (Figure 7.2) can be expressed as

$$z_{ij} = \frac{x_{ij}^2}{\left[d_{ij} \left(1 \pm \frac{v_w}{v_s} \right)^2 \right]} \tag{7.3}$$

where x_{ij} and z_{ij} are the coordinate of the cutting edge relative to the x and z local coordinate system with the origin O', d_{ij} is the distance from cutting edge to the centre of

the grinding wheel and can be estimated by the following equation

$$d_{ij} = d_s + h_{ij} \tag{7.4}$$

with d_s is the nominal diameter of the grinding wheel, and h_{ij} is the grinding wheel surface height relative to the nominal grinding wheel diameter. h_{ij} can be obtained from grinding wheel topography.

7.2.2 Mapping of cutting point trajectories to the workpiece surface

All kinematic–based simulations of the grinding process require some schemes of mapping the cutting path to the workpiece surface. The approach used in this paper is similar to other authors (Salisbury et al. 2001b, Zhou and Xi 2002). Suppose that the workpiece surface can be presented by a topographical array $[g_{ij}]$. Each member of g_{mn} of the array is defined in the global coordinate system $Oxyz$, with the indices m and n corresponding to the positions of the workpiece surface height g_{mn} in the x and y direction respectively (Figure 7.2). The origin O is selected so that

$$max\{g_{mn}\} = 0 \tag{7.5}$$

Similarly, the grinding wheel topography can be described by an array of height $[h_{ij}]$ (Figure 7.2) with the indices i and j corresponding to the positions of the topographical point h_{ij} in the peripheral and axial directions of the wheel respectively. The position of the local origin O' of each cutting point relative to the global coordinate system can be estimated from the equation

$$\Delta O_{ij} = \frac{\Delta L_{ij} v_w}{v_s} \tag{7.6}$$

where ΔL_{ij} is the peripheral distance from the cutting point h_{ij} to the first cutting point; v_w is the velocity of the workpiece; v_s is the peripheral velocity of the wheel. ΔL_{ij} can be estimated as

$$\Delta L_{ij} = i\Delta x_s \tag{7.7}$$

with Δx_s is the step between rows of the grinding wheel topographic array $[h_{ij}]$ in the peripheral direction.

The trajectory of the cutting point, translated to the global coordinate $Oxyz$ is

$$z_{ij} = -r_{ij} + \frac{\left(x - \Delta O_{ij}\right)^2}{\left[d_{ij}\left(1 \pm \frac{v_w}{v_s}\right)^2\right]} \tag{7.8}$$

where r_{ij} is the distance in z coordinate from the local coordinate origin O' to the global coordinate O. r_{ij} is equal to the actual depth of cut of the cutting point h_{ij}, which can be estimated as

$$r_{ij} = h_{ij} - h_{max} + a \tag{7.9}$$

where $h_{max} = max\{h_{ij}\}$, and a is the specified depth of cut.

For each point mn of the workpiece topographic array the above equation can be written as

$$z_{mn} = r_{ij} + \frac{\left(m\Delta x_w - \Delta O_{ij}\right)^2}{\left[d_{ij}\left(1 \pm \frac{v_w}{v_s}\right)^2\right]} \tag{7.10}$$

where Δx_w is the distance between rows of the workpiece topographic array $[g_{ij}]$. Then, the workpiece topographic array can be updated as

$$g_{mn}^{i} = min\left\{g_{mn}^{i-1}, z_{mn}\right\} \tag{7.11}$$

with g_{mn}^{i-1}, g_{mn}^{i} are the workpiece surface heights at point mn before and after the cutting point h_{ij} passes through.

7.3 Interaction of the abrasive grain and the workpiece surface

Depending on the grinding condition, only a small number of the abrasive grains on the grinding wheel will contact the workpiece surface. Among this small number of active grains, only a small portion will cut and form chips while the others will only plough or rub the workpiece surface. Therefore, an algorithm is first proposed to identify the active grains. After this, the attack angle of the active grain is estimated, based on which the grain will be determined to either cut, or plough, or rub the workpiece surface.

7.3.1 Identification of the abrasive grain

The active abrasive grains can be identified from the topographical array $[h_{ij}]$ by sliding the topography at the specified depth of cut a as follows:

$$h_{ij} \geq h_{max} - a \tag{7.12}$$

where $h_{max} = max\{h_{ij}\}$ is the highest point in the grinding wheel topography and a is the specified depth of cut . Equation (7.12) implies that the highest cutting point of $[h_{ij}]$ will cut the workpiece surface at the depth a.

Figure 7.3 gives an example of a slicing plane across the wheel topography. The clusters of the topographical points remaining on the grinding wheel topography can be classified as the active abrasive grains. Strictly speaking, these abrasive grains are only static-active, as in the grinding process they may or may not contact the workpiece surface.

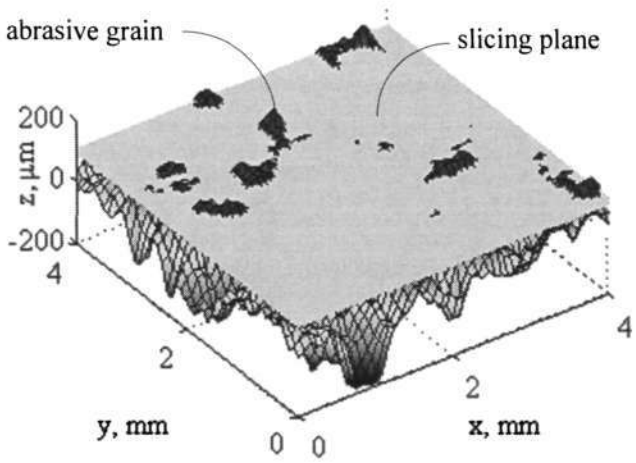

Figure 7.3 Slicing plane

In order to identify the active abrasive grain from the topographical array, a search algorithm is proposed. The search process starts with the first point of the abrasive grain (circle point in Figure 7.4a). By searching the neighbourhood points of the circle point, the next search front is identified (all the rectangular points). The searching of all the neighbourhood points is repeated for the rectangular points for identifying the successive search front (all the triangular points). The process continues until all the adjacent points are identified. All the found points are considered as belonging in the same abrasive grains. Strictly speaking, the two closely- positioned clusters of the cutting points can possibly belong to the same abrasive grain (Figure 7.4b). This situation can be remedied by considering the distance between two clusters. If the distance is smaller than the average grain diameter, they can be considered as

belonging to the same grain. Nevertheless, in this simulation, two non-adjacent clusters are considered as two separated grains.

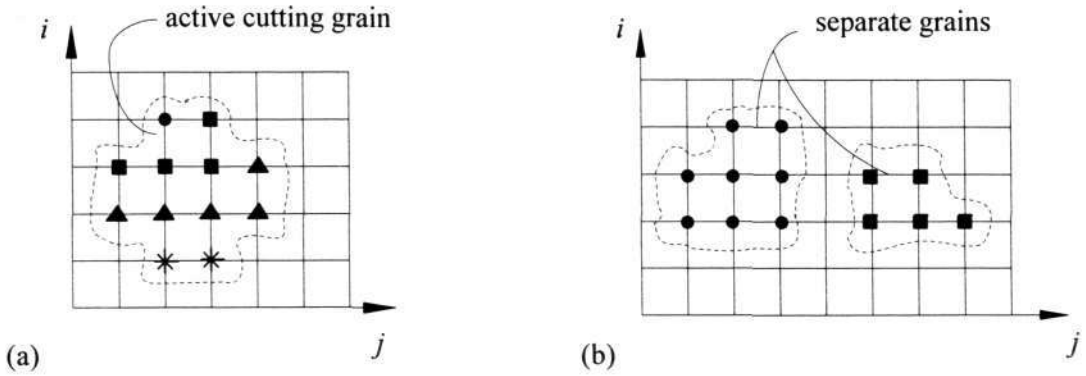

Figure 7.4 Active grain identification

7.3.2 Attack angle of the abrasive grain

In grinding metals three distinct phases can be identified at the interface of the abrasive grain and the workpiece: rubbing, ploughing and cutting (Hahn and Lindsay 1982). When the depth of cut is shallow, the grain only slides on the work causing elastic deformation in the work material with essentially no material removal; this is the rubbing phase. Ploughing occurs as the grain causes more plastic flow of the work material in the direction of sliding with material being thrown up and broken off the sides of the groove.

Komanduri (1971) , carrying out single point turning with negative rake angle tools, found that the value of the rake angle decided whether the tool cut, ploughed or rubbed. Takenaka (1966) observed that there was a critical depth of cut when the grain stopped cutting. Xie and William (1996) studied abrasive wear by repeatedly sliding a hard asperity on the workpiece surface. They established that the deformation modes of the material depended essentially on the following factors: lubrication, the mechanical properties of the softer material and the distance between adjacent tracks in repeated

pass situations. Kato (1992) conducted a scratch test in SEM apparatus, and observed that the material removal mode was affected by the degree of penetration, lubrication, and the hardness ratio of the abrading tip and the wear surface. Butler et al. (2002) showed that the grinding performance was correlated with the arithmetic sum of the curvature of the grinding wheel surface.

The above review shows that attack angle of the cutting edge has certain influence on the interaction of the abrasive grain with workpiece. In this study, the action of the abrasive grain is assumed to depend on the attack angle of the abrasive

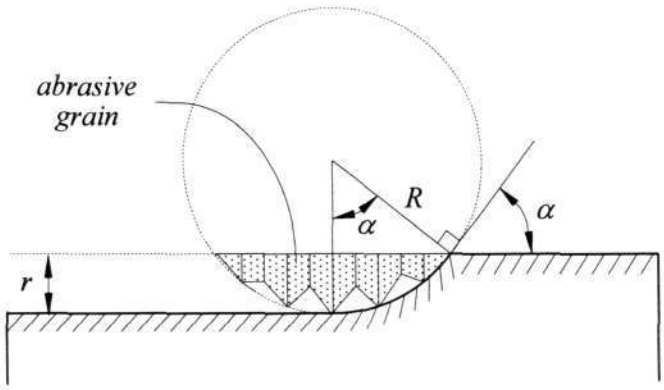

Figure 7.5 Attack angle of an abrasive grain

grain. It means that there exists a critical value α_p of attack angles at which the grinding action of the cutting edge will transit from cutting to ploughing. Similarly, the grinding action of the cutting edge will involve only rubbing action when its attack angle is smaller than a certain critical value α_r. Such critical values can be obtained from experimentation. If the abrasive grain tip is approximated as the sphere (Shaw 1995), the attack angle α can be estimated as follows (Figure 7.5)

$$\alpha = arccos\left(\frac{R-r}{R}\right) \tag{7.13}$$

where R is the radius of a spherical tip, and r is the grain depth of cut.

The radius of the abrasive grain tip can be found from the curvature of the grain. Since the sum of the curvatures of a surface at a point along any two orthogonal directions is equal to the sum of the principal curvatures (Stout et al. 1993). The curvature of the abrasive grain can be defined as the arithmetic mean summit curvature κ of all the cutting points forming the abrasive grain.

$$\kappa = -\frac{1}{2n}\sum_{k=1}^{n}\left(\frac{h_{i+1,j}+h_{i-1,j}-2h_{ij}}{\Delta x_s^2}+\frac{h_{i,j+1}+h_{ii,j-1}-2h_{ij}}{\Delta y_s^2}\right) \tag{7.14}$$

where n is the number of the cutting points forming the abrasive grain. i and j are the indices of the height point. Subsequently, the radius of the abrasive grain sphere is deduced as

$$R = \frac{1}{\kappa} \tag{7.15}$$

7.3.3 Update side flow profile

A portion of the displaced material, when the grains cut or plough, will remain on the workpiece surface and form side ridges along the groove. For the simulation, the cross section of the side ridges can be modelled as an isosceles triangle with base angle α equivalent to the attack angle of the abrasive grain. The size of the cross section can be estimated as follows (Figure 7.6).

$$A_r = \frac{1}{2}hl \tag{7.16a}$$

$$h = \sqrt{A_r tg\alpha} \tag{7.16b}$$

$$l = 2\sqrt{A_r \cot\alpha} \tag{7.16c}$$

where h is the perpendicular bisector (or median), l is the base side of the side ridge, and A_r is the area of the side ridge. The area A_r is estimated using the ploughing coefficient φ as follows

$$\varphi = \frac{2A_r}{A_d} \tag{7.17}$$

where A_d is the cross-section area of the groove. A similar approach was used by Chen and Rowe (1996b), except that a ridge was approximated as a parabola.

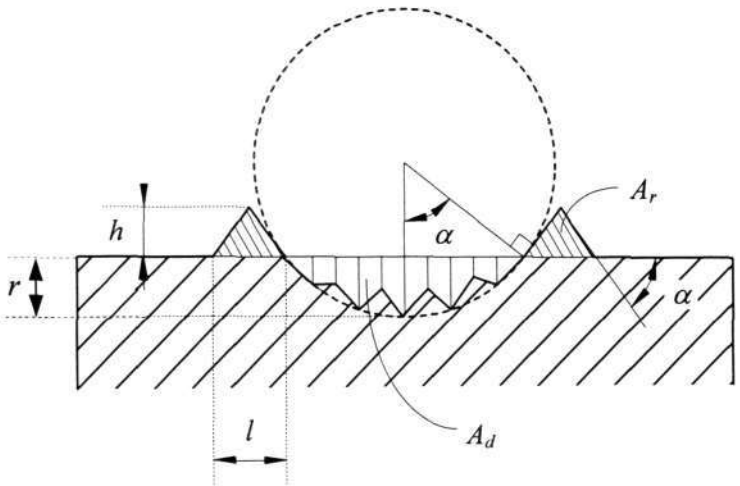

Figure 7.6 Side ridges of grooves

For investigation of the ploughing coefficient φ, a fly-milling test was conducted. An action of a single abrasive grain was simulated by using a single point diamond dresser attached to an aluminium flywheel. The flywheel was installed on a surface grinder Okamoto 63DXV as a grinding wheel. A series of grooves were scratched on a mould steel workpiece by moving rapidly the workpiece past the rotating flywheel. The workpiece surface was polished to a mirror finish for facilitating groove inspection. Figure 7.7a shows the flywheel with the diamond dresser attached. The diamond tip of the dresser had a pyramid form (Figure 7.7b).

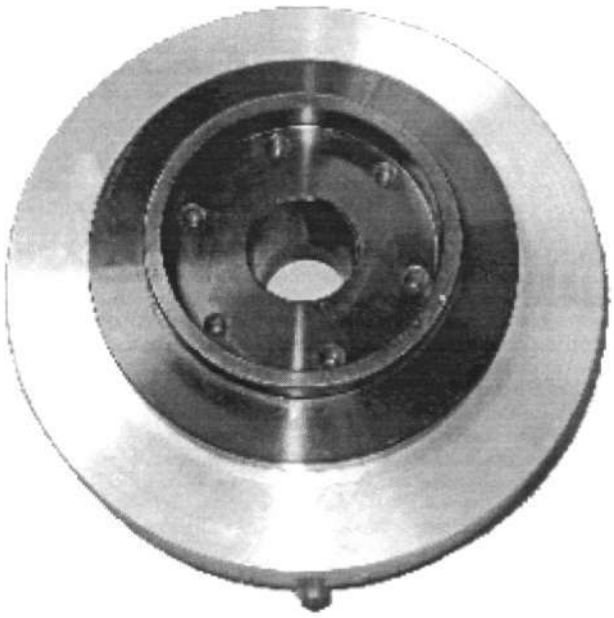

(a)

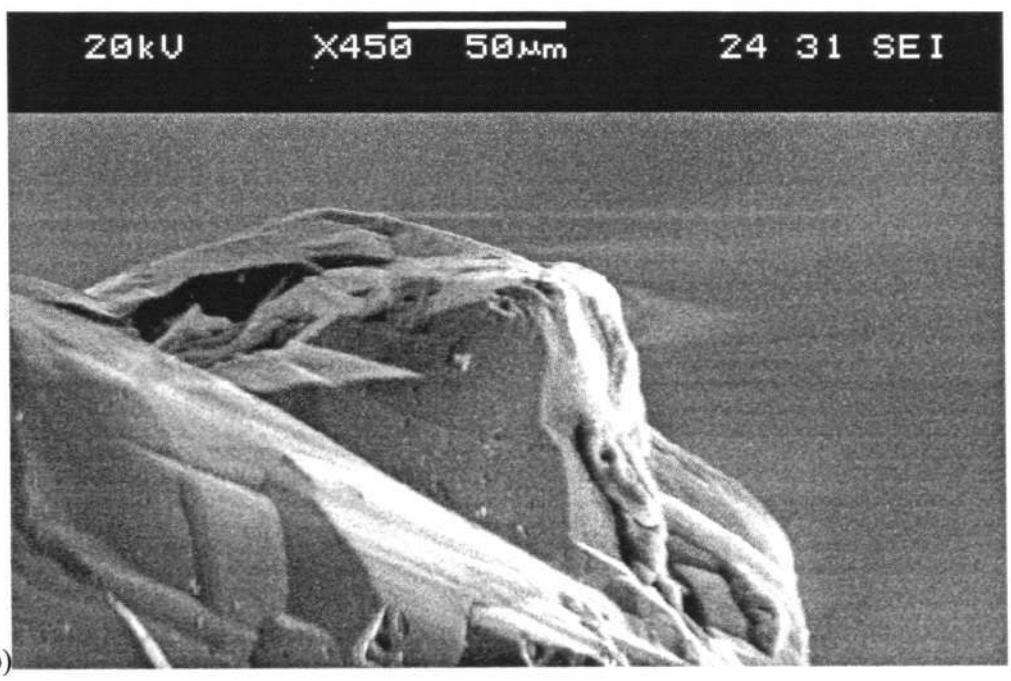

(b)

Figure 7.7. Fly-milling test: (a) aluminium flywheel, (b) SEM of a diamond tip

The grooves were measured on the stylus system Talyscan 150 to evaluate the cross section area at different depths of cut. Typical groove cross sections, where ploughing and cutting are dominating modes, are shown on Figure 7.8a, b. The single grit scratch testing showed that the coefficient φ could be varied from 70% to 100% for ploughing, and 10% to 50% for cutting.

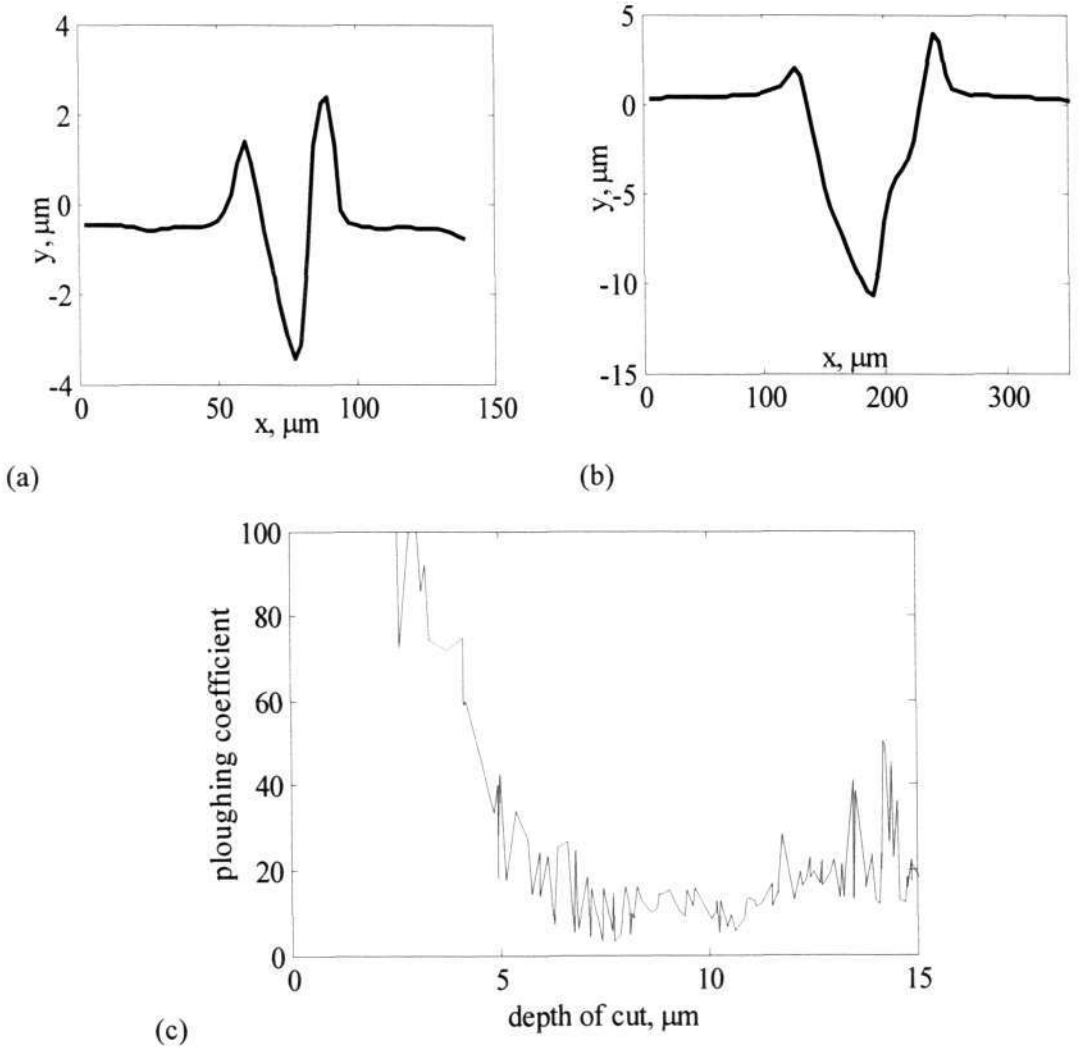

Figure 7.8. Cross sections of a scratch: (a) ploughing is dominating, (b) cutting is dominating, (c) ploughing coefficient φ at various depth of cut

Figure 7.8c displays the relationship between the ploughing coefficient φ and the depth of cut. It shows that there is a clear transition at which the cutting ratio drops substantially. This depth of cut can be considered as the transition from ploughing to cutting action of an abrasive grain. The average value of the plouging coefficient φ is approximately 34% for cutting action and 80% for ploughing action.

7.4 Simulation procedure

Figure 7.9 shows the procedure for simulating the grinding process. The input for the simulation includes the samples of the wheel topography, wheel velocity v_s, workpiece velocity v_w, grinding wheel diameter d_s, and depth of cut a. The simulation procedure starts with the generation of the grinding wheel topography based on the sampled wheel data. The algorithm for generating the grinding wheel topography is described in the previous chapter.

The generated topographical array $[h_{ij}]$ is then sorted to identify the static active grains, together with the estimation of the radii of the grains. Using the given depth of cut a, wheel velocity v_s and workpiece velocity v_w, the grinding wheel data $[h_{ij}]$ is mapped to the workpiece surface texture $[g_{mn}]$ as described in Section 7.2.

At each cross-section m of the workpiece surface $[g_{mn}]$, the grain depth of cut and the area of the displaced workpiece material are found. Next, the attack angle of the active grain at the m^{th} section of the workpiece surface is evaluated, based on which the grinding mode of the active grain (cutting, ploughing, or rubbing) is decided. The workpiece surface is updated by superimposing the grooving and side ridge cross section.

The MATLAB scripts for simulation are given in Appendix J.

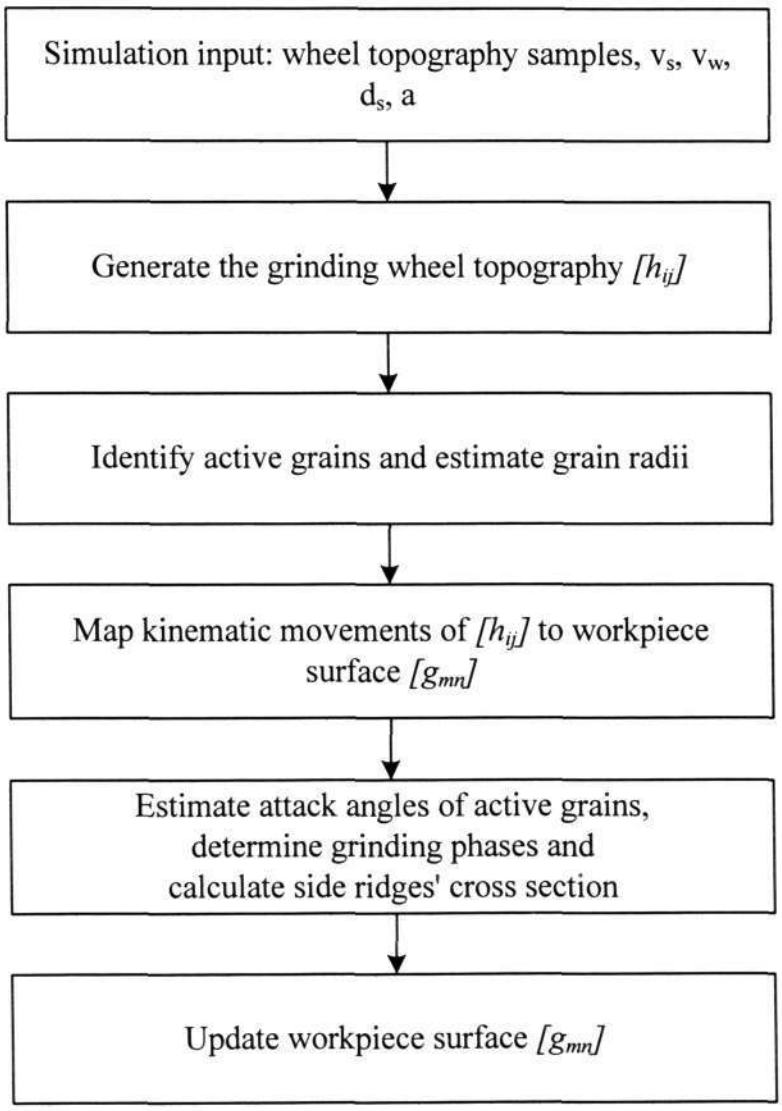

Figure 7.9 Simulation procedure

7.5 Model verification

For the purpose of model verification, two grinding experiments were conducted on an Okamoto 63DXV surface-grinding machine. The workpiece material is mild steel and tool steel D2. The spindle system was balanced by a microbalancer Okamoto MB-3. The amplitude of the wheel head vibration was adjusted to be less than 0.1 μm peak-to-peak at a maximum rotational speed of 1500 rpm.

The grinding wheel was made of aluminum oxide A80J8V and A80H8V. The wheel was trued with 30 μm depth of cut, 4 passes and a crossfeed velocity of 5 mm/sec (0.2 mm/rev). Then it was dressed with 15 μm depth of cut, 2 passes and a crossfeed velocity of 2.5 mm/sec (0.1mm/rev). For the case of the D2 workpiece, two additional idle passes were carried out following the dressing operation. After dressing, the wheel surface was replicated at 4 locations, and its topography was captured using Talyscan 150 3D stylus measuring system.

The mild steel workpiece was first ground flat with 20 μm down-feed set on the grinding machine. A layer of 0.2 mm was removed. Then, it was finished with 10 μm downfeed. For the D2 workpiece, a layer of 0.3 mm was removed with 20 μm down-feed set on the grinding machine. Then, it was ground with 10 μm downfeed with 5 grinding passes. The last 5 passes were carried out at 5 μm downfeed. The grinding conditions are summarized in Table 7.1. Four samples of the topography for each workpiece were taken by Talyscan 150 system.

Table 7.1 Grinding conditions

Parameter	Mild steel	D2
Grinding wheel rotation speed φ_s, rpm	1500	1500
Workpiece velocity v_w, m/s	0.1	0.13
Depth of cut a (finish), μm	10	5
Coolant	water-soluble coolant	water-soluble coolant
Grinding wheel	A80J8V	A80H8V

The critical attack angles α_p and α_r for this grinding condition were chosen based on the equation suggested by Xie and William (1996). For steel, α_p is roughly 25.5° and α_r is about 1°. Another important input is the actual depth of cut used in the simulation. Due to the deflection of the machine, workpiece and grinding wheel, the actual depth of cut may be far from the down-feed set on the grinding machine. The actual depth of cut can be approximated from the ground grooves on the workpiece surface or from the following equation (Malkin 1989):

$$a_r = \frac{a}{1 + \frac{k_c}{k_e}} \tag{7.18}$$

where a_r is the actual depth of cut, a is the depth of cut set on the grinding machine, k_c is the cutting stiffness, and k_e is the effective stiffness, estimated as (Malkin 1989)

$$\frac{1}{k_e} = \frac{1}{k_m} + \frac{1}{k_a} \tag{7.19}$$

with k_m is the machine stiffness and k_a is the contact stiffness. The range of stiffness k_c, k_m, and k_a found in grinding are: k_m = 10-100kN/mm; k_c/b = 2-10 kN/mm^2; k_a/b = 1-10 kN/mm^2.

The simulation was run on the PC Pentium II-500MHz. A total of 4 simulations for each experiment were conducted. Computer time for one simulation was approximately 10 min. The averaged 3D characterization parameters of the surfaces, obtained from the experiment and the simulation, are given in Table 7.2 (full data is given in Appendix K). A comparison between the two data sets shows that amplitude (S_q, S_z, S_{sk} and S_{ku}), autocorrelation (S_{tr}, S_{al}, S_{td}) and functional (S_{bi}, S_{ci}, S_{vi}) parameters are in good agreement while other parameters (S_{ds} and S_{dr}) show larger variation. These variations can be explained by the fact that the parameters are strongly influenced by frequency components of the surface texture. The simulated surface however has less high frequency components compared to the real surface. Figure 7.10 and Figure 7.11 show the topographies of the ground workpieces and the simulated surfaces, which clearly resemble each other.

Table 7.2 Three- dimensional surface characterization of the workpiece surface

Parameter	Mild steel		D2	
	Experiment	Simulation	Experiment	Simulation
S_q, μm	0.78	1.05	0.34	0.39
S_z, μm	4.71	5.39	2.26	2.41
S_{sk}	-0.1	-0.19	-0.48	-0.74
S_{ku}	2.6	2.7	3.7	4.5
S_{tr}	0.05	0.05	0.05	0.05
S_{al}, mm	0.04	0.04	0.04	0.04
S_{td}, °	0	0	0	0
S_{ds}, mm^{-2}	51.34	14.97	54.88	22.71
$S_{\Delta q}$	0.03	0.04	0.01	0.01
S_{sc}, μm^{-1}	0.001	0.001	0.005	0.005
S_{dr}, %	0.04	0.07	0.007	0.01
S_{bi}	0.63	0.63	0.65	0.7
S_{ci}	1.63	1.59	1.56	1.35
S_{vi}	0.14	0.15	0.17	0.26

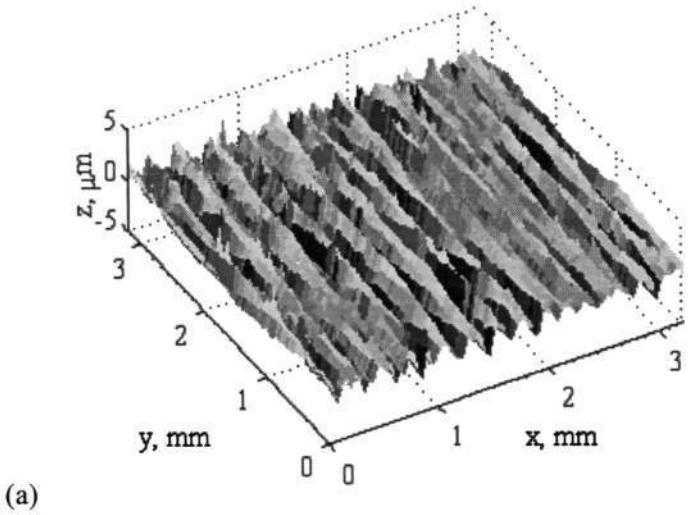

(a)

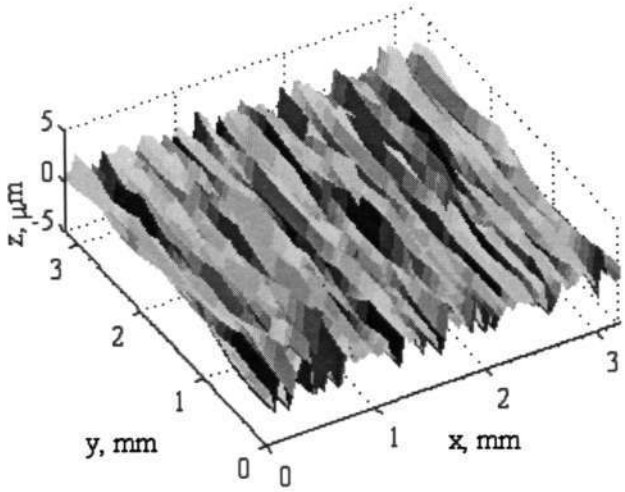

(b)

Figure 7.10 The topography of the mild steel ground workpiece (a) and the simulated surface (b)

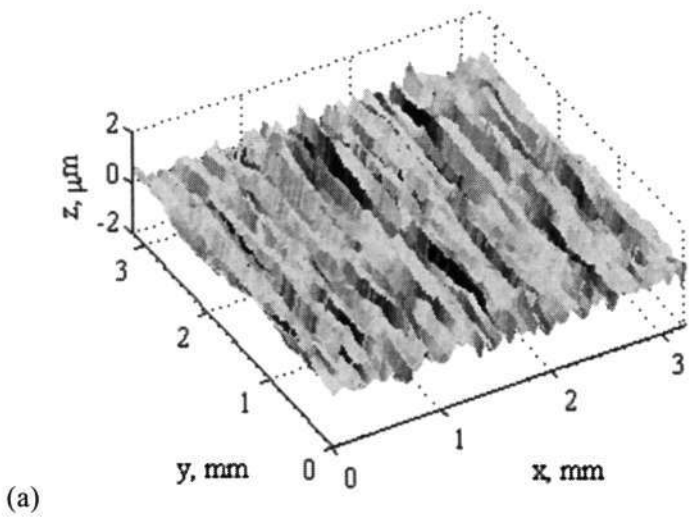

(a)

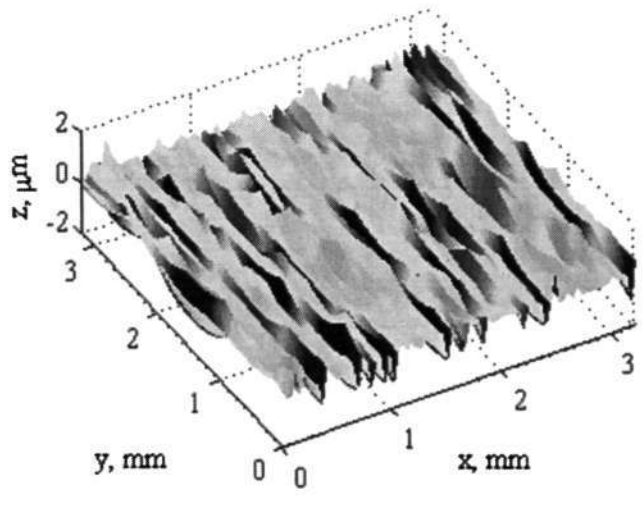

(b)

Figure 7.11 The topography of the D2 ground workpiece (a) and the simulated surface (b)

7.6 Model limitation

In this simulation model, the interaction mode between the abrasive grain and the workpiece is assumed to be dependent on the attack angle. In reality, the interaction could be more complex, influenced by many factors such as material behaviour, interfacial friction and size effect. Although in the scope of the study, the model has been verified successfully for a limited set of workpiece materials and grinding conditions, it needs more experiments in order to apply to a broader framework of grinding.

7.7 Chapter summary

A numerical procedure is proposed for the kinematic simulation of the grinding process. The procedure takes into consideration the complex nature of the wheel-workpiece interaction by assuming that the attack angle of the abrasive grain will decide the interaction mode. An algorithm is proposed for the identification and estimation of the attack angle using the summit curvature of the topographical point. The workpiece surface is updated according to the estimated material removal mode. The agreement between the simulated and experimental result proves the validity of the technique.

Chapter 8

Conclusions

This thesis describes the research on fundamental aspects of grinding: characterisation of the grinding wheel and analytical model of the grinding process. The grinding process is often considered as milling at a smaller scale. However, the grinding wheel is a unique tool, differing completely from other cutting tools. Its size and non-stationary nature have made grinding one of most difficult-to-understand manufacturing processes. Furthermore, the investigation of the grinding process is complicated by many factors such as machine setting or workpiece materials.

The thesis has built a framework for the grinding wheel surface characterisation. A methodology that covers surface replication, measurement and parameter estimation has been established. The proposed kinematic model has taken into account the main factors that influence the grinding quality. It helps correlate the characteristics of wheel topography and the workpiece surface finish. The model can be used to illucidate the effects of these factors on the grinding process as well as predict its performance. In summary, the contributions of this thesis are listed as follows

8.1 MATLAB toolbox for 3-D surface characterisation

A set of MATLAB functions have been implemented for estimating the 3-D parameters. The toolbox supports a broad set of 3-D parameters. The main advantages of the toolbox are batch processing and graphical utilities.

8.2 A novel technique is verified for grinding wheel characterization

A comprehensive verification of the novel technique for wheel surface replication was carried out. The technique was verified against a broad set of grinding wheels of various abrasive materials, wheel conditionings and grain sizes. It was shown that it can be reliably used for replicating grinding wheel surfaces.

8.3 Sampling conditions

A thorough analysis of the dependence of 3-D parameters on the sampling conditions was conducted. The parameters' dependency on the sampling was studied on the basis of the power spectrum analysis. From the analysis, it is clear that surfaces such as the grinding wheel and ground workpiece are dominated by a few low-frequency components. The relationship between the dominating components and parameters S_{al} was proven experimentally and analytically. A set of criteria for selecting the sampling conditions is suggested for the grinding wheel surface and ground workpiece. These criteria can be extended to other isotropic and anisotropic surfaces.

8.4 Correlation of wheel topography and grinding performance

The correlation of the wheel, grinding performance and 3-D parameters was robustly established through a factorial experiment. The investigation reveals that the sampling condition should be chosen carefully in order to successfully use 3-D parameters. Its results are beneficial for understanding the process, and can be used to select the truing conditions for CBN wheels.

8.5 Kinematic model

A kinematic model was proposed for simulating the grinding process. The input of the model includes wheel, workpiece, machine, and processing setting factors. Its output is the workpiece topography. In comparison with previous models, the current model accounts for non-Gaussian probability distributions of the wheel surface and the complex interaction of the workpiece and the abrasive grain.

For the generation of non-Gaussian grinding wheel surfaces, an effective numerical procedure that relies on a simple transformation is proposed. The sufficient condition for the procedure is that the transform function is monotonic with non-zero Jacobian. Numerical examples prove that the procedure is effective for a broad range of grinding wheels. The main advantages of the procedure over existing algorithms include computational effectiveness and avoiding arbitrary judgement of model orders.

The cutting, ploughing, and rubbing modes of the wheel-workpiece interaction are taken into account through the attack angle of the abrasive grain. An algorithm is proposed for the identification and estimation of the attack angle using the summit curvature of the topographical point. The model also takes into consideration ridges formed on the workpiece surface during the wheel-workpiece interaction. The model

can be used to study the influence of the grinding wheel topography on the grinding performance.

Although the simulation model has been successfully verified for a limited set of grinding conditions, a more extensive set of experiment would be necessary in order to generalise the model into a broader applicability. Furthermore, a benchmark with previous models would be beneficial. However, it will demand the same experiement setup for all the models, which is difficult to achieve as well as the information provided the literature is limited and insufficient in order to reproduce the previous models.

Chapter 9

Future work

Future work can be aimed at verifying the characterisation method on new types of grinding wheels, extending the kinematic model to incorporate more complex grinding phenomena and its applicability for less ductile materials such as ceramics.

9.1 Grinding wheel wear simulation

As grinding takes place, the grinding wheel is subjected to various wear mechanisms such as attritious wear, grain fracture, and bond fracture (Malkin 1989). These mechanisms produce a change in the topography, and then the grinding performance. It is important to be able to simulate its wear behavior. The wear behavior of the grinding wheel surface can be studied through its surface height distribution and autocorrelation function. The information about the changes of the probability distribution and autocorrelation function in time and under the influence of wear mechanisms can be used as an input to the numerical procedure described in Chapter 6.

9.2 Replication of grinding wheels with small grain size

Recent developments have seen grinding wheels with small grain sizes being used in the workshop. Ultra-precision grinding is now possible with nanograin sizes (Komanduri et al. 1997). The two-stage replication technique has been successfully tested for the grinding wheel with a grain size of up to 140 mesh size. Verification should be done to check the applicability of the technique for a smaller size of grains.

9.3 Summit definition

The summit definition used in this study is "the eight nearest neighbours". This definition is not completely perfect as the ridges and saddles can be miscounted as the summit or prevent the real summit from identification (Stout et al.1993). Furthermore, current summit definitions have not taken into account the amplitude factors. Future work on a new definition of the summit should aim at overcoming these shortcomings.

9.4 Interaction of the workpiece and abrasive grain

The current model of the interaction between the workpiece and abrasive grain is rather simplified, based mostly on the attack angle of the abrasive grain. In reality, its interaction is very complex, affected by many factors such as material behaviour, interfacial friction and size effect. Modelling the single grit interaction would be helpful for understanding the process. One approach of modelling the interaction is using slip-line or upper-bound theory such as the work of William and Xie (1992) or Oxley (1997). However, such a model is limited by assuming simple material behaviour based on plane strain. Real materials display a more complicated behaviour including work-hardening or thermal softening. Especially in grinding, the workpiece material is subject

to extreme conditions of high strain rate, strain gradient, and temperature. Alternatively, finite element method (FEM) would help in more realistically modelling the interaction.

9.5 Grinding chatter

In the kinematic model proposed in this thesis, grinding chatter is not taken into account. The occurrence of chatter during a grinding operation has a major influence on the geometry of the grinding wheel and the workpiece. There are basically two types of vibration: forced vibration and self-excited vibration. Regarding surface quality, there is not much evidence that chatter has an influence on the workpiece roughness, rather than macro-geometrical deterioration is the main result to be obtained from chatter vibrations during grinding (Inasaki 2001). In respect to kinematic models, the presence of vibrations will introduce long-wavelength wave components into the kinematic relationship between the wheel and the workpiece. Thus, the trajectory equations of the cutting edges need to be amended to incorporate this vibration factor.

9.6 Grinding force prediction

The kinematic model can be broadened to estimate grinding forces. From the kinematic model, it is possible to calculate the number of abrasive grains contacting the surface, and the contact area of each grain. Then, grinding forces are the multiplication of the total contact area and specific grinding forces. Specific grinding forces can be found directly from experiments. Alternatively, they can be estimated from models of single grit interaction. For an accurate result, the interaction between chip and bond, and the hydrodynamic effect of coolants would also need to be considered.

9.7 Simulation of ceramic grinding

As ceramics continue to find application in industry, grinding has received extensive attention. The current kinematic model, which is applicable to ductile material, can be adjusted for ceramics grinding. The main difference between ductile and ceramic grinding is the interaction mode between the grain and the workpiece. While grinding of ductile materials involves mainly ductile fracture, ceramic grinding is dominated by brittle fracture (Marinescu et al. 2000). Hence, in order to apply the kinematic model for ceramics, the interaction model needs to be modified.

References

Badger, J.A. and Torrance, A.A. (2000). A comparison of two models to predict grinding forces from wheel surface topography. *International Journal of Machine Tools and Manufacture*, 40 (8), pp. 1099-1120.

Bendat, J. S. and Piersol, A. G. (2000). *Random Data: Analysis and Measurement Procedure*, 3rd ed. New York, John Wiley. ISBN 0471317330.

Bhateja, C.P. (1977). An enveloping profile approach for the generation of ground surface texture. *Annals of CIRP*, 25 (1), pp. 333-337.

Blunt, L. and Ebdon, S. (1996). The application of three-dimensional surface measurement techniques to characterizing grinding wheel topography. *International Journal of Machine Tools and Manufacture*, 36 (11), pp.1207-1226.

Brinksmeier, E. and Werner, F. (1992). Monitoring of grinding wheel. *Annals of CIRP*, 41 (1), pp. 373-376.

Butler, D.L. (1999). *The Topographic Characterization of Cylinder Liner Wear.* Ph.D. thesis, The University of Birmingham.

Butler, D. L., Blunt, L. A., See, B.K., Webster J.A., and Stout, K.J. (2002). The characterisation of grinding wheels using 3D surface measurement techniques. *Journal of Materials Processing Technology*, 127 (2), pp. 234-237.

Butler D.L., Chan, S.C., Ramesh, K., and Huang, H. (2004). CBN grinding of Inconel – a topographic approach to process characterization. In : Tor, S.B., Tung, S.K., and Enomoto, S. ed. *Proceedings of International Conference on Precision Engineering*, 2-5 March, Singapore, pp. 159-166.

Cai, R., Rowe, W.B., Morgan, M.N., and Mills, B. (2003). Measurement of vitrified CBN grinding wheel topography. *Key Engineering Materials*, 238-239, pp. 301-306.

Challen, J.M. and Oxley, P.L.B. (1979). An explanation of the different regimes of friction and wear using asperity deformation models. *Wear*, 53 (2), pp. 229- 243.

Challen, J.M., McLean, L.J., and Oxley, P.L.B. (1984). Plastic deformation of a metal surface in sliding contact with hard wedge: its relation to friction and wear. *Proceedings of Royal Society London,* A394, pp. 161-181.

Chen, X. and Rowe, W.B. (1996a). Analysis and simulation of the grinding process. part 1: generation of the grinding wheel surface. *International Journal of Machine Tools and Manufacture,* 36 (8), pp. 871-882.

Chen, X. and Rowe, W.B. (1996b). Analysis and simulation of the grinding process, part 2: mechanics of grinding. *International Journal of Machine Tools and Manufacture*, 36 (8), pp. 883-896.

Chen, X. and Rowe, W. B. (1996c). Analysis and simulation of the grinding process, part 3: comparison with experiment. *International Journal of Machine Tools and Manufacture*, 36 (8), pp. 897-906.

Chen, X., Rowe, W.B., and Cai, R. (2002). Precision grinding using CBN wheels. *International Journal og Machine Tools and Manufacture*, 42 (5), pp. 585-593.

De Chiffre, L., Lonardo, P. Trumpold, H., Lucca, D.A., Goch, G., Brown, C.A., Raja, J., and Hansen, H.N. (2000). Quantitative characterisation of surface texture. *Annals of CIRP*, 49 (2), pp. 635-638.

Cooper, W. and Lavine, A.S. (2000). Grinding process size effect and kinematics numerical analysis, *Journal of Manufacturing Science and Engineering*, 122 (1), pp. 59-69.

Cressie, N. A. (1993). *Statistics for Spatial Data,* New York, Wiley. ISBN 0471002550.

Deodatis, G. and Micaletti, R. (2001). Simulation of highly skewed non-Gaussian stochastic processes. *Journal of Engineering Mechanics*, 127 (12), pp. 1284-1295.

Dong, W.P., Sullivan, P.J., and Stout K.J. (1994). Comprehensive study of parameters for characterizing three-dimensional surface topography. part 4: parameters for characterizing spatial and hybrid properties. *Wear*, 178 (2), pp. 45-60.

EMO (2001). EMO Hannover 2001: statistics. Available from:<http://www.emo-hannover.de/statistics> [Accessed September 25th, 2004]

Gong, Y.D., Wang, B., and Wang, W.S. (2002). The simulation of grinding wheels and ground surface roughness based on virtual reality technology. *Journal of Materials Processing Technology* ,129 (1-3), pp. 123-126.

Goldstein, J. (2003). *Scanning Electron Microscopy and X-ray Microanalysis*. New York, Kluwer Academics. ISBN 0306472929.

Ghosh, S. (1993). *Modeling and Analysis of the Grinding Process.* MSc Thesis, University of Maryland.

Greenwood, J.A. (1984). A unified theory of surface roughness. *Proceedings of Royal Society of London, Series A*, 393 (1804), pp. 133-157.

Grigoriu, M. (1995). *Applied Non-Gaussian Processes: Examples, Theory, Simulation, Linear Random Vibration, and MATLAB Solutions.* New Jersey, Prentice Hall. ISBN 0133670953.

Hahn, R.S. and Lindsay, R.P. (1982). Principles of grinding, part 1: basic relationships in precision grinding. In: Bhateja C. and Lindsay R. ed., *Grinding Theory Techniques and Troubleshooting.* Michigan, SME , pp.3-10.

Hasegawa, M. (1974). Statistical analysis for the generating mechanism of ground surface roughness, *Wear*, 29 (1), pp.31-39.

Hecker, R. (2002). *Part Surface Roughness Modeling and Process Optimal Control of Cylindrical Grinding.* Ph.D. thesis, Georgia Institute of Technology.

Hegeman, J.B.J.W. (2000). *Fundamentals of Grinding: Surface Conditions of Ground Material.* Ph.D. Thesis, University of Groningen.

Higuchi, M., Yano, A., Yamamoto, N., Adachi, T., and Yamashita, K. (1994). Quantitative analysis grain using fractal geometry. *International Journal of Japan Society of Precision Engineering*, 28 (3), pp. 227-228.

Hill, I.D., Hill, R., and Holder, R.L. (1976). Algorithm as 99: fitting Johnson curves by moments. *Applied Statistics*, 25 (2), pp. 180-189.

Hou, Z.B. and Komanduri, R. (2003). On the mechanics of the grinding process –part 1: stochastic nature of the grinding process. *International Journal of Machine Tools and Manufacture*, 43 (15), pp. 1579-1593.

Inasaki, I. (1996). Grinding process simulation based on the wheel topography. *Annals of CIRP*, 45 (1), pp. 347-350.

Inasaki, I. (2001). Grinding chatter- origin and suppression. *Annals of CIRP,* 50 (2), pp. 515-534.

Ishikawa, T. and Kumar, K.V. (1991). Conditioning of vitrified bond superabrasive wheels, In: *Superabarsive 91,* 11-13 June, Chicago. Michigan, SME, pp.7.91-110.

Jackson, M.J., Davis, C.J., Hitchiner, M.P. and Mills, B. (2001). High-speed grinding with CBN grinding wheels- applications and future technology, *Journal of Materials Processing Technology*, 110 (1), pp. 78-88.

Johnson, N.L. (1949). Systems of frequency curves generated by methods of translation. *Biometrika*, 36 (1-2), pp. 149-176.

Kato, K. (1992). Micro-mechanisms of wear – wear modes, *Wear*, 153 (1), pp. 277-295.

Kim, K. W., Lee, W.Y., and Sin, H. (1999). A Finite element analysis for the characteristics of temperature and stress in micro-machining considering the size effect. *International Journal of Machine Tools and Manufacture*, 29 (9), 1999, 1507-1524.

Komanduri, R. (1971). Some aspects of machining with negative rake tools simulating grinding. *International Journal of Machine and Tool Design Research*, 11, pp. 223-233.

Komanduri, R., Lucca, D.A., and Tani, Y. (1997). Technological advances in fine abrasive processes. *Annals of CIRP,* 46 (2), pp. 545-596.

Koshy, P., Jain, V.K., and Lal, G.K. (1997). Stochastic simulation approach to modeling diamond wheel topography. *International Journal of Machine Tools and Manufacture,* 37 (6), pp. 751-761.

Koshy, P., Ives, L.K., and Jahanmir, S. (1999). Simulation of diamond-ground surfaces. *International Journal of Machine Tools and Manufacture*, 39 (9), pp. 1451-1470.

Kumar, K.V., Ishikawa, T., and Kosley, J. (1991). Superabrasive grinding of superalloys, In: *Superabrasives 91*, 11-13 June, Chicago. Michigan, SME, pp. 17.17--30.

Li, Y.Y. and Chen, Y. (1989). Simulation of surface grinding. *Journal of Engineering Materials and Technology,* 111 (1), pp. 46-53

Liao, T.W. (1995). Fractal and DDS characterization of diamond wheel profiles. *Journal of Materials Processing Technology,* 53 (3-4), pp. 567-581.

Lin, T. (1993). *Characterisation, Sampling and Measurement Variation of Surface Topography: A Viewpoint from Standardization.* Ph.D. Thesis, The University of Birmingham.

Lonardo, P. M., Trumpold, H., and Chiffre, L.D. (1996). Progress in 3D surface microtopography characterization. *Annals of CIRP*, 45 (2), pp. 589-598.

Machinability Data Center (1980). *Machining Data Handbook*, 3rd edition. Cincinnati, MDC. ISBN: 0936974028.

Malkin, S. (1989). *Grinding Technology: theory and application of machining with abrasives.* Chichester, Ellis Horwood. ISBN 0853127565.

Malkin, S. and Huang, T.W. (1996). Grinding mechanics for ceramics. *Annals of CIRP,* 42 (2), pp. 569-580.

Mahdi, M. and Zhang, L. (1997). Applied mechanics in grinding- part 5: thermal residual stresses. *International Journal of Machine Tools and Manufacturing*, 37 (5), pp. 619-633.

Mahdi, M. and Zhang, L. (1998). Applied mechanics in grinding- part 6: residual stresses and surface hardening by coupled thermo-plasticity and phase transformation. *International Journal of Machine Tools and Manufacturing*, 38 (10-11), pp. 619-633.

Mahdi, M. and Zhang, L. (1999). Applied mechanics in grinding- part 6: residual stresses included by the full coupling of mechanical deformation, thermal deformation and phase transformation. *International Journal of Machine Tools and Manufacturing*, 39 (8), pp. 619-633.

Montgomery, D.C. (1997). *Design and Analysis of Experiments*, 4th edition. New York, Wiley. ISBN 0471157465

Marinescu, I., Tonshoff, H.K., and Inasaki, I. (2000). *Handbook of Ceramic Grinding and Polishing*. Park Ridges, Noyes Publication. ISBN 0815514247.

Marple, S. L. (1987). *Digital Spectral Analysis*. Englewood Cliffs, Prentice-Hall. ISBN 0132141493.

Mayinger, F. (2001). *Optical Measurements: Techniques and Applications.* New York, Springer. ISBN 3540666907.

Oxley, P.L.B. (1997). Modelling the related processes of abrasion, wear and polishing. In: Zhang, L.C., and Yasunaga, N. ed. *Proceedings of the International Symposium on Advances in Abrasive Technology*, 8-10 July, Sydney. Singapore, World Scientific, pp. 1-17.

Pandit, S.M. and Wu, S.M. (1973). Characterization of abrasive tools by continuous time series, *ASME Journal of Engineering for Industry*, 95B, pp. 821-826.

Pandit, S.M. and Sathyanarayanan, G. (1982). A model for surface grinding based on abrasive geometry and elasticity. *Journal of Engineering for Industry*, 104 (4), pp. 349-357.

Pandit, S.M., and Sathyanarayanan, G. (1984). Data-Dependent Systems approach to surface generation in grinding. *Journal of Engineering for Industry*, 106 (3), pp.205-212

Papoulis, A. (1962). *The Fourier integral and its applications*. New York, McGraw-Hill.

Papoulis, A. (1990). *Probability & Statistics.* New York, Prentice-Hall. ISBN 0137116985.

Pearson, E.S. (1972). *Biometrika Tables for Statisticians.* Cambridge, University Press.

Prigarin, S. M. (2001). *Spectral Models of Random Fields in Monte Carlo Methods.* Utrecht, VSP. ISBN 9067643432.

Prusak, Z., Webster, J. A., and Marinescu, I. D. (1997). Influence of dressing parameters on grinding performance of CBN/seeded gel hybrid wheels on cylindrical grinding. *International Journal of Production Research*, 35 (10), pp. 2899-2916.

Rowe, G. W., Sturgess, C.E.N., Hartley, P., and Pillinger, I. (1991). *Finite Element Plasticity and Metalforming Analysis*. Cambridge, Cambridge University Press. ISBN 0521383625.

Sacerdotti, F., Griffiths, B.J., Benati, F., Butler, C., Jonasson, M., Liraut, G., Rosen, B.G., Scheers, J., Scott, P., Wentink, D.J. (2001). Hardware variability in the three-dimensional measurement of autobody steel panel surfaces. *International Journal of Machine Tools and Manufacture*, 41 (13-14), pp. 2051-2060.

Salisbury, E. J., Domala, K. V., Moon, K.S., Miller, M.H., and Sutherland, J.W. (2001a). A three-dimensional model for the surface texture in surface grinding, part 1: surface generation model. *Journal of Manufacturing Science and Engineering*, 123 (4), pp. 576-581.

Salisbury, E. J., Domala, K. V., Moon, K.S., Miller, M.H., and Sutherland, J.W. (2001b). A three-dimensional model for the surface texture in surface grinding, part 2: grinding wheel surface texture model, *Journal of Manufacturing Science and Engineering*, 123 (4), pp. 582-590.

Sayles, R.S. (1982). The profiles as a random process. In: Thomas, T.R. ed. *Rough Surfaces*. London, Longman.

Scott, W. and Baul, R.M. (1979). Analysis of the active profile of grinding wheel surfaces. *Wear,* 57 (2), pp. 247-254.

Scott, P.J. (2001). An algorithm to extract critical points from lattice height data. *International Journal of Machine Tools and Manufacture*, 41(13-14), pp. 1889-1897.

Shaw, M.C. (1996). *Principles of Abrasive Processing.* Oxford, Clarendon Press. ISBN 0198590210.

Sharp, K.W., Miller, M.H., and Scattergood, R.O. (2000). Analysis of the grain depth-of-cut in plunge grinding. *Precision Engineering,* 24 (3), pp. 220-230.

Shinozuka, M. and Deodatis, G. (1996). Simulation of multi-dimensional Gaussian stochastic fields by spectral representation. *Applied Mechanics Reviews*, 49 (1), pp. 29-53.

Stephenson, D.J., Laine, E., Johnstone, E., Baldwin, A., and Corbett, J. (2001) Burn threshold studies for superabrasive grinding using electroplated CBN wheels, SME Technical Paper MR01-219.

Stout, K.J., Sullivan, P.J., Dong, W.P., Mainsah, E., Luo, N., Mathia, T., Zahouani, H. (1993). *The Development of Methods for the Characterization of Roughness in Three Dimensions*. Luxembourg, Commission of the European Communities.

Takenaka, N. (1966). A study on the grinding action by single grit. *Annals of CIRP,* 13 (1), pp.183-190.

Taniguchi, N. (1992). Future trends of nanotechnology. *International Journal of the Japan Society for Precision Engineering*, 27, pp. 1-7.

Tamaki, J. and Kitagawa, T. (1995). Evaluation of surface topography of metal bonded diamond wheel utilizing three-dimensional profilometry. *International Journal of Machine Tools and Manufacture*, 35 (10), pp. 1339-1351.

Tawfik, M. (1997). Prediction of surface quality through cutting conditions in the grinding process. In: Strafford, K.N. and Subramanian, C. ed. *Quality Control and Assurance in Advanced Surface Engineering*. London, Institute of Materials, pp. 127-140.

Taylor, A.E. and Mann, W.R. (1972). *Advanced Calculus.* New York, John Wiley & Sons. ISBN 0471005878.

Tichy, J. and DeVries, W. (1989). A model for cylindrical grinding based on abrasive wear theory. In: Malkin, S. and Kovach, J.A. ed. *Grinding Fundamental and Applications*, PED-39. New York, ASME, pp. 335-347.

Tonshoff, H.K, Peters, J., Inasaki, I., and Paul, I. (1992). Modelling and simulation of grinding processes. *Annals of CIRP*, 41 (2), pp. 677-688.

Tonshoff, H.K., Karpuschewski, B., Andrae, P., and Turich, A. (1998). Grinding performance of superhard abrasive wheels- final report concerning CIRP co-operative work in STC "G", *Annals of CIRP,* 47 (2), pp. 723-732.

Torrance, A.A. and Brenner, N. (1994). A slip-line field model of the mechanics of grinding. In: Cosmacini, E. ed. *Proceedings of the Eurometalworking 94 Conference*, Udine, 28-30 September. Udine, University of Udine, pp. 076.1-7.

Vanmarcke, E., (1984). *Random Fields*. Cambridge, MIT Press. ISBN 0262220261.

Verkerk, J. (1977). Final report concerning CIRP cooperative work on the characterization of grinding wheel topography. *Annals of CIRP*, 26 (2), pp. 385-395.

Wang, Y. and Moon, K.S. (1997). A methodology for the multi-resolution simulation of grinding wheel surface. *Wear*, 211 (2), pp. 218-225.

Warnecke, G. and Zitt, U. (1998). Kinematic simulation for analyzing and predicting high-performance grinding processes. *Annals of CIRP*, 47 (1), pp. 265-270.

Warnecke, G., and Barth, C. (1999). Optimization of the dynamic behavior of grinding wheels for grinding of hard and brittle materials using the finite element methods. *Annals of CIRP,* 48 (1), pp. 261-264.

Weinert K. and Schneider, M. (2000). Simulation of too-grinding with finite element method. *Annals of CIRP*, 49 (1), pp. 253-256.

Westkamper, E. and Tonshoff, H.K. (1993). CBN or CD grinding of profiles, *Annals of CIRP,* 42 (1), pp. 371-374.

Whitehouse, D.J. and Archard, J.F. (1970). The properties of random surfaces of significance in their contact. *Proceedings of the Royal Society of London, Series A*, 316 (1524), pp. 97-121.

Williams, J.A., and Xie, Y. (1992a). The generation of wear surfaces. *Journal of Physics, D: Applied Physics,* 25, A158-A164.

Williams, J.A., and Xie, Y. (1992b). The generation of wear surfaces by the interaction of parallel grooves. *Wear*, 155, pp.363-379

Woodbury, R.S. (1972). *History of the Grinding Machine.* Cambridge, MIT Press. ISBN 02627300332.

Xie, Y. and Williams, J.A. (1996). The prediction of friction and wear when a soft surface slides against a harder rough surface, *Wear*, 196 (1), pp. 21-34.

Yamazaki, F. and Shinozuka, M. (1988). Digital generation of non-Gaussian stochastic fields. *Journal of Engineering Mechanics*, 114 (7), pp. 1183-1197.

Yim, D.Y. and Kim, S. W. (1991). Optimum sampling interval for Ra roughness measurement. *Proceedings of Institution of Mechanical Engineers*, 205 (2), pp. 139-142.

Zhou, X. and Xi, F. (2002). Modelling and predicting surface roughness of the grinding process. *International Journal of Machine Tools & Manufacture*, 42 (8), pp. 967-977.

Appendix A

Three-dimensional surface parameters

Root mean square S_q

This is a statistical amplitude parameter defined as the root-mean-square value of surface deviation from the reference datum within the sampling area. The 2-D equivalent is a widely-known parameter and acts as an indication of the scale of surface roughness in a well defined statistical form.

$$S_q = \sqrt{\frac{1}{MN}\sum_{j=1}^{N}\sum_{i=1}^{M}\left|\eta^2\left(x_i, y_j\right)\right|} \tag{A.1}$$

where M and N are the number of data points in x and y direction; $\eta(x, y)$ is the surface height from the reference plane.

Ten point height of the surface S_z

This is an extreme parameter defined as the average value of the absolute heights of the five highest summits and the depths of the five deepest pits or valleys within the sampling area. To avoid parameter ambiguity whenever the parameter is calculated the definition of the summit must be clearly specified. The ten point height parameter may be usefully employed in situations when spurious and unrepresentative peaks or valleys may be experienced.

$$S_z = \frac{\sum_{j=1}^{5}\left|\eta_{pi}\right| + \sum_{i=1}^{5}\left|\eta_{vi}\right|}{5} \tag{A.2}$$

Total height of the surface S_t

This is the height between the highest summit and the deepest valley. S_t, S_p, and S_v are not defined in the Birmingham set. It is very sensitive to sampling location, and can be useful in cases such as comparing the surface and it replica. It equals the sum of S_p and S_v.

$$S_t = \left|\max\{\eta(x,y)\}\right| + \left|\min\{\eta(x,y)\}\right| \tag{A.3}$$

Highest peak of the surface S_p

This is the height between the highest summit and the mean plane.

$$S_p = \left|\max\{\eta(x,y)\}\right| \tag{A.4}$$

Deepest valley of the surface S_v

This is the depth between the mean plane and the deepest valley.

$$S_v = \left|\min\{\eta(x,y)\}\right| \tag{A.5}$$

Skewness of topography height distribution S_{sk}

This is the measure of asymmetry of surface deviations about the mean plane. A negative S_{sk} indicates that the surface is composed with principally one plateau and deep fine valleys. A positive S_{sk} indicates a surface with lots of summits.

$$S_{sk} = \frac{1}{MNS_q^3}\sum_{j=1}^{N}\sum_{i=1}^{M}\eta^3(x_i, y_j) \tag{A.6}$$

Kurtosis of topography height distribution S_{ku}

This parameter characterises the spread of the height distribution. A centrally distributed surface has a kurtosis value larger than three whereas the kurtosis of a well spread distribution is smaller than three. By a combination of the skewness and the kurtosis, it may be possible to identify surfaces that have a relatively flat top and deep valleys.

$$S_{ku} = \frac{1}{MNS_q^4} \sum_{j=1}^{N} \sum_{i=1}^{M} \eta^4(x_i, y_j) \tag{A.7}$$

Density of summits of the surface S_{ds}

This is the number of summits of a unit sampling area, which relies on the summit definition.

$$S_{ds} = \frac{number\ of\ summits}{(M-1)(N-1)\Delta x \Delta y} \tag{A.8}$$

Texture aspect ratio of the surface S_{tr}

This is a parameter used to identify topographic texture pattern. It is defined as the ratio of the fastest to slowest decay to correlation length of the areal autocorrelation function (AACF). In principle the texture aspect ratio would be in the range of 0 to 1. Larger value (S_{tr} >0.5) indicates stronger uniform texture aspect in different directions, whereas smaller values (S_{tr} <0.3) indicates stronger anisotropy.

$$S_{tr} = \frac{the\ distance\ that\ the\ normalised\ AACF\ has\ the\ fastest\ decay\ to\ 0.2}{the\ distance\ that\ the\ normalised\ AACF\ has\ the\ slowest\ decay\ to\ 0.2} \tag{A.9}$$

Fastest decay autocorrelation length S_{al}

This parameter characterises the autocorrelation function (AACF) of the surface. It is defined as the horizontal distance of the AACF which has the fastest decay to 0.2. A large value of S_{al} denotes that the surface is dominated by low frequency (or long wavelength) components while a small value of the S_{al} indicates the opposite situation.

$$S_{al} = min\left(\sqrt{\tau_x^2 + \tau_y^2}\right) \quad R(\tau_x, \tau_y) \leq 0.2 \tag{A.10}$$

Texture direction of the surface S_{td}

This is a parameter used to determine the most pronounced direction of the surface texture with respect to the (y-axis) lay direction of the surface. In other words it gives the lay of the surface. This parameter is extracted from the angular power spectral density. The texture direction would be meaningless if the isotropy index, S_{tr}, is larger than, say 0.5.

$$S_{td} = \begin{cases} -\beta, & \beta \leq \dfrac{\pi}{2} \\ \pi - \beta, & \dfrac{\pi}{2} < \beta \leq \pi \end{cases} \tag{A.11}$$

where β is the position where the maximum value of the angular spectrum appears.

Root-mean-square slope of the surface $S_{\Delta q}$

This is the root mean square of the surface slope within the sampling area. This parameter has some relevance to the reflectivity of surfaces which is particularly important to optical mirror.

$$S_{\Delta q} = \sqrt{\frac{1}{(M-1)(N-1)}\sum_{j=2}^{N}\sum_{i=2}^{M}\left[\left(\frac{\eta(x_i,y_j)-\eta(x_{i-1},y_j)}{\Delta x}\right)^2+\left(\frac{\eta(x_i,y_j)-\eta(x_i,y_{j-1})}{\Delta y}\right)^2\right]} \quad \text{(A.12)}$$

Arithmetic mean summit curvature of the surface S_{sc}

This is defined as the average of the principal curvatures of the summits within the sampling area. This parameter is dependent on the definition of summit. The parameter is sensitive to the sampling interval and has relevance to electrical contacts, welded surfaces, as well as any contacts placed under compression.

$$S_{sc} = -\frac{1}{2n}\sum_{k=1}^{n}\left(\frac{\partial\eta^2(x,y)}{\partial x^2}+\frac{\partial\eta^2(x,y)}{\partial y^2}\right)_{\textit{for any summit}} \quad \text{(A.13)}$$

Developed interfacial area ratio S_{dr}

This is the ratio of the increment of the interfacial area of a surface over the sampling area. A large value of the parameter indicates the significance of either the amplitude or the spacing or both. This parameter is useful in situations where two surfaces are to be brought into contact and can be used to assist with understanding deformability of materials.

$$S_{dr} = \frac{\sum_{j=1}^{N-1}\sum_{i=1}^{M-1}A_{ij}-(M-1)(N-1)\Delta x\Delta y}{(M-1)(N-1)\Delta x\Delta y}100\% \quad \text{(A.14)}$$

where A_{ij} is the interfacial area of the sampling quadrilateral, estimated as follows

$$\begin{aligned} A_{ij} &= \frac{1}{4}\left\{\left[\Delta y^2+\left(\eta(x_i,y_j)-\eta(x_i,y_{j+1})\right)^2\right]^{1/2}+\left[\Delta y^2+\left(\eta(x_{i+1},y_{j+1})-\eta(x_{i+1},y_j)\right)^2\right]^{1/2}\right) \\ &= \left(\left[\Delta x^2+\left(\eta(x_i,y_j)-\eta(x_{i+1},y_j)\right)^2\right]^{1/2}+\left[\Delta x^2+\left(\eta(x_i,y_{j+1})-\eta(x_{i+1},y_{j+1})\right)^2\right]^{1/2}\right\} \end{aligned} \quad \text{(A.15)}$$

Surface bearing index S_{bi}

This is the ratio of the RMS deviation over the surface height at 5% bearing area. A larger surface bearing index indicates a good bearing property. This parameter is a development of a similar two-dimensional surface finish parameter which is often used by the motor industry to assess bearing and cylinder bore components (DIN4776).

$$S_{bi} = \frac{S_q}{h_{0.05}} \tag{A.16}$$

where $h_{0.05}$ is the surface height at 5% bearing area.

Core fluid retention index S_c

This is the ratio of the void volume of the unit sampling area at the core zone (5% ~ 80% bearing area) over the RMS deviation. A larger S_{ci} indicates a good fluid retention in the core zone.

$$S_{ci} = \frac{V_v(h_{0.05}) - V_v(h_{0.8})}{S_q(M-1)(N-1)\Delta x \Delta y} \tag{A.17}$$

where $V_v(.)$ is the void volume at the specified surface height.

Valley fluid retention index S_{vi}

This is the ratio of the void volume of the unit sampling area at the valley zone (80% ~ 100%) over the RMS deviation. A larger S_{vi} indicates a good fluid retention in the valley zone.

$$S_{ci} = \frac{V_v(h_{0.8})}{S_q(M-1)(N-1)\Delta x \Delta y} \tag{A.18}$$

Following is the listing of MATLAB scripts used for estimating the 3-D parameters.

```
-------------------------------------------------------------------
  function f=sq(z)
  % F=SQ(Z) estimates root-mean-square deviation Sq
  % Z: residual surface

  [n,m]=size(z);
  f=z.^2;
  f=sum(sum(f))/(n*m);
  f=sqrt(f);

-------------------------------------------------------------------
  function f=sz(p,v)
  % F=SZ(Z) estimates ten point height Sz
  % P: array of summits in the surface
  % V: array of valleys in the surface

  pi=p(end-4:end,3); vi=v(1:5,3);
  f=(sum(abs(pi))+sum(abs(vi)))/5;

-------------------------------------------------------------------
  function f=st(p,v)
  % F=ST(P,V) estimates total height St
  % P: array of summits in the surface
  % V: array of valleys in the surface

  pi=p(end,3); vi=v(1,3);
  f=abs(pi-vi);

-------------------------------------------------------------------
  function f=sp(p)
  % F=SP(Z) gives the highest summit Sp
  % P: array of summits in a surface

  f=abs(p(end,3));

-------------------------------------------------------------------
  function f=sv(v)
  % F=SV(Z) gives the deepest valley Sv
  % V: array of valleys in the surface

  f=abs(v(1,3));

-------------------------------------------------------------------
  function f=ssk(z)
  % F=SSK(Z) estimates skewness of topography height distribution Ssk
  % z: residual surface
  % Ssk <-1: a surface has a few significant outlier (pits, troughs)
  % Ssk >1 : a surface has a few spikes

  [n,m]=size(z);
  f=z;
  f=f.^3;
  f=sum(sum(f));
  f1=sq(z);
```

```
  f=f/(m*n*f1^3);

-------------------------------------------------------------------
  function f=sku(z)
  % F=SKU(Z) estimates Kurtosis of topography height distribution Sku
  % Z: residual surface

  [n,m]=size(z);
  f=z;
  f=f.^4;
  f=sum(sum(f));
  f1=sq(z);
  f=f/(m*n*f1^4);

-------------------------------------------------------------------
  function f=sds(p,r,c,stepx,stepy)
  % F=SDS(P,R,C,STEPX,STEPY) estimates density of summit Sds
  % P: summit array of the surface
  % R,C: the number of data points in rows and column (in points)
  % STEPX, STEPY: the spacing in x and y directions
  % F has unit as 1/(STEPX*STEPY)

  nos=size(p,1);
  f=nos/((r-1)*(c-1)*stepx*stepy);

-------------------------------------------------------------------
  function [fd,sd]=sal(acf, stepx, stepy)
  % [FD,SD]=SAL(ACF, STEPX, STEPY) finds
  % the fastest decay autocorrelation length Sal (FD)
  % and texture aspect Str (SD)
  % ACF: normalized autocorrelation function (estimated by pafm)
  % STEPX, STEPY: step in x,y direction
  % FD will have the same dimension unit as STEPX, STEPY

  [ra,ca]=size(acf);
  rc=floor(ra/2)+1; cc=floor(ca/2)+1; % R(0)
  % fastest decay autocorrelation less than 0.2

  [xy(:,1),xy(:,2)]=find(abs(acf)<0.2);
  [rxy,cxy]=size(xy);
  for r=1:rxy
      xy(r,3)=((rc-xy(r,1))*stepx)^2+((cc-xy(r,2))*stepy)^2;
      xy(r,3)=sqrt(xy(r,3));
  end
  xy=sortrows(xy,3);
  fd=xy(1,3);
  % slowest decay autocorrelation less than 0.2
  xy=[];
  [xy(:,1),xy(:,2)]=find(acf>=0.2);
  [rxy,cxy]=size(xy);
  for r=1:rxy
      xy(r,3)=((abs(rc-xy(r,1)))*stepx)^2+((abs(cc-xy(r,2)))*stepy)^2;
      xy(r,3)=sqrt(xy(r,3));
  end
  xy=sortrows(xy,3);
  sd=sqrt(((abs(rc-xy(r,1))+1)*stepx)^2+((abs(cc-y(r,2))+1)*stepy)^2);
  sd =fd/sd;

 -------------------------------------------------------------------
```

```
function f=stx(psden,inta,stepx,stepy)
% F=STX(PSDEN,STEPX,STEPY) estimates texture direction Std
% PSD: power spectral density (estimated by pafm)
% INTA: number of datapoints between 0-180 degree
% STEPX, STEPY: step in x and y directions
% F: angular in degree

a=apsd(psden,inta,stepx,stepy);
amax=max(a(1:end-1,2));
apos=find(a(1:end-1,2)==amax);
amax=a(apos,1)*180/pi;
if amax<90
    f=-amax;
else
    f=180-amax;
end
```

```
function f=sdeltaq(z,stepx,stepy)
% F=SDELTAQ(Z,STEPX,STEPY) estimates
% root-mean-square slope of surface Sdeltaq
% Z: residual surface
% STEPX, STEPY: step in x,y direction
% Z, STEPX, STEPY should have the same unit.

[n,m]=size(z);
stepx=stepx*1000; stepy=stepy*1000;
f=0;
for r=2:n
    for c=2:m
        f=f+((z(r,c)-z(r,c-1))/stepx)^2;
        f=f+((z(r,c)-z(r-1,c))/stepy)^2;
    end
end
f=f/((n-1)*(m-1));
f=sqrt(f);
```

```
function f=ssc(z,summit,stepx,stepy)
% F=SSC(Z) estimates arithmetic mean summit curvature Ssc
% Z: residual surface
% SUMMIT: array of summits
% STEPX, STEPY: step in x and y directions
% a summit is defined using 8 neighbor points
% Z, STEPX, STEPY should have the same unit.
% unit of f as 1/stepx

[rz,cz]=size(z);
m=size(summit,1);
f=0;
count=0;
for r=1:m
    rp=summit(r,1); cq=summit(r,2);
    if (rp>1)&(rp<rz)&(cq>1)&(cq<cz)
        count=count+1;
        f1=(z(rp+1,cq)+z(rp-1,cq)-2*z(rp,cq))/(stepy^2);
        f2=(z(rp,cq+1)+z(rp,cq-1)-2*z(rp,cq))/(stepx^2);
        f=f+f1+f2;
    end
end
```

```
f=-f/(2*count);
function f=sdr(z,stepx,stepy)
% F=SDR(Z,STEPX,STEPY) estimates developed interfaced area ratio Sdr
% Z: residual surface
% STEPX, STEPY: step in x,y directions
% a large value of Sdr indicates the significance of
% either amplitude or % spacing or both.
% Z, STEPX, STEPY should have the same unit

[n,m]=size(z);
a=0;
for r=1:(n-1)
    for c=1:(m-1)
        a1=sqrt(stepy^2+(z(r,c)-z(r+1,c))^2);
        a1=a1+ sqrt(stepy^2+(z(r+1,c+1)-z(r,c+1))^2);
        a2=sqrt(stepx^2+(z(r,c)-z(r,c+1))^2);
        a2=a2+ sqrt(stepx^2+(z(r+1,c)-z(r+1,c+1))^2);
        a=a+ (a1*a2)/4;
    end
end
f=(a-(m-1)*(n-1)*stepx*stepy)/((m-1)*(n-1)*stepx*stepy);
f=f*100;
```

```
function f=sbi(bc)
% F=SBI(BC) estimates surface bearing index of surface
% BC: bearing curve etsimated by stp

a=bc(1:end-1,3)-bc(2:end,3);
bc(find(a==0),:)=[];
f=interp1(bc(:,3),bc(:,1),5);
f=1/f;
```

```
function f=sci(bc,m,n,delx,dely,s)
% F=SCI(BC,M,N,STEPX,STEPY,S) estimates
% core fluid retention index Sci
% BC: bearing curve estimated by stp
% M,N: sample points in x,y direction
% STEPX, STEPY: sampling steps in x,y direction
% S: Sq of the surface

a=bc(1:end-1,3)-bc(2:end,3);
bc(find(a==0),:)=[];
h5=interp1(bc(:,3),bc(:,1),5);
h80=interp1(bc(:,3),bc(:,1),80);
void5=voidvolume(h5,bc);
void80=voidvolume(h80,bc);
f=(void5-void80)/(s*(m-1)*(n-1)*delx*dely);
```

```
function f=svi(bc,m,n,delx,dely,s)
% F=SVI(BC,M,N,STEPX,STEPY,S) estimates
% valley fluid retention index Sci
% BC: bearing curve (estimated by stp)
% M,N: sample points in x and y directions
% STEPX, STEPY: step in x,y direction
% S: Sq of surface

a=bc(1:end-1,3)-bc(2:end,3);
bc(find(a==0),:)=[];
```

```
h80=interp1(bc(:,3),bc(:,1),80);
void80=voidvolume(h80,bc);
f=void80/(s*(m-1)*(n-1)*delx*dely);
```

```
function [psd, acf]=pafm(source)
% [PSD,ACF]=PAFM(SOURCE) estimates autocorrelation function
% and power spectral density of surface.
% Estimation is based on Fourier transform
% SOURCE: surface
% PSD: power spectral density (normalized so that sum(sum(psd))=sq)
% ACF= autocorrelation function acf (as Numerical recipe)

[rs,cs]=size(source);
rb=floor(rs/2); cb=floor(cs/2);
s=source;
s(rs*2,cs*2)=0;
% psd
psd=fft2(source);
psd=abs(psd).^2;
psd=fftshift(psd);
psd=psd./(rs*cs)^2;
% acf
acf=fft2(s);
acf=abs(acf).^2;
acf=ifft2(acf);
acf=real(acf);
acf=fftshift(acf);
acf=acf./acf(rs+1,cs+1);
acf=acf((rs+1-rb):(rs+1+rb),(cs+1-cb):(cs+1+cb));
```

Appendix B

Technical specifications of the equipments used in the study

B.1 Stylus system Talyscan 150

Talyscan 150 (Taylor Hobson Ltd.) is a three-dimensional contact and non-contact scanning instrument. It is a dedicated surface topography system. The non-contact probe uses laser triangulation technology with a gauge range of 10 mm. The contact probe is an inductive gauge with 2.5 mm range (Figure B.1).

Figure B.1 Talyscan 150

The system can be specified with contact, non-contact or both gauges. Single or multiple measurements can be taken with a scanning range from a minimum of 50x 0 μm to a maximum of 97x97 mm. A maximum scanning speed is 10 mm/s. The system is supplied with the metrology software Talymap. The specification of the system is summarised in Table B.1 .

Table B.1 Technical specification of Talyscan 150

Scanning range	maximum, mm	97x97
	minimum, μm	50x50
Minimum spacing	x direction, μm	0.5
	y direction, μm	5
Vertical range	inductive gauge, mm	2.5
	laser gauge, mm	10
Vertical resolution	inductive gauge, μm	0.06
	laser gauge, μm	1
Maximum scanning speed, mm/s		10
Maximum sample load, kg		5
Stylus radius, μm		5

B.2 Grinding machine Okamoto 63DXNC

Okamoto 63DXNC is a precision surface grinding machine (Figure B.2).

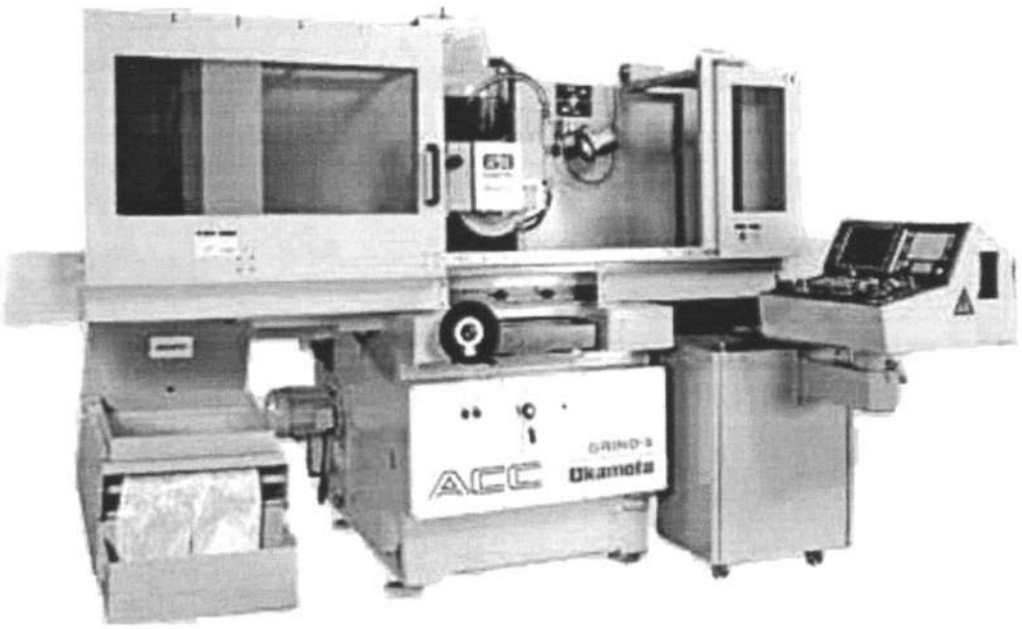

Figure B.2 Okamoto 63DXNC

The machine is fully CNC operated with simple conversational input. The high accuracy of the machine is ensured by precision ball screw and thermal control mechanism. The machine is equipped with a high-speed and high-power spindle for high-speed grinding. The specification of the machine is given in Table B.2.

Table B.2 Technical specification of Okamoto 63DXNC

Capacity	Table work area (length x width), mm	605x300
	Table travel distance, mm	750x340
	Standard chuck size, mm	600x300x80
	Maximum workpiece weight, kg	420
Feedrate	Longitudinal feedrate, mm/min	0.3-25
	Crosswise feedrate, mm/min	1-790
	Vertical feedrate, mm/min	1-790
	Minimum vertical increment, mm	0.0001
Grinding wheel	O.D.x width x I.D., mm	355x38x127
	Wheel speed, rpm	0-10000
Power	Wheel spindle drive motor, kW	4
	Vertical feed motor, kW	0.9
	Crosswise feed motor, kW	0.55
	Hydraulic pump motor, kW	1.5
Space and weight	Width x length x height, m	2.7x2x.2.4
	Machine weight, kg	2800

B.3 Grinding machine Okamoto 63DXV

Figure B.3 shows an Okamoto 63DXV used in this study.

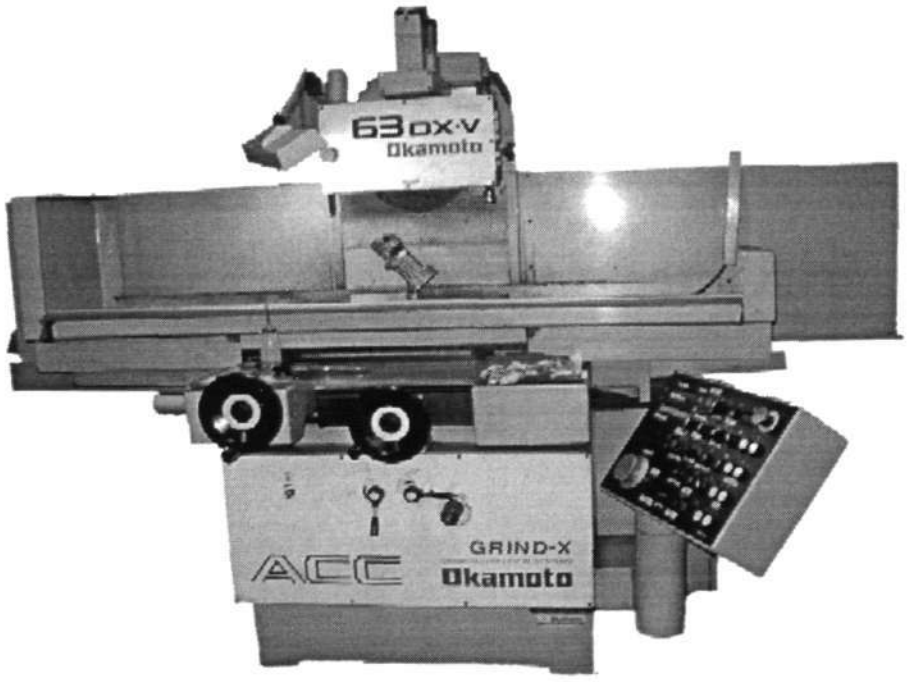

Figure B.3 Okamoto 63DXV

Okamoto 63DXV is a fully automatic surface grinding machine. Despite the lack of CNC feature, its electronic control allows a simplified set up and operator convenience with rough grinding, finish grind and spark out in one set-up. The specification of the machine is given in Table B.3.

Table B.3 Technical specification of Okamoto 63DXV

Capacity	Table work area (length x width), mm	605x300
	Table travel distance, mm	750x340
	Standard chuck size, mm	600x300x80
	Maximum workpiece weight, kg	420
Feedrate	Longitudinal feedrate, m/min	0.3-25
	Continuous crossfeed, mm/min	0.1-1
	Intermittent crossfeed, mm	0.2-20
	Automatic downfeed, mm/min	0.0001-0.03
	Minimum vertical increment, mm	0.0001
Grinding wheel	O.D.x width x I.D., mm	355x38x127
	Wheel speed, rpm	1500
Power	Wheel spindle drive motor, kW	3.7
	Vertical feed motor, kW	0.4
	Hydraulic pump motor, kW	1.5
Space and weight	Width x length x height, m	2.7x1.9x.1.7
	Machine weight, kg	2500

Appendix C

Technical specifications of imprint materials

Table C.1 Technical specification of ExamixTM NDS (hydrophilic vinyl polysiloxane impression material)

Total working time, min.	2
Setting time, min.	4
Recovery from deformation, %	99.7
Maximum strain in compression, %	≤ 7
Linear dimensional change after 24 hrs, %	≤ 2

Table C.2 Technical specification of TechnovitTM 3040 (methyl methacrylate-based resin)

Processing time, min.	2
Curing time, min.	5
Peak temperature during curing, °C	110
Heat resistance, °C	100
Solubility	Soluble in chlorinated hydrocarbons

Appendix D

Three-dimensional surface characterisation parameters of grinding wheel samples and their replicas

Table D.1 3-D surface characterisation parameters of A80KV grinding wheel samples and their replicas

Parameter	Sample				Replica			
	A	B	C	D	A	B	C	D
S_q, μm	32.60	28.16	42.65	37.58	36.12	29.74	44.42	39.11
S_z, μm	206.84	199.25	252.32	227.09	226.58	209.05	281.20	232.96
S_{sk}	-1.19	-1.25	-0.73	-0.64	-1.19	-1.39	-0.71	-0.70
S_{ku}	4.90	5.81	3.46	3.53	5.01	6.07	3.65	3.70
S_{ds}, mm^{-2}	51.00	51.44	42.56	44.56	46.56	49.00	43.44	46.22
S_{al}, mm	0.24	0.21	0.25	0.28	0.26	0.24	0.24	0.29
S_{tr}	0.78	0.65	0.76	0.84	0.79	0.71	0.70	0.88
S_{td}, °	0.00	0.00	89.50	89.50	89.50	0.00	89.50	89.50
$S_{\Delta q}$	0.57	0.52	0.63	0.58	0.58	0.48	0.65	0.56
S_{sc}, μm^{-1}	0.018	0.017	0.024	0.020	0.016	0.014	0.020	0.017
S_{dr}, %	14.50	12.30	17.79	15.47	15.24	10.89	19.20	14.32
S_{bi}	0.75	0.72	0.71	0.67	0.75	0.79	0.68	0.68
S_{ci}	1.31	1.42	1.43	1.51	1.33	1.27	1.51	1.48
S_{vi}	0.21	0.21	0.19	0.18	0.21	0.23	0.19	0.18
S_t, μm	216.27	229.10	278.45	244.21	243.60	221.82	320.57	246.80
S_p, μm	62.11	61.10	97.64	80.57	73.23	64.08	92.96	81.47
S_v, μm	154.16	168.01	180.82	163.64	170.36	157.74	227.61	165.34

Table D.2 3-D surface characterisation parameters of C120J8V grinding wheel samples and their replicas

Parameter	Sample				Replica			
	A	B	C	D	A	B	C	D
S_q, μm	10.66	8.24	13.82	9.53	11.79	9.07	15.82	11.16
S_z, μm	96.97	65.58	113.97	69.72	103.92	70.35	125.10	77.16
S_{sk}	-2.46	-1.77	-2.71	-1.45	-2.35	-1.58	-2.33	-1.42
S_{ku}	12.75	7.45	12.09	5.44	11.69	6.34	10.58	5.17
S_{ds}, mm^{-2}	91.89	122.11	90.56	111.00	87.89	86.33	81.33	79.78
S_{al}, mm	0.18	0.13	0.21	0.13	0.20	0.15	0.23	0.16
S_{tr}	0.86	0.81	0.17	0.65	0.84	0.85	0.20	0.65
S_{td}, °	-63.35	-45.25	0.00	89.50	-63.35	-45.25	0.00	89.50
$S_{\Delta q}$	0.25	0.23	0.26	0.25	0.24	0.22	0.27	0.25
S_{sc}, μm^{-1}	0.016	0.012	0.016	0.014	0.012	0.010	0.013	0.009
S_{dr}, %	3.02	2.56	3.34	3.16	2.72	2.38	3.44	3.01
S_{bi}	0.86	0.80	0.86	0.82	0.90	0.90	0.95	0.93
S_{ci}	1.18	1.30	1.17	1.23	1.12	1.13	1.05	1.07
S_{vi}	0.27	0.26	0.29	0.24	0.26	0.23	0.26	0.23
S_t, μm	101.44	88.21	136.99	81.19	108.78	73.27	134.29	81.11
S_p, μm	19.88	17.22	20.25	18.30	20.66	15.04	24.54	17.36
S_v, μm	81.57	70.99	116.75	62.89	88.12	58.23	109.75	63.75

Table D.3 3-D surface characterisation parameters of B120H200V grinding wheel samples and their replicas

Parameter	Sample				Replica			
	A	B	C	D	A	B	C	D
S_q, µm	24.00	20.51	14.70	11.57	26.47	23.61	15.05	12.05
S_z, µm	137.15	142.69	93.28	89.65	152.36	157.71	101.24	92.33
S_{sk}	-1.16	-0.76	-1.76	-1.75	-1.20	-0.74	-1.88	-1.95
S_{ku}	4.51	4.05	6.31	7.39	4.69	3.92	7.37	8.93
S_{ds}, mm^{-2}	230.00	253.25	292.25	234.25	172.50	163.50	246.50	224.75
S_{al}, mm	0.25	0.18	0.17	0.14	0.26	0.18	0.19	0.16
S_{tr}	0.65	0.16	0.74	0.65	0.64	0.16	0.71	0.48
S_{td}, °	0.00	0.00	-45.25	-45.25	0.00	89.50	-45.25	-45.25
$S_{\Delta q}$	0.45	0.41	0.35	0.30	0.43	0.49	0.33	0.29
S_{sc}, μm^{-1}	0.037	0.036	0.029	0.029	0.029	0.034	0.024	0.023
S_{dr}, %	9.00	7.91	5.70	4.44	8.49	10.27	5.26	4.13
S_{bi}	0.77	0.68	0.96	0.82	0.77	0.68	0.99	0.81
S_{ci}	1.26	1.47	0.97	1.22	1.27	1.50	0.98	1.25
S_{vi}	0.21	0.22	0.26	0.25	0.22	0.21	0.25	0.25
S_t, µm	140.70	147.98	98.60	96.95	164.71	171.49	105.35	102.96
S_p, µm	43.93	60.59	22.57	22.46	51.48	64.83	22.16	24.90
S_v, µm	96.77	87.39	76.04	74.49	113.24	106.66	83.18	78.06

Appendix E

Three-dimensional surface characterisation parameters of grinding wheel samples at various stylus speeds

Table E.1 3-D surface characterisation parameters of A80KV grinding wheel samples at various stylus speeds (mm/s)

Parameter	Sample A				Sample B				Sample C				Sample D			
	0.3	0.5	0.75	1	0.3	0.5	0.75	1	0.3	0.5	0.75	1	0.3	0.5	0.75	1
S_q, μm	50.13	49.72	49.12	49.14	38.85	38.95	39.06	38.95	32.62	32.93	32.48	32.24	30.03	30.84	31.42	31.44
S_z, μm	295.59	272.87	281.64	292.15	233.20	232.21	228.30	236.59	197.24	201.68	197.60	194.69	220.93	222.90	224.59	223.34
S_{sk}	-0.99	-1.01	-1.01	-1.01	-0.90	-0.91	-0.91	-0.86	-1.20	-1.21	-1.20	-1.20	-1.46	-1.56	-1.58	-1.57
S_{ku}	3.99	3.98	4.00	4.19	4.08	4.06	4.03	3.91	4.69	4.72	4.67	4.69	6.35	6.67	6.73	6.63
S_{ds}, mm^{-2}	37.44	43.00	45.44	35.78	42.67	41.56	45.00	41.44	40.56	39.22	42.22	38.67	42.89	40.89	44.00	39.22
S_{al}, mm	0.32	0.32	0.32	0.30	0.27	0.29	0.29	0.27	0.24	0.24	0.24	0.24	0.24	0.24	0.25	0.25
S_{tr}	0.67	0.73	0.73	0.72	0.84	0.86	0.86	0.84	0.75	0.75	0.76	0.75	0.79	0.79	0.82	0.81
S_{td}, °	0.00	0.00	0.00	0.00	89.50	89.50	89.50	89.50	89.50	89.50	89.50	89.50	0.00	0.00	0.00	0.00
$S_{\Delta q}$	0.60	0.60	0.62	0.60	0.56	0.55	0.56	0.55	0.49	0.49	0.50	0.48	0.48	0.46	0.47	0.46
S_{sc}, μm^{-1}	0.017	0.017	0.021	0.015	0.022	0.018	0.018	0.017	0.012	0.012	0.015	0.012	0.015	0.013	0.013	0.012
S_{dr}, %	16.46	16.23	17.14	16.65	14.42	13.82	14.37	13.94	11.32	11.50	11.96	10.97	10.53	9.91	10.35	9.80
S_{bi}	0.76	0.77	0.78	0.76	0.72	0.73	0.73	0.72	0.81	0.81	0.81	0.81	0.82	0.84	0.84	0.83
S_{ci}	1.27	1.25	1.24	1.29	1.36	1.35	1.35	1.37	1.18	1.19	1.19	1.19	1.21	1.17	1.17	1.17
S_{vi}	0.21	0.21	0.21	0.21	0.19	0.19	0.19	0.19	0.22	0.21	0.21	0.21	0.22	0.22	0.22	0.23
S_t, μm	325.45	315.66	311.94	330.43	251.75	251.58	249.79	253.83	209.76	217.86	211.44	209.03	230.02	236.41	237.18	235.31
S_p, μm	101.96	98.71	96.24	101.68	83.94	83.70	83.76	83.20	55.82	58.69	56.77	55.78	63.22	63.38	64.71	64.79
S_v, μm	223.49	216.95	215.69	228.75	167.81	167.88	166.02	170.63	153.94	159.18	154.67	153.25	166.80	173.03	172.48	170.52

Table E.2 3-D surface characterisation parameters of B120H200V grinding wheel samples at various stylus speeds (mm/s)

Parameter	Sample A				Sample B				Sample C				Sample D			
	0.3	0.5	0.75	1	0.3	0.5	0.75	1	0.3	0.5	0.75	1	0.3	0.5	0.75	1
S_q, μm	14.71	14.54	14.49	14.33	15.71	15.83	15.86	15.84	13.95	14.19	14.20	14.13	16.46	16.44	16.36	16.27
S_z, μm	86.41	84.79	86.11	84.15	110.39	109.25	112.46	111.53	97.67	98.60	93.33	91.95	92.19	88.47	88.84	87.59
S_{sk}	-1.20	-1.23	-1.25	-1.26	-1.43	-1.46	-1.46	-1.46	-1.56	-1.67	-1.70	-1.68	-1.28	-1.29	-1.31	-1.32
S_{ku}	4.28	4.37	4.41	4.43	5.92	5.97	5.95	6.00	6.68	7.15	7.33	7.40	4.11	4.15	4.21	4.23
S_{ds}, mm^{-2}	189.50	197.75	247.25	185.00	194.00	185.00	217.75	219.75	188.75	184.50	222.75	175.50	216.00	213.00	253.50	207.75
S_{al}, mm	0.14	0.15	0.14	0.15	0.18	0.18	0.18	0.18	0.16	0.16	0.16	0.17	0.15	0.16	0.15	0.16
S_{tr}	0.54	0.55	0.54	0.55	0.87	0.84	0.84	0.84	0.77	0.74	0.73	0.74	0.67	0.70	0.68	0.68
S_{td}, °	89.50	89.50	89.50	89.50	89.50	89.50	89.50	89.50	0.00	0.00	0.00	0.00	89.50	89.50	89.50	89.50
$S_{\Delta q}$	0.38	0.37	0.39	0.36	0.41	0.40	0.42	0.42	0.40	0.38	0.39	0.36	0.40	0.40	0.42	0.39
S_{sc}, μm^{-1}	0.019	0.019	0.028	0.023	0.032	0.030	0.035	0.036	0.031	0.031	0.036	0.027	0.021	0.020	0.021	0.018
S_{dr}, %	6.93	6.63	7.33	6.36	7.76	7.56	8.38	8.27	7.20	6.83	7.32	6.24	7.69	7.60	8.17	7.32
S_{bi}	0.85	0.83	0.85	0.86	0.80	0.80	0.80	0.81	0.81	0.81	0.85	0.86	0.92	0.91	0.97	0.92
S_{ci}	1.16	1.17	1.16	1.14	1.30	1.27	1.27	1.27	1.25	1.24	1.19	1.19	1.05	1.04	0.99	1.03
S_{vi}	0.22	0.21	0.22	0.22	0.24	0.24	0.23	0.23	0.23	0.24	0.23	0.23	0.21	0.21	0.21	0.21
S_t, μm	92.22	90.28	91.82	89.48	147.26	135.46	135.35	137.85	115.45	118.09	116.55	115.44	95.74	90.30	91.48	88.63
S_p, μm	23.29	21.55	21.68	21.41	43.22	31.50	32.06	33.31	25.55	26.72	24.90	23.83	25.43	20.75	21.28	19.95
S_v, μm	68.93	68.74	70.14	68.07	104.04	103.96	103.29	104.53	89.90	91.37	91.65	91.61	70.31	69.55	70.21	68.69

Table E.3 3-D surface characterisation parameters of C120J8V grinding wheel samples at various stylus speeds (mm/s)

Parameter	Sample A				Sample B				Sample C				Sample D			
	0.3	0.5	0.75	1	0.3	0.5	0.75	1	0.3	0.5	0.75	1	0.3	0.5	0.75	1
S_q, μm	8.28	8.28	7.60	7.46	8.79	8.60	8.49	8.47	9.43	9.22	8.74	8.76	8.05	8.04	8.09	8.07
S_z, μm	71.67	71.94	70.32	65.18	77.73	72.00	69.3	68.99	76.41	74.2	69.18	69.31	74.83	65.41	65.06	65.72
S_{sk}	-1.74	-1.73	-2.01	-2.09	-1.98	-1.92	-1.84	-1.81	-1.59	-1.51	-1.75	-1.75	-1.72	-1.72	-1.63	-1.62
S_{ku}	9.15	9.11	10.33	10.71	9.1	8.83	8.72	8.60	6.88	6.56	7.35	7.34	8.19	8.25	7.96	8.03
S_{ds}, mm^{-2}	127.00	127.00	128.89	123	123.89	119.11	97.11	98.78	123.22	122.44	119.67	118.11	121.33	122.11	100.78	97.89
S_{al}, mm	0.13	0.13	0.13	0.13	0.13	0.13	0.13	0.14	0.13	0.13	0.13	0.13	0.13	0.13	0.13	0.13
S_{tr}	0.67	0.67	0.64	0.64	0.67	0.67	0.71	0.75	0.54	0.55	0.54	0.54	0.67	0.67	0.69	0.69
S_{td}, °	89.50	89.50	89.50	89.5	45.25	45.25	45.25	45.25	89.5	89.5	89.5	89.5	89.5	89.5	89.5	89.5
$S_{\Delta q}$	0.27	0.27	0.24	0.22	0.27	0.26	0.26	0.25	0.28	0.28	0.26	0.25	0.26	0.26	0.26	0.25
S_{sc}, μm^{-1}	0.019	0.019	0.015	0.015	0.017	0.018	0.017	0.017	0.019	0.02	0.016	0.015	0.017	0.018	0.017	0.017
S_{dr}, %	3.50	3.50	3.40	3.70	3.62	3.39	3.26	3.30	3.94	3.91	3.72	3.66	3.33	3.3	3.25	2.99
S_{bi}	0.72	0.72	0.74	0.71	0.85	0.86	0.79	0.77	0.77	0.76	0.78	0.81	0.74	0.81	0.74	0.73
S_{ci}	1.47	1.47	1.43	1.41	1.23	1.19	1.29	1.33	1.31	1.34	1.3	1.24	1.48	1.33	1.41	1.43
S_{vi}	0.23	0.23	0.24	0.24	0.26	0.26	0.25	0.24	0.25	0.24	0.25	0.25	0.25	0.25	0.26	0.26
S_t, μm	85.75	85.76	80.51	75.13	89.99	80.93	77.1	78.26	80.33	79.22	72.62	74.68	102.04	88.75	86.84	89.64
S_p, μm	19.62	19.63	19.16	13.24	22.24	20.08	16.3	17.12	23.96	25.3	18.69	21.28	25.07	22.64	23.49	21.75
S_v, μm	66.12	66.13	61.35	61.89	67.75	60.84	60.8	61.14	56.38	53.92	53.93	53.4	76.98	73.11	69.35	71.89

Appendix F

Three-dimensional surface characterisation parameters of grinding wheel samples at various sampling intervals

Table F.1 3-D surface characterisation parameters of A46H7V grinding wheel samples at various sampling intervals

	Sampling interval, mm	S_q, μm	S_z, μm	S_{sk}	S_{ku}	S_{ds}, mm^{-2}	S_{al}, mm	S_{tr}	S_{td}, °	$S_{\Delta q}$	S_{sc}, μm^{-1}	S_{dr}, %	S_{bi}	S_{ci}	S_{vi}
Sample A	0.005	83.01	473.34	-0.63	2.72	319.69	0.34	0.84	0.00	2.44	0.773	135.12	0.74	1.36	0.17
	0.010	82.65	465.64	-0.64	2.75	88.13	0.34	0.82	0.00	1.34	0.222	55.58	0.74	1.36	0.17
	0.015	83.05	456.42	-0.63	2.72	57.79	0.34	0.82	0.00	1.20	0.095	50.49	0.76	1.33	0.17
	0.020	82.60	456.37	-0.64	2.76	34.00	0.34	0.80	0.00	1.00	0.052	37.36	0.76	1.32	0.17
	0.030	82.75	445.63	-0.64	2.75	17.71	0.34	0.79	0.00	0.87	0.023	30.73	0.75	1.34	0.17
	0.040	82.57	428.83	-0.64	2.75	10.63	0.34	0.76	0.00	0.81	0.016	27.95	0.75	1.33	0.17
	0.050	82.43	430.21	-0.65	2.75	7.81	0.35	0.77	0.00	0.77	0.009	25.44	0.76	1.32	0.17
	0.060	82.72	416.64	-0.64	2.74	6.31	0.35	0.75	0.00	0.74	0.007	24.29	0.75	1.34	0.17
	0.070	82.38	424.50	-0.64	2.76	5.53	0.35	0.71	0.00	0.71	0.006	22.74	0.76	1.31	0.17
	0.080	82.38	411.30	-0.65	2.76	4.56	0.36	0.70	0.00	0.68	0.004	21.36	0.76	1.32	0.16
	0.100	82.23	386.83	-0.65	2.77	4.06	0.36	0.72	0.00	0.64	0.004	19.26	0.76	1.32	0.16
	0.120	82.54	390.88	-0.64	2.75	3.44	0.38	0.71	0.00	0.61	0.004	17.65	0.75	1.34	0.17
	0.140	82.46	377.57	-0.63	2.77	2.80	0.40	0.67	0.00	0.59	0.003	16.59	0.76	1.32	0.16

Table F.1 (Continued)

	Sampling interval, mm	S_q, μm	S_z, μm	S_{sk}	S_{ku}	S_{ds}, mm^{-2}	S_{al}, mm	S_{tr}	S_{td}, °	$S_{\Delta q}$	S_{sc}, μm^{-1}	S_{dr}, %	S_{bi}	S_{ci}	S_{vi}
Sample B	0.005	78.20	470.29	-0.59	2.76	255.06	0.32	0.88	89.50	2.28	0.744	110.44	0.71	1.41	0.17
	0.010	78.12	438.83	-0.60	2.79	72.31	0.32	0.87	89.50	1.36	0.224	53.94	0.72	1.41	0.17
	0.015	78.16	438.78	-0.59	2.78	46.48	0.32	0.86	89.50	1.18	0.099	46.05	0.72	1.41	0.17
	0.020	78.09	432.98	-0.60	2.80	29.88	0.33	0.85	89.50	1.00	0.051	36.04	0.72	1.41	0.17
	0.030	78.16	427.58	-0.60	2.81	15.89	0.33	0.84	89.50	0.88	0.028	30.48	0.72	1.40	0.17
	0.040	78.21	423.76	-0.61	2.83	9.88	0.33	0.82	89.50	0.80	0.015	27.11	0.72	1.41	0.17
	0.050	78.28	414.10	-0.61	2.84	7.25	0.34	0.78	89.50	0.77	0.009	24.95	0.72	1.39	0.17
	0.060	77.97	408.06	-0.62	2.87	6.31	0.32	0.76	89.50	0.72	0.006	23.11	0.72	1.39	0.17
	0.070	78.11	405.49	-0.62	2.87	5.65	0.35	0.79	89.50	0.70	0.005	21.59	0.72	1.39	0.17
	0.080	78.51	404.59	-0.62	2.83	4.94	0.33	0.71	89.50	0.68	0.005	20.81	0.73	1.38	0.17
	0.100	78.51	403.82	-0.65	2.94	3.94	0.36	0.72	89.50	0.64	0.004	18.86	0.73	1.37	0.17
	0.120	77.79	398.58	-0.65	3.02	2.93	0.34	0.69	89.50	0.60	0.003	16.98	0.74	1.37	0.16
	0.140	77.99	385.27	-0.67	3.05	2.60	0.40	0.78	89.50	0.58	0.003	15.84	0.73	1.38	0.17

Table F.2 3-D surface characterisation parameters of A80J8V grinding wheel samples at various sampling intervals

	Sampling interval, mm	S_q, µm	S_z, µm	S_{sk}	S_{ku}	S_{ds}, mm^{-2}	S_{al}, mm	S_{tr}	S_{td}, °	$S_{\Delta q}$	S_{sc}, μm^{-1}	S_{dr}, %	S_{bi}	S_{ci}	S_{vi}
Sample A	0.005	44.89	247.63	-0.13	2.47	197.67	0.30	0.55	89.50	0.60	0.095	14.82	0.63	1.64	0.13
	0.010	44.90	242.93	-0.13	2.47	83.67	0.30	0.55	89.50	0.49	0.035	11.08	0.63	1.64	0.13
	0.015	44.92	240.86	-0.14	2.46	54.22	0.30	0.55	89.50	0.48	0.021	10.62	0.63	1.63	0.14
	0.020	44.94	240.28	-0.14	2.46	38.89	0.30	0.55	89.50	0.46	0.015	9.81	0.63	1.63	0.13
	0.030	44.97	235.90	-0.14	2.45	19.33	0.30	0.55	89.50	0.44	0.009	8.99	0.63	1.62	0.13
	0.040	44.99	224.18	-0.15	2.45	10.78	0.30	0.55	89.50	0.42	0.006	8.48	0.63	1.61	0.13
	0.050	45.03	223.69	-0.15	2.44	8.11	0.32	0.56	89.50	0.41	0.004	7.93	0.64	1.61	0.14
	0.060	44.97	222.43	-0.15	2.42	6.00	0.30	0.55	89.50	0.39	0.003	7.45	0.64	1.60	0.13
	0.070	45.03	224.88	-0.13	2.48	6.48	0.31	0.55	89.50	0.39	0.003	7.19	0.63	1.62	0.14
	0.080	45.07	210.79	-0.14	2.45	5.25	0.33	0.56	89.50	0.38	0.003	6.85	0.63	1.62	0.14
	0.090	44.91	213.03	-0.13	2.42	4.76	0.32	0.57	89.50	0.36	0.003	6.37	0.63	1.61	0.13
	0.100	45.07	209.01	-0.16	2.41	4.22	0.32	0.57	89.50	0.36	0.003	6.21	0.64	1.60	0.13
	0.120	45.11	205.60	-0.18	2.40	3.33	0.34	0.59	89.50	0.34	0.003	5.73	0.64	1.60	0.13

Table F.2 (Continued)

	Sampling interval, mm	S_q, µm	S_z, µm	S_{sk}	S_{ku}	S_{ds}, mm^{-2}	S_{al}, mm	S_{tr}	S_{td}, °	$S_{\Delta q}$	S_{sc}, μm^{-1}	S_{dr}, %	S_{bi}	S_{ci}	S_{vi}
Sample B	0.005	48.56	315.22	-0.25	3.24	192.44	0.35	0.52	45.25	0.65	0.097	15.99	0.58	1.76	0.16
	0.010	48.55	287.06	-0.25	3.24	77.67	0.35	0.52	45.25	0.51	0.033	11.12	0.58	1.76	0.16
	0.015	48.53	281.91	-0.26	3.24	51.56	0.36	0.51	45.25	0.48	0.021	10.70	0.59	1.75	0.16
	0.020	48.51	280.45	-0.25	3.23	35.00	0.36	0.51	45.25	0.46	0.014	9.69	0.59	1.75	0.16
	0.030	48.51	265.12	-0.25	3.24	17.11	0.36	0.51	45.25	0.43	0.009	8.89	0.59	1.75	0.16
	0.040	48.52	259.82	-0.26	3.26	10.67	0.36	0.50	45.25	0.42	0.006	8.33	0.59	1.74	0.16
	0.050	48.59	256.00	-0.27	3.31	8.00	0.36	0.49	45.25	0.41	0.004	7.86	0.59	1.74	0.16
	0.060	48.39	249.69	-0.25	3.24	5.56	0.37	0.49	45.25	0.39	0.003	7.27	0.59	1.73	0.17
	0.070	48.59	249.67	-0.28	3.29	5.90	0.36	0.50	45.25	0.38	0.003	7.08	0.59	1.74	0.17
	0.080	48.48	248.31	-0.30	3.33	4.79	0.36	0.47	45.25	0.37	0.003	6.65	0.60	1.71	0.16
	0.090	48.28	241.24	-0.26	3.24	4.08	0.37	0.48	45.25	0.36	0.003	6.35	0.58	1.73	0.16
	0.100	48.46	240.01	-0.27	3.30	4.22	0.40	0.50	45.25	0.35	0.003	6.13	0.59	1.74	0.17
	0.120	48.41	237.98	-0.30	3.37	3.44	0.38	0.47	45.25	0.34	0.002	5.58	0.59	1.71	0.17

Table F.3 3-D surface characterisation parameters of B120H200V grinding wheel samples at various sampling intervals

	Sampling interval, mm	S_q, µm	S_z, µm	S_{sk}	S_{ku}	S_{ds}, mm^{-2}	S_{al}, mm	S_{tr}	S_{td}, °	$S_{\Delta q}$	S_{sc}, μm^{-1}	S_{dr}, %	S_{bi}	S_{ci}	S_{vi}
Sample A	0.005	11.82	92.24	-1.94	8.28	756.25	0.13	0.64	89.50	0.38	0.084	6.65	0.92	1.10	0.25
	0.010	11.81	89.08	-1.94	8.26	268.25	0.13	0.62	89.50	0.32	0.037	4.98	0.87	1.14	0.25
	0.015	11.82	88.39	-1.94	8.27	138.44	0.13	0.62	89.50	0.29	0.021	4.16	0.87	1.14	0.25
	0.020	11.82	87.54	-1.93	8.23	93.00	0.13	0.62	89.50	0.28	0.015	3.72	0.88	1.14	0.24
	0.030	11.81	84.52	-1.96	8.37	49.99	0.13	0.57	89.50	0.25	0.008	3.12	0.88	1.12	0.24
	0.040	11.78	83.73	-1.90	8.15	29.00	0.14	0.62	89.50	0.23	0.006	2.67	0.87	1.14	0.24
	0.050	11.67	73.82	-1.92	8.18	22.50	0.14	0.57	89.50	0.22	0.004	2.36	0.89	1.09	0.25
	0.060	11.95	75.17	-1.93	8.08	20.15	0.13	0.53	89.50	0.21	0.003	2.16	0.91	1.07	0.25
	0.070	11.68	70.62	-1.95	8.36	15.88	0.14	0.55	89.50	0.20	0.002	1.90	0.88	1.11	0.25
	0.080	11.55	63.74	-1.86	8.00	14.25	0.16	0.55	89.50	0.19	0.002	1.74	0.85	1.16	0.25
Sample B	0.005	14.51	107.10	-1.41	5.33	672.75	0.16	0.82	89.50	0.39	0.077	6.90	0.81	1.24	0.24
	0.010	14.56	103.24	-1.42	5.36	265.25	0.16	0.79	89.50	0.34	0.032	5.27	0.81	1.24	0.24
	0.015	14.60	100.86	-1.42	5.42	139.20	0.16	0.78	89.50	0.31	0.018	4.50	0.83	1.21	0.24
	0.020	14.64	93.69	-1.41	5.33	90.25	0.16	0.76	89.50	0.29	0.012	4.12	0.83	1.19	0.23
	0.030	14.76	95.72	-1.44	5.58	45.66	0.17	0.78	89.50	0.27	0.007	3.54	0.85	1.18	0.23
	0.040	14.77	86.00	-1.41	5.36	26.50	0.17	0.73	89.50	0.25	0.004	3.08	0.82	1.20	0.23
	0.050	15.01	86.22	-1.44	5.49	21.00	0.18	0.72	89.50	0.25	0.003	2.93	0.83	1.18	0.23
	0.060	15.00	82.43	-1.44	5.62	17.09	0.17	0.63	89.50	0.23	0.003	2.59	0.84	1.17	0.23
	0.070	15.04	77.93	-1.39	5.42	12.49	0.20	0.78	89.50	0.22	0.002	2.28	0.83	1.18	0.23
	0.080	15.00	78.91	-1.40	5.40	11.75	0.18	0.62	89.50	0.20	0.002	2.07	0.83	1.18	0.23

Table F.4 3-D surface characterisation parameters of B140N200V grinding wheel samples at various sampling intervals

	Sampling interval, mm	S_q, μm	S_z, μm	S_{sk}	S_{ku}	S_{ds}, mm^{-2}	S_{al}, mm	S_{tr}	S_{td}, °	$S_{\Delta q}$	S_{sc}, μm^{-1}	S_{dr}, %	S_{bi}	S_{ci}	S_{vi}
Sample A	0.005	11.26	90.55	-0.62	4.35	496.75	0.14	0.74	89.50	0.31	0.041	4.68	0.67	1.59	0.19
	0.010	11.25	88.51	-0.62	4.35	181.25	0.14	0.72	89.50	0.28	0.025	3.75	0.67	1.58	0.19
	0.015	11.26	85.44	-0.63	4.37	111.81	0.15	0.72	89.50	0.26	0.018	3.42	0.67	1.58	0.19
	0.020	11.25	82.51	-0.63	4.35	76.75	0.14	0.68	89.50	0.25	0.013	3.12	0.67	1.57	0.20
	0.030	11.26	78.46	-0.64	4.39	46.93	0.15	0.69	89.50	0.23	0.007	2.70	0.67	1.56	0.19
	0.040	11.26	75.64	-0.65	4.42	32.00	0.14	0.62	89.50	0.22	0.004	2.38	0.67	1.56	0.19
	0.050	11.22	72.58	-0.62	4.28	19.25	0.16	0.71	89.50	0.21	0.003	2.08	0.68	1.52	0.20
	0.060	11.21	68.71	-0.66	4.35	14.28	0.17	0.67	89.50	0.20	0.003	1.89	0.68	1.53	0.19
	0.070	11.22	65.46	-0.56	4.06	13.28	0.16	0.62	89.50	0.19	0.002	1.73	0.66	1.55	0.18
	0.080	11.25	68.94	-0.76	4.77	12.25	0.16	0.71	89.50	0.18	0.002	1.58	0.67	1.54	0.19
Sample B	0.005	9.79	79.12	-1.10	6.11	478.25	0.13	0.84	89.50	0.29	0.037	4.21	0.68	1.54	0.22
	0.010	9.79	75.05	-1.10	6.11	187.75	0.13	0.82	89.50	0.26	0.023	3.41	0.69	1.52	0.21
	0.015	9.78	73.85	-1.10	6.09	118.09	0.13	0.83	89.50	0.25	0.016	3.09	0.69	1.51	0.22
	0.020	9.79	72.82	-1.11	6.11	81.25	0.13	0.79	89.50	0.24	0.011	2.82	0.69	1.49	0.23
	0.030	9.76	69.48	-1.08	6.03	45.15	0.13	0.77	89.50	0.22	0.006	2.42	0.69	1.49	0.21
	0.040	9.80	67.31	-1.10	6.01	29.50	0.14	0.81	89.50	0.21	0.004	2.10	0.71	1.47	0.22
	0.050	9.84	65.14	-1.12	6.18	22.75	0.14	0.78	89.50	0.19	0.004	1.87	0.70	1.48	0.21
	0.060	9.83	65.70	-1.17	6.56	17.35	0.13	0.62	89.50	0.18	0.003	1.67	0.73	1.42	0.22
	0.070	9.92	61.27	-1.12	6.06	13.02	0.14	0.63	89.50	0.18	0.003	1.54	0.70	1.46	0.21
	0.080	9.70	58.21	-0.99	5.30	12.75	0.16	0.63	89.50	0.16	0.002	1.29	0.68	1.49	0.21

Table F.5 3-D surface characterisation parameters of C80M7V grinding wheel samples at various sampling intervals

	Sampling interval, mm	S_q, µm	S_z, µm	S_{sk}	S_{ku}	S_{ds}, mm^{-2}	S_{al}, mm	S_{tr}	S_{td}, °	$S_{\Delta q}$	S_{sc}, μm^{-1}	S_{dr}, %	S_{bi}	S_{ci}	S_{vi}
Sample A	0.005	9.65	79.97	-1.01	5.01	498.00	0.12	0.77	89.50	0.30	0.059	4.41	0.73	1.49	0.21
	0.010	9.66	77.34	-1.00	5.00	163.11	0.12	0.75	89.50	0.27	0.029	3.60	0.73	1.48	0.21
	0.015	9.66	75.97	-1.00	4.99	102.56	0.13	0.76	89.50	0.25	0.017	3.16	0.72	1.48	0.21
	0.020	9.67	73.48	-1.01	5.01	73.56	0.13	0.74	89.50	0.24	0.012	2.86	0.72	1.48	0.21
	0.030	9.67	71.93	-1.00	5.02	45.89	0.13	0.67	89.50	0.22	0.007	2.46	0.72	1.48	0.20
	0.040	9.67	66.84	-1.02	5.07	30.22	0.13	0.63	89.50	0.21	0.005	2.14	0.71	1.47	0.22
	0.050	9.72	65.98	-0.99	4.95	22.78	0.14	0.69	89.50	0.20	0.004	1.91	0.72	1.48	0.21
	0.060	9.64	64.58	-1.01	5.18	18.22	0.13	0.62	89.50	0.18	0.003	1.67	0.72	1.49	0.20
	0.070	9.74	62.60	-1.03	5.12	14.35	0.14	0.63	89.50	0.18	0.002	1.56	0.74	1.41	0.21
	0.080	9.82	60.92	-1.09	5.51	12.67	0.16	0.71	89.50	0.17	0.002	1.40	0.72	1.44	0.22
Sample B	0.005	8.94	70.74	-0.89	4.17	512.33	0.11	0.76	0.00	0.29	0.058	4.08	0.71	1.47	0.22
	0.010	8.95	71.15	-0.89	4.17	163.44	0.11	0.75	0.00	0.26	0.027	3.29	0.72	1.45	0.21
	0.015	8.94	66.80	-0.89	4.19	105.22	0.11	0.73	0.00	0.24	0.016	2.91	0.73	1.44	0.21
	0.020	8.95	66.34	-0.89	4.16	76.56	0.12	0.71	0.00	0.23	0.011	2.65	0.72	1.45	0.20
	0.030	8.94	63.28	-0.89	4.18	48.11	0.12	0.69	0.00	0.22	0.007	2.28	0.71	1.45	0.20
	0.040	8.95	61.44	-0.88	4.12	28.67	0.12	0.67	0.00	0.20	0.005	1.99	0.70	1.46	0.20
	0.050	8.94	62.10	-0.90	4.33	20.78	0.14	0.78	0.00	0.19	0.004	1.76	0.71	1.46	0.20
	0.060	8.95	55.95	-0.87	4.02	16.56	0.12	0.55	0.00	0.18	0.003	1.57	0.70	1.44	0.21
	0.070	9.10	55.52	-0.94	4.43	14.23	0.14	0.71	0.00	0.17	0.002	1.46	0.73	1.42	0.21
	0.080	9.11	58.91	-0.95	4.46	11.53	0.16	0.71	0.00	0.16	0.002	1.32	0.73	1.41	0.19

Table F.6 3-D surface characterisation parameters of C120J8V grinding wheel samples at various sampling intervals

	Sampling interval, mm	S_q, μm	S_z, μm	S_{sk}	S_{ku}	S_{ds}, mm^{-2}	S_{al}, mm	S_{tr}	S_{td}, °	$S_{\Delta q}$	S_{sc}, μm^{-1}	S_{dr}, %	S_{bi}	S_{ci}	S_{vi}
Sample A	0.005	7.51	74.46	-1.96	10.05	1227.11	0.13	0.71	89.50	0.37	0.075	6.19	0.75	1.39	0.25
	0.010	7.53	69.26	-1.96	10.06	359.11	0.13	0.71	89.50	0.29	0.032	4.01	0.84	1.26	0.25
	0.015	7.53	70.59	-1.96	10.02	194.22	0.13	0.68	89.50	0.26	0.021	3.21	0.76	1.39	0.24
	0.020	7.57	66.92	-1.99	10.22	130.89	0.13	0.64	89.50	0.23	0.014	2.70	0.83	1.28	0.24
	0.030	7.56	58.35	-1.95	9.97	73.56	0.13	0.67	89.50	0.21	0.009	2.08	0.85	1.24	0.25
	0.040	7.59	54.78	-2.02	10.39	45.22	0.13	0.59	89.50	0.18	0.006	1.62	0.84	1.23	0.25
	0.050	7.60	54.30	-2.02	10.42	32.67	0.14	0.63	89.50	0.17	0.004	1.36	0.78	1.34	0.24
	0.060	7.65	49.89	-1.97	9.84	23.44	0.13	0.54	89.50	0.15	0.003	1.15	0.85	1.21	0.24
	0.070	7.40	49.66	-1.91	9.86	17.93	0.14	0.55	89.50	0.14	0.002	0.96	0.81	1.27	0.25
	0.080	7.34	45.18	-1.84	9.34	13.92	0.16	0.63	89.50	0.13	0.002	0.80	0.85	1.22	0.24
Sample B	0.005	8.32	74.66	-1.89	8.80	961.11	0.13	0.74	45.25	0.37	0.069	6.26	0.82	1.25	0.26
	0.010	8.31	72.85	-1.87	8.74	264.22	0.13	0.72	45.25	0.29	0.030	4.11	0.84	1.23	0.27
	0.015	8.31	70.63	-1.89	8.84	144.89	0.14	0.72	45.25	0.27	0.019	3.41	0.79	1.30	0.26
	0.020	8.33	66.41	-1.88	8.77	95.33	0.14	0.71	45.25	0.24	0.014	2.91	0.83	1.23	0.25
	0.030	8.30	67.74	-1.91	8.95	56.56	0.13	0.67	45.25	0.22	0.009	2.32	0.78	1.30	0.26
	0.040	8.31	65.98	-1.90	8.97	39.00	0.14	0.67	45.25	0.20	0.006	1.90	0.83	1.23	0.24
	0.050	8.32	63.63	-1.91	8.98	30.44	0.14	0.63	45.25	0.18	0.004	1.60	0.76	1.32	0.25
	0.060	8.18	59.15	-1.87	8.70	23.11	0.17	0.78	45.25	0.16	0.003	1.32	0.77	1.31	0.25
	0.070	8.13	58.71	-1.80	8.31	19.55	0.16	0.62	45.25	0.15	0.003	1.12	0.77	1.29	0.24
	0.080	8.09	56.33	-1.87	8.95	16.55	0.16	0.71	45.25	0.14	0.002	0.95	0.75	1.33	0.25

Table F.7 3-D surface characterisation parameters of ground workpieces at various sampling intervals

	Sampling interval, mm	S_q, µm	S_z, µm	S_{sk}	S_{ku}	S_{ds}, mm^{-2}	S_{al}, mm	S_{tr}	S_{td}, °	$S_{\Delta q}$	S_{sc}, μm^{-1}	S_{dr}, %	S_{bi}	S_{ci}	S_{vi}
O1	0.005	0.26	2.30	-0.15	3.17	3985.15	0.05	0.06	0.00	0.04	0.012	0.09	0.60	1.81	0.17
	0.010	0.26	2.23	-0.16	3.13	826.59	0.04	0.07	0.00	0.02	0.003	0.03	0.60	1.78	0.17
	0.015	0.26	2.12	-0.15	3.15	504.99	0.05	0.06	0.00	0.02	0.002	0.02	0.62	1.73	0.17
	0.020	0.26	2.01	-0.19	3.14	220.18	0.06	0.09	0.00	0.01	0.001	0.01	0.62	1.71	0.16
	0.030	0.26	1.93	-0.17	3.13	97.90	0.06	0.11	0.00	0.01	0.000	0.01	0.63	1.69	0.17
	0.040	0.26	1.84	-0.22	3.22	55.39	0.04	0.08	0.00	0.01	0.000	0.00	0.63	1.67	0.17
D2	0.005	0.35	3.21	-0.18	2.99	3460.21	0.03	0.02	0.00	0.07	0.020	0.23	0.61	1.77	0.17
	0.010	0.36	2.98	-0.19	2.97	807.69	0.03	0.02	0.00	0.04	0.004	0.07	0.61	1.72	0.18
	0.015	0.36	2.95	-0.18	3.00	515.65	0.03	0.02	0.00	0.03	0.003	0.05	0.62	1.73	0.18
	0.020	0.36	2.60	-0.16	2.95	235.19	0.04	0.02	0.00	0.02	0.001	0.03	0.61	1.71	0.16
	0.030	0.37	2.53	-0.25	3.00	114.47	0.03	0.02	0.00	0.02	0.001	0.01	0.62	1.66	0.17
Mild steel	0.005	0.40	3.32	-0.13	3.20	3815.04	0.03	0.04	0.00	0.06	0.0187	0.21	0.60	1.79	0.18
	0.010	0.41	3.30	-0.13	3.24	814.26	0.03	0.04	0.00	0.03	0.0038	0.06	0.60	1.79	0.18
	0.015	0.40	2.99	-0.14	3.19	534.19	0.03	0.04	0.00	0.03	0.0029	0.05	0.60	1.76	0.17
	0.020	0.41	2.99	-0.15	3.33	217.97	0.04	0.05	0.00	0.02	0.0013	0.03	0.62	1.69	0.18
	0.030	0.40	2.65	-0.14	3.18	94.04	0.03	0.04	0.00	0.02	0.0007	0.02	0.62	1.69	0.16

Appendix G

Three-dimensional surface characterisation parameters of the grinding wheel topography in the 2^3 factorial experiment

Table G.1 Replication 1/ Sample 1 of the grinding wheel topography

Parameter	Replica 1/Sample 1							
	Run 1	Run 2	Run 3	Run 4	Run 5	Run 6	Run 7	Run 8
S_q, μm	12.45	12.72	9.86	13.18	12.24	8.94	12.53	9.95
S_z, μm	76.20	82.20	62.18	74.02	75.69	60.95	72.72	61.87
S_{sk}	-0.78	-0.67	-1.24	-0.39	-0.61	-0.30	-0.62	-0.79
S_{ku}	3.60	3.88	4.90	2.90	3.24	3.69	3.15	3.67
S_{ds}, mm^{-2}	23.92	24.94	31.86	19.73	25.73	28.68	27.32	28.00
S_{al}, mm	0.180	0.180	0.162	0.180	0.162	0.162	0.162	0.162
S_{tr}	0.63	0.50	0.67	0.63	0.72	0.67	0.67	0.67
S_{td}, °	89.50	89.50	89.50	89.50	0.00	89.50	0.00	89.50
$S_{\Delta q}$	0.23	0.22	0.19	0.23	0.23	0.19	0.23	0.19
S_{sc}, μm^{-1}	0.005	0.004	0.004	0.004	0.005	0.005	0.005	0.004
S_{dr}, %	2.50	2.48	1.70	2.56	2.67	1.78	2.63	1.82
S_{bi}	0.70	0.68	0.78	0.65	0.70	0.64	0.71	0.70
S_{ci}	1.45	1.52	1.29	1.57	1.46	1.63	1.43	1.46
S_{vi}	0.19	0.18	0.22	0.17	0.18	0.18	0.17	0.19
S_t, μm	85.48	95.15	69.62	85.56	80.67	68.51	80.07	72.22
S_p, μm	25.23	29.80	18.46	34.54	27.41	30.14	28.01	25.81
S_v, μm	60.24	65.36	51.16	51.02	53.26	38.36	52.06	46.41

Table G.2 Replication 1/ Sample 2 of the grinding wheel topography

Parameter	Replica 1/Sample 2							
	Run 1	Run 2	Run 3	Run 4	Run 5	Run 6	Run 7	Run 8
S_q, μm	14.78	13.68	13.02	14.97	15.48	10.92	13.87	11.31
S_z, μm	84.55	81.15	78.87	88.85	89.40	74.79	76.74	63.51
S_{sk}	-0.64	-0.61	-1.11	-0.50	-0.48	-0.71	-0.46	-0.59
S_{ku}	3.27	3.33	4.33	3.16	2.95	3.97	2.86	3.10
S_{ds}, mm^{-2}	20.52	22.11	23.92	20.29	21.65	25.73	24.83	25.51
S_{al}, mm	0.191	0.162	0.180	0.201	0.201	0.162	0.186	0.180
S_{tr}	0.75	0.67	0.74	0.54	0.71	0.72	0.73	0.74
S_{td}, °	89.50	0.00	89.50	89.50	89.50	89.50	89.50	89.50
$S_{\Delta q}$	0.24	0.24	0.23	0.25	0.26	0.22	0.24	0.21
S_{sc}, μm^{-1}	0.004	0.004	0.004	0.004	0.004	0.004	0.005	0.004
S_{dr}, %	2.88	2.92	2.55	2.96	3.26	2.30	2.83	2.17
S_{bi}	0.69	0.69	0.78	0.66	0.65	0.69	0.69	0.68
S_{ci}	1.47	1.49	1.28	1.56	1.56	1.52	1.48	1.49
S_{vi}	0.18	0.18	0.21	0.17	0.17	0.19	0.17	0.18
S_t, μm	90.15	96.25	89.85	103.86	102.76	89.42	86.07	73.12
S_p, μm	30.14	32.88	24.90	36.98	33.00	33.55	31.27	23.39
S_v, μm	60.01	63.37	64.96	66.88	69.77	55.87	54.80	49.73

Table G.3 Replication 2 /Sample 1 of the grinding wheel topography

Parameter	Replica 2/Sample 1							
	Run 1	Run 2	Run 3	Run 4	Run 5	Run 6	Run 7	Run 8
S_q, μm	14.68	12.91	12.02	12.58	15.69	11.13	14.34	10.79
S_z, μm	84.48	73.09	75.18	78.13	92.29	66.37	83.14	62.69
S_{sk}	-0.40	-0.60	-1.16	-0.56	-0.71	-0.50	-0.49	-0.74
S_{ku}	2.96	3.15	4.53	3.39	3.54	3.10	2.94	3.24
S_{ds}, mm^{-2}	15.99	22.22	26.53	20.97	21.20	27.78	18.25	32.08
S_{al}, mm	0.162	0.186	0.180	0.162	0.191	0.201	0.162	0.186
S_{tr}	0.62	0.77	0.69	0.67	0.63	0.77	0.62	0.57
S_{td}, °	89.50	89.50	89.50	89.50	89.50	89.50	89.50	89.50
$S_{\Delta q}$	0.24	0.23	0.22	0.23	0.26	0.20	0.25	0.20
S_{sc}, μm^{-1}	0.004	0.004	0.004	0.005	0.004	0.005	0.004	0.005
S_{dr}, %	2.81	2.57	2.29	2.66	3.33	2.00	3.03	1.90
S_{bi}	0.65	0.69	0.82	0.65	0.69	0.66	0.67	0.72
S_{ci}	1.58	1.48	1.22	1.57	1.46	1.54	1.53	1.41
S_{vi}	0.17	0.18	0.21	0.18	0.18	0.18	0.17	0.19
S_t, μm	91.76	81.50	80.70	88.00	99.27	71.12	95.60	71.12
S_p, μm	37.03	27.46	20.34	32.58	34.24	28.07	31.63	21.96
S_v, μm	54.74	54.05	60.36	55.43	65.03	43.05	63.97	49.16

Table G.4 Replication 2 /Sample 2 of the grinding wheel topography

Parameter	Replica 2/Sample 2							
	Run 1	Run 2	Run 3	Run 4	Run 5	Run 6	Run 7	Run 8
S_q, µm	16.20	13.22	10.99	12.52	14.85	10.54	14.17	10.59
S_z, µm	93.48	78.96	76.61	70.37	83.23	68.56	78.82	65.52
S_{sk}	-0.39	-0.64	-0.73	-0.38	-0.54	-0.87	-0.46	-0.88
S_{ku}	2.93	3.46	4.03	2.83	3.07	4.03	3.05	3.91
S_{ds}, mm^{-2}	13.72	21.20	25.73	23.01	20.75	27.89	19.16	27.10
S_{al}, mm	0.180	0.162	0.186	0.142	0.180	0.186	0.162	0.186
S_{tr}	0.63	0.67	0.73	0.50	0.69	0.77	0.67	0.71
S_{td}, °	89.50	89.50	0.00	89.50	0.00	89.50	-45.25	89.50
$S_{\Delta q}$	0.26	0.24	0.20	0.24	0.26	0.20	0.25	0.20
S_{sc}, μm^{-1}	0.003	0.004	0.004	0.004	0.004	0.004	0.004	0.005
S_{dr}, %	3.23	2.71	2.06	2.76	3.29	2.00	3.11	1.98
S_{bi}	0.64	0.68	0.73	0.65	0.67	0.73	0.65	0.73
S_{ci}	1.59	1.48	1.43	1.57	1.52	1.41	1.54	1.38
S_{vi}	0.16	0.18	0.20	0.16	0.17	0.20	0.17	0.20
S_t, µm	101.86	84.98	91.50	78.85	90.46	76.03	82.33	72.75
S_p, µm	39.78	31.14	32.79	30.60	36.47	23.34	29.72	22.92
S_v, µm	62.08	53.84	58.71	48.26	53.99	52.69	52.61	49.83

Table G.5 Replication 3 /Sample 1 of the grinding wheel topography

Parameter	Replica 3/Sample 1							
	Run 1	Run 2	Run 3	Run 4	Run 5	Run 6	Run 7	Run 8
S_q, µm	13.92	13.98	10.01	13.63	12.87	7.40	13.71	8.99
S_z, µm	83.87	77.73	71.08	82.23	76.04	51.61	84.39	56.51
S_{sk}	-0.55	-0.32	-0.63	-0.66	-0.83	-0.62	-0.69	-1.09
S_{ku}	3.40	2.87	3.97	3.51	3.59	4.32	3.59	4.84
S_{ds}, mm^{-2}	24.83	20.86	26.76	20.86	26.19	35.82	17.46	35.48
S_{al}, mm	0.191	0.162	0.162	0.180	0.180	0.162	0.162	0.162
S_{tr}	0.66	0.67	0.72	0.74	0.74	0.72	0.72	0.67
S_{td}, °	89.50	89.50	63.35	45.25	0.00	89.50	89.50	89.50
$S_{\Delta q}$	0.23	0.25	0.20	0.24	0.23	0.16	0.25	0.19
S_{sc}, μm^{-1}	0.005	0.005	0.004	0.004	0.005	0.004	0.004	0.005
S_{dr}, %	2.66	3.03	1.96	2.88	2.61	1.29	3.06	1.69
S_{bi}	0.67	0.62	0.71	0.68	0.74	0.66	0.68	0.73
S_{ci}	1.53	1.63	1.47	1.49	1.37	1.61	1.48	1.40
S_{vi}	0.18	0.16	0.20	0.18	0.20	0.19	0.19	0.21
S_t, µm	95.15	86.62	79.88	89.03	84.88	63.81	90.30	71.31
S_p, µm	40.26	35.35	36.68	29.66	28.93	22.87	28.39	18.18
S_v, µm	54.89	51.28	43.20	59.37	55.95	40.94	61.92	53.14

Table G.6 Replication 3 /Sample 1 of the grinding wheel topography

Parameter	Replica 3/Sample 2							
	Run 1	Run 2	Run 3	Run 4	Run 5	Run 6	Run 7	Run 8
S_q, µm	13.73	14.17	10.96	13.79	12.64	10.78	15.47	9.62
S_z, µm	74.99	79.64	80.83	73.61	72.87	77.73	84.71	58.97
S_{sk}	-0.35	-0.25	-0.65	-0.59	-0.53	-0.04	-0.47	-0.89
S_{ku}	2.64	2.72	4.75	2.98	3.17	4.05	2.81	3.98
S_{ds}, mm^{-2}	21.31	19.61	26.53	21.09	24.37	27.21	16.78	33.67
S_{al}, mm	0.162	0.186	0.162	0.180	0.180	0.186	0.180	0.162
S_{tr}	0.67	0.73	0.72	0.74	0.63	0.49	0.50	0.67
S_{td}, °	89.50	0.00	-34.19	89.50	89.50	-45.25	89.50	89.50
$S_{\Delta q}$	0.24	0.25	0.21	0.24	0.23	0.19	0.26	0.19
S_{sc}, μm^{-1}	0.004	0.004	0.004	0.004	0.005	0.004	0.004	0.005
S_{dr}, %	2.87	2.99	2.12	2.92	2.57	1.80	3.35	1.76
S_{bi}	0.66	0.65	0.71	0.69	0.67	0.55	0.68	0.74
S_{ci}	1.55	1.59	1.48	1.46	1.52	1.88	1.50	1.37
S_{vi}	0.16	0.15	0.21	0.18	0.17	0.18	0.17	0.20
S_t, µm	78.77	86.99	86.17	86.86	76.35	87.37	95.66	68.52
S_p, µm	33.02	37.70	35.43	27.07	29.61	36.63	33.60	21.55
S_v, µm	45.75	49.28	50.74	59.79	46.74	50.73	62.06	46.96

Appendix H

Three-dimensional surface characterisation parameters of the ground workpieces of the 2^3 factorial experiment

Table H.1 Replication 1 of the 2^3 factorial experiment

Parameter	Replica 1							
	Run 1	Run 2	Run 3	Run 4	Run 5	Run 6	Run 7	Run 8
S_q, µm	0.43	0.32	0.38	0.29	0.47	0.33	0.33	0.20
S_z, µm	2.72	2.11	2.63	1.57	3.17	1.99	2.32	1.60
S_{sk}	-0.19	-0.09	0.05	0.15	-0.10	-0.51	0.39	-0.16
S_{ku}	2.69	3.17	3.03	2.47	3.26	3.37	2.81	3.44
S_{ds}, mm^{-2}	$3.40x10^3$	$4.14x10^3$	$3.55x10^3$	$3.48x10^3$	$4.04x10^3$	$3.79x10^3$	$3.73x10^3$	$4.53x10^3$
S_{al}, mm	0.030	0.025	0.020	0.020	0.045	0.025	0.020	0.025
S_{tr}	0.05	0.04	0.03	0.03	0.07	0.04	0.03	0.04
S_{td}, °	0.00	0.00	0.00	0.00	0.00	0.00	0.00	0.00
$S_{\Delta q}$	0.07	0.06	0.07	0.06	0.07	0.06	0.06	0.04
S_{sc}, μm^{-1}	0.016	0.015	0.018	0.014	0.017	0.016	0.017	0.012
S_{dr}, %	0.22	0.16	0.26	0.15	0.25	0.19	0.20	0.08
S_{bi}	0.63	0.62	0.60	0.57	0.64	0.64	0.53	0.59
S_{ci}	1.66	1.66	1.76	1.81	1.63	1.57	2.01	1.80
S_{vi}	0.15	0.16	0.14	0.13	0.15	0.18	0.14	0.17
S_t, µm	2.80	2.13	2.69	1.63	3.20	2.04	2.73	1.66
S_p, µm	1.30	1.06	1.43	0.83	1.58	0.89	1.72	0.68
S_v, µm	1.50	1.07	1.26	0.80	1.62	1.16	1.01	0.98

Table H.2 Replication 2 of the 2^3 factorial experiment

Parameter	Replica 2							
	Run 1	Run 2	Run 3	Run 4	Run 5	Run 6	Run 7	Run 8
S_q, μm	0.52	0.33	0.37	0.30	0.46	0.36	0.38	0.18
S_z, μm	3.31	2.56	2.42	1.62	2.54	2.53	2.31	1.39
S_{sk}	0.21	-0.01	0.04	0.17	0.05	-0.65	0.07	-0.14
S_{ku}	3.15	3.21	2.98	2.48	2.50	3.59	2.69	3.16
S_{ds}, mm^{-2}	$3.36x10^3$	$4.15x10^3$	$3.65x10^3$	$3.25x10^3$	$4.18x10^3$	$3.53x10^3$	$3.73x10^3$	$4.62x10^3$
S_{al}, mm	0.030	0.025	0.020	0.020	0.065	0.025	0.040	0.020
S_{tr}	0.05	0.04	0.03	0.03	0.11	0.04	0.07	0.03
S_{td}, °	0.00	0.00	0.00	0.00	0.00	0.00	0.00	0.00
$S_{\Delta q}$	0.08	0.06	0.07	0.06	0.07	0.06	0.07	0.04
S_{sc}, μm^{-1}	0.018	0.016	0.018	0.015	0.019	0.016	0.017	0.011
S_{dr}, %	0.33	0.17	0.26	0.16	0.25	0.20	0.21	0.08
S_{bi}	0.56	0.60	0.60	0.57	0.61	0.66	0.58	0.60
S_{ci}	1.88	3.23	1.73	1.82	1.69	3.16	1.77	3.23
S_{vi}	0.15	0.25	0.14	0.13	0.13	0.34	0.15	0.33
S_t, μm	3.96	3.28	2.46	1.75	2.56	2.94	2.38	1.62
S_p, μm	2.43	2.23	1.26	0.94	1.36	1.63	1.20	0.95
S_v, μm	1.53	1.06	1.20	0.81	1.19	1.31	1.18	0.67

Table H.3 Replication 3 of the 2^3 factorial experiment

Parameter	Replica 3							
	Run 1	Run 2	Run 3	Run 4	Run 5	Run 6	Run 7	Run 8
S_q, μm	0.52	0.31	0.34	0.27	0.47	0.39	0.38	0.20
S_z, μm	3.31	2.32	2.22	2.33	3.16	2.63	2.26	1.71
S_{sk}	0.22	0.18	0.31	-0.98	-0.05	-0.56	0.04	-0.03
S_{ku}	3.23	3.26	3.27	5.65	3.27	3.36	2.58	3.20
S_{ds}, mm^{-2}	$3.49x10^3$	$4.03x10^3$	$3.87x10^3$	$3.90x10^3$	$4.12x10^3$	$4.33x10^3$	$3.86x10^3$	$3.98x10^3$
S_{al}, mm	0.030	0.020	0.020	0.015	0.046	0.025	0.042	0.030
S_{tr}	0.05	0.03	0.03	0.03	0.08	0.04	0.07	0.05
S_{td}, °	0.00	0.00	0.00	0.00	0.00	0.00	0.00	0.00
$S_{\Delta q}$	0.08	0.07	0.07	0.06	0.07	0.08	0.07	0.04
S_{sc}, μm^{-1}	0.017	0.017	0.020	0.016	0.018	0.019	0.017	0.011
S_{dr}, %	0.32	0.21	0.26	0.19	0.25	0.30	0.21	0.09
S_{bi}	0.57	0.60	0.58	0.65	0.64	0.70	0.59	0.60
S_{ci}	1.83	1.77	1.81	1.62	1.65	1.46	1.74	1.79
S_{vi}	0.14	0.16	0.14	0.22	0.15	0.18	0.14	0.17
S_t, μm	3.37	2.41	2.24	2.68	3.17	2.67	2.38	1.81
S_p, μm	1.83	1.29	1.30	1.36	1.54	1.07	1.26	1.09
S_v, μm	1.55	1.12	0.94	1.32	1.63	1.59	1.12	0.72

Appendix I

Three-dimensional surface characterisation parameters of the measured and generated grinding wheel surfaces

Table I.1 A80J8V

Parameter	Sample 1			Sample 2			Sample 3			Sample 4		
	Measured	Johnson	Inverse	Measured	Johnson	Inverse	Measured	Johnson	Inverse	Measured	Johnson	Inverse
S_q, μm	70.60	70.38	70.69	67.25	67.03	67.03	68.02	68.43	67.33	67.08	68.52	68.09
S_z, μm	356.4	351.6	363.1	351.82	351.58	349.59	365.95	363.23	359.97	342.08	333.29	332.45
S_{sk}	-0.37	-0.41	-0.43	-0.69	-0.72	-0.67	-0.50	-0.58	-0.47	-0.39	-0.43	-0.38
S_{ku}	2.60	2.65	2.73	3.03	3.12	3.10	3.04	3.10	3.05	2.62	2.70	2.49
S_{ds}, mm^{-2}	11.22	12.33	13.22	14.33	15.78	16.44	14.67	15.33	15.22	13.00	14.78	14.44
S_{al}, mm	0.22	0.22	0.19	0.22	0.22	0.22	0.25	0.24	0.22	0.22	0.22	0.22
S_{tr}	0.81	0.81	0.71	0.67	0.72	0.72	0.73	0.74	0.71	0.64	0.72	0.72
S_{td}, °	0.0	0.0	0.0	-56.31	-56.31	-56.31	45.25	45.25	45.25	45.25	45.25	45.25
$S_{\Delta q}$	0.94	1.01	1.03	0.89	0.98	1.02	0.90	0.97	0.98	0.89	1.00	0.96
S_{sc}, μm^{-1}	0.02	0.02	0.02	0.02	0.02	0.02	0.02	0.02	0.02	0.02	0.02	0.02
S_{dr}, %	34.47	38.29	39.23	35.66	42.15	45.54	36.91	42.00	41.70	35.75	43.76	40.52
S_{bi}	0.71	0.70	0.71	0.73	0.73	0.72	0.68	0.67	0.67	0.68	0.67	0.69
S_{ci}	1.30	1.29	1.28	1.37	1.36	1.39	1.48	1.51	1.51	1.50	1.50	1.48
S_{vi}	0.14	0.14	0.14	0.18	0.18	0.18	0.17	0.18	0.17	0.16	0.17	0.15
S_t, μm	387.41	374.07	390.007	386.22	365.94	379.12	395.49	446.71	385.78	378.08	357.25	373.98
S_p, μm	146.03	150.28	142.778	131.50	133.30	132.59	149.57	143.66	144.25	160.87	141.20	165.21
S_v, μm	241.38	223.79	247.229	254.72	232.64	246.53	245.92	303.05	241.53	217.21	216.05	208.77
p-value		0.56	0.88		0.76	0.85		0.70	0.94		0.72	0.56

Table I.2 B120H200V

Parameter	Sample 1			Sample 2			Sample 3			Sample 4		
	Measured	Johnson	Inverse	Measured	Johnson	Inverse	Measured	Johnson	Inverse	Measured	Johnson	Inverse
S_q, μm	38.20	38.14	38.43	33.76	34.28	33.74	32.32	32.55	32.86	34.83	36.41	34.49
S_z, μm	223.8	222.6	226.3	168.12	165.66	170.55	181.17	169.33	197.19	168.31	175.61	173.76
S_{sk}	-0.78	-0.76	-0.92	-0.60	-0.67	-0.73	-0.48	-0.48	-0.60	-0.69	-0.78	-0.63
S_{ku}	4.01	3.63	4.04	2.78	2.87	3.13	3.10	2.74	3.34	2.94	3.11	2.92
S_{ds}, mm^{-2}	31.25	35.25	36.25	34.00	37.75	32.00	28.50	34.75	31.75	30.75	37.75	35.75
S_{al}, mm	0.17	0.17	0.17	0.14	0.13	0.13	0.14	0.13	0.14	0.16	0.14	0.13
S_{tr}	0.65	0.65	0.58	0.67	0.59	0.62	0.81	0.71	0.81	0.80	0.81	0.71
S_{td}, °	0.0	0.0	0.0	0.00	0.00	0.00	-45.25	-45.25	-45.25	45.25	45.25	45.25
$S_{\Delta q}$	0.70	0.82	0.85	0.69	0.79	0.75	0.65	0.71	0.71	0.70	0.87	0.81
S_{sc}, μm^{-1}	0.02	0.02	0.02	0.02	0.02	0.02	0.01	0.02	0.02	0.02	0.02	0.02
S_{dr}, %	20.45	26.47	27.70	22.20	28.11	25.57	19.50	23.41	23.21	22.20	33.49	29.18
S_{bi}	0.75	0.74	0.77	0.73	0.74	0.74	0.69	0.68	0.70	0.73	0.75	0.70
S_{ci}	1.20	1.20	1.17	1.38	1.35	1.34	1.51	1.50	1.46	1.35	1.33	1.42
S_{vi}	0.15	0.17	0.18	0.17	0.17	0.18	0.17	0.16	0.18	0.18	0.18	0.18
S_t, μm	246.55	246.89	240.56	180.86	174.45	181.26	223.07	194.46	218.69	182.92	193.49	185.68
S_p, μm	97.03	87.41	96.10	64.44	61.85	66.05	99.47	75.62	97.65	62.78	58.76	65.87
S_v, μm	149.52	159.49	144.45	116.42	112.61	115.21	123.60	118.84	121.04	120.13	134.73	119.81
p-value		0.18	0.35		0.65	0.35		0.37	0.41		0.24	0.72

Table I.3. C120J8V

Parameter	Sample 1			Sample 2			Sample 3			Sample 4		
	Measured	Johnson	Inverse	Measured	Johnson	Inverse	Measured	Johnson	Inverse	Measured	Johnson	Inverse
S_q, µm	30.00	29.53	29.60	33.95	34.43	36.59	29.56	29.87	30.93	24.00	24.28	24.47
S_z, µm	207.9	201.4	208.9	175.61	182.01	206.91	167.14	164.04	165.22	138.04	131.50	134.72
S_{sk}	-0.37	-0.41	-0.21	-0.74	-0.69	-0.90	-0.72	-0.72	-0.71	-0.57	-0.63	-0.55
S_{ku}	4.18	3.59	3.99	3.26	3.07	3.89	3.36	3.34	3.32	3.23	3.12	3.23
S_{ds}, mm^{-2}	42.75	37.25	38.00	39.25	42.25	39.25	42.50	39.75	46.00	47.75	46.25	48.50
S_{al}, mm	0.13	0.13	0.11	0.13	0.11	0.11	0.12	0.11	0.11	0.14	0.13	0.11
S_{tr}	0.63	0.65	0.57	0.71	0.69	0.67	0.73	0.67	0.67	0.81	0.77	0.63
S_{td}, °	0.0	0.0	0.0	89.50	89.50	89.50	0.00	0.00	0.00	63.35	-45.25	63.35
$S_{\Delta q}$	0.74	0.77	0.80	0.81	0.93	0.98	0.75	0.83	0.85	0.63	0.68	0.69
S_{sc}, μm^{-1}	0.02	0.03	0.03	0.02	0.02	0.03	0.02	0.02	0.02	0.02	0.02	0.02
S_{dr}, %	22.60	24.07	25.51	29.81	38.69	42.18	26.04	31.01	32.55	18.85	21.30	22.10
S_{bi}	0.70	0.69	0.66	0.72	0.73	0.74	0.72	0.71	0.72	0.67	0.71	0.66
S_{ci}	1.29	1.32	1.38	1.40	1.38	1.35	1.40	1.41	1.40	1.52	1.42	1.53
S_{vi}	0.17	0.16	0.16	0.18	0.17	0.18	0.19	0.18	0.17	0.18	0.18	0.17
S_t, µm	30.00	29.53	29.60	219.32	196.98	215.76	182.10	179.92	172.72	150.93	152.59	148.41
S_p, µm	207.9	201.4	208.9	69.43	63.42	68.63	66.46	56.38	62.27	58.28	53.47	61.13
S_v, µm	-0.37	-0.41	-0.21	149.89	133.56	147.13	115.64	123.54	110.45	92.65	99.12	87.28
p-value		0.17	0.39		0.72	0.17		0.94	0.51		0.20	0.58

Table I.4. A46H7V

Parameter	Sample 1			Sample 2			Sample 3			Sample 4		
	Measured	Johnson	Inverse	Measured	Johnson	Inverse	Measured	Johnson	Inverse	Measured	Johnson	Inverse
S_q, μm	78.75	79.33	78.38	69.98	72.21	70.46	82.38	85.86	80.83	78.51	77.28	79.24
S_z, μm	391.64	382.52	403.92	349.34	364.48	338.66	411.30	391.71	391.94	404.59	355.89	409.74
S_{sk}	-0.89	-0.92	-0.84	-0.88	-0.93	-0.83	-0.65	-0.74	-0.57	-0.62	-0.69	-0.78
S_{ku}	3.35	3.40	3.27	3.37	3.63	3.08	2.76	2.93	2.75	2.83	3.03	3.35
S_{ds}, mm^{-2}	4.25	6.44	7.44	4.63	6.56	6.75	4.56	4.06	5.25	4.94	4.06	5.38
S_{al}, mm	0.36	0.36	0.33	0.34	0.34	0.29	0.36	0.39	0.33	0.33	0.32	0.33
S_{tr}	0.77	0.77	0.71	0.73	0.67	0.72	0.70	0.64	0.73	0.71	0.80	0.73
S_{td}, °	0.00	0.00	0.00	18.10	18.10	18.10	0.00	0.00	0.00	89.50	89.50	89.50
$S_{\Delta q}$	0.62	0.69	0.69	0.60	0.71	0.67	0.68	0.80	0.75	0.68	0.73	0.73
S_{sc}, μm^{-1}	0.00	0.01	0.01	0.00	0.01	0.01	0.00	0.01	0.01	0.00	0.00	0.01
S_{dr}, %	17.73	21.60	21.74	16.37	22.74	20.59	21.36	28.63	25.38	20.81	24.22	24.01
S_{bi}	0.78	0.78	0.75	0.78	0.78	0.77	0.76	0.75	0.74	0.73	0.73	0.75
S_{ci}	1.27	1.24	1.33	1.27	1.25	1.27	1.32	1.29	1.36	1.38	1.36	1.33
S_{vi}	0.19	0.20	0.19	0.19	0.21	0.18	0.16	0.18	0.16	0.17	0.18	0.18
S_t, μm	433.42	399.44	447.62	388.08	395.71	361.08	440.70	402.20	427.04	439.70	430.39	438.51
S_p, μm	126.94	117.30	142.09	115.24	118.89	120.05	157.58	143.94	162.78	144.28	148.63	146.12
S_v, μm	306.48	282.14	305.53	272.84	276.82	241.02	283.12	258.26	264.26	295.43	281.76	292.38
p-value		0.15	0.41		0.20	0.67		0.26	0.47		0.38	0.67

Table I.5. B140H200V

Parameter	Sample 1			Sample 2			Sample 3			Sample 4		
	Measured	Johnson	Inverse	Measured	Johnson	Inverse	Measured	Johnson	Inverse	Measured	Johnson	Inverse
S_q, µm	13.68	13.55	13.67	13.56	13.54	12.87	11.04	11.85	11.12	11.25	11.69	12.98
S_z, µm	87.04	78.41	83.55	77.73	75.18	67.49	66.66	74.28	70.38	68.81	77.67	75.86
S_{sk}	-0.66	-0.54	-0.61	-0.57	-0.58	-0.31	-1.62	-1.60	-1.65	-1.30	-1.36	-1.54
S_{ku}	3.48	3.03	3.26	3.31	3.12	2.55	6.86	6.80	6.51	5.47	5.72	6.31
S_{ds}, mm^{-2}	32.56	39.89	40.56	28.70	35.15	34.75	46.61	52.04	57.41	48.46	50.19	52.26
S_{al}, mm	0.16	0.15	0.15	0.15	0.15	0.15	0.15	0.15	0.15	0.15	0.14	0.15
S_{tr}	0.80	0.75	0.75	0.69	0.41	0.57	0.75	0.64	0.53	0.75	0.57	0.61
S_{td}, °	89.50	0.00	89.50	89.50	89.50	89.50	-45.25	-45.25	-45.25	89.50	89.50	89.50
$S_{\Delta q}$	0.27	0.28	0.29	0.28	0.30	0.31	0.23	0.35	0.29	0.24	0.32	0.29
S_{sc}, μm^{-1}	0.01	0.01	0.01	0.01	0.01	0.01	0.01	0.01	0.01	0.01	0.01	0.01
S_{dr}, %	3.67	3.89	3.99	3.80	4.46	4.54	2.64	5.80	4.01	2.76	4.86	4.09
S_{bi}	0.68	0.69	0.68	0.68	0.69	0.65	0.81	0.82	0.93	0.78	0.83	0.82
S_{ci}	1.50	1.47	1.51	1.53	1.46	1.56	1.23	1.22	1.05	1.30	1.22	1.19
S_{vi}	0.19	0.17	0.18	0.17	0.17	0.15	0.23	0.24	0.24	0.21	0.22	0.23
S_t, µm	92.95	86.87	91.04	97.01	79.91	71.58	86.85	98.70	76.62	85.99	86.76	85.72
S_p, µm	29.18	30.60	28.47	27.26	30.43	26.28	20.97	16.07	16.90	21.35	19.19	22.96
S_v, µm	63.78	56.27	62.57	69.75	49.48	45.30	65.88	82.62	59.72	64.64	67.57	62.76
p-value		0.70	0.56		0.42	0.28		0.16	0.21		0.26	0.21

Table I.6. C80M7V

Parameter	Sample 1			Sample 2			Sample 3			Sample 4		
	Measured	Johnson	Inverse	Measured	Johnson	Inverse	Measured	Johnson	Inverse	Measured	Johnson	Inverse
S_q, μm	8.02	7.81	7.90	10.01	11.40	9.78	9.64	9.61	9.66	8.95	8.91	8.97
S_z, μm	62.00	60.82	61.42	64.65	77.39	70.68	64.58	62.34	63.81	55.95	52.04	55.45
S_{sk}	-1.83	-1.60	-1.61	-1.77	-1.99	-1.68	-1.01	-1.01	-0.94	-0.87	-0.75	-0.86
S_{ku}	10.14	7.55	7.39	7.16	8.29	7.05	5.18	5.33	4.21	4.02	3.59	3.88
S_{ds}, mm^{-2}	23.56	22.44	21.00	21.33	20.44	19.11	18.22	19.11	18.67	16.56	17.11	18.22
S_{al}, mm	0.17	0.13	0.12	0.17	0.13	0.13	0.13	0.13	0.13	0.12	0.12	0.12
S_{tr}	0.78	0.62	0.56	0.78	0.71	0.62	0.62	0.62	0.62	0.56	0.63	0.56
S_{td}, °	89.50	89.50	89.50	89.50	89.50	89.50	89.50	45.25	89.50	0.00	0.00	0.00
$S_{\Delta q}$	0.15	0.17	0.17	0.19	0.24	0.20	0.18	0.19	0.19	0.18	0.18	0.18
S_{sc}, μm^{-1}	0.00	0.00	0.00	0.00	0.00	0.00	0.00	0.00	0.00	0.00	0.00	0.00
S_{dr}, %	1.05	1.35	1.39	1.77	2.83	2.05	1.67	1.74	1.81	1.57	1.59	1.61
S_{bi}	0.75	0.79	0.78	0.87	0.90	0.85	0.72	0.69	0.72	0.70	0.70	0.73
S_{ci}	1.43	1.32	1.30	1.15	1.07	1.19	1.49	1.53	1.41	1.44	1.44	1.38
S_{vi}	0.24	0.23	0.25	0.24	0.26	0.24	0.20	0.20	0.19	0.21	0.19	0.19
S_t, μm	89.85	71.26	70.12	84.20	82.45	83.02	95.05	87.35	68.84	65.89	57.31	58.98
S_p, μm	24.37	15.47	16.73	18.04	14.43	17.95	25.83	22.13	19.92	22.13	17.56	19.37
S_v, μm	65.48	55.80	53.39	66.16	68.03	65.06	69.22	65.22	48.92	43.75	39.75	39.61
p-value		0.53	0.74		0.22	0.87		0.93	0.99		0.81	0.99

Appendix J

MATLAB scripts for the kinematic model

```
function f=gw_simulationa(vw,vs,ds,depth,wsurf,stepr_o,...
lenseg,varargin)

% F=GW_SIMULATIONA(VW,VS,DS,A,WORKPIECE,STEP,LENGTH,PSD,CPF)
% simulates surface grinding using
% probability distribution function.
% VW: workpiece speed, m/s.
% VS: wheel speed, rpm.
% DS: diameter of wheel, mm.
% A: depth of cut, micron.
% WORKPIECE: workpiece surface. max(max(wsurf))=0.
% STEP: distance between lines in workpiece
% and wheel topography, micron.
% LENGTH: a number of wheel samples in one wheel segment
% generated each times.
% PSD: power spectral densities of normalized wheel topography.
% CPF: probability distribution function.
% PSD and CPF should be paired. There could be more than
% one pairs of PSD and CPF in the arguments.
% F: result workpiece surface, in forms of array variables.


% setting critical attack angles.
% rub is angle at which grain starts to rub only.
% plough is angle at which grain starts to plough only
rub=0.0;
plough=0.0;
%*********************************************************************
% INITIATE
%*********************************************************************
% check whether there is pairs of power spectral density and Johnson
% parameters/ probability function.
LenVar= length(varargin); % number of arrays in varargin
if mod(LenVar,2)~=0
    error('there should be pairs of PSD and JS/CPF')
end
% Store PSD and JS/CPF
LenPair=LenVar/2;
gausspec=cell(LenPair,1);
js=cell(LenPair,1);
for r=0:(LenPair-1)
    gausspec{r+1}=varargin{2*r+1};
    js{r+1}=varargin{2*r+2};
end
% convert data unit
% convert wheel diamter -> radius mm -> micron
WheelRadius = (1000*ds)/2;
% convert wheel speed rpm -> rad/s
WheelSpeed = (2*pi*vs)/60;
```

```
% convert work speed
WorkSpeed = vw*10e6;
% store random state to re-simulate the same wheel surface
RandState=rand('state');

% simulate 1st wheel topography
TopoEdge=wheelsegment(gausspec,js,lenseg);
%  store wheel data
% number of datapoints per line in wheel topographical arrays

TopoPoint = size(TopoEdge,2);
% number of lines in wheel topographical arrays

TopoLine = size(TopoEdge,1) ;
% perimeter of wheel in micron

WheelPeri=2*WheelRadius*pi;
% step between lines in wheel topography

WheelStepy=stepr_o;
% number of simulations to complete one perimeter of wheel

TopoSim=round(WheelPeri/(WheelStepy*TopoLine));
[TopoEdge, TopoGrain]=sortgrainsep2...
(TopoEdge,depth,WheelStepy,WheelStepy);
% number of rows of array

TopoLine1=size(TopoEdge,1);
TopoEdge (active cutting edge)
TopoEdge=[TopoEdge; [0 0 0 0 0 0]];


% workpiece surface
% array for storage of workpiece topography

Result=wsurf;
% number of datapoints per line from workpiece

ResultPoint = size(Result,2);
% variable for number of lines in
%the result workpiece topography array

ResultLine = size(Result,1);
% step between lines in workpiece topography

WorkStepy=stepr_o;
% length of the workpiece specimen
WorkLen=(ResultLine-1)*stepr_o;

%*********************************************************************
% LOOP 1
%*********************************************************************

% variables for looping
% starting point for simulation

kh=-round(sqrt(WheelRadius^2-(WheelRadius-depth)^2)/WheelStepy);
stop_e=0.3;      % set the allowance for stopping loop 2
stop_loop=0;     % initiate the stopping criteria for loop 1
dis_count=1;     % counter of simulations of wheel topography
while (stop_loop==0)  % 1
```

```
%*********************************************************************
% LOOP TopoEdge TO CALCULATE CUTTING EDGE DEPTH OF CUT
%*********************************************************************
    r2=0;
    while r2<TopoLine1
        % loop through TopoEdge
        r2=r2+1;
        k=TopoEdge(r2,1);
        c2=TopoEdge(r2,2);
        WheelDisp = ((kh+k-1)*WheelStepy*WorkSpeed)/...
                (WheelSpeed*WheelRadius); % in micron
        WheelDispStep = round(WheelDisp/WorkStepy) ;
        GrainIndex = find(TopoGrain(:,1)==TopoEdge(r2,5));
        GrainRadius = TopoGrain(GrainIndex,2);
        % starting point for simulation

        TopoCen=[];
        % array for storing cutting edge depth of cut

        TopoDepth=[];
        TopoCen(1) = WheelRadius + TopoEdge(r2,4);
        TopoDepth(1) = TopoEdge(r2,3);
        % store the state of the interaction
        % between the grains and the workpiece

        TopoState=[];
        % get cross section of grain
        while (k==TopoEdge(r2+1))&(TopoEdge(r2,5)==TopoEdge(r2+1,5))
            r2=r2+1;
            m=TopoEdge(r2,2)-TopoEdge(r2-1,2)-1;
            for r=1:m
                TopoCen =[TopoCen (WheelRadius+TopoEdge(r2,4))];
                TopoDepth = [TopoDepth 0];
            end
            TopoCen =[TopoCen (WheelRadius + TopoEdge(r2,4))];
            TopoDepth = [TopoDepth TopoEdge(r2,3)];
        end
        % column position of last cutting edge
        c3=TopoEdge(r2,2);
%*********************************************************************
% CALCULATE CUTTING EDGES FORWARD
%*********************************************************************
        TopoCoordy = -1;
        x = WheelDispStep*WorkStepy;
        if x<0
            x=0;
            s_stepc=0;
        else
            s_stepc=WheelDispStep;
        end
        % calculated coordinate of cutting edge until
        % no cutting edge is lower surface
        while any(TopoCoordy < 0)&(x<=WorkLen)
                den=2*((TopoCen + (WorkSpeed/WheelSpeed)).^2);
                num=TopoCen*((x-WheelDisp)^2);
                TopoCoordy= - TopoDepth + (num./den)  ;
                if any(TopoCoordy < 0)
                x= x + stepr_o;
                s_stepc=s_stepc+1;
```

```
                % update workpiece surface
                [TopoCoordy,fc2,fc3,GrainState,GrainDepth,...
                 GrainAngle]=resultupdate2(Result(s_stepc,c2:c3),...
                 TopoCoordy, WorkStepy, c2, c3, TopoPoint,...
                 GrainRadius,rub, plough);
                TopoState=[TopoState;...
                 GrainIndex k GrainState GrainDepth GrainAngle];
                immed=TopoCoordy((c2-fc2+1):(c3-fc2+1));
                Result(s_stepc,c2:c3)=min(Result(s_stepc,c2:c3),...
                 immed);
                if fc2<c2
                    Result(s_stepc,fc2:c2-1)=Result...
                      (s_stepc,fc2:c2-1)+TopoCoordy(1:(c2-fc2));
                end
                if c3<fc3
                    Result(s_stepc,(c3+1):fc3)=Result(s_stepc,...
                      (c3+1):fc3)+TopoCoordy((c3-fc2+2):end);
                end
            end
        end
        % end calculated coordinate of cutting edge
%*********************************************************************
% CALCULATE CUTTING EDGES BACKWARD
%*********************************************************************
        TopoCoordy = -100.*ones(1,(c3-c2+1));
        stop5=0;
        x = (WheelDispStep - 1)*WorkStepy;
        if x>WorkLen
            x=WorkLen;
            s_stepc=ResultLine;
            s_stepd=ResultLine;
        else
            s_stepc=WheelDispStep;
            s_stepd=WheelDispStep;
        end
        % calculated coordinate of cutting edge
        % until no cutting edges is lower surface
        while (stop5==0)&(s_stepc>0) %5
                den=2*((TopoCen + (WorkSpeed/WheelSpeed)).^2);
                num=TopoCen*((x-WheelDisp)^2);
                TopoCoordy= - TopoDepth + (num./den);
            if any(TopoCoordy <Result(s_stepc,c2:c3) )
                x= x - stepr_o;
                [TopoCoordy,fc2,fc3,GrainState,GrainDepth,...
                GrainAngle]=resultupdate2(Result(s_stepc,c2:c3),...
                TopoCoordy, WorkStepy, c2, c3, ...
                TopoPoint, GrainRadius, rub,plough);
                TopoState=[GrainIndex k GrainState...
                GrainDepth GrainAngle; TopoState];
                immed=TopoCoordy((c2-fc2+1):(c3-fc2+1));
                Result(s_stepc,c2:c3)=(Result(s_stepc,c2:c3)>...
                immed).*immed+(Result(s_stepc,c2:c3)<...
                =immed).*Result(s_stepc,c2:c3);
                if fc2<c2
                    Result(s_stepc,fc2:c2-1)=Result...
                      (s_stepc,fc2:c2-1)+TopoCoordy(1:(c2-fc2));
                end
                if c3<fc3
                    Result(s_stepc,(c3+1):fc3)=Result...
                     (s_stepc,(c3+1):fc3)+TopoCoordy((c3-fc2+2):end);
                end
```

```
                s_stepc=s_stepc-1;
            else
                stop5=1;
            end
        end
        % check stop_loop condition whether
        % cutting edges is far above workpiece surface
        if (s_stepc>0)&(s_stepd==ResultLine)
            if (TopoCoordy - Result(s_stepc,c2:c3))>=stop_e
                stop_loop=1;
            end
        end
    end
    % end loop through TopoEdge
% ********************************************************************
% END LOOP TO CALCULATE CUTTING EDGE DEPTH OF CUT
% ********************************************************************
    kh=kh+TopoLine;
    % reset random state if the number of
    % wheel simulation is larger perimeter
    if (dis_count > TopoSim)
        rand('state',RandState);
        dis_count=0;
    end
    % simulate wheel topography
    TopoEdge=wheelsegment(gausspec,js,lenseg);
    [TopoEdge, TopoGrain]=sortgrainsep2...
    (TopoEdge,depth,WheelStepy,WheelStepy);
    fe=[fe; TopoEdge];
    fg=[fg; TopoGrain];
    TopoLine1=size(TopoEdge,1);
    TopoEdge=[TopoEdge; [0 0 0 0 0 0]];
    dis_count=dis_count+1;
end
% ********************************************************************
% END LOOP 1
% ********************************************************************
f=Result;

% ********************************************************************
% subfunction
%*********************************************************************
function f=wheelsegment(gausspec,js,lenseg)
%  F=WHEELSEGMENT(GAUSSPEC,JS,LENSEG) simulates
% grinding wheel topography using inverse probability
% distribution function.
% GAUSSPEC: power spectral density.
% JS: probability distribution function.
% LENSEG: a number of topography is required.
LenVar=length(gausspec);
[rg cg]=size(gausspec{1});
LenSeg=round(lenseg/LenVar);
f=zeros(LenSeg*LenVar*rg, cg);
r=1;
for r1=1:LenSeg
    for r2=1:LenVar
        f(r:(r+rg-1),:)=gw_inverse(gausspec{r2},js{r2});
        r=r+rg;
    end
end
```

```
%*********************************************************************
%subfunction
%*********************************************************************
function [fz,fc]=sortgrainsep1(distopo,depth,stepx,stepy)
% [FZ,FC]=SORTGRAINSEP1(DISTOPO,DEPTH,STEPX, STEPY) accepts
% a topography array of wheel (DISTOPO) and returns an array that
% contains topographical points of the wheel surface at which
% the grains will likely cut the workpiece
% DISTOPO: topographical array of wheel
% DEPTH: depth of cut
% STEPX: step between points in one line of topography
% STEPY: step between lines of topography
% FZ(:,1): row position of data points (k)
% FZ(:,2): column position of data points
% FZ(:,3): grain depth of cut (dis_sur)
% FZ(:,4): topographical data (dis_topo)
% FZ(:,5): index of grain that the cutting edge belongs
% FZ(:,6): curvature at cutting edge
% FC(:,1): grain index
% FC(:,2): grain mean radius
% FC(:,3): grain slope
% FC(:,4): maximum grain depth of cut

% find summit
[rz,cz]=size(distopo);
datamax=max(max(distopo));
z=depth + distopo - datamax;
pcount=0;
% non-zero depth of cut
for r=1:rz
    for c=1:cz
        if z(r,c)>0
            pcount=pcount+1;
            p(pcount,1)=r; p(pcount,2)=c; p(pcount,3)=z(r,c);
         end
     end
end
%
dissummit=zeros(rz,cz);          % array for storing grain index
discurve=zeros(rz,cz);           % array for storing curvature
cgrain=0;                        % counter for grit/grain
% identify grains
% loop 1
for rp=1:pcount
    rindex=p(rp,1);
    cindex=p(rp,2);
    boundary=[];
    % identify new grain
    if dissummit(rindex,cindex)==0
        k=1;
        boundary(1,1)=rindex;
        boundary(1,2)=cindex;
        cgrain=cgrain+1;
        dissummit(rindex,cindex)=cgrain;
    else
        k=0;
    end
    % identify grain membership
    % loop 2
    while k>0
        k1=0;
```

```
boundary1=[];
% loop through boundary
for rb=1:k
    rbindex=boundary(rb,1);
    cbindex=boundary(rb,2);
    curvepoint=0;
    % NW point
    r=rbindex-1; c=cbindex-1;
    if (r>0)&(c>0)
        if (z(r,c)>0)&(dissummit(r,c)==0)
            k1=k1+1;
            boundary1(k1,1)=r;
            boundary1(k1,2)=c;
            dissummit(r,c)=dissummit(rbindex,cbindex);
        end
    end
    % N point
    r=rbindex-1; c=cbindex;
    if (r>0)
        if  (z(r,c)>0)&(dissummit(r,c)==0)
            k1=k1+1;
            boundary1(k1,1)=r;
            boundary1(k1,2)=c;
            dissummit(r,c)=dissummit(rbindex,cbindex);
        end
    end
    % NE point
    r=rbindex-1; c=cbindex+1;
    if (r>0)&(c<=cz)
        if (z(r,c)>0)&(dissummit(r,c)==0)
            k1=k1+1;
            boundary1(k1,1)=r;
            boundary1(k1,2)=c;
            dissummit(r,c)=dissummit(rbindex,cbindex);
        end
    end
    % SW point
    r=rbindex+1; c=cbindex-1;
    if (r<=rz)&(c>0)
        if (z(r,c)>0)&(dissummit(r,c)==0)
            k1=k1+1;
            boundary1(k1,1)=r;
            boundary1(k1,2)=c;
            dissummit(r,c)=dissummit(rbindex,cbindex);
        end
    end
    % S point
    r=rbindex+1; c=cbindex;
    if (r<=rz)
        if (z(r,c)>0)&(dissummit(r,c)==0)
            k1=k1+1;
            boundary1(k1,1)=r;
            boundary1(k1,2)=c;
            dissummit(r,c)=dissummit(rbindex,cbindex);
        end
    end
    %
    if (rbindex-1)<=0
        discurve(rbindex,cbindex)=(distopo...
        (rbindex,cbindex)+ distopo(rbindex+2,cbindex)...
        -2*distopo(rbindex+1,cbindex))/stepy^2;
```

```
        elseif (rbindex+1)>rz
            discurve(rbindex,cbindex)=(distopo(rbindex,...
            cbindex)+distopo(rbindex-2,cbindex)...
            -2*distopo(rbindex-1,cbindex))/stepy^2;
        else
            discurve(rbindex,cbindex)=(distopo
            (rbindex+1,cbindex)+distopo(rbindex-1,cbindex)...
            -2*distopo(rbindex,cbindex))/stepy^2;
        end
        %
        % SE
        r=rbindex+1; c=cbindex+1;
        if (r<=rz)&(c<=cz)
            if (z(r,c)>0)&(dissummit(r,c)==0)
                k1=k1+1;
                boundary1(k1,1)=r;
                boundary1(k1,2)=c;
                dissummit(r,c)=dissummit(rbindex,cbindex);
            end
        end
        % W point
        r=rbindex; c=cbindex-1;
        if (c>0)
            if (z(r,c)>0)&(dissummit(r,c)==0)
                k1=k1+1;
                boundary1(k1,1)=r;
                boundary1(k1,2)=c;
                dissummit(r,c)=dissummit(rbindex,cbindex);
            end
        end
        % E point
        r=rbindex; c=cbindex+1;
        if (c<=cz)
            if (z(r,c)>0)&(dissummit(r,c)==0)
                k1=k1+1;
                boundary1(k1,1)=r;
                boundary1(k1,2)=c;
                dissummit(r,c)=dissummit(rbindex,cbindex);
            end
        end
        %
        if (cbindex-1)<=0
            curvepoint=(distopo(rbindex,cbindex)+...
            distopo(rbindex,cbindex+2)-2*distopo...
            rbindex,cbindex+1))/stepx^2;
        elseif (cbindex+1)>cz
            curvepoint=(distopo(rbindex,cbindex)+...
            distopo(rbindex,cbindex-2)-2*distopo...
            (rbindex,cbindex-1))/stepx^2;
        else
            curvepoint=(distopo(rbindex,cbindex+1)+...
            distopo(rbindex,cbindex-1)-2*distopo...
            (rbindex,cbindex))/stepx^2;
        end
        discurve(rbindex,cbindex)=-(discurve...
        (rbindex,cbindex)+curvepoint)/2;
    end
    % end loop through boundary
    k=k1;
    boundary=boundary1;
end
```

```
    % end loop 2
end
% end loop 1

% storing info
pcount=0;
for r=1:rz
    for c=1:cz
        if z(r,c)>0
            pcount=pcount+1;
            fz(pcount,1)=r;      % row position
            fz(pcount,2)=c;      % column position
            fz(pcount,3)=z(r,c);         % grain depth of cut
            fz(pcount,4)=distopo(r,c);   % topography
            fz(pcount,5)=dissummit(r,c); % grain grouping
            fz(pcount,6)=discurve(r,c); % curvature
        end
    end
end
% sort in order of grain membership, row, column positions
fz=sortrows(fz,[5 2 1]);
% average curvature of grains
fc=zeros(cgrain,4);
fz2=[];
for r=1:cgrain
    ff=fz(fz(:,5)==r,:);
    fc(r,1)=r;
    fc(r,2)=sum(ff(:,6))/size(ff,1);
    fc(r,2)=1/fc(r,2);
    fc(r,4)=max(ff(:,3));
    fc(r,3)=acos((fc(r,2)-fc(r,4))/fc(r,2));
    [rff,cff]=size(ff);
    rowindex=ff(ff(:,3)==fc(r,4),1);
    fz1=[];
    fz1=ff(1,:);
    fz1(1,1)=rowindex(1);
    for rf=2:rff
        if (ff(rf,2)~=fz1(end,2))
            fz1=[fz1; ff(rf,:)];
            fz1(end,1)=rowindex(1);
        elseif (ff(rf,2)>fz1(end,3))
            fz1(end,3:end)=ff(rf,3:end);
        end
    end
    fz2=[fz2; fz1];
end
fz=fz2;
%*********************************************************************
%subfunction
%*********************************************************************
function [fdis,fc2,fc3,fstate,fdepth,fangle]...
=resultupdate2(worksurf, topocoordy, stepx,...
c2, c3, point, radius,rub,plough)
% [FDIS,FC2,FC3,STATE,FDEPTH] =RESULTUPDATE(
% WORKSURF, TOPOCOORDY, STEPX, C2, C3, POINT, RADIUS, RUB, PLOUGH)
% Updates  profile of cross section of workpiece,
% accounting ploughing action.
% FDIS: displaced profile.
% FC2, FC3: limit points (left, right) of the ridge.
% FSTATE: 1: the grain rubs, 2: the grain plows,
% 3: the grain cuts, 0: undecided or untouched.
```

```
% FDEPTH: maximum grain depth of cut.
% FANGLE: attack angle.
% WORKSURF: profile of workpiece surface.
% TOPOCOORDY: coordinate of cutting edge section.
% STEPX: step between points in one line of workpiece topography.
% C2, C3: column positions of 1st and
% last cutting edges in cutting section.
% POINT: number of points in one line of workpiece topography.
% RADIUS: grain radius.
% RUB: the critical attack angle at which
% or smaller the grain will only rub.
% PLOUGH: the critical attack angle at which
% or smaller the grain will only plough.


% set plowing ratio at which displaced material
% will form ridge for plowing and cutting
 PloughRatio=0.0;
 CutRatio=0.0;
 fc2=c2;
 fc3=c3;
 fdis=worksurf;
 fangle=0;
 % decide the maximum grain depth of cut
 TopoDif=topocoordy-worksurf;
 fdepth=-min(TopoDif);
 % if the cutting edges do not cut the surface
 % or grain radius<=0 then return
 if (fdepth<0)|(radius<=0)
     fstate=0;
     return
 end
 % determine the attack angle
 GrainAngle=acos((radius-fdepth)/radius); fangle=GrainAngle;
  % detremine if rub, plough or cut
 if GrainAngle<=rub
     fstate=1;       % the grain rubs
 elseif GrainAngle<=plough
     fstate=2;       % the grain plough
 else
     fstate=3;       % the grain cuts
 end
 % if the grain rubs or one-point grain then return
 if (fstate==1)
     return
 end
 % determine the removed area
 TopoPoint=size(topocoordy,2);
 RemovedArea=0;
 for c=1:(TopoPoint-1)
     h1=TopoDif(c);
     h2=TopoDif(c+1);
     if (h1<=0)&(h2<=0)
         RemovedArea=RemovedArea + abs(stepx*(h1+h2)/2);
     elseif (h1<=0)
         RemovedArea=RemovedArea + 0.5*stepx...
         *(h1^2)/(abs(h1)+abs(h2));
     else
         RemovedArea=RemovedArea + 0.5*stepx...
          *(h2^2)*(h2<0)/(abs(h1)+abs(h2));
     end
```

```
end
%
RemovedArea=RemovedArea+stepx*abs(TopoDif(1))*(TopoDif(1)<0)/2;
RemovedArea=RemovedArea+stepx*abs(TopoDif(end))*(TopoDif(end)<0)/2;
% triangular ridge
if fstate==3
    RemovedArea=RemovedArea*CutRatio;
else
    RemovedArea=RemovedArea*PloughRatio;
end
nridge=round(sqrt(RemovedArea/(2*tan(GrainAngle)))/stepx);
% update TopoCoordy
if nridge >1
    hridge=(stepx*tan(GrainAngle)).*[[0:nridge] [nridge-1:-1:1]];
elseif nridge==1
    hridge=[0 0.5*RemovedArea/stepx];
end
if nridge~=0
    % right ridge
    if (2*nridge+c3)>point
        topocoordy=[topocoordy hridge(1:(point-c3))];
        fc3=point;
    else
        topocoordy=[topocoordy hridge];
        fc3=c3+2*nridge;
    end
    % left ridge
    if (c2-2*nridge)<=0
        topocoordy=[hridge(end:-1:(2*nridge-c2+2)) topocoordy];
        fc2=1;
    else
        topocoordy=[hridge topocoordy];
        fc2=c2-2*nridge;
    end
end
fdis=topocoordy;
```

Appendix K

Three-dimensional surface characterisation parameters of the measured and generated grinding wheel surfaces

Table K.1 3-D surface characterisation parameters of the mild steel ground surfaces

Parameter	Sample 1	Sample 2	Sample 3	Sample 4	Average
S_q, μm	0.73	0.77	0.78	0.84	0.78
S_z, μm	4.18	4.34	4.97	5.33	4.71
S_{sk}	0.04	-0.15	-0.10	-0.20	-0.10
S_{ku}	2.46	2.69	2.55	2.71	2.60
S_{ds}, mm^{-2}	51.17	43.75	54.00	56.45	51.34
S_{al}, mm	0.04	0.04	0.04	0.04	0.04
S_{tr}	0.06	0.04	0.05	0.03	0.04
S_{td}, °	0.00	0.00	0.00	0.00	0.00
$S_{\Delta q}$	0.03	0.03	0.03	0.03	0.03
S_{sc}, μm^{-1}	0.001	0.001	0.001	0.001	0.001
S_{dr}, %	0.04	0.04	0.04	0.04	0.04
S_{bi}	0.62	0.63	0.63	0.65	0.63
S_{ci}	1.65	1.61	1.69	1.58	1.63
S_{vi}	0.12	0.15	0.15	0.16	0.14
S_t, μm	4.36	4.75	7.35	6.36	5.70
S_p, μm	2.27	2.49	4.44	3.91	3.28
S_v, μm	2.09	2.26	2.91	2.46	2.43

Table K.2 3-D surface characterisation parameters of the simulated mild steel ground surfaces

Parameter	Sample 1	Sample 2	Sample 3	Sample 4	Average
S_q, µm	1.10	1.07	1.03	1.00	1.05
S_z, µm	5.52	5.13	5.61	5.30	5.39
S_{sk}	-0.06	-0.15	-0.19	-0.35	-0.19
S_{ku}	2.69	2.41	2.90	2.81	2.70
S_{ds}, mm^{-2}	13.48	15.14	15.82	15.43	14.97
S_{al}, mm	0.04	0.04	0.04	0.04	0.04
S_{tr}	0.04	0.05	0.04	0.04	0.04
S_{td}, °	0.00	0.00	0.00	0.00	0.00
$S_{\Delta q}$	0.04	0.04	0.04	0.04	0.04
S_{sc}, μm^{-1}	0.001	0.001	0.001	0.001	0.001
S_{dr}, %	0.08	0.08	0.07	0.07	0.07
S_{bi}	0.60	0.63	0.66	0.65	0.64
S_{ci}	1.67	1.61	1.55	1.54	1.59
S_{vi}	0.14	0.13	0.16	0.16	0.15
S_t, µm	6.39	5.58	6.90	6.10	6.24
S_p, µm	3.61	2.79	4.17	3.21	3.44
S_v, µm	2.78	2.80	2.73	2.89	2.80

Table K.3 3-D surface characterisation parameters of the measured D2 ground surfaces

Parameter	Sample 1	Sample 2	Sample 3	Sample 4	Average
S_q, µm	0.33	0.35	0.31	0.35	0.34
S_z, µm	2.33	2.52	2.00	2.21	2.26
S_{sk}	-0.69	-0.38	-0.46	-0.40	-0.48
S_{ku}	4.55	3.50	3.44	3.20	3.67
S_{ds}, mm^{-2}	53.52	55.47	55.08	55.47	54.89
S_{al}, mm	0.04	0.04	0.04	0.04	0.04
S_{tr}	0.06	0.06	0.05	0.05	0.05
S_{td}, °	0.00	0.00	0.00	0.00	0.00
$S_{\Delta q}$	0.01	0.01	0.01	0.01	0.01
S_{sc}, μm^{-1}	3.03×10^{-4}	3.40×10^{-4}	2.90×10^{-4}	3.57×10^{-4}	3.23×10^{-4}
S_{dr}, %	0.01	0.01	0.01	0.01	0.01
S_{bi}	0.69	0.65	0.64	0.66	0.66
S_{ci}	1.52	1.61	1.60	1.58	1.58
S_{vi}	0.20	0.18	0.18	0.17	0.18
S_t, µm	2.85	2.71	2.21	2.43	2.55
S_p, µm	1.02	1.05	1.07	1.17	1.08
S_v, µm	1.83	1.65	1.14	1.26	1.47

Table K.4 3-D surface characterisation parameters of the simulated D2 ground surfaces

Parameter	Sample 1	Sample 2	Sample 3	Sample 4	Average
S_q, µm	0.42	0.41	0.37	0.40	0.40
S_z, µm	2.46	2.38	2.46	2.33	2.41
S_{sk}	-0.70	-0.80	-0.76	-0.69	-0.74
S_{ku}	4.22	4.09	5.38	4.13	4.46
S_{ds}, mm^{-2}	22.46	23.63	23.05	21.68	22.71
S_{al}, mm	0.04	0.04	0.04	0.04	0.04
S_{tr}	0.06	0.06	0.06	0.06	0.06
S_{td}, °	0.00	0.00	0.00	0.00	0.00
$S_{\Delta q}$	0.02	0.01	0.01	0.01	0.01
S_{sc}, μm^{-1}	$3.75x10^{-4}$	$3.52 x10^{-4}$	$3.30 x10^{-4}$	$3.68 x10^{-4}$	$3.56 x10^{-4}$
S_{dr}, %	0.01	0.01	0.01	0.01	0.01
S_{bi}	0.69	0.74	0.69	0.69	0.70
S_{ci}	1.41	1.30	1.44	1.40	1.39
S_{vi}	0.26	0.27	0.26	0.27	0.26
S_t, µm	2.56	2.53	2.74	2.41	2.56
S_p, µm	1.34	1.34	1.45	1.21	1.34
S_v, µm	1.21	1.19	1.29	1.20	1.22